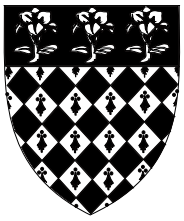
Investigation of plasticity mechanisms in shock-compressed matter via femtosecond x-ray diffraction



Marcin Sliwa

Magdalen College

University of Oxford



A thesis submitted for the degree of

Doctor of Philosophy

Hilary 2019

Acknowledgements

I would like to thank a number of people who made this work possible.

First of all, I would like to express my gratitude to my supervisor, Justin Wark, for giving me the opportunity to work on this project and for his guidance over the course of my graduate career. I would like to thank all members, past and present, of the Wark group; in particular, David McGonegle, who introduced me to the field of high-pressure research and who always offered invaluable advice, and Paddy Heighway, for his helpful insights and contribution to our research. My thanks go to my collaborators, especially to Chris Wehrenberg, for the opportunity to work on his experimental campaign as well as to all the researchers contributing to that work, to Rob Rudd, without whom a large portion of the work on simulations would not have been possible, and to Bruce Remington and LLNL for funding my research and their continuing support.

I would like to thank my friends, who made my stay in Oxford a wonderful experience. Thanks goes out to Elizabeth, a pianist with a suspiciously extensive knowledge of high-pressure crystallography and to Nile Rodgers for keeping me sane.

Finally, I thank my parents and Coco for the support and unlimited dedication they have given me throughout my life.

Abstract

The microstructural evolution of dynamically-compressed metals has been an area of active research for decades. This work uses a method of x-ray diffraction from highly-textured tantalum foils in order to identify plastic mechanisms mediating plastic deformations in shock-compressed tantalum. The obtained data provides evidence of shock-induced lattice rotations as well as the first *in situ* observation of shock-induced twinning. The study extends into an analysis of data capturing material as it returns to ambient conditions. It outlines a method of extracting time and depth-dependent strain profiles within the Ta target as the release wave travels back into the bulk of the sample. In agreement with molecular dynamics simulations, the lattice rotation and the twins that are formed under shock compression are observed to be almost fully eliminated by the rarefaction process. Finally, the investigation of thermal effects present during shock release is performed. Immediately after release, the temperatures of the samples are inferred from changes in the atomic lattice spacing which are the result of thermal expansion. It is found that simulations and experimental data suggest significantly larger temperatures of a material after its return to ambient condition than predicted by the theory of isentropic release.

Contents

List of Figures **vii**

List of Abbreviations **x**

1 Introduction **1**
1.1 Shock compression of solids and motivations for this study 1
1.2 Compression methods and diagnostics 3
1.3 Thesis layout and role of the author 6
1.4 List of publications 7

2 Background theory **9**
2.1 Crystallography 10
2.1.1 Crystal structure 10
2.1.2 Directions and planes 13
2.1.3 Reciprocal lattice 14
2.1.4 Strain 16
2.1.5 Stress 19
2.1.6 Elasticity 21
2.1.7 Plasticity 23
2.2 X-ray diffraction 29
2.2.1 Bragg's law 31
2.2.2 Laue condition 31
2.2.3 Equivalence of Bragg and Laue conditions 32
2.2.4 Scattering amplitude 33
2.2.5 Powder diffraction 35
2.2.6 Ewald sphere 36
2.2.7 Fibre diffraction 38
2.3 Shock waves 38
2.3.1 The Rankine-Hugoniot equations 39
2.3.2 Hugoniot 43
2.3.3 Shock waves in solids 44
2.3.4 Release 46

2.4 Computational methods 47
2.4.1 Molecular dynamics simulations 47
2.4.2 The LAMMPS code 48
2.4.3 Interatomic potentials 49
2.4.4 X-ray diffraction pattern simulation from MD 50
2.4.5 Hydrodynamic simulations 51
2.5 X-ray Free Electron Laser 51

3 Shock compression of tantalum **54**
3.1 Motivation and literature overview 55
3.2 Experimental setup 59
3.2.1 Laser-driven shocks 59
3.2.2 X-ray source 61
3.2.3 Targets 63
3.2.4 VISAR 64
3.2.5 CSPADs and data collection 67
3.2.6 Ambient data 70
3.2.7 Driven data 73
3.3 Liquid diffraction 76
3.4 Data analysis 88
3.5 Residual elastic shear stress 91
3.6 Driven textural changes 93
3.7 Equivalent plastic shear strain 102
3.8 Molecular dynamics simulations (shock) 106
3.9 Summary 113

4 Shock release of tantalum **115**
4.1 Introduction 116
4.2 Diffraction pattern interpretation 118
4.2.1 Inverted lattice rotations 119
4.2.2 Detwinning 120
4.3 Molecular dynamics simulations (release) 123
4.4 Strain profile evolution 125
4.4.1 X-ray halo 126
4.4.2 Algorithm 127
4.4.3 Release modelling 132
4.4.4 Strain profile in simulations (MD) 137
4.4.5 Strain profile in simulations (HYADES) 138
4.4.6 Results 140
4.5 Summary 142

5 Thermal effects upon shock breakout **144**
5.1 Introduction 145
5.2 Grüneisen parameter in MD 146
5.3 Elastic release 151
5.4 Heating upon shock breakout (MD) 158
5.5 Heating upon shock breakout (experiment) 163
5.6 Summary 171

6 Summary and future work **173**
6.1 Summary 173
6.2 Future work 175

Appendices

A HYADES **177**

References **180**

List of Figures

2.1 Primitive lattice vectors 11
2.2 Conventional unit cell 11
2.3 Cubic Bravais structures 12
2.4 Basis 12
2.5 Lattice planes 14
2.6 Normal and share strains 16
2.7 Deformation of infinitesimal element 17
2.8 Displacement tensor decomposition 19
2.9 Stress tensor 20
2.10 Slip in a perfect crystal 24
2.11 Edge dislocation 25
2.12 Screw dislocation 26
2.13 Glide 27
2.14 Slip 28
2.15 Twinning 30
2.16 Bragg's law 31
2.17 Laue condition 33
2.18 Powder diffraction 36
2.19 Ewald construction 37
2.20 Fibre diffraction 39
2.21 Shock steepening 40
2.22 Moving piston 41
2.23 Hugoniot 43
2.24 Shock waves in solids 44
2.25 Release 47
2.26 XFEL setup 52
2.27 Electron microbunching 53

3.1 Ta Phase Diagram 56
3.2 Laser-ablation 59
3.3 Laser pulse shape 60
3.4 X-ray attenuation coefficient 61

3.5 Ta pole plots . . . 63
3.6 Liquid Ta - hydrodynamic shock position modeling . . . 64
3.7 VISAR setup . . . 65
3.8 VISAR images . . . 68
3.9 VISAR - velocity profile . . . 68
3.10 Experimental setup . . . 69
3.11 Ambient XRD . . . 71
3.12 χ angle illustration . . . 72
3.13 Driven XRD lineout . . . 73
3.14 Pressure state - XRD vs VISAR . . . 74
3.15 XRD peak lineout fit . . . 75
3.16 Liquid XRD . . . 77
3.17 Liquid XRD - mask . . . 78
3.18 Liquid XRD - background noise removal . . . 78
3.19 Driving laser influence on the XRD signal . . . 79
3.20 Self-attenuation geometry analysis . . . 80
3.21 X-ray attenuation factor . . . 82
3.22 Atomic form factor . . . 83
3.23 Structure factors of liquid Ta . . . 85
3.24 Atomic pair distribution in liquid Ta . . . 85
3.25 Liquid XRD - peak position extraction . . . 86
3.26 Pressure vs. density comparison - liquid Ta analysis . . . 87
3.27 Example of Pseudo-Voigt fit to XRD data . . . 89
3.28 'Crater' peak . . . 90
3.29 Strength measurement sensitivity . . . 91
3.30 Strength measurement analysis . . . 92
3.31 Driven XRD data . . . 94
3.32 Twin fraction vs. pressure . . . 96
3.33 Plane multiplicity for twin fraction calculation . . . 97
3.34 Lattice rotations . . . 98
3.35 Peak broadening analysis - rotations . . . 98
3.36 Lattice rotation vs. pressure . . . 99
3.37 Rotations induced by twinning . . . 101
3.38 Equivalent plastic strain . . . 104
3.39 Shear stress during shock in MD . . . 108
3.40 Lattice rotations in MD . . . 109
3.41 Shocked Ta FT . . . 110
3.42 Fibre-Textured FT . . . 111
3.43 Raytraced FT . . . 112

4.1 XRD on release . . . 119
4.2 Residual lattice rotations . . . 120
4.3 Ta sample – micrograph . . . 121
4.4 Release in molecular dynamics simulations (100GPa) . . . 122
4.5 Release in molecular dynamics simulations (50GPa) . . . 122
4.6 MD: dislocation evolution . . . 124
4.7 X-ray halo removal . . . 126
4.8 X-ray halo removal (lineouts) . . . 128
4.9 Extraction of release path . . . 130
4.10 Strain extraction algorithm performance . . . 131
4.11 Strain extraction of the known profile . . . 133
4.12 XRD lineout fit . . . 134
4.13 Stain profile extraction: free parameters $\delta\omega$ and w . . . 134
4.14 Release modelling . . . 135
4.15 Release isentrope and bulk sound speed . . . 136
4.16 Release profiles in simulations . . . 138
4.17 Strain profile evolution on release . . . 141

5.1 Grüneisen paramter in MD . . . 148
5.2 Grüneisen parameter based on Zhou potential . . . 149
5.3 Theoretical isentropic cooling in MD . . . 150
5.4 Grüneisen parameter temperature dependence in MD . . . 150
5.5 Elastic release at different timescales . . . 153
5.6 Grüneisen parameter: 1D vs. 3D . . . 154
5.7 Grüneisen parameter: static vs. dynamic at 300 K . . . 155
5.8 Elastic release at 1000 K . . . 157
5.9 Thermal history of a Ta element: MD . . . 159
5.10 Quasi-isentropic elastic release in MD . . . 160
5.11 Plastic heating on release in MD . . . 162
5.12 Thermal expansion in XRD . . . 163
5.13 HYADES (Ta in tension) . . . 164
5.14 VISAR trace - pressure reduction . . . 165
5.15 Coefficients *kappa* in MD . . . 167
5.16 Equivalent strain analysis . . . 168
5.17 Temperature on release: XRD data . . . 169

List of Abbreviations

bcc . . . . . Body Centred Cubic

CSPADs . . . Cornell-SLAC Pixel Array Detector

EAM . . . . . Embedded Atom Model

EOS . . . . . Equation of State

fcc . . . . . Face Centred Cubic

FT . . . . . Fourier Transform

HEL . . . . . Hugoniot Elastic Limit

ICF . . . . . Inertial Confinement Fusion

LAMMPS . . Large-scale Atomic/Molecular Massively Parallel Simulator

LCLS . . . . . Linac Coherent Light Source

LLNL . . . . . Lawrence Livermore National Laboratory

MD . . . . . Molecular Dynamics

MEC . . . . . Matter in Extreme Conditions

PADG . . . . . Per-Atom Deformation Gradient

SLAC . . . . . Stanford Linear Collider

VISAR . . . . Velocity Interferometer System for Any Reflector

XFEL . . . . . X-ray Free Electron Laser

XRD . . . . . X-ray Diffraction

1 Introduction

Contents

1.1 Shock compression of solids and motivations for this study 1
1.2 Compression methods and diagnostics 3
1.3 Thesis layout and role of the author 6
1.4 List of publications 7

1.1 Shock compression of solids and motivations for this study

The second half of the 19th century is widely regarded as the inception of the field of shock physics research. Scottish engineer William J.M. Rankine and French engineer Pierre-Henri Hugoniot laid down the theoretical foundations for modern shock compression research by deriving a set of conservation laws, famously known as the Rankine-Hugoniot equations, which describe the evolution of a shock wave. Rankine's famous paper, 'On the Thermodynamic Theory of Waves of Finite Longitudinal Disturbance' [1] asserted that derived relations must hold for: 'any substance, whether gaseous, liquid, or solid'. However, the subsequent decades showed an unbalanced progress between the various states of matter in terms of

shock physics research [2], with solid-compression developing relatively slowly. The main reason for these early struggles was the lack of experimental diagnostics fast enough to capture sub microsecond shock phenomena in solids, which become available – with few exceptions – only after World War II [3]. Military motivations, including the race to create the atomic bomb, brought attention to solids at high pressure conditions. It is not a coincidence that the period of the 1940s and 1950s was when experimental shock compression started taking off.

These initial reasons for solid-compression research rapidly evolved into an area of interest shared by a wide scientific community, with a broad range of possible applications. One of the beneficiaries of the emerging technologies was the geophysics community. The study of minerals at high pressures was found to be critical to understanding the composition and structure of planetary interiors [4]. However, the study of high pressure conditions *in situ* remained challenging due to the limitations of the static compression methods available at the time. In order to better explore high density states, scientists used dynamic compression methods enabling them to access higher compression conditions. Perhaps one of the most spectacular contributions to early experimental shocked material research was the work conducted on shock-induced polymorphic phase transitions. By analysing the shock wave profile in iron, Bancroft [5] and Walsh [6], observed a crystallographic structure change α–ϵ (body-centred cubic to hexagonal close packed). The importance of their discovery in the geophysics community was enhanced by iron's significant presence in the Earth's core composition.

Since the 1960s, another active area of research where shock waves find their application is the pursuit of Internal Confinement Fusion (ICF). This concept relies on the powerful shock compression of a capsule containing a mixture of deuterium and tritium to sufficiently high density conditions that would initiate nuclear reaction and release a significant amount of energy. ICF has come to be widely regarded as a technology which has the potential to become a means of obtaining clean energy in the future [7].

Throughout many years of research, it has been proven that static and dynamic compression methods are complementary, not interchangeable, in their nature, as different methods of compression result in a different responses of the system. For example, the planarity of shock waves is associated with uniaxial compression, which causes materials to behave differently depending on the crystallographic direction of the compression [8, 9]. Weak shock causes temporary elastic deformation which, according to Hook's law, maintains the original structure of materials after the return to ambient conditions. However, once the crystal is shocked above its yield limit, the built-up shear stress is relieved and the material starts to flow plastically. Such plastic deformation can occur via multiple mechanisms. The material can experience the martensitic phase transformation, or the generation of structural defects and their subsequent motion. An understanding of the details of these mechanisms is crucial for engineering. For example, high strain-rate deformations are the main subject of designing ballistic penetrators [10], high-performance ceramics [11] and spacecraft shielding [12, 13]. Moreover, structural deformations at asteroid impact sites can give us information about the history of those destructive events [14]. It is clear that the investigations of mechanisms underlying deformation processes are an important part of active research. Despite many experimental, theoretical and computational efforts to understand shock plasticity physics, many questions, such as what mechanisms mediate deformations, how they vary for different crystallographic structures, and what the temperature of the shocked material is, remain as yet unanswered. This thesis will tackle a few of these challenges.

1.2 Compression methods and diagnostics

Over the years, a number of methods allowing researchers to generate shock waves in controllable conditions have been developed, progressively pushing the limit of achievable pressures. At their origin, shock experiments relied on the use of explosive materials in direct contact with the examined sample reaching pressures of a few tenths of GPa [6, 15]. By utilising the flying plate technology, pressures of the order of a Mbar became accessible [16, 17]. The limit on the amount of

compression generated by this method was related to the maximal particle velocity, which could not exceed the detonation velocity of the explosives (∼5 km/s).

The next stage of technological development was the invention of the gas-gun [18]. This concept relied on the energy transfer from pressurised gas to a high velocity flying plate, which was able to reach higher pressure states in a more controllable manner [19]. Those methods, generating particle velocities up to 15 km/s, pushed high pressure studies to several hundreds of GPa range [20, 21].

The invention of the laser in 1960 quickly found its application worldwide including among the shock compression community. Pioneering works in the field of laser-matter interaction brought to life many new technological advancements. Among the most important of these was the generation of shocks [22–24]. The idea of laser-induced shocks relies on the use of high-power laser systems interacting with the surface of a driven sample via a process called *laser ablation*. Through this process the energy of the electromagnetic wave is transferred to the energy of the ions in the solid. If the energy of the light is high enough, the surface of the driven material is transformed into plasma, which expands away from the sample. According to Newton's action-reaction law, this rapid process launches a compression wave into the bulk of the investigated material. The continual improvement of the power of lasers recently resulted in 5 TPa shock compression using over 2 TW-system available at the National Ignition Facility at the Lawrence Livermore National Laboratory (LLNL) in California, USA [25]. Such high-power transfer is not the only valuable feature of laser-compression experiments. Complex pulse-shaping capabilities enable the customisation of the driver's evolution, the most prominent of which is ramp compression, where the intensity of the pulse (and therefore the strength of the compression wave) increases in time [26]. By reducing the strain rate associated with the deformation, ramp compression reduces the amount of heating induced in the sample, providing an opportunity to keep it in the solid phase for a larger range of pressures than a shock wave would achieve before crossing the melting curve.

Lasers have found their application not only in producing compression waves, but also in detecting properties of compressed solids. An example of a well established diagnostic of shocks in solids is the Velocity Interferometer System for Any Reflector (VISAR) [27, 28]. By monitoring the velocity of the free surface of a shocked sample, it provides information about the features of shock including its strengths and localisation in time.

X-rays are the most effective means of studying crystalline materials since their wavelength is comparable to the distance between atoms in a crystal structure. The application of x-ray diffraction techniques to a dynamically-compressed sample was initiated in an experiment by Johnson *et al.* [29–32] in the 1970s in which x-rays, produced by a flash diode, were diffracted from a shock-compressed LiF crystal. The need for improving data quality and the ability to capture deformation events at shorter timescales led x-ray generation development towards laser plasma sources [33–36]. In the 1980s Wark *et al.* [37, 38] pioneered the use of laser pulses for both driving and probing samples. By utilising a quasi-monochromatic x-ray source, their analysis of the single diffraction line provided the *in situ* evidence for crystal deformation at the lattice level. Similar experiments performed by Kalantar *et al.* [39, 40] incorporated a wide-angle geometry allowing for the analysis of multiple reflections. Within the last several years, 3rd-generation light sources have become a popular option for studying dynamically-compressed systems [41–44], including the recent capture of multiple subsequent images of a single shock event through high probe repetition rate [45]. With the advent of XFELs such as the Linac Coherent Light Source (LCLS) at the Stanford Linear Accelerator Center (SLAC), single-shot 100-fs diffraction patterns can be obtained from laser-shocked crystals, providing lattice-level information on a timescale shorter than even the fastest phonon period. An improvement in x-ray brightness of the order of 10^9 in comparison to other available light sources, as well as a high operational repetition rate have facilitated a significant amount of work to be produced [46–50] since LCLS's first run in 2009.

The work presented in this thesis describes a dynamic compression experiment performed at SLAC using the LCLS beam. It describes a study of plasticity during

shock compression and subsequent release as well as an investigation of thermal effects during unloading to ambient conditions.

1.3 Thesis layout and role of the author

Due to their high complexity, the dynamic compression experiments at major US laser facilities very often require the joint effort of a large number of researchers at various stages of the experimental campaign. The experimental work presented in this thesis is no exception; collaboration between the University of Oxford and LLNL was supported by scientists from the University of York and Los Alamos National Laboratory as well as staff scientists from SLAC. The purpose of this section is to provide an outline of the content of the chapters and indicate the contributions of the author. The contributions of other researchers will be explicitly identified.

Chapter 2 provides an outline of the background theory used in this thesis. It covers basic crystallography, x-ray diffraction methods, the physics of shock waves, and computational methods. This section is based on a variety of resources appropriately referenced.

Chapter 3 introduces the x-ray diffraction experiment to study plastic deformation in shock-compressed Ta. The experiment was performed by C. E. Wehrenberg, D. McGonegle, C. Bolme, A. Higginbotham, A. Lazicki, H. J. Lee, B. Nagler, H. S. Park, B. A. Remington, D. Swift, and J. S.Wark. The experimental targets were designed, manufactured, and characterized by C. E. Wehrenberg and LLNL. The analysis and interpretation of the experimental data, leading to the observation of shock-induced lattice rotations and twinning, was performed by the author, C. E. Wehrenberg, D. McGonegle, A. Higginbotham, A. Lazicki, B. A. Remington, R. E. Rudd, M. Suggit, and J. S.Wark. The work on molecular dynamics (MD) simulations was performed by the author, D. McGonegle, A. Higginbotham, L. Zepeda-Ruiz, and R. E. Rudd. During the analysis of the MD simulations, the author used some of the codes developed by other members of the Wark group, specifically Son-of-Howard, per-atom deformation gradient code, and DIFFRACT, which were developed by A. Higginbotham, and code for x-ray diffraction (XRD)

image warping to (2θ, ϕ) space developed by D. McGonegle. The rest of the analysis was performed using tools developed by the author.

Chapter 4 continues with investigations of plasticity on a dataset capturing Ta in release. It describes the reversal of microstructural evolution, specifically reversed lattice rotations and detwinning. The chapter describes the study of the evolution rarefaction waves in Ta during unloading. The details of the code, developed by the author to extract strain profiles from the XRD images, are provided. The results are compared against the output of the molecular dynamics and hydrodynamics simulations. The output of HYADES, a hydrodynamics code, was preprocessed by the code developed by P. G. Stubley.

Chapter 5 describes the study of thermal effects during shock release. It starts with a detailed study of the Grüneisen parameter and thermoelastic cooling and continues with an analysis of plastic heating in MD. It outlines the idea of non-isentropic release based on the results of the MD simulations and analysis of the thermal expansion of tantalum observed in the XRD data. A significant contribution to this work was made by P. G. Heighway, who performed the energy budget and R. E. Rudd, who performed large scale MD simulations.

Chapter 6 summarises the work presented in this thesis and discusses ideas for future research projects.

1.4 List of publications

- C. E. Wehrenberg, D. McGonegle, C. Bolme, A. Higginbotham, A. Lazicki, H. J. Lee, B. Nagler, H. S. Park, B. A. Remington, R. E. Rudd, M. Sliwa, M. Suggit, D. Swift, F. Tavella, L. Zepeda-Ruiz, and J. S.Wark, Nature (London) **550**, 496 (2017).

- M. Sliwa, D. McGonegle, C. E. Wehrenberg, C. Bolme, P. G. Heighway, A. Higginbotham, A. Lazicki, H. J. Lee, B. Nagler, H. S. Park, B. A. Remington, R. E. Rudd, M. Suggit, D. Swift, F. Tavella, L. Zepeda-Ruiz, and J. S.Wark, Phys. Rev. Lett. **120**, 265502 (2018)

- P. G. Heighway, M. Sliwa, D. McGonegle, C. E. Wehrenberg, C. Bolme, A. Higginbotham, A. Lazicki, H. J. Lee, B. Nagler, H. S. Park, B. A. Remington, R. E. Rudd, M. Suggit, D. Swift, F. Tavella, L. Zepeda-Ruiz, and J. S.Wark, Phys. Rev. Lett. **123**, 245501 (2019)

2
Background theory

Contents

2.1 Crystallography 10
2.1.1 Crystal structure 10
2.1.2 Directions and planes 13
2.1.3 Reciprocal lattice 14
2.1.4 Strain 16
2.1.5 Stress 19
2.1.6 Elasticity 21
2.1.7 Plasticity 23
2.2 X-ray diffraction 29
2.2.1 Bragg's law 31
2.2.2 Laue condition 31
2.2.3 Equivalence of Bragg and Laue conditions 32
2.2.4 Scattering amplitude 33
2.2.5 Powder diffraction 35
2.2.6 Ewald sphere 36
2.2.7 Fibre diffraction 38
2.3 Shock waves 38
2.3.1 The Rankine-Hugoniot equations 39
2.3.2 Hugoniot 43
2.3.3 Shock waves in solids 44
2.3.4 Release 46
2.4 Computational methods 47
2.4.1 Molecular dynamics simulations 47
2.4.2 The LAMMPS code 48
2.4.3 Interatomic potentials 49
2.4.4 X-ray diffraction pattern simulation from MD 50
2.4.5 Hydrodynamic simulations 51
2.5 X-ray Free Electron Laser 51

The nature of the dynamic compression studies is interdisciplinary [2]. It is directly connected to fields of physics such as crystallography [51], physics of shock waves [52], and x-ray diffraction research [53]; where investigations can be divided into two approaches: experiments [25, 35, 36] and computer simulations [54–56].

This chapter contains fundamental background information that will be further developed and applied in the following chapters of this thesis. It is divided into five main sections, with material drawn from derivations and descriptions presented in textbooks by Kelly & Knowles [51], Nye [57], Simon [58], and Meyers [52], as well as other sources that will be referenced appropriately.

2.1 Crystallography

2.1.1 Crystal structure

A crystal is a solid made of atoms or molecules arranged periodically on a *lattice* - an infinite collection of points in space which can be described by the superposition of linearly independent *primitive lattice vectors* $\mathbf{a}_i$. In three dimensions, the location of lattice points is:

$$\mathbf{R} = n_1\mathbf{a}_1 + n_2\mathbf{a}_2 + n_3\mathbf{a}_3 \quad , \tag{2.1}$$

where n_i are integers. The selection of primitive lattice vectors is not unique as there are an infinite number of sets of vectors which span the entire lattice. Figure 2.1 shows an example of a selection of two sets of primitive lattice vectors for the case of two-dimensional space. A shaded parallelogram (or parallelepiped in three dimensions), called a *primitive unit cell*, is the building block of this periodic structure which, once repeated according to equation 2.1, fills the entire space. The unique feature of the primitive unit cell is the fact that it contains exactly one lattice point, and as a result, it is the smallest region with a full periodicity of the volume $\mathbf{a}_1 \cdot \mathbf{a}_2 \times \mathbf{a}_3$.

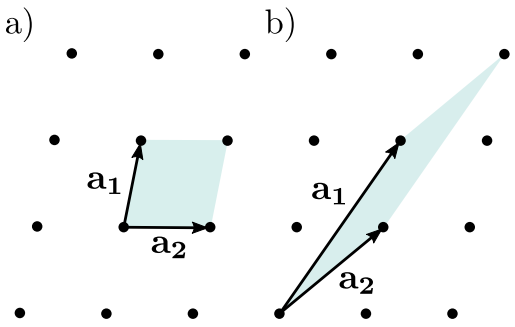


Figure 2.1: Two sets of non-unique primitive lattice vectors and corresponding unit cells (shaded regions) in a two-dimensional lattice.

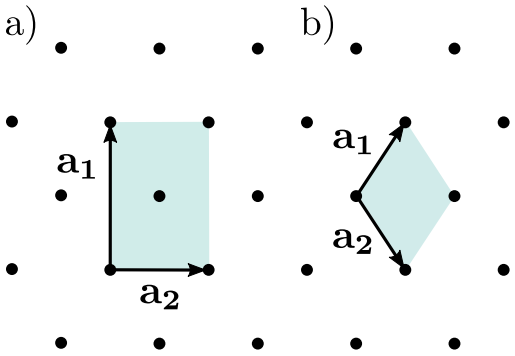


Figure 2.2: An example of conventional (a), and primitive (b) lattice cells for a two-dimensional lattice.

In general, all lattice structures can be classified into seven categories. In the simplest case, all primitive unit vectors are orthogonal ($\alpha = \beta = \gamma$) and of the same length ($a = b = c$) forming a cubic structure. In the most general case (triclinic), the edges of the unit cell ($a \neq b \neq c$) as well as angles ($\alpha \neq \beta \neq \gamma$) differ in size. Despite the fundamental properties of the primitive unit cell in the context of the periodicity of the lattice, the common approach is an analysis the symmetry of the structure via the *conventional unit cell*. Such a unit cell, despite its larger size with respect to the primitive unit cell, preserves the ability of full lattice description through discrete translation, as shown in Figure 2.2. Selection of the conventional unit cell leads to the expansion of the set of possible lattice configurations. Their geometry introduces additional lattice points in a unit cell, generating a new classification of unit cells depending on centring type:

- Primitive – lattice points only on the cell's corners,

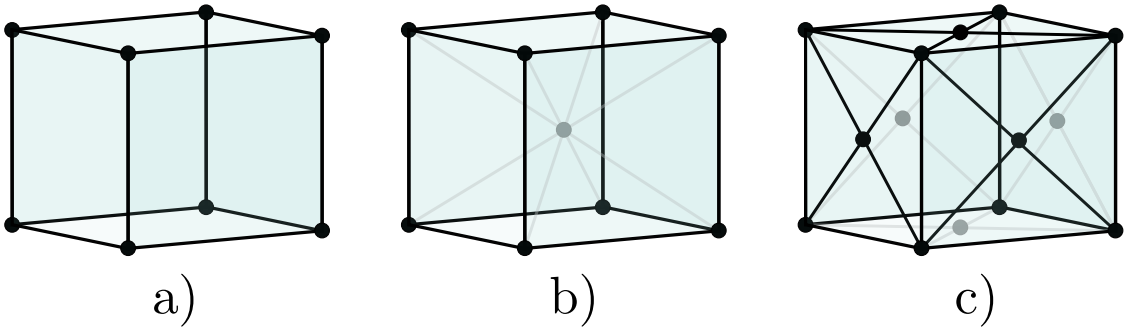


Figure 2.3: Three examples of cubic Bravias structures: simple (a), body-centred (b), and face-centred (c).

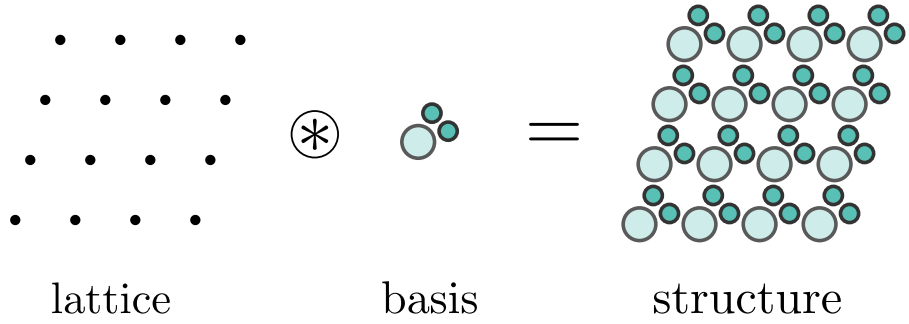


Figure 2.4: An example of the convolution of a lattice and a basis forming a structure.

- Base-centred – additional points at the centres of parallel faces,
- Body-centred – additional point at the unit's geometric centre,
- Face-centred – additional points at the centres of all faces.

Taking into account three subtypes of base-centred lattices, this classification combined with seven primitive lattice types generates 42 combinations (7x6). However, due to the degeneracy of those structures, we can reduce them to 16 unique so-called *Bravais lattices*.

The element which converts the geometric concept of the lattice to a real crystal structure is the idea of *basis* - a repeated motif at every lattice point. Therefore the position of every atom in a crystal can be described as:

$$\mathbf{R}_{\text{atom}} = \mathbf{r}_{\text{basis}} + \mathbf{R}_{\text{lattice}} \quad , \tag{2.2}$$

where $\mathbf{r}_{\text{basis}}$ is the location of the atom with respect to the chosen unit cell, and $\mathbf{R}_{\text{lattice}}$ is the position of the lattice point. In other words, a crystal structure is a convolution

of the lattice and basis. For example, body-centred cubic (bcc) and face-centred cubic (fcc) structures can be considered as simple cubic structures with basis:

$$\mathbf{r}_1 = \mathbf{0} \quad , \quad \mathbf{r}_2 = \frac{1}{2}(\mathbf{a}_1 + \mathbf{a}_2 + \mathbf{a}_3) \quad \text{(bcc)}; \tag{2.3}$$

$$\mathbf{r}_1 = \mathbf{0}\ ,\ \mathbf{r}_2 = \frac{1}{2}(\mathbf{a}_1 + \mathbf{a}_2)\ ,\ \mathbf{r}_2 = \frac{1}{2}(\mathbf{a}_2 + \mathbf{a}_3)\ ,\ \mathbf{r}_3 = \frac{1}{2}(\mathbf{a}_1 + \mathbf{a}_3)\ ,\ \text{(fcc)}. \tag{2.4}$$

2.1.2 Directions and planes

Further discussions presented in this work involve the analysis of the directions and planes of atoms. The conventional way to describe a direction is to provide a set of integer numbers, called *Miller indices* $[uvw]$. Each of these numbers refers to the multiplicity of primitive lattice vectors which, when combined linearly, form a vector in a desired direction:

$$[uvm] = u\mathbf{a}_1 + v\mathbf{a}_2 + w\mathbf{a}_3 \quad . \tag{2.5}$$

There are multiple conventions in literature concerning the use of negative numbers. The one followed in this work uses a 'bar' sign above an integer, e.g. $[1\bar{1}0]$ for u=1, v=−1, w=0. Due to the symmetry of the lattice, we can group multiple directions into families denoted by angled brackets $\langle uvw \rangle$. For example, the $\langle 100 \rangle$ family contains [100], [010], [001], $[\bar{1}00]$, ...

In order to define the orientation of a plane of atoms, a different set of h, k, and l Miller indices is used between round brackets (hkl). Given an infinite set of parallel and equally-spaced planes, a coordinate system can be arranged such that its origin coincides with one them. By convention, the next neighbouring plane is described by a set of unit vectors and Miller indices. The unit vectors with their origins at point (0,0,0) are intersected by a plane at points:

$$\frac{h}{\mathbf{a}_1}, \quad \frac{k}{\mathbf{a}_2}, \quad \frac{l}{\mathbf{a}_3} \quad , \tag{2.6}$$

as shown in Figure 2.5. In a similar manner to the families of directions, equivalent planes can be grouped into one family denoted by Miler indices in curly brackets: $\{hkl\}$ which introduces the idea of the *multiplicity* of crystallographic planes (i.e. the number of lattice planes in one family).

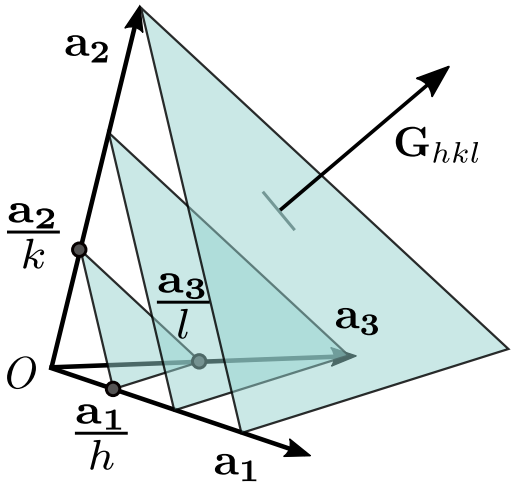


Figure 2.5: A set of lattice planes (hkl) dividing primitive lattice vectors $\mathbf{a_i}$ into segments of length $|a_1|/h$, $|a_2|/k$ and $|a_3|/l$. Vectors normal to the family (hkl) can be interpreted as reciprocal lattice vectors $\mathbf{G_{hkl}}$.

2.1.3 Reciprocal lattice

The *reciprocal lattice*, which is directly linked to the idea of lattice plane, is a crucial concept for diffraction studies. Assuming $\mathbf{R}$ is the position of a point in a direct lattice given by equation 2.1, a point $\mathbf{G}$ belongs to the reciprocal lattice only if:

$$e^{\mathbf{G}\cdot\mathbf{R}} = 1 \quad , \tag{2.7}$$

which holds for every point $\mathbf{R}$ in a lattice. Similarly to the direct lattice, points in the reciprocal lattice can be described as a linear superposition of linearly independent *primitive reciprocal lattice vectors* $\mathbf{b}_i$:

$$\mathbf{G} = m_1\mathbf{b}_1 + m_2\mathbf{b}_2 + m_3\mathbf{b}_3 \quad , \tag{2.8}$$

where m_i are integers. Each of the primitive vectors in the reciprocal space has one corresponding primitive vector in real space to which it is collinear according to the following relation:

$$\mathbf{a}_i \cdot \mathbf{b}_j = 2\pi\delta_{ij} \quad , \tag{2.9}$$

where δ_{ij} is a Kronecker which takes value of 1 if $i = j$, and 0 otherwise. Therefore in order to satisfy the property 2.9, a set of $\mathbf{b}_i$ vectors can be constructed using

primitive lattice vectors:

$$\mathbf{b}_1 = \frac{2\pi \mathbf{a}_2 \times \mathbf{a}_3}{\mathbf{a}_1 \cdot (\mathbf{a}_2 \times \mathbf{a}_3)} \quad , \tag{2.10}$$

$$\mathbf{b}_2 = \frac{2\pi \mathbf{a}_3 \times \mathbf{a}_1}{\mathbf{a}_2 \cdot (\mathbf{a}_3 \times \mathbf{a}_1)} \quad , \tag{2.11}$$

$$\mathbf{b}_3 = \frac{3\pi \mathbf{a}_1 \times \mathbf{a}_2}{\mathbf{a}_3 \cdot (\mathbf{a}_1 \times \mathbf{a}_2)} \quad . \tag{2.12}$$

Having defined reciprocal and direct lattice vectors, we can substitute equations 2.1 and 2.8 into 2.7 to obtain:

$$\exp\Big[2\pi i(n_1 m_1 + n_2 m_2 + n_3 m_3)\Big] = 1 \quad , \tag{2.13}$$

which is always satisfied only if m_i are integers, proving $\mathbf{b_i}$ are in fact primitive. The investigated reciprocal lattice vector has a specific interpretation in a real space. Replacing m_1, m_2, and m_3 with the integers h, k, and l introduced in the description of lattice planes, we notice that $\mathbf{G_{hkl}}$ is a vector normal to plane (hkl). This can be demonstrated by calculating the dot product of the reciprocal lattice vector and non-collinear vectors parallel to the investigated lattice plane (hkl):

$$(h\mathbf{b}_1 + k\mathbf{b}_2 + l\mathbf{b}_3)\Big(\frac{\mathbf{a_1}}{h} - \frac{\mathbf{a_2}}{k}\Big) = 2\pi\Big(\frac{h}{h} - \frac{k}{k}\Big) = 0 \quad , \tag{2.14}$$

$$(h\mathbf{b}_1 + k\mathbf{b}_2 + l\mathbf{b}_3)\Big(\frac{\mathbf{a_2}}{k} - \frac{\mathbf{a_3}}{l}\Big) = 2\pi\Big(\frac{k}{k} - \frac{l}{l}\Big) = 0 \quad . \tag{2.15}$$

The distance between two neighbouring planes from the same family (often called the d-spacing) can be expressed as a component of the vector connecting both planes and perpendicular to both of them (e.g. length of the perpendicular component of $\mathbf{a_1}/h$):

$$d_{hkl} = \frac{\mathbf{a_1}}{h} \cdot \hat{\mathbf{n}} = \frac{\mathbf{a_1}}{h} \cdot \frac{\mathbf{G_{hkl}}}{|\mathbf{G_{hkl}}|} = \frac{2\pi}{|\mathbf{G_{hkl}}|} \quad , \tag{2.16}$$

where $\hat{\mathbf{n}}$ is a unit vector normal to the lattice planes. Assuming that the axes of the primitive lattice vectors $\mathbf{b_i}$ are orthogonal, we can further expand equation 2.16:

$$d_{hkl} = \frac{2\pi}{\mathbf{G_{hkl}}} = \frac{2\pi}{\sqrt{h^2|\mathbf{b_1}|^2 + k^2|\mathbf{b_2}|^2 + l^2|\mathbf{b_3}|^2}} \quad . \tag{2.17}$$

While from equation 2.9 we have $|b_i| = 2\pi/|a_i|$ which leads to:

$$\frac{1}{|d_{hkl}|^2} = \frac{h^2}{a_1^2} + \frac{k^2}{a_2^2} + \frac{l^2}{a_3^2} \quad . \tag{2.18}$$

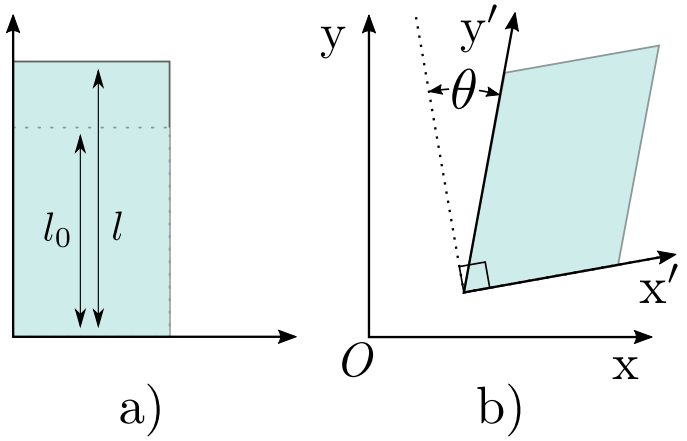


Figure 2.6: Examples of normal a) and shear b) strains. In a), deformation results in the change in length of an element from l to l', while in b), deformation causes a change of the material's shape without changing its volume.

For a cubic lattice, where $a_i = a$, the above equation can be further simplified:

$$d_{hkl}^{cubic} = \frac{a}{\sqrt{h^2 + k^2 + l^2}} \quad . \tag{2.19}$$

The above derivations show a fundamental connection between the reciprocal lattice vector and lattice planes. This relationship will be extensively explored during the analysis of planes diffracting x-rays in the following chapter.

2.1.4 Strain

When a force is applied to a crystal, the relative position of its atoms changes. This change in atomic position is called *strain*, and it takes one of three forms: normal, shear, or a combination of both.

As depicted in Figure 2.6a, due to the application of normal strain, the object changes its length from l to l_0 along the direction of deformation. A simple quantity associated with this kind of elongation is the *engineering strain*, which provides information about the overall change in the material's length:

$$e = \frac{l_0 - l}{l_0} \quad , \tag{2.20}$$

where l_0 and l are the material's lengths before and after the application of strain. Defined this way, compressive deformations result in positive strain while tensile

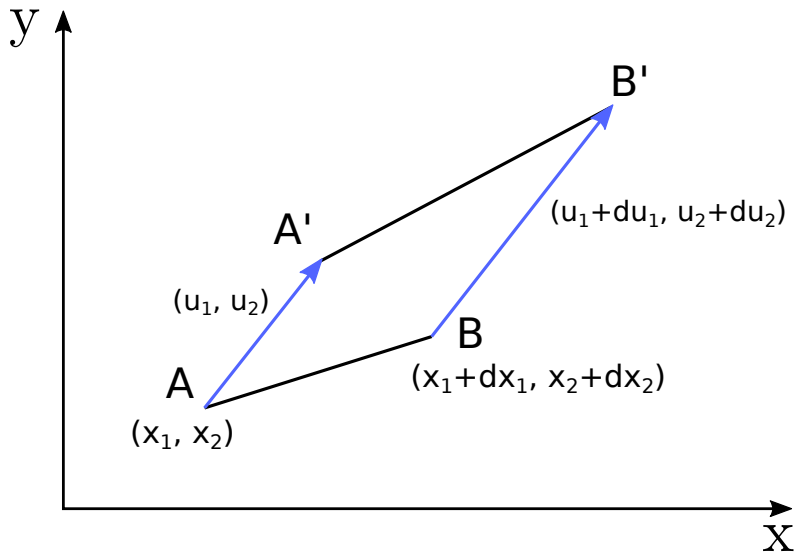


Figure 2.7: Deformation of infinitesimal material element.

deformations result in negative strain [1]. By reducing the amount of strain to an infinitesimally small amount due to a small change in length we have:

$$de = \frac{dl}{l_0} \quad . \tag{2.21}$$

Integration of both sides leads to the definition of *true strain*:

$$e = \frac{\ln l}{l_0} \quad . \tag{2.22}$$

The other type of strain – shear, is a measure of the change in angle between two perpendicular lines when the body is distorted. Figure 2.6b shows an example of a shear strain which is defined as:

$$\gamma = \tan\theta \quad . \tag{2.23}$$

For small shear strains, the above expression can be simplified through the Taylor expansion to:

$$\gamma \approx \theta \quad . \tag{2.24}$$

To explore the idea of infinitesimal strains, the geometry presented in Figure 2.7

[1] This convention has been chosen because the majority of the work presented in this thesis is concerned with metals under compression.

is used. A segment AB of a small length experiences a deformation where the position of its end points is moved to $A'B'$. Point A, initially at location (x_1, x_2), is displaced to A at $(x_1 + u_1, x_2 + u_2)$, while point B at $(x_1 + dx_1, x_2 + dx_2)$ is moved by a vector $(u_1 + du_1, u_2 + du_2)$. In a strained body, at least one of the additional elements du_i takes a non-zero value. Expanding the expression for du_i, which is a function of x_i, we obtain:

$$du_1 = \frac{\partial u_1}{\partial x_1} dx_1 + \frac{\partial u_1}{\partial x_2} dx_2 \quad , \tag{2.25}$$

$$du_2 = \frac{\partial u_2}{\partial x_1} dx_1 + \frac{\partial u_2}{\partial x_2} dx_2 \quad . \tag{2.26}$$

These two equations can be compactly written in the following form:

$$du_i = e_{ij} dx_j \quad \text{with:} \quad e_{ij} = \frac{\partial u_i}{\partial x_j} \quad , \tag{2.27}$$

where e_{ij} is a second-rank *relative displacement tensor*. It can be noticed that $i = j$ displacements correspond to compressions and extensions along certain directions, while $i \neq j$ correspond to rotations. Since the relative displacement tensor is not a satisfactory metric to describe deformation, it can be decomposed in the following way:

$$e_{ij} = \epsilon_{ij} + \omega_{ij} \quad , \tag{2.28}$$

where:

$$\epsilon_{ij} = \frac{1}{2}(e_{ij} + e_{ji}) \quad \text{and} \quad \omega_{ij} = \frac{1}{2}(e_{ij} - e_{ji}) \quad . \tag{2.29}$$

The geometric interpretation of equation 2.29 is shown in Figure 2.8. The antisymmetric part (ω_{ij}) describes pure rotation, while the symmetric part (ϵ_{ij}) is the object of our interest as it describes *pure strain*. These ideas can be easily extended into three-dimensional space, where the pure strain tensor takes the form:

$$\epsilon = \begin{pmatrix} e_{11} & \frac{1}{2}(e_{12} + e_{21}) & \frac{1}{2}(e_{13} + e_{31}) \\ \frac{1}{2}(e_{21} + e_{12}) & e_{22} & \frac{1}{2}(e_{23} + e_{32}) \\ \frac{1}{2}(e_{31} + e_{13}) & \frac{1}{2}(e_{32} + e_{23}) & e_{33} \end{pmatrix} \quad . \tag{2.30}$$

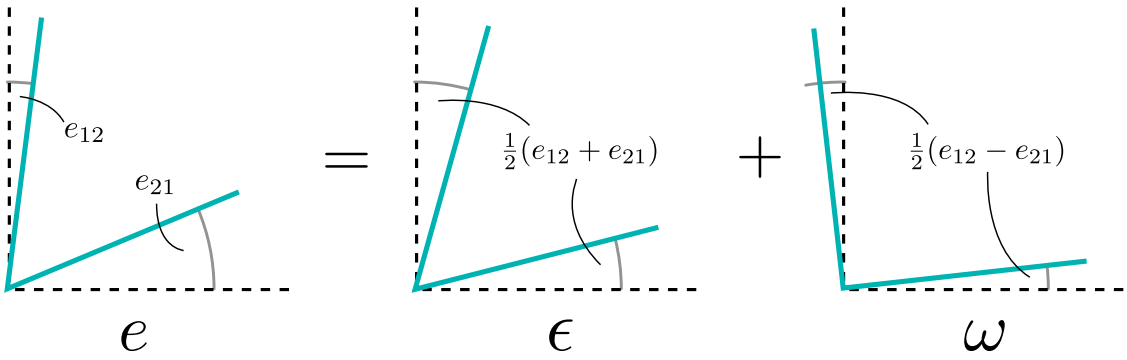


Figure 2.8: Displacement tensor decomposition into strain ϵ and rotation ω.

It can be noticed that the off-diagonal elements of the strain tensor describe the shear part of the deformation:

$$\frac{1}{2}(e_{ij}+e_{ji})=\gamma_{ij} \quad \text{, where} \quad i\neq j. \tag{2.31}$$

Therefore, pure strain tensor can be written in a compact form for three-dimensional space (x,y,z):

$$\epsilon=\begin{pmatrix} e_x & \gamma_{xy} & \gamma_{xz} \\ \gamma_{xy} & e_y & \gamma_{yz} \\ \gamma_{xz} & \gamma_{yz} & e_z \end{pmatrix} \quad , \tag{2.32}$$

where due to the symmetry the number of unique elements has been reduced to three diagonal normal components and three off-diagonal shear components.

2.1.5 Stress

A physical quantity closely related to strain, *stress* is defined as the force acting on a body per unit area. When atoms in a crystal are displaced relative to one another, the forces that act on them tend to restore their normal spatial relationships. In the simplest case of uniaxial compression, force F acting on surface A generates stress $\sigma = F/A$. When expanding this definition into three dimensions, the influence of forces acting in a non-parallel direction to the normal of the surface needs to be considered. Like strain, stress can be normal or shear:

$$\sigma_n=\lim_{\delta A\to 0}\frac{f_n}{\delta A} \quad , \tag{2.33}$$

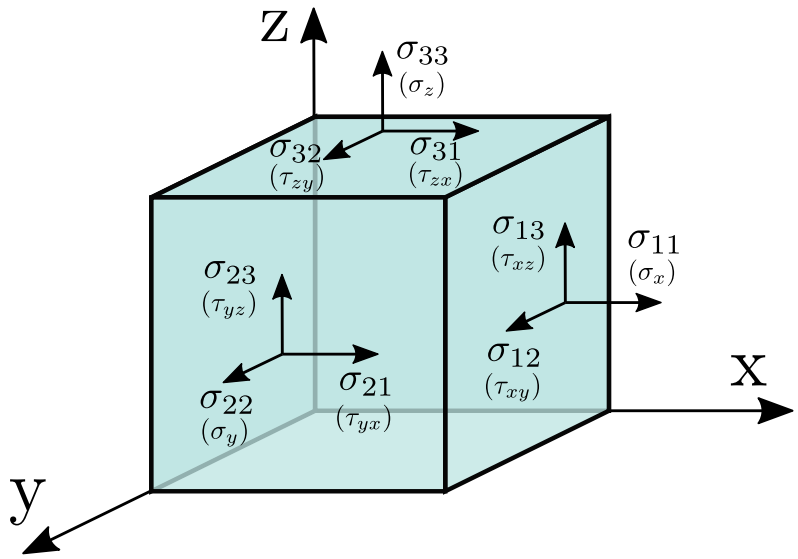


Figure 2.9: Three-dimensional stress tensor components.

$$\tau = \lim_{\delta A \to 0} \frac{f_s}{\delta A} \quad , \tag{2.34}$$

where σ_n is normal stress, τ is shear stress, f_n and f_s are parallel and perpendicular forces acting on a surface δA, respectively. The relationship between forces and surfaces in a material is written in the compact form of a second rank tensor:

$$\sigma = \begin{pmatrix} \sigma_{11} & \sigma_{12} & \sigma_{13} \\ \sigma_{21} & \sigma_{22} & \sigma_{23} \\ \sigma_{31} & \sigma_{32} & \sigma_{33} \end{pmatrix} \quad , \tag{2.35}$$

where a component σ_{ij} denotes stress due to a force along the j direction acting on a surface with a normal in the i direction as shown in Figure 2.9. The diagonal elements of this tensor are normal stresses as defined by equation 2.33. The off-diagonal elements correspond to shear stress components. To conserve the angular momentum in equilibrium, the tensor has to be symmetric, which reduces the number of unique shear stress components from six to three: $\sigma_{12} = \sigma_{21}$, $\sigma_{13} = \sigma_{31}$, and $\sigma_{23} = \sigma_{32}$.

When describing a compressed solid, the term *pressure* is used to refer to a trace of stress tensors:

$$P = \frac{1}{3}(\sigma_{11} + \sigma_{22} + \sigma_{33}) \quad . \tag{2.36}$$

The convention applied to the formula above defines compressive pressures as the ones with a positive sign, while tensile pressures have a negative sign. In the

dynamic compression community, the term shear stress often denotes the mean of the shear stress components for the plane perpendicular to the compression direction. For example, a compression wave propagating along the z direction generates a shear stress defined as:

$$\tau = \frac{1}{2}(\sigma_{31} + \sigma_{32}) \quad . \tag{2.37}$$

2.1.6 Elasticity

This section combines the ideas introduced in the previous two sections by outlining the connection between strain and stress.

Provided that the stress does not exceed a certain limiting value called the *elastic limit*, the relatively small induced strain deformations are reversible. That is to say, material obeys Hook's famous law which states that for sufficiently small stresses, strain is directly proportional to the magnitude of the applied stress. In the simplest one-dimensional case of an isotropic load stress σ and longitudinal strain ϵ related by a proportionality constant called *elastic compliance constant* s:

$$\epsilon = s\sigma \quad . \tag{2.38}$$

The alternative term is *elastic stiffness constant* C, which is the inverse of the elastic compliance constant:

$$\sigma = C\epsilon \quad \text{where:} \quad C = \frac{1}{s} \quad , \tag{2.39}$$

C is also known as Young's modulus. Equations 2.38 and 2.39 can be generalised to three-dimensional space via tensor transformations:

$$\sigma_{ij} = C_{ijkl}\epsilon_{kl} \quad , \tag{2.40}$$

$$\epsilon_{ij} = s_{ijkl}\sigma_{kl} \quad . \tag{2.41}$$

Since strain and stress are second rank tensors, stiffness and compliance are fourth rank tensors consisting of $3^4 = 81$ elements each. However, as it has been explained in previous sections, stress and strain tensors are symmetric which reduces the

number of their unique elements to 6. At this point the Voigt notation can be introduced, replacing strain and stress tensors with 6-dimensional vectors:

$$\epsilon = \begin{pmatrix} \epsilon_{11} & \epsilon_{12} & \epsilon_{13} \\ \epsilon_{12} & \epsilon_{22} & \epsilon_{23} \\ \epsilon_{13} & \epsilon_{23} & \epsilon_{33} \end{pmatrix} = \begin{pmatrix} \epsilon_1 & \epsilon_5 & \epsilon_6 \\ \epsilon_6 & \epsilon_2 & \epsilon_4 \\ \epsilon_5 & \epsilon_4 & \epsilon_3 \end{pmatrix} \quad \rightarrow \quad (\epsilon_1, \epsilon_2, \epsilon_3, \epsilon_4, \epsilon_5, \epsilon_6) \quad , \tag{2.42}$$

$$\epsilon = \begin{pmatrix} \sigma_{11} & \sigma_{12} & \sigma_{13} \\ \sigma_{12} & \sigma_{22} & \sigma_{23} \\ \sigma_{13} & \sigma_{23} & \sigma_{33} \end{pmatrix} = \begin{pmatrix} \sigma_1 & \sigma_5 & \sigma_6 \\ \sigma_6 & \sigma_2 & \sigma_4 \\ \sigma_5 & \sigma_4 & \sigma_3 \end{pmatrix} \quad \rightarrow \quad (\sigma_1, \sigma_2, \sigma_3, \sigma_4, \sigma_5, \sigma_6) \quad . \tag{2.43}$$

The power of Voigt notation relies on the fact that it simplifies calculations by replacing stiffness and compliance fourth rank tensors with 6-dimensional second rank tensors, which in turn reduces the number of tensor elements from 81 to 36. The presence of structural symmetry in a crystal further simplifies the form of the tensors. In the case of cubic structure, which is the main interest of this work, there are only 3 independent components in the stiffness tensors:

$$\sigma = \begin{pmatrix} C_{11} & C_{12} & C_{12} & 0 & 0 & 0 \\ C_{12} & C_{11} & C_{12} & 0 & 0 & 0 \\ C_{12} & C_{12} & C_{11} & 0 & 0 & 0 \\ 0 & 0 & 0 & C_{44} & 0 & 0 \\ 0 & 0 & 0 & 0 & C_{44} & 0 \\ 0 & 0 & 0 & 0 & 0 & C_{44} \end{pmatrix} \quad , \tag{2.44}$$

where the notation has been reduced such that $C_{iijj} = C_{ij}$. While stiffness or compliance tensors can define the elastic properties of a single crystal, they fail at describing the properties of polycrystalline samples. In a material which consists of multiple randomly-arranged grains, direction-specific properties such as elasticity need to be described by a variety of isentropic macroscopic constants, e.g. Young's modulus or Poisson's ratio (the ratio between the strain transverse to the direction of the force and the strain parallel to the force) [57].

2.1.7 Plasticity

As it has been mentioned in the previous section, solid materials resist small external forces by deforming elastically. Such forces are shear forces and once they exceed a certain limiting value, material either breaks or yields. If it yields it does so in a plastic manner, which means that if sufficiently large shear stresses are applied over a sufficiently long period of time, material will change its shape permanently while remaining in one piece. There are multiple plastic mechanisms and whether one or another mechanism is activated during deformation depends on a variety of factors. For instance a special type of plastic deformation is a phase transition where material remains solid while changing its crystallographic lattice type. A historically important example of this is kind of deformation is the transition from body-centred cubic structure to hexagonal-base packed structure in iron above ∼13GPa [5, 6]. However, the most common types of crystal deformation are *slip* and *twinning*, both of which are mediated by the relative translation of entire atomic planes. While slip relies on the generation and motion of crystal defects, pure twinning forms two separate crystal regions sharing the same lattice points in a symmetric manner.

Crystal defects

Most crystalline materials differ from the perfect atomic arrangement presented in the previous sections. Materials usually contain defects which alter their perfect structure and change their mechanical properties. The nature of these defects is twofold - they arise either due to a lack of atoms at their designated lattice sites or due to the appearance of additional atoms in between the atoms of the perfect crystal.

Crystallographic defects can be categorised based on their dimensionality. We can distinguish defects in: 0D - points, 1D - lines, 2D - planes, and 3D - volumes. Point defects are simply small groups of extra or missing atoms which do not extend in any direction. On the other hand, volume effects are associated with macroscopic bulk defects such as pores, cracks, or inclusions. The types of defects this work is most concerned with are one and two-dimensional defects, as described below.

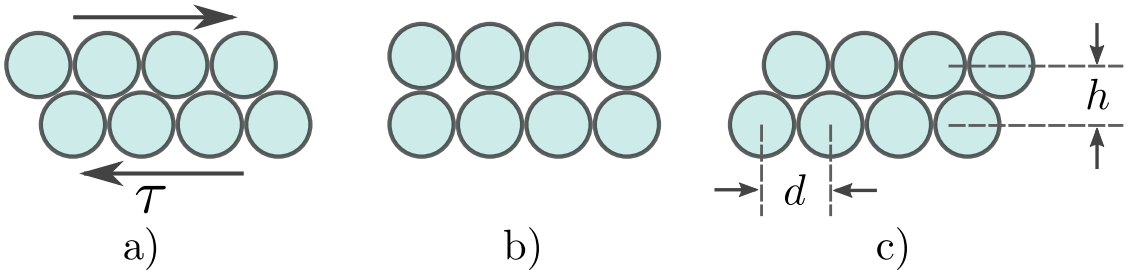


Figure 2.10: Relative displacement of two planes of atoms under the influence of external shear force τ.

Dislocations

Dislocations are one-dimensional defects. Their presence and their motion are closely related to idea of slip. Figure 2.10 gives an example of a perfect two-dimensional close-packed structure. In order to move two layers of atoms from position a) to position c), the energetic barrier associated with atomic interactions needs to be overcome. The shear force τ that maintains the relative motion of these two layers is a period function with zero values in positions a), b), and c). Therefore in a simple approximation it can be described as:

$$\tau = \tau_c \sin \frac{2\pi x}{d} \quad , \tag{2.45}$$

where τ_c is the critical value in position a) in order to glide two planes past each other, and x is their relative position with $x = 0$ in position b). Shear force can be correlated with shear stress via shear modulus G:

$$\tau = G\gamma = G\frac{x}{h} \quad . \tag{2.46}$$

Hence, in a small angle approximation we obtain:

$$\tau_c = \frac{G}{2\pi}\frac{d}{h} \quad . \tag{2.47}$$

The above theoretical derivation suggests that the stress required to deform a crystal is of the order $G/(2\pi)$, which for metals is about 50GPa. However, experimental works at relatively low strain rates have shown that metals yield under influence of stresses an order of magnitude lower than the theoretical prediction. This discrepancy has been a subject of research since the first half of the 20th century.

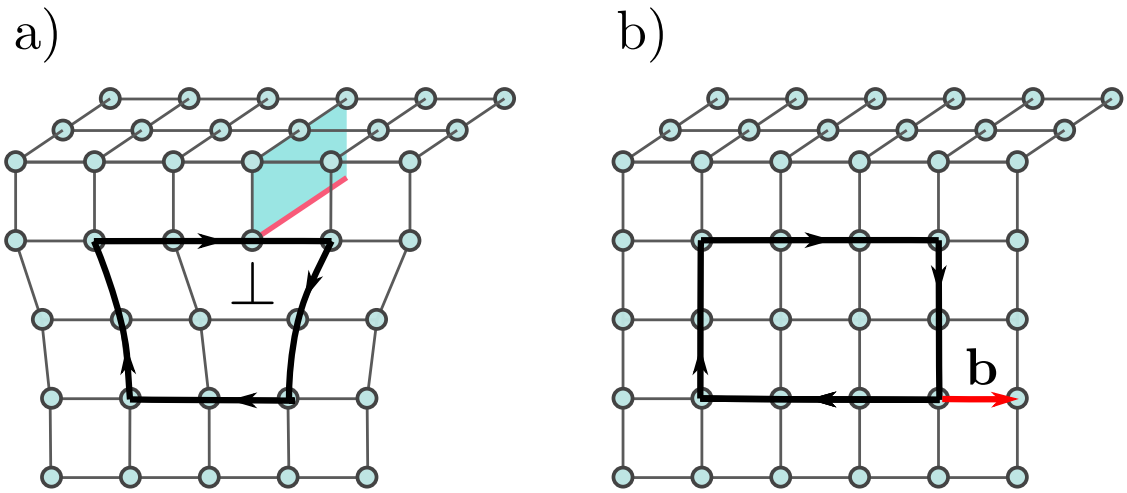


Figure 2.11: a) illustrates an example of an edge dislocation marked with a red line. The path (bold line) surrounding it differs from the path connecting the same atoms in a non-defective lattice b) by Burgers vector **b**.

The main contributions towards understanding this phenomenon were made by Orowan, Polanyi and Taylor who independently proposed separate solutions which all relied on the idea of the presence of defects [59, 60]. They postulated that instead of entire layers of atoms simultaneously slipping, line defect would create regions separating those parts of the crystal where slip occurred and those where it did not. The movement of such dislocations would successively shift entire planes with flow stresses much smaller than the initial theoretical predictions, since they needed to displace only a small part of the crystal. Initial theories of crystal dislocations were met with a skeptical response on the part of the metallurgic community. As Read [61] points out, 'It became the fashion to invent a dislocation theory of almost every experimental result in plastic deformation. Finally, it became apparent that dislocations could explain not only any actual result but virtually any conceivable result, usually in several different ways'. The existence of dislocations was confirmed in the 1950s with the advent of electron microscopy [62]. It has to pointed out that at high strain rates the above picture of plastic deformation may not be valid. The small timescale of deformation with respect to the timescale of dislocation motion leads to the more complex behaviour of materials [46].

In order for material to flow via dislocation motion, these dislocations need to be present in the first place. One way a dislocation may be formed is through

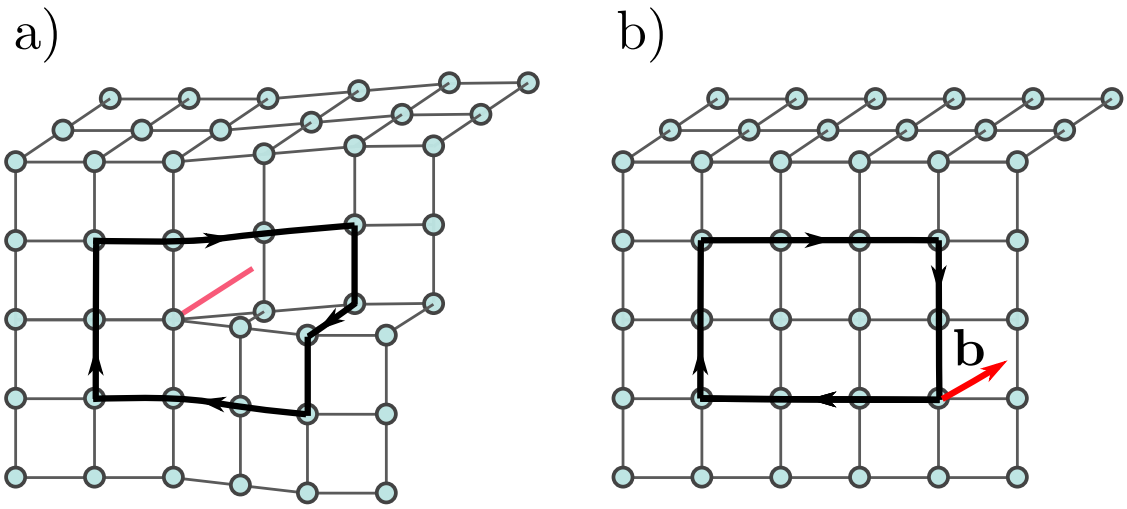


Figure 2.12: a) illustrates an example of a screw dislocation marked with a red line. The path (bold line) surrounding it differs from the path connecting the same atoms in a non-defective lattice b) by Burgers vector **b**.

homogenous nucleation, in which defects are spontaneously generated in a perfect crystal. However dislocations are more commonly generated from pre-existing defects such as grain boundaries.

There are two main types of dislocation. The first of these is *edge dislocation*, an example of which is illustrated in Figure 2.11. Edge dislocation can be considered as the insertion of a half-plane of atoms into a lattice (in Figure 2.11 this is marked with the symbol $\perp$). Once a crystal defect in a crystal lattice is identified, a circuit surrounding it can be drawn. Mapping the same loop between atoms of a non-defective crystal results in an open path of which the two ends form endpoints of the *Burgers vector*. The Burgers vector provides information about the magnitude and direction of the distortion in the lattice. In Figure 2.11, it can be seen that the Burgers vector is perpendicular to the dislocation line.

The second basic type of line defect is a *screw dislocation*. It can be visualised as the displacement of lattice points due to shear force applied to one side of a block of atoms, while keeping the opposite side unaffected, as shown in Figure 2.12. Unlike in the case of edge dislocation, the Burgers vector is parallel to a screw dislocation.

Dislocation density is defined as the length of dislocation lines l within a volume

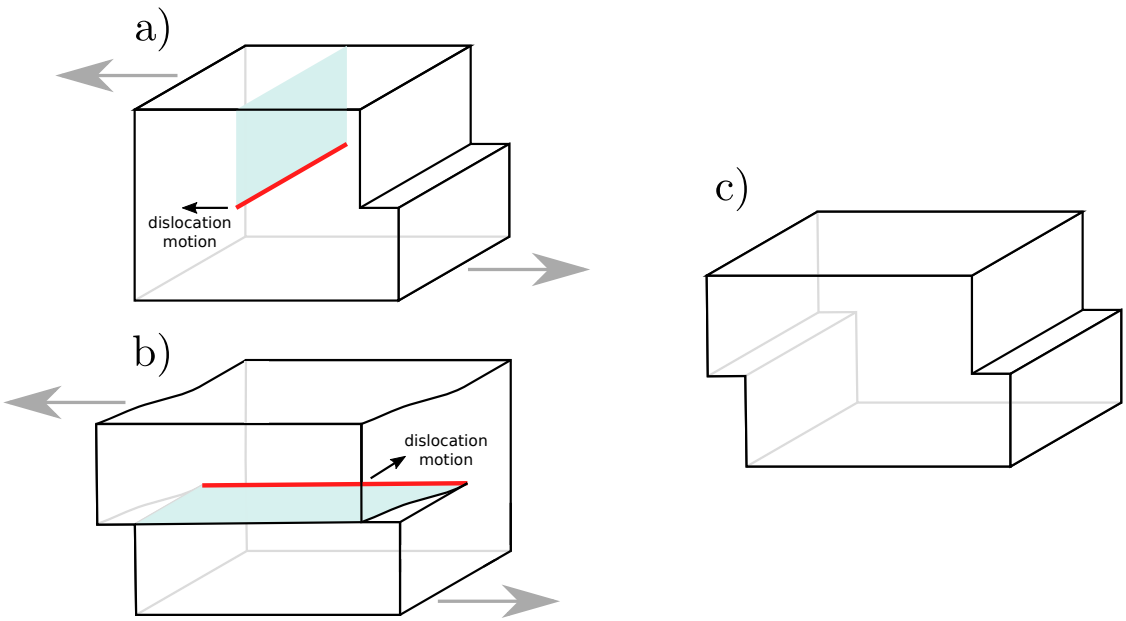


Figure 2.13: Illustrations a) and b) demonstrate the motion of edge and screw dislocations respectively. Gray arrows indicate the direction of the applied shear forces while c) represents the final state of the crystal.

V, or the number of dislocations N intersecting unit area A:

$$\rho_d = \frac{l}{V}, \quad \rho_d = \frac{N}{A} \quad . \tag{2.48}$$

Therefore, dislocation density is usually expressed in units of cm^{-2}. The specific number may vary depending on the material involved and its mechanical and thermal history. Annealing or manufacturing processes are examples of factors affecting the number of defects, with typical dislocation densities ranging between $10^6 - 10^{11}\mathrm{cm}^{-2}$.

As mentioned before, dislocation motion is directly related to resolving the shear stress generated in a solid. The successive translation of a dislocation under the influence of an external shear force leads to a glide of dislocation within a plane containing a Burgers vector and the dislocation line. A full translation of the entire atomic plane is called *slip*. An example of this process is shown in Figure 2.13. The motion of edge and screw dislocations differ, with edge dislocation traveling parallel and screw dislocation traveling perpendicular to the direction of stress. The plane on which the slip occurs is called the *slip plane*. The slip plane can normally be characterised by its high density of atoms. For example, in bcc metals, the most common slip planes are {110} and {112}. The direction of slip is defined by the

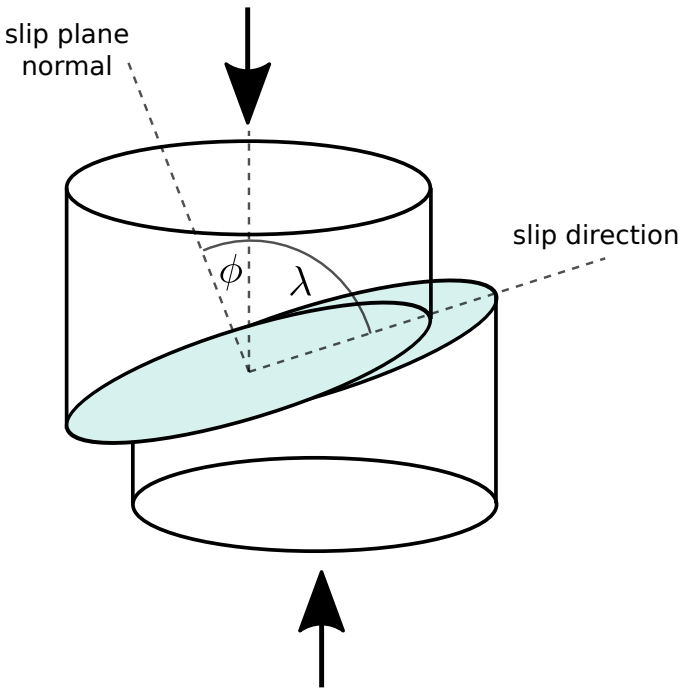


Figure 2.14: Illustration of a slip induced by a compressive (vertical) force.

direction of the Burgers vector. The Burgers vector is often the shortest possible one for a particular slip plane. The combination of slip plane and slip direction forms a *slip system*. Bcc metals usually slip along the <111> direction meaning that there are 12 {110}<111> and 12 {112}<111> slip systems.

The amount of shear stress resolved by slip can derived from Figure 2.14. If a vertical compressive or tensile force **F** is applied to a crystal of cross-sectional area A, the stress parallel to the force direction is $\mathbf{F}/A$. The component of F along the slip direction is $F\cos\lambda$, where λ is the angle between the direction of **F** and the slip direction. Since the area over which shear force acts is equal to $A/\cos\phi$, the resolved shear stress τ is:

$$\tau = \frac{F}{A}\cos\phi\cos\lambda \quad . \tag{2.49}$$

It has to be pointed out that slip direction, plane normal, and compressive force do not have to be coplanar, meaning that $\phi + \lambda = 90°$ is a special case. The quantity $\cos\phi\cos\lambda$ is known as the *Schmid factor*. It helps to determine which slip systems are activated first during compression or tension. That is to say, the slip systems

with the highest Schmid factor require the smallest forces, and therefore dominate over the other ones – this phenomenon is known as the Schmid criterion.

Dislocation motion during glide can be directly correlated to the timescale of the deformation. Orowan's equation states [59]:

$$\dot{\epsilon} = b\rho_m\langle v\rangle \quad , \tag{2.50}$$

where $\dot{\epsilon}$ is the plastic strain rate, b is the magnitude of the Burgers vector, ρ_m is the density of mobile dislocations, and $\langle v\rangle$ is their mean speed.

Twinning

When a crystal is composed of parts that are oriented with respect to one another according to a rule of symmetry, the crystal is said to be twinned. The most common appearance of twinning is the generation of a crystal region that exhibits reflectional symmetry, which means that the structure of one part of the crystal is a mirror image of a different part. The plane of symmetry which separates the two regions is called the *twinning plane*. Twinning is often achieved during a crystal's growth, when a solid is formed at random from a liquid or a vapour. However, twinning can also be induced mechanically via the resolution of shear stress.

Twinning is a popular deformation mechanism in bcc metal. As illustrated in Figure 2.15, the original bcc structure is produced by the repetition of a sequence of 6 consecutive (112) layers of atoms. This stacking process creates a sequence $ABCDEFABC...$ where each letter refers to one plane, as shown in Figure 2.15a. Twinning occurs when the stacking order is reversed: $ABCDEFEDC...$. It is achieved by moving every layer on one side of the twinning plane by $\frac{1}{6}[\bar{1}\bar{1}0]$ with respect to the neighbouring plane, as shown in 2.15b.

2.2 X-ray diffraction

X-ray diffraction (XRD) methods are extremely important experimental techniques which, since their first appearance at the beginning of the 20th century, have found an established place in the field of crystallography. The typical size of interatomic

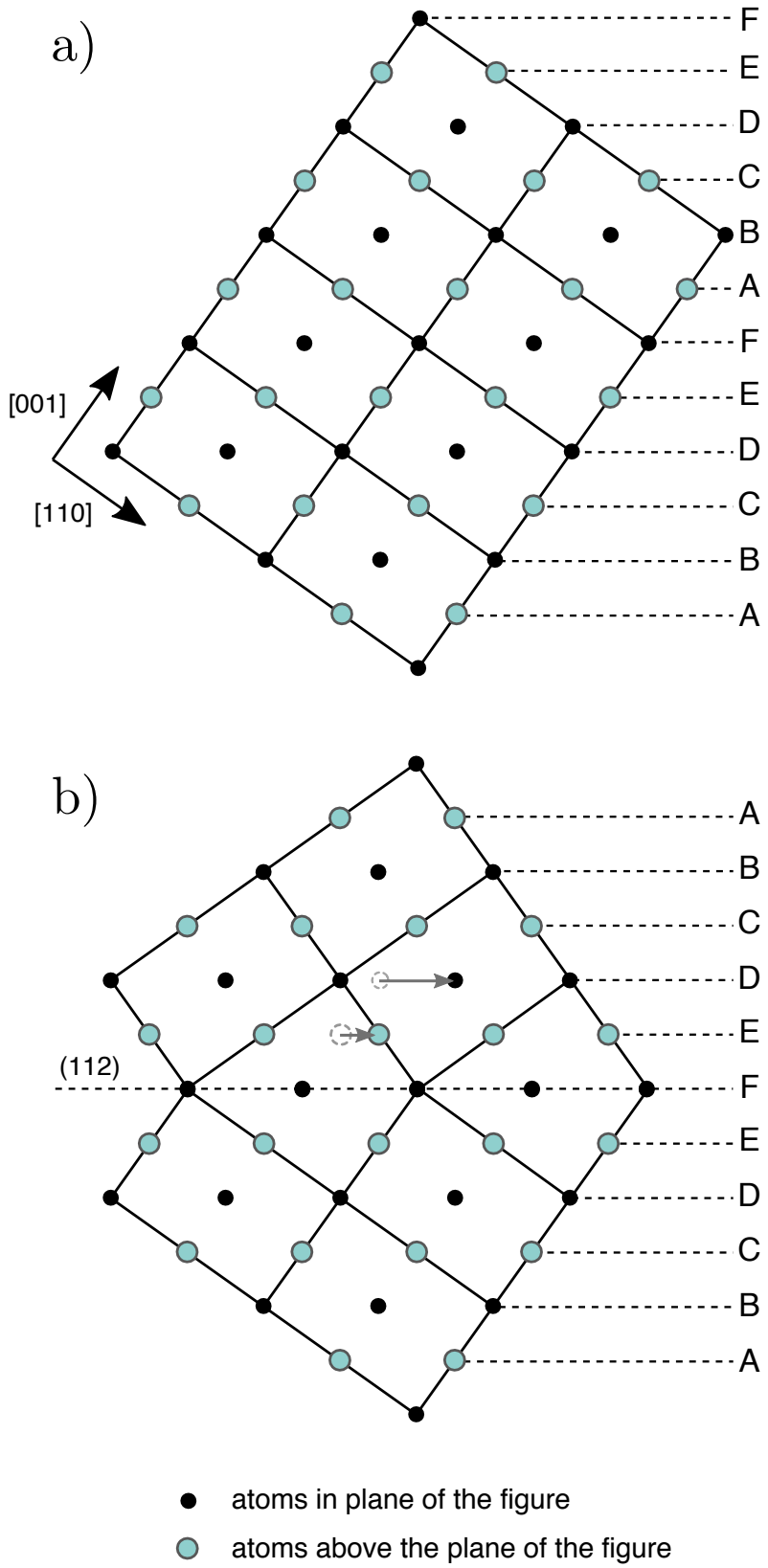


Figure 2.15: a) the bcc lattice illustrated as a stack of (112) planes. b) twinning in a bcc lattice due to the reversed stacking of (112) atomic planes achieved by the slipping of the neighbouring layers in a twinned part. Examples of atomic translations in layers D and E are shown with grey vectors.

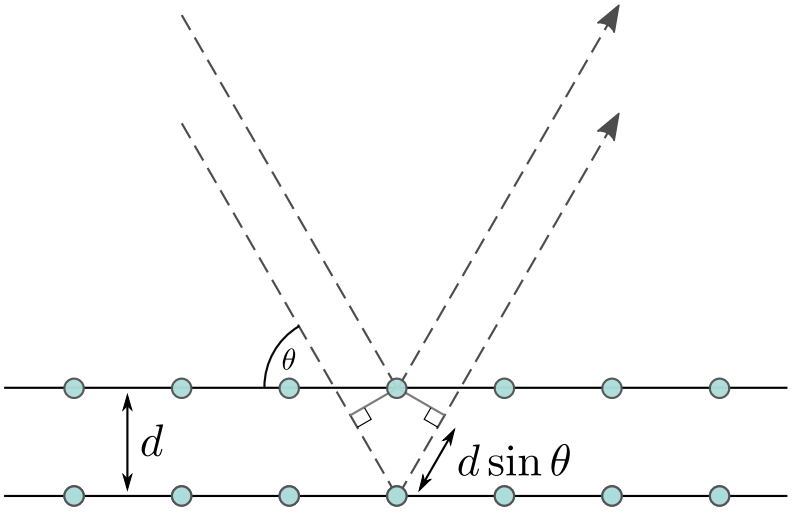


Figure 2.16: Demonstration of Bragg's law. Two rays of light interfere constructively once the difference in their traveled paths is equal to the integer number of their wavelengths.

spacing in solid crystals is several Angstrom long ($1\text{A} = 10^{-10}\text{m}$). This means that x-rays, electromagnetic radiation with wavelengths in the range of 100 eV - 100 keV, or 0.01 nm - 10 nm, are a perfect probing tool for such small-length scales. The following section gives a brief description of x-ray diffraction techniques.

2.2.1 Bragg's law

Figure 2.16 shows two x-ray rays incident onto two layers of atoms. In order to achieve constructive interference upon reflection, geometric analysis indicates that the path difference taken by these two rays must be equal to the integer number of their wavelength λ, which leads to *Bragg's law*:

$$2d\sin\theta = n\lambda \quad , \tag{2.51}$$

where d is the spacing between atomic planes, θ is the angle of the incidence of incoming x-rays, and n is an integer.

2.2.2 Laue condition

Another approach to the constructive interference of the scattered beam is based on Fermi's Golden Rule. If incoming x-rays are considered as photons, their interactions with the lattice can be analysed as the interaction with the potential

$V(\mathbf{r})$. According to Fermi's Golden Rule, the transition rate Γ of particles scattering from wavevector $\mathbf{k}$ to $\mathbf{k}'$ is:

$$\Gamma = \frac{2\pi}{\hbar}|\langle \mathbf{k}'|V|\mathbf{k}\rangle|^2 \delta(E_{\mathbf{k}'} - E_{\mathbf{k}}) \quad , \tag{2.52}$$

with the matrix element:

$$\langle \mathbf{k}'|V|\mathbf{k}\rangle \propto \int e^{-i\mathbf{k}'\cdot\mathbf{r}} V(\mathbf{r}) e^{-i\mathbf{k}'\cdot\mathbf{r}} \mathbf{dr} = \int e^{-i(\mathbf{k}'-\mathbf{k})\cdot\mathbf{r}} V(\mathbf{r}) \mathbf{dr} \quad , \tag{2.53}$$

which is simply the Fourier Transform (FT) of the potential. The above equation is general in the sense that it does not make any assumption about the periodicity of the lattice. However, once it is assumed that the sample is periodic, the matrix element vanishes unless the difference between the incident and scattered wavevectors is equal to the reciprocal lattice vector. This can be shown by expressing $\mathbf{r}$ as a combination of position $\mathbf{x}$ within the unit cell and lattice vector position $\mathbf{R}$:

$$\mathbf{r} = \mathbf{R} + \mathbf{x} \quad . \tag{2.54}$$

Since the potential is periodic ($V(\mathbf{x} + \mathbf{R}) = V(\mathbf{x})$), the matrix element can be written as:

$$\langle \mathbf{k}'|V|\mathbf{k}\rangle \propto \sum_{\mathbf{R}} e^{-i(\mathbf{k}'-\mathbf{k})\cdot\mathbf{R}} \int_{unit-cell} e^{-i(\mathbf{k}'-\mathbf{k})\cdot\mathbf{x}} V(\mathbf{x}) \mathbf{dx} \quad . \tag{2.55}$$

According to the crystallographic relation given by equation 2.7, the first term on the right hand side is reduced to zero unless:

$$\mathbf{k}' - \mathbf{k} = \mathbf{G} \quad . \tag{2.56}$$

Equation 2.56 is known in literature as the *Laue condition*, which needs to be satisfied in order to obtain constructive interference.

2.2.3 Equivalence of Bragg and Laue conditions

Bragg's and Laue's approaches to the problem of x-ray scattering lead to solutions which are in fact equivalent. By rearranging and squaring equation 2.56 we have:

$$\mathbf{k}^2 = (\mathbf{k}' + \mathbf{G})^2 \quad . \tag{2.57}$$

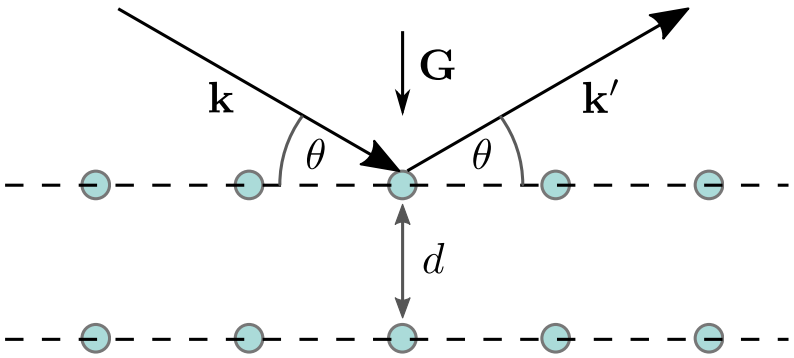


Figure 2.17: Demonstration of the Laue condition. The difference between the incoming wavevector **k** and the scattered wavevector **k** is equal to the reciprocal lattice vector **G**.

Since the magnitude of the wavevector during scattering is preserved:

$$k^2 = k^2 + 2\mathbf{k}' \cdot \mathbf{G} + G^2 \quad , \tag{2.58}$$

$$2\mathbf{k}' \cdot \mathbf{G} = -G^2 \quad . \tag{2.59}$$

From equation 2.16, it can be inferred that the reciprocal vector is an integral multiple of $2\pi/d$, where integer $n \neq 1$ refers to planes with spacings d/n. The geometry in Figure 2.17 illustrates that:

$$\hat{\mathbf{k}}' \cdot \hat{\mathbf{G}} = \sin\theta \quad . \tag{2.60}$$

Hence:

$$2k \sin\theta = \frac{2\pi n}{d} \quad . \tag{2.61}$$

Substituting $k = 2\pi/\lambda$ Bragg's law is obtained:

$$2d \sin\theta = n\lambda \quad . \tag{2.62}$$

2.2.4 Scattering amplitude

X-ray diffraction in a solid is the result of photons scattering from electrons. So far it has been assumed that all lattice points perfectly scatter light in a constructive manner. However, two important elements need to be considered: the contribution from an individual atom f based on the structure of its electronic cloud, and

the destructive interference due to multiple atoms in a unit cell. Combining these two factors we obtain:

$$S(\mathbf{G}) \sim \sum_j f_j(\mathbf{G}) e^{i\mathbf{G}\cdot\mathbf{x}_j} \quad , \tag{2.63}$$

where summation is performed over all atoms in a unit cell. $S(\mathbf{G})$ is the *structure factor* of the unit cell and is proportional to the amplitude of the scattered light. Hence, the intensity of the scattered x-rays is:

$$I_{hkl} \propto |S_{hkl}|^2 \quad . \tag{2.64}$$

The amplitude of the scattered beam from a single atom is a function of electron distribution $\rho(\mathbf{r})$ around the atomic nucleus. The scattering factor from an individual atom is called the *atomic form factor* and is defined as a Fourier Transform of this electronic distribution:

$$f(\mathbf{k}' - \mathbf{k}) = \int e^{i(\mathbf{k}'-\mathbf{k})\cdot\mathbf{r}} \rho(\mathbf{r}) \mathbf{dr} \quad . \tag{2.65}$$

It is worth noting that for the case of $\mathbf{k}' = \mathbf{k}$ the atomic form factor is proportional to Z, the number of electrons in the atom.

It is not possible to further analyse the form of structure factor 2.63. Considering the relationships between lattice vectors 2.1 and reciprocal lattice vectors 2.8 we have:

$$S_{hkl} = \sum_j f_j e^{i(h\mathbf{b_1}+k\mathbf{b_2}+l\mathbf{b_3})\cdot(x_j\mathbf{a_1}+x_j\mathbf{a_2}+x_j\mathbf{a_3})} \quad , \tag{2.66}$$

$$S_{hkl} = \sum_j f_j e^{2\pi i(hx_j+ky_j+lz_j)} \quad , \tag{2.67}$$

where $[x_j, y_j, z_j]$ are coordinates of atom j in a unit cell, in units of primitive lattice vectors.

In the case of a simple cubic lattice with a single atom at each lattice point, the above formula reduces to $S(\mathbf{G}) = f$. In a bcc crystal, the unit cell contains an atom at every lattice point $[0, 0, 0]$ and at the centre of the unit cell $[1/2, 1/2, 1/2]$. Therefore, for bcc metal, structure factor is:

$$S_{hkl} = f[1 + e^{i\pi(h+k+l)}] = f[1 + (-1)^{h+k+l}] \quad . \tag{2.68}$$

Structure	Allowed Reflections
cubic	any h, k, l
bcc	$h + k + l$ is even
fcc	h, k, l all even or all odd
hcp	l is even and $h + 2k$

Table 2.1: Selection rules for different crystallographic structures.

It can be noticed that planes where $h+k+l$ is an even number generate constructive interference. However, if this number is odd, the structure factor vanishes, which leads to the concept of 'forbidden' reflections. Different structures follow different *selection rules*, as summarised in Table 2.1.

2.2.5 Powder diffraction

There are a number of methods of performing scattering experiments, but the fundamental principles are the same for all of them. If the wavelength of light fired at a crystal is known, then the spacing between lattice planes can be deduced from the diffraction image.

The most basic method uses *Laue geometry* where x-rays with a broad frequency spectrum probe a single crystal from one direction. Since the Laue condition is met only for particular wavelengths, we can determine the structure of the crystal by analysing which x-rays are scattered constructively.

A slightly different approach to the problem of meeting the Laue condition is to vary the orientation of the crystal with respect to incoming x-rays, rather than varying their wavelength. The rotating crystal method uses this technique to make sure a constructive interference pattern from a single crystal is found.

The method that is the main focus of this work is known as *powder diffraction* (or the Debye-Scherrer method). Powder diffraction uses a monochromatic (or at least pseudo-monochromatic) source of light to probe a polycrystalline sample. Crystal grains are randomly oriented, meaning that a small subset of grains constructively diffracts x-rays coming from a fixed direction – a similar rule is used in the rotating crystal method. In powder diffraction geometry, scattered light forms a cone with an

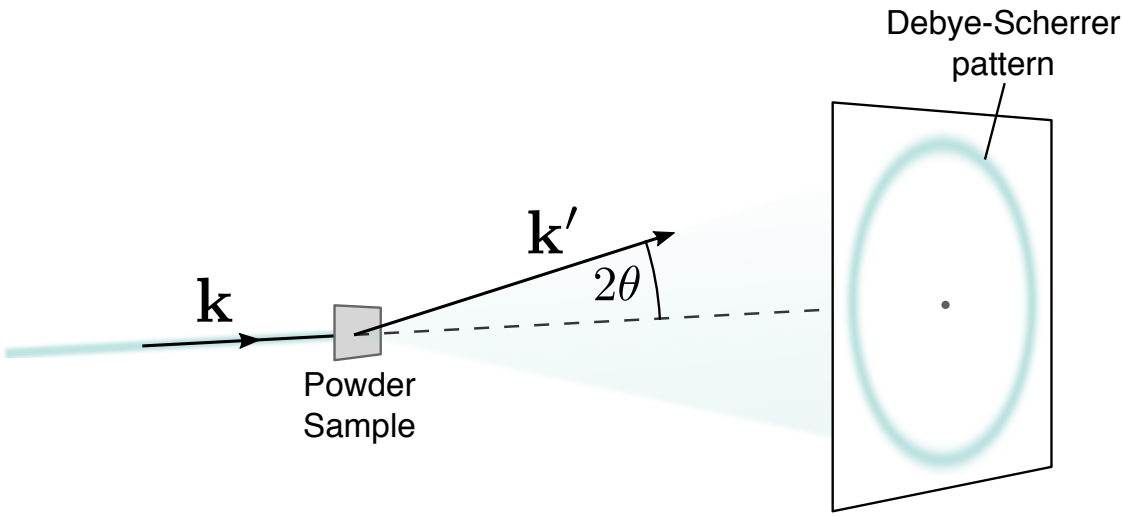


Figure 2.18: A schematic of powder diffraction geometry.

angle 2θ to the direction of incoming x-rays, as shown in Figure 2.18. The diffracted signal, collected by a detector, forms a series of rings known as *Debye-Sherrer rings*.

2.2.6 Ewald sphere

It is worth revisiting the Laue condition in the context of experimental geometry, as it is beneficial to consider reciprocal space when describing diffraction. From the Laue condition we have two criteria: photons are elastically scattered, which means that the magnitude of incoming and scattered wavevectors is the same, and the difference between those two wavevectors is equal to the reciprocal lattice vector.

Ewald's construction helps to understand when the Laue condition is satisfied by using the geometry of the experimental setup via the use of *Ewald's sphere*. The latter is a sphere in a reciprocal space with radius $|\mathbf{k}|$ (as shown in Figure 2.19), centered at the end of the incident wavevector $|\mathbf{k}|$. The reciprocal lattice space has its origin at point O, the beginning of vector $|\mathbf{k}|$. Since $|\mathbf{k}| = |\mathbf{k}'|$, the vector $\mathbf{k} - \mathbf{k}'$ has its two ends at O and any other point on a Ewald sphere. In a setup with a monochromatic light source probing a single crystal, obtaining constructive interference is challenging as its geometric interpretation is an overlap of reciprocal lattice points and Ewald's sphere. In the 2D case shown in Figure 2.19a only one such point exists.

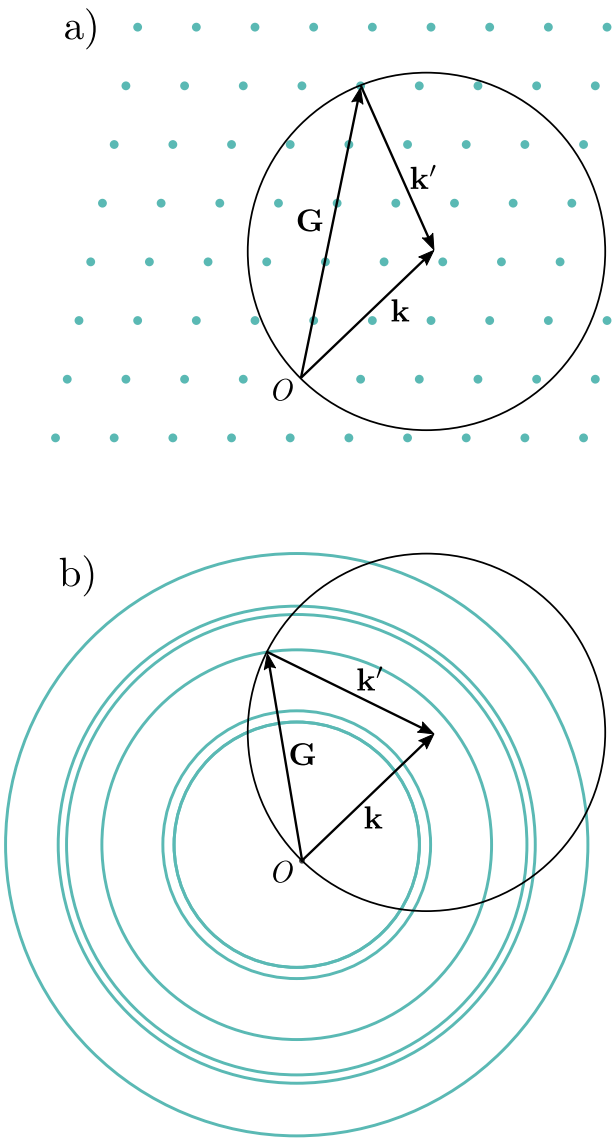


Figure 2.19: Two-dimensional Ewald's construction for two experimental setups: a) single crystal and b) a polycrystalline sample probed by a monochromatic source of x-rays.

In a powder diffraction, grains are randomly oriented so that reciprocal lattice space is generated by the summation of a single-crystal reciprocal lattice revolved by 4π around O. This leads to the generation of concentric spheres with their origin at O, shown in Figure 2.19b. The intersection of these spheres and Ewald's sphere produces a number of rings, and so the diffraction pattern produces Debye-Scherrer rings in a diffraction plane.

2.2.7 Fibre diffraction

One characteristic feature of a perfect powder material is the complete randomness of grain orientation, which leads to full Debye-Scherrer rings on diffraction planes. However, manufacturing processes may lead to the creation of textured materials where the polycrystalline sample is not isotropic in a macroscopic sense. An example of texture is *fibre texture*, where all grains have random azimuthal orientation, but the same axial orientation. Texture influences the diffraction pattern since the number of possible grain orientations is reduced in comparison to powder diffraction. This can be explained using the approach developed by Polanyi [63–66] illustrated in Figure 2.20. Fibre-diffraction analysis is an extension of Ewald's construction where the intercept of two spheres satisfies the Laue condition. In a powder diffraction case the rotation of the reciprocal lattice generates a set of Polanyi spheres, which span all possible orientations of $\mathbf{G}$ vectors in a sample. On the other hand, the reciprocal space of fibre-textured material is generated by the rotation of a single-crystal reciprocal lattice about a single axis (or fibre-texture direction). Thus, instead of the entire sphere, only a set of rings on a Polanyi sphere is spanned. Diffraction occurs where the Ewald sphere intersects the rings on the Polanyi sphere, so that a set of spots (or arcs in case of non-perfect texture) appears on a diffraction plane instead of full Debye-Scherrer rings. Different fibre orientations diffract light in different directions, therefore information about the azimuthal location of diffraction spots can provide information about the orientation of crystallines in a sample. Analysis of the diffraction pattern from fibre-texture material refers to a specific case, which can be generalised to materials with grain orientation defined by any orientation distribution function (ODF).

2.3 Shock waves

A *shock wave* is defined as a propagating disturbance in a medium with a characteristic shock front – a discontinuity in pressure, density and internal energy. The sound speed in matter increases with the amount of compression, therefore

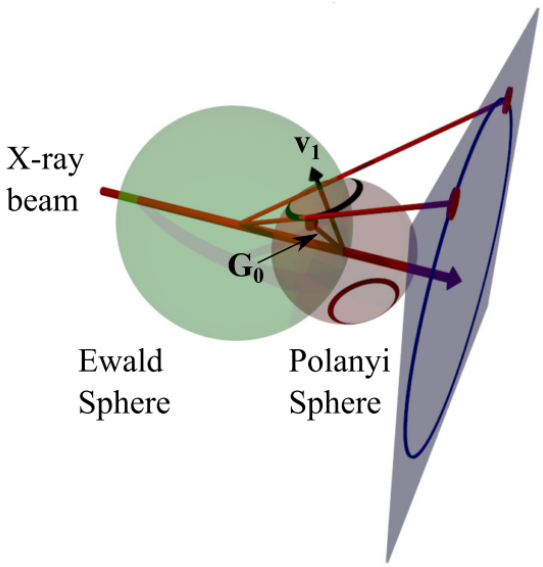


Figure 2.20: Illustration showing the formation of a diffraction pattern in fibre-texture geometry (adapted from McGonegle *et al.* [66]).

every disturbance in a material leads to shock formation, as long as the natural energy decay does not suppress it. The mechanism of shock front generation is shown in Figure 2.21. Since a disturbance with a higher amplitude travels faster than a disturbance with a lower amplitude, the high-amplitude disturbance will start catching up with the front of the low-amplitude disturbance, forming a shock front. In real materials, perfect discontinuity cannot be achieved, as the lattice spacing limits the size of the shock front.

2.3.1 The Rankine-Hugoniot equations

The fundamentals of shock physics are described by the Rankine-Hugoniot equations. This set of equations is valid for fluids and solids where the yield strength is exceeded by the stress. In order to derive them, we consider a cylindrical piston with cross-section area A pushing on a block of material, as shown in Figure 2.22. At time $t < 0$ the system is at ambient conditions in terms of pressure, density and internal energy per unit mass of P_0, ρ_0 and E_0 respectively. At time $t = 0$ the piston instantly starts to move at a constant velocity U_p along the z axis. This process causes a shock wave to travel through the material. At a later time t, the compressed

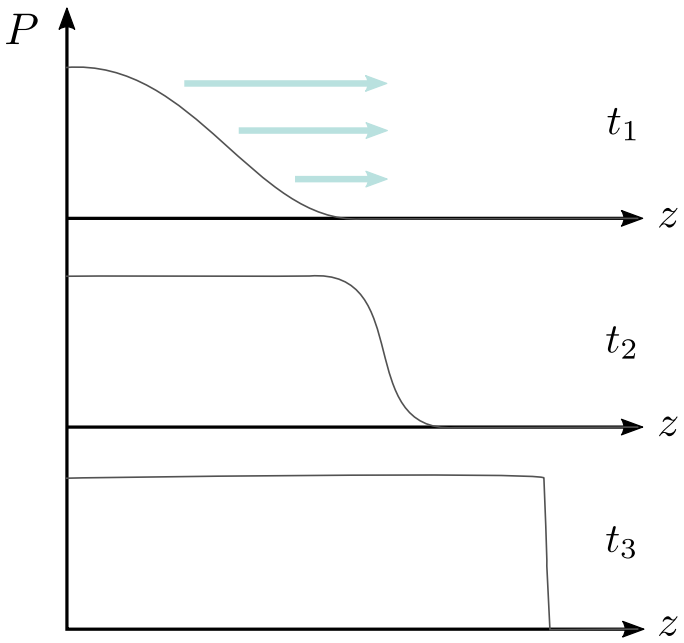


Figure 2.21: Three time steps $t_1 < t_2 < t_3$ of propagating pressure disturbance along the z axis. Due to the sound speed increase with the increase of disturbance amplitude (blue arrows) the high pressure part starts to catch up with the front of the disturbance. This leads to the formation of a pressure discontinuity in c) which defines a shock wave.

part of the medium is at elevated pressure, density and internal energy per unit mass of P, ρ, and E respectively.

The shock wave propagation induced by a moving piston is often compared to a snow plough moving into snow. The compressed region travels at the velocity of the piston pushing it at U_p (commonly named particle velocity). However, the boundary separating the compressed region from the region at ambient conditions travels faster at U_s - the velocity of the shock wavefront. A similar effect is observed when the region separating compressed snow from non-compressed snow travels faster than the snow plough pushing it.

Within time dt from the start of the motion of the piston, the shock front moves by $U_s dt$ while the piston moves by $U_p dt$. During this time the volume of the shocked region increases by $A(U_s - U_p)dt$, while the volume of the unshocked material decreases by $U_s dt$.

Applying the conservation of mass to the shocked part of the material we find

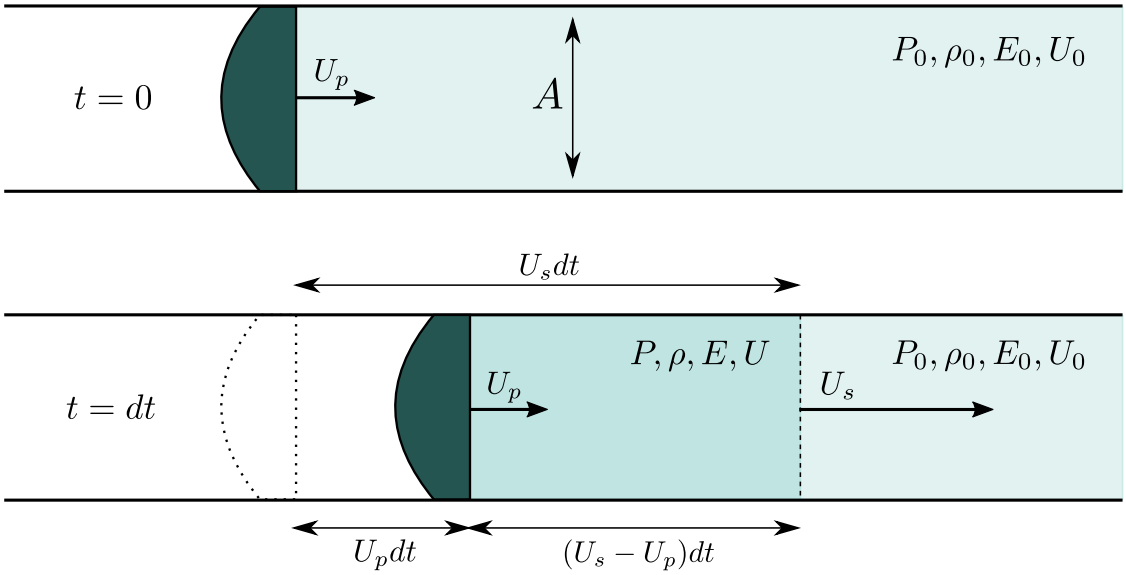


Figure 2.22: Schematic of shock wave propagation.

that:

$$\rho_0 U_s = \rho(U_s - U_p) \quad , \tag{2.69}$$

where the term Adt has been dropped. Within time dt the compressed mass is accelerated to the velocity of the piston. The difference in momentum of the compressed material is:

$$\rho(U_s - U_p)AdtU_p \quad . \tag{2.70}$$

From Newton's second law of dynamics it can be determined that this change is the result of an impulse generated by the piston, which can be described by the pressure difference:

$$Fdt = (P - P_0)Adt \quad , \tag{2.71}$$

where F is the force the piston exerts on the compressed material. Equating expressions 2.70 and 2.71 we describe the conservation of momentum:

$$(P - P_0) = \rho(U_s - U_p)U_p \quad . \tag{2.72}$$

By using equation 2.69 we have:

$$(P - P_0) = \rho_0 U_s U_p \quad . \tag{2.73}$$

The final piece of the derivation of the Rankine-Hugoniot equations is the analysis of energy. The work done by the piston is:

$$W = (P_1 - P_0)AU_p dt \quad , \tag{2.74}$$

and the kinetic energy of the compressed material is:

$$E_k = \frac{1}{2}(A\rho_0 U_s dt)U_p^2 \quad . \tag{2.75}$$

The change in internal energy is expressed by:

$$\Delta E_i = (A\rho_0 U_s dt)(E_1 - E_0) \quad . \tag{2.76}$$

Combining equations 2.74, 2.75, and 2.76 we can describe the energy conservation in the following way:

$$W = E_k + \Delta E_i \quad , \tag{2.77}$$

$$P_1 U_p = \frac{1}{2}\rho_0 U_s U_p^2 + \rho_0 U_s (E_1 - E_0) \quad . \tag{2.78}$$

Substituting equations 2.69 and 2.73 into 2.78 we find:

$$E_1 - E_0 = \frac{1}{2}(P_1 + P_0)(V_0 - V_1) \quad , \tag{2.79}$$

where V_i is the specific volume given by $V_i = \rho_i^{-1}$.

Once derived, the three Rankine-Hugoniot equations (equations 2.69, 2.73 ,2.79) contain five independent variables. In order to calculate all of them as a function of one quantity, an additional equation is needed. This additional piece of information is the relationship between shock and particle velocities, which is determined experimentally and which is of the form:

$$U_s = C_0 + S_1 U_p + S_2 U_p^2 + ... \quad , \tag{2.80}$$

where C_0 is the sound velocity at ambient conditions, and S_i are empirical parameters. Formula 2.80 is often known as the *equation of state* (EOS) of a material. For the majority of materials, the non-linear contributions of the particle velocity in equation 2.80 are negligible, and EOS can be written in a simple form:

$$U_s = C_0 + SU_p \quad . \tag{2.81}$$

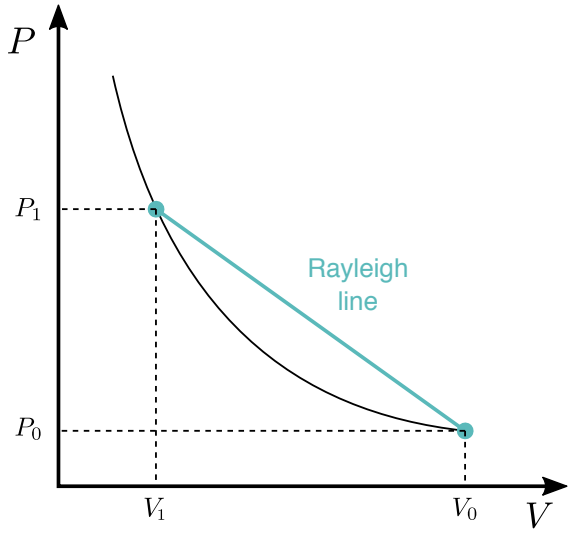


Figure 2.23: Illustration showing the Hugoniot curve in P-V space. The Rayleigh line, in blue, connects the initial and the final (shocked) states.

2.3.2 Hugoniot

Combining the conservation equations derived in the previous section with the EOS provides the relationship between the pressure and specific volume known as *Hugoniot*. Hugoniot defines all the points in P-V space that can be reached via shock compression as shown in Figure 2.23. The straight line joining (P_0, V_0) and (P_1, V_1) is known as the *Rayleigh line* and refers to the shocked state at P_1. It is important to point out that a material experiencing shock compression does not go through the continuum of all states on Hugoniot, as the shock is a discontinuous jump between the initial and final state. This discontinuity is explained by the slope of the Rayleigh line, which can be derived by manipulating equations 2.69 and 2.73 showing quadratic dependence on the shock velocity:

$$\frac{P_1 - P_0}{V_1 - V_0} = -\frac{U_s^2}{V^2} \quad , \tag{2.82}$$

By combining the conservation equations with the linear EOS model, the expression for the shock speed as a function of V, C_0, and S can be found:

$$U_s = \frac{C_0 V_0}{V_0 - S(V_0 - V_1)} \quad . \tag{2.83}$$

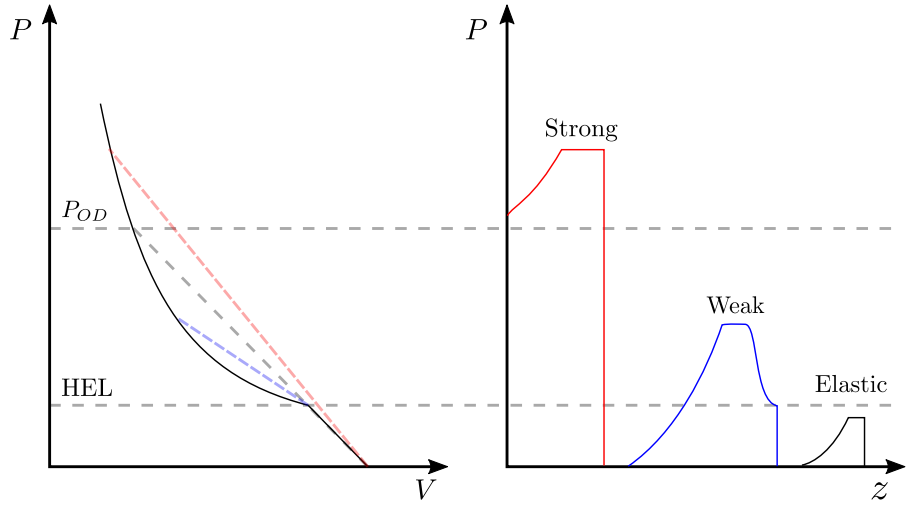


Figure 2.24: Illustration of three idealised shock regimes in a solid. On the left-hand side, the P-V curve indicates HEL and P_{OD} – Hugoniot state with a Rayleigh line parallel to the elastic portion of Hugoniot. On the right-hand side, the pressure profile along the direction of shock propagation z is shown. In the case of the shock below HEL, purely elastic wave is formed. Weak shock in the intermediate region between HEL and P_{OD} exhibiting two-wave structure is shown in blue while the overdriven shock is shown in red.

By substituting equation 2.83 into 2.82, the $P - V$ relationship shown in Figure 2.23 is obtained:

$$P - P_0 = \frac{C_0^2(V_0 - V_1)}{[V_0 - S(V_0 - V_1)]^2} \quad . \tag{2.84}$$

2.3.3 Shock waves in solids

The above description of shock waves is accurate for fluids as they do not support shear stress and deform hydrostatically. The analysis of shock waves in solids requires more complex description. Solids can accommodate shear stresses, as previously discussed, by deforming elastically. Shock traveling in the z-direction supports shear stress such that $\sigma_{zz} > \sigma_{xx}, \sigma_{yy}$ which causes uniaxial compression in the shock direction. If the strength of the compression does not exceed a certain threshold called the *Hugoniot Elastic Limit* (HEL), the deformation is purely elastic and once the compression wave has passed through, the material returns to its original state upon release.

For shock above HEL, the solid starts to flow plastically. The shear stress is reduced, relaxing material back towards hydrostatic conditions. During plastic

deformation, energy is used to preform plastic work within the sample. This energy is absorbed at a cost of a kinetic energy which leads to a decrease in the velocity of the shock. From equation 2.83, we can notice that a rapid change in the velocity of a shock wave results in a sharp change in the gradient of Hugoniot in P-V space as shown in Figure 2.24. Shock can be divided into two categories depending on its strength: weak and strong. Weak shocks are ones that compress the solid just above the HEL. They are characterised by a two-wave structure where the elastic wave travels ahead of the plastic wave due to the difference in the shock speed. If the strength of the shock is large enough, the velocity of the plastic wave is larger than the velocity of the elastic wave. These conditions are described as overdriven when only one, purely plastic, wave is generated. This transition is illustrated in Figure 2.24. The strength of the shock in the overdriven case is represented by the Rayleigh line directly connecting the ambient conditions with the Hugoniot state, since the gradient of this line is larger than the gradient of the elastic part of the Hugoniot.

Experimental pressure profiles may differ from the idealised profiles described above, since a number of factors may affect their shape. For example, polymorphic phase transitions induced by high pressure conditions result in an abrupt change in the velocity of the shock wave, which splits the plastic deformation into two waves (historically this phenomenon helped to identify these transitions using velocimetry techniques) [67]. Often HEL is much lower than the typical shock pressure and may be difficult to detect. In this dissertation, attention will be given to overdriven shock conditions. These kinds of conditions are desirable if shock steadiness (i.e. no change of a wave profile as a function of time) is an important element. Shock front steadiness and its shape was a subject of research published by Bland. By investigating viscous solids he noticed that the shock profile becomes steady once the shock wave travels a distance of about 5 times its thickness [68, 69]. The thickness of the shock wave is proportional to the viscosity of the medium and therefore the relaxation time of the material. This steady state is reached when the balance between the viscous and nonlinear pressures (with respect to strain) is achieved [70].

Bland condition helps to define a set of parameters for which steadiness is achieved:

$$\frac{3LS\dot{\epsilon}}{8C_0} \geq 1 \quad , \tag{2.85}$$

where L is the distance over which the compression wave steepens up, and $\dot{\epsilon}$ is the strain rate. The Rankine-Hugoniot equations are applicable if the distance required for the shock to become steady is less than the sample thickness. The strain state can be estimated using *Swegle-Grady's* empirical relation which correlates strain rate with shock pressure:

$$\dot{\epsilon} = kP^4 \quad , \tag{2.86}$$

where k is an experimentally-measured constant [71].

Once the Hugoniot state is reached, the material remains at elevated high pressure conditions. The length of the plateau in the shock's profile depends on the length of the impact pulse.

2.3.4 Release

After the impact of the external force generating the shock is stopped, the material starts to return to ambient conditions upon release. The rarefaction wave following the plateau of the shock is an isentropic expansion, which means that the strain rate during release is lower than strain rate during the shock. Isentropic expansion is governed by the sound speed of the material [72, 73]. Since the sound speed increases with the amount of compression, the rarefaction wave exhibits dispersion – this effect is opposite to the steepening at the shock's front. Similar to compression waves, initial uniaxial deformation along the shock's direction on release is supported by the material's strength. This means that the elastic precursor traveling at the longitudinal sound speed is observed in the pressure profile, as shown in Figure 2.25. Once the strength of the material is exceeded, the sample starts to expand plastically. This plastic deformation travels at the bulk sound speed (which is slower than the longitudinal sound speed). Therefore a two-wave structure in the release wave profile emerges. It is worth pointing out that the size of the elastic precursor on release

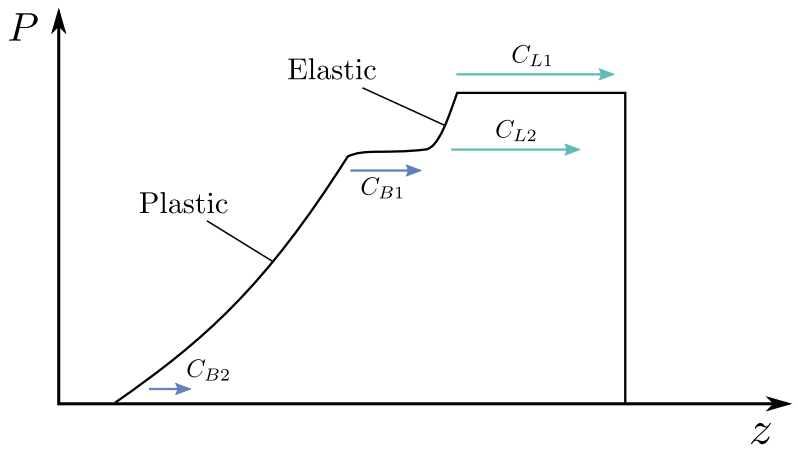


Figure 2.25: Illustration of the pressure profile of an idealised release wave following a shock. Elastic and plastic parts of the rarefaction fan are indicated. Due to the difference in the longitudinal sound velocity C_L and bulk sound velocity C_B, a two-wave structure emerges.

does not have to be the same size as the elastic precursor on compression. Properties of a material prior to compression change dramatically after the passage of the shock's wavefront. For example, shock-induced defects may increase a material's strength via work hardening while the increase in temperature of the compressed sample may reduce its ability to maintain large amounts of shear stress.

2.4 Computational methods

Computer simulations are an important branch of research that helps the material scientist to study solids. In the field of dynamically-compressed matter, two popular approaches can be distinguished: molecular dynamics (MD) modelling and hydrodynamic modelling. These two methods are complimentary: their underlying principles target the analysis of the same problems at different scales.

2.4.1 Molecular dynamics simulations

Molecular dynamics methods look at the Angstrom scale of material by treating the sample as a set of discrete elements – atoms – interacting with one another. The principle of this approach relies on the numerical calculation of equations of motion of every atom. In this case, the simulation size is often a limiting factor in a direct comparison between the simulation and a macro-scale experiment.

According to Newton's second law, the equation of motion is given by:

$$\mathbf{F_i}(\mathbf{r_1}, \mathbf{r_2}, ..., \mathbf{r_N}) = m_i \frac{d^2\mathbf{r_i}}{dt^2} \quad , \tag{2.87}$$

where $\mathbf{F_i}$ is the force acting on one of N atoms with mass m_i located at a position $\mathbf{r_i}$. These forces are calculated using a potential function as one of the input parameters of the scheme to effectively describe atomic interactions between neighboring atoms. Such calculations are subject to a set of certain initial and spatial boundary conditions. After calculating the forces acting on every atom for a particular time step, the atomic positions and velocities can be updated and the calculation proceeds to the next step where the process is repeated.

2.4.2 The LAMMPS code

The MD simulations presented in this work have been performed using a Large-scale Atomic/Molecular Massively Parallel Simulator (LAMMPS) code developed by Sandia National Laboratory [74]. The architecture of the code allows for a highly-efficient parallelisation of the computation between cores, which is an important factor for high-performance modelling, as it enables simulations up to billions of atoms [75].

The code implements the velocity Verlet algorithm for the integration of motion atoms in time [76]. At every step, the positions $\mathbf{r}$ and velocities $\mathbf{v}$ are updated according to the following rules:

$$\mathbf{r}(t + \Delta t) = \mathbf{r}(t) + \mathbf{v}(t)\Delta t + \frac{1}{2}\mathbf{a}(t)\Delta t^2 \quad , \tag{2.88}$$

$$\mathbf{v}(t + \Delta t) = \mathbf{v}(t) + \frac{1}{2}\mathbf{a}(t)\Delta t^2 \quad , \tag{2.89}$$

$$\mathbf{a}(t + \Delta t) = -\frac{\nabla V_{\text{field}}}{m}\mathbf{r}(t + \Delta t) \quad , \tag{2.90}$$

$$\mathbf{v}(t + \Delta t) = \mathbf{v}(t + \frac{\Delta t}{2}) + \frac{1}{2}\mathbf{a}(t + \Delta t)\Delta t \quad , \tag{2.91}$$

where **a** is the acceleration due to the gradient in the potential field V_{field}. This version of the algorithm differs slightly from the classical Verlet algorithm, which requires information about two consecutive timesteps. The modified version of the algorithm allows for reduced memory usage and more efficient operation. The length of time between two timesteps Δt is an important element to consider, as too large of a value would introduce cumulative errors of the order $O(\Delta t^4)$. In MD simulations this value is typically equal to a femtosecond, a period of time which balances the precision of calculations and high performance.

The analysis of macroscopic quantities based on microscopic calculations is desirable. Simulations are carried out using an appropriate ensemble. The majority of this work employs a microcanonical ensemble (NVE ensemble), where the number of particles N in a simulation, the volume V and the energy E are conserved quantities. Other forms of ensembles, commonly used for equilibration processes, are NVT and NPT, where T and P stand for conserved temperature and pressure, respectively.

2.4.3 Interatomic potentials

Another key factor in simulation investigations is the choice of an appropriate potential which effectively defines the behaviour of atoms. Potential development is itself an active area of research with two standard approaches discussed in this section.

The simplest form of an interatomic potential, known as the Lennard-Jones potential, takes the following form:

$$V_{LJ}(r) = 4\epsilon_{\text{pot}}\left[\left(\frac{\sigma_{\text{pot}}}{r}\right)^{12} - \left(\frac{\sigma_{\text{pot}}}{r}\right)^{6}\right] \quad , \tag{2.92}$$

where ϵ_{pot} and σ_{pot} are parameters that are a subject of potential development. It can be noticed that the only variable in equation 2.92 is the distance between two particles $r = |\mathbf{r_1} - \mathbf{r_2}|$. The positive r^{12} refers to short-range repulse forces due to overlapping electron clouds, while r^6 refers to long-range attractive van der Waals forces. The Lennard-Jones potential does not often perform well in terms of modelling solids due to significant many-body effects. A solution to this problem is

provided by the embedded atom method (EAM) potential. This form of potential, which is achieved by expanding the Lennard-Jones potential with the many-body component F, is widely used for modelling metals [77]:

$$V_{EAM} = \frac{1}{2}\sum_{i\neq j}^{N}\phi(r_{ij}) + \sum_{i}^{N}F_i(\rho_i) \quad , \tag{2.93}$$

where N is the total number of particles within the cutoff radius from the considered atom (the marginal influence of distance atoms in the system is neglected). The additional parameter F refers to the energy required to place an atom in the electronic cloud of neighbouring particles ρ. The majority of work on MD simulations presented in this thesis was performed using EAM potential developed by Ravelo *et. al.* [55].

2.4.4 X-ray diffraction pattern simulation from MD

One of the most powerful methods of MD modelling in the context of x-ray crystallographic investigations is the ability to generate diffraction patterns using the spatial positions of atoms in a simulated material.

As previously discussed in section 2.2.2, the reciprocal space is obtained by Fourier Transforming atomic potential. The atomic positions, which are one of the outputs of MD simulations, are modeled as a set of Kronecker delta function. By applying a discrete Fourier Transform to such a real lattice a reciprocal lattice of the simulated material can be found:

$$I = |FT(\mathbf{k})| = |\sum_{j}^{N} e^{-i\mathbf{k}\cdot\mathbf{r}}|^2 \quad . \tag{2.94}$$

The Discrete Fourier Transform is often replaced by the Fast Fourier Transform in the context of multi-million atom simulations, significantly reducing the time of computation as described by Kimminau *et al.* [78]. Such reciprocal 3D intensity space can be used to generate diffraction images for a comparison against experimental x-ray patterns. In order to do it, a 2D mapping on a plane at a desired orientation from 3D reciprocal intensity space is performed. Depending on the experimental needs, additional custom transformations to the reciprocal intensity can be applied: e.g. fibre-texture diffraction generation via rotation of the entire reciprocal space.

2.4.5 Hydrodynamic simulations

Another important class of computational techniques are hydrodynamic simulations [79]. Contrary to MD, hydrodynamic simulations focus on the macroscopic properties of materials by solving conservation equations of mass, momentum and energy for a grid of small layers. For the case of a fluid, a common subject of hydrodynamic simulations, these conservation equations read:

$$\frac{\partial \rho}{\partial t} + \rho \nabla \cdot \mathbf{u} = 0 \quad , \tag{2.95}$$

$$\rho \frac{\partial \mathbf{u}}{\partial t} = -\nabla P + \mathbf{f} \quad , \tag{2.96}$$

$$\rho \frac{\partial \epsilon_{\text{in}}}{\partial t} + P(\nabla \cdot \mathbf{u}) = 0 \quad , \tag{2.97}$$

where ρ is the mass density, $\mathbf{u}$ is the velocity of an element of the grid, P is the hydrostatic pressure of the fluid, $\mathbf{f}$ is an external force acting on a material, and ϵ_{in} is the internal energy. Modelling behaviour of solids using the hydrodynamic approach requires certain modifications to the above equations [80–82]. The most popular of these modifications is the addition of the material's strength to the equation. In order to simulate the behaviour of a material in a way that supports shear stress, hydrostatic pressure in equation 2.96 needs to be replaced by a full stress tensor:

$$\rho \frac{\partial \mathbf{u}}{\partial t} = -\nabla \cdot \sigma + \mathbf{f} \quad . \tag{2.98}$$

Additionally a series of relationships between other elements (e.g. stress, strain, or strain rate) may be provided, increasing the complexity of the fundamental hydrodynamic rules.

2.5 X-ray Free Electron Laser

The advent of X-ray Free Electron Laser (XFEL) has become a milestone in the development of x-ray generation. Its extremely small bandwidth and increase in brightness by a factor of 10^9 [83] with respect to the previously available light

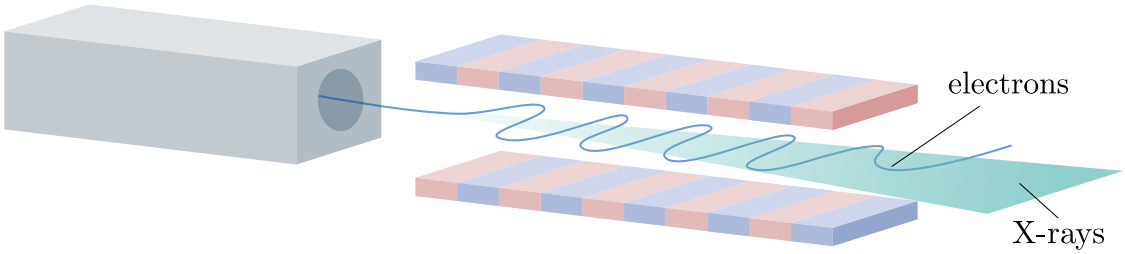


Figure 2.26: Illustration showing a simple XFEL setup. A beam of electrons (red line) is coming out of the linear accelerator depicted by a grey box on the left. An undulator made of periodically arranged magnets (blue – north, red – south) converts linear electron motion into a sinusoidal path. Emitted x-rays (blue) increase in strength along the undulator.

sources have already proven its significance by enabling previously inaccessible research opportunities.

A basic schematic of XFEL setup is illustrated in Figure 2.26. At the initial stage electrons are accelerated nearly to light speed via a linear accelerator. This high energy electron bunch is sent through an undulator (i.e. a periodic arrangement of magnets with alternating poles). The undulator creates a spatially periodic magnetic field perpendicular to the direction of the incoming electrons. This perpendicular magnetic field results in a Lorentz force applied to the electrons, which in turn leads to their oscillatory motion transverse to the direction of their flight. Accelerating electrons in the force field emit electromagnetic radiation. In the case of oscillating electrons in the magnetic field of the undulator, the wavelength of this field is expressed by:

$$\lambda = \frac{L}{2\gamma^2}\left(1 + \frac{K^2}{2}\right) \quad , \tag{2.99}$$

where L is the periodicity of the magnetic field, K is the undulator's strength and γ is the relativistic Lorentz factor [84]. For small values of K, the above formula suggests that the wavelength of the emitted radiation is proportional to the length scale of the undulator by $(2\gamma^2)^{-1}$. This phenomenon can be explained by a combination of two relativistic effects. Firstly, in the frame of reference of the traveling electron, the distance between neighbouring magnetic poles is reduced by a factor of γ due to the Lorentz contraction. Secondly, the produced electromagnetic

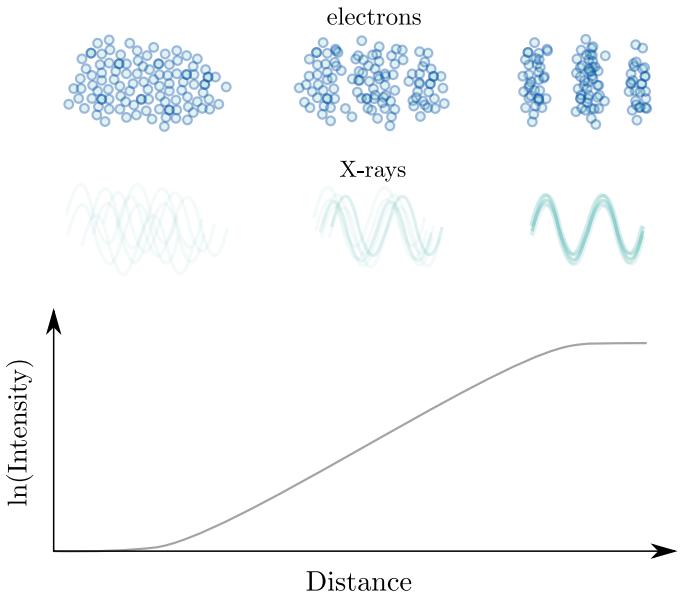


Figure 2.27: Simplified illustration of the electron microbunching at various positions within the undulator. The plot demonstrates the exponential growth of the x-ray intensity along the undulator with the saturation region at large 'Distance' values.

radiation experiences a Doppler shift due to the conversion from the electron's frame of reference to the laboratory frame of reference, which introduces another 2γ factor.

At an early stage, the generated radiation is incoherent within the undulator – emitted x-rays from randomly-distributed electrons interfere with each other in a random way. This means that the power of the produced electromagnetic radiation scales linearly with the number of electrons. However as the intensity of the generated radiation increases, it starts interacting with the electrons producing it via pendomorative force. The result is a change in the relative electron distribution along the longitudinal direction. These self-modulations cause electron microbunching with a periodicity λ as shown in Figure 2.27. At this point groups of electrons oscillate collectively, producing coherent radiation. The main advantage of this effect is an exponential growth in the x-ray's intensity as a function of the distance traveled by an electron, until the saturation level is reached (i.e. perfect microbunching occurs).

3

Shock compression of tantalum

Contents

3.1 Motivation and literature overview 55
3.2 Experimental setup 59
3.2.1 Laser-driven shocks 59
3.2.2 X-ray source 61
3.2.3 Targets 63
3.2.4 VISAR 64
3.2.5 CSPADs and data collection 67
3.2.6 Ambient data 70
3.2.7 Driven data 73
3.3 Liquid diffraction 76
3.4 Data analysis 88
3.5 Residual elastic shear stress 91
3.6 Driven textural changes 93
3.7 Equivalent plastic shear strain 102
3.8 Molecular dynamics simulations (shock) 106
3.9 Summary 113

This chapter describes an experiment performed at the SLAC National Accelerator Laboratory using LCLS to primarily investigate shock-induced plasticity in fibre-textured tantalum foils. It will begin with a short review of the scientific motivations and overview of the literature which informed this study, and continue with a presentation of the theoretical details of the developed experimental method, a description of the experimental setup, an analysis of the collected data, a description

of the performed MD simulations of the investigated processes and finally, the data-driven conclusions. This chapter also contains a small section describing the analysis of the liquid diffraction signal. The majority of the work presented in this chapter forms the core of the publication C. E. Wehrenberg, M. Sliwa *et al.* Nature (London), **550**, 496 (2017).

3.1 Motivation and literature overview

Since its discovery at the beginning of the 19th century, tantalum has been used for a wide range of applications in the industry. One of the distinctive purposes of tantalum is its use in the production of superalloys for engine components, nuclear reactors, or military equipment [85]. These superalloys are characterised by high melting points, strength and ductility, which makes them extremely desirable in situations when an object needs to withstand the application of large shear forces. Therefore, good understanding of the plasticity mechanisms of tantalum at elevated pressures and strain rates is crucial to designing such compounds. One way of achieving these high-energy-density conditions is through shock compression – a method extensively used for tantalum due to its high shock impedance. *In situ* investigations of dynamically-compressed metals are challenging due to the very small timescales of the studied processes. This problem is solved by x-ray diffraction experiments with a sub-ns resolution of the probing beam, which can provide an insight into the dynamic behaviour of materials. Due to its high atomic number (Z=73), tantalum is highly opaque to x-rays, which scatter elastically from a large electronic cloud, making the high quality diffraction signal convenient to work with.

At ambient conditions tantalum can mostly be found in a crystallographic α-Ta (bcc) form; however, small amounts of metastable β-Ta can be present in thin foils depending on the manufacturing method used [88]. This work is entirely focused on bcc Ta as it is the primary crystallographic form of the studied samples (>99.5%). It is believed that materials of the same crystallographic structure show similarities in the way they deform under the influence of high shear stress. Therefore, tantalum can be considered as a model bcc material due to its specific physical properties

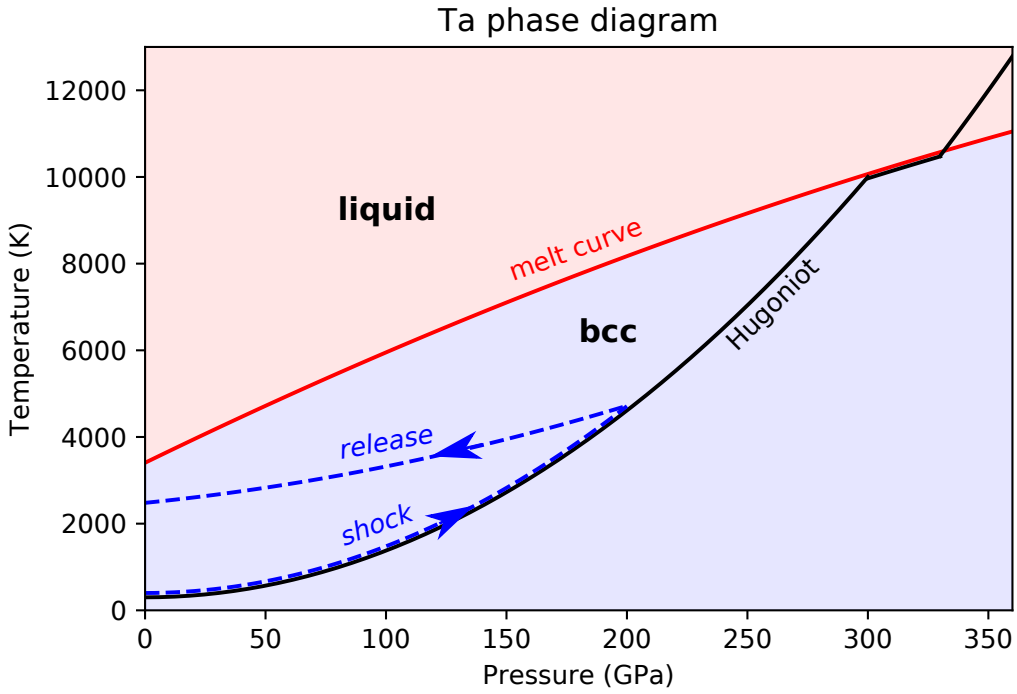


Figure 3.1: Phase diagram of tantalum. The melt curve corresponds to the DFT calculations [86] and Hugoniot curve up to the melting point corresponds to the calculations based on the generalized pseudopotential theory [87]. The proposed shape of the Hugoniot curve beyond the melting point has been constructed for the approximate overview of the Hugoniot curve at high pressure states. Blue dashed curves give an example history of Ta during the shock compression to 200 GPa and the subsequent release. It is important to point out that during the shock compression, the material does not experience all states along the Hugoniot path, but rather jumps discontinuously between the initial and the final states.

which make it an ideal candidate for high pressure studies of plastic deformations in bcc metals. In addition to its aforementioned high shock impedance and high x-ray opacity, tantalum's high melting temperature and resistivity to crystallographic phase transformations also make it suitable for high pressure research of plasticity. Apart from individual studies [89, 90], which have shown a small amount of pressure-induced phase transformation to a hexagonal form, it is believed that tantalum remains in a bcc form, which means that the additional effects associated with phase transformations can be excluded from the analysis of plastic deformations 3.1. Previous investigations of tantalum on a Hugoniot reported that the metal remains solid under compression for a wide range of pressures up to about 300

GPa, beyond which it melts [91]. Thus tantalum allows for the investigation of a larger variety of high pressure states than many other metals would. The melting of metals on a Hugoniot is a subject of active research itself [47, 92]. There is a great interest in studying tantalum above its melt curve during dynamic compression as the properties of these states are to a large degree unexplored. It is because the characteristic features of liquid XRD such as its diffused signal make experiments probing liquid conditions on short time scales challenging.

Interestingly, tantalum exhibits a competition between multiple plasticity mechanisms, making it a particularly appealing material to study plastic deformations [93]. The built-up shear stress can be either relieved by dislocation motion, which leads to slip [56], or by deformation twinning [94]. Despite many efforts involving theoretical, computational and experimental techniques to understand the nature of shock-induced plasticity in tantalum, there is still a lot of disagreement in terms of the fundamentals of the deformation mechanisms involved. For example, a molecular dynamics study by Higginbotham *et al.* [94] of shocked single-crystal tantalum along the crystallographic [100] direction reported a twin fraction (the percentage of the sample which formed twins) of about 95% using the Finnis-Sinclair potential. Similar observations have been shown by Tramontina *et al.* [93]. In their simulations, based on the EAM potential developed by Ravelo *et al.* [55], they reported an increasing twin fraction with the strength of the shock traveling along the [100] direction in a single crystal, including a regime of 'massive' twin nucleation above 70 GPa. On the other hand, simulations performed by Rudd *et al.* [56] using the Model Generalised Pseudopotential Theory potential demonstrated pure slip via significant generation of dislocations. Clearly, therefore, different theoretical potentials predict different behaviour, emphasising the need for unambiguous experimental data.

Previous experimental works investigating plasticity in dynamically-compressed tantalum have been largely limited to *ex situ* analysis [89, 95–98]. In such studies, fragments of the shocked material are recovered by capturing small pieces of the driven target in a special recovery chamber, which is followed by an analysis of their microstructure. The most prominent sign of twinning in a recovered sample

was reported by Florando and co-workers [97]. Their shock-compression gas-gun experiments along the [100] direction in single-crystal tantalum induced twins in up to 25% of the target. Polycrystalline samples with a variety of grain sizes have been the subject of multiple shock experiments investigating a wide range of high pressure conditions and producing a variety of different results. Examples include observations made by Murr *et al.* [95] who reported significant amounts of pressure-induced twinning, and investigations made by Lu *et al.* [98] who observed the absence of twins in a similar pressure range. A common problem associated with recovery experiments is the lack of temporal resolution of the dynamic events; that is to say, it is impossible to distinguish whether the observed features are the result of the initial compression, release, subsequent reverberations, or post-shock annealing. For this reason, the application of experimental techniques with the ability to capture shock propagation *in situ* becomes desirable. Previous studies using *in situ* x-ray diffraction techniques as a diagnostic used white-light Laue geometry to investigate the strength [35] as well as the elastic-to-plastic lattice relaxations [36] of tantalum with a sub-nanosecond probe resolution. These experiments were not able to distinguish between contributions to plastic deformation from twinning and slip due to high noise-to-signal ratio.

A resolution to the experimental challenges outlined above is provided by XFELs - light sources which enable the probing of matter at a femtosecond scale with signal-to-noise ratios unachievable on any other platform. Since the timescale of the x-ray probe (100fs) is shorter than the shortest phonon period ($\sim$ 200fs in Ta [99]), XFELs effectively 'freeze' the atomic motion of a studied material by capturing the position of its atoms in a reciprocal space. This chapter describes experimental work where, by using unique non-collinear fibre-texture geometry combined with the use of XFEL, plasticity mechanisms in shock-compressed tantalum are identified with the first measurement of twinning fraction *in situ*.

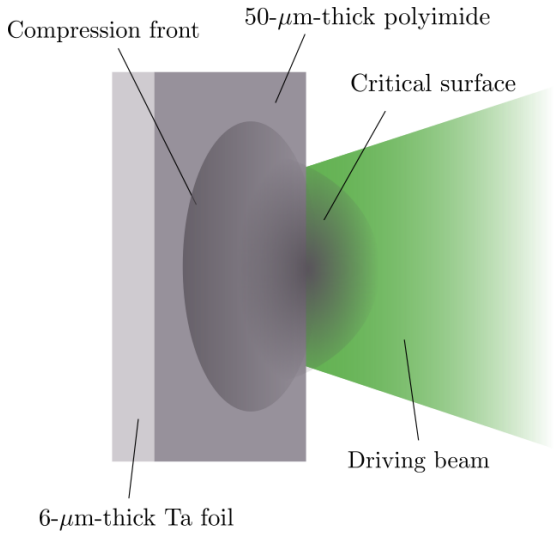


Figure 3.2: Schematic illustration of the laser ablation process.

3.2 Experimental setup

The experiment was performed at the Matter in Extreme Conditions (MEC) endstation of LCLS. The characteristic feature of MEC is a combination of a high-power optical laser setup with the XFEL's beam which is designed for pump-probe type experiments.

3.2.1 Laser-driven shocks

In our experimental configuration, a high-power laser which produced frequency-doubled (527 nm) 16 J square pulses of temporal length in range 5-10 ns was used to generate a shock wave in a target (Figure 3.3). In this scheme, compression is achieved by irradiating a spot with a diameter of a 100, 150, or 250 μm in size on a surface of the sample with a high-power laser. This leads to a process known as laser-ablation, as illustrated in Figure 3.2. This process relies on the absorption of light by the surface of the target which results in the transformation of the solid into a plasma. The conversion of the solid into a gas leads to a rapid plasma expansion of the target which according to Netwon's third principle of mechanics must be counteracted by a force acting in the opposite direction to the plasma expansion. This force launches an acoustic compression wave into the bulk of the target, which steepens up into a shock wave once it travels a certain distance. Following the

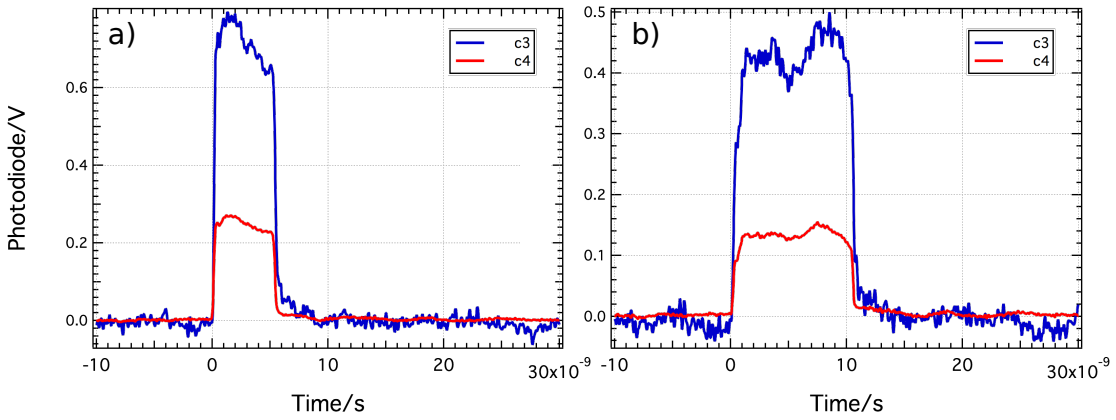


Figure 3.3: Temporal voltage profile of the two (c3 and c4) driving laser photodiodes. The signals were designed to generate 5ns (a) and 10ns (b) long flat top pulses.

Bland condition (equation 2.85) and Swegle-Grady relation (equation 2.86), we can determine the minimum distance required for an acoustic wave to form a strong shock. For $C_0 = 3,293$ ms^{-1}, $S = 1.307$ and $k = 27.37$ s^{-1} GPa^{-4} at about 100 GPa [100], this distance is about 3 μm. The expanding plasma continues to absorb light via inverse Bremsstrahlung process meaning that the duration of the constant elevated pressure depends on the length of the laser pulse.

In the experimental setup the intensity of the driving laser beam ranged from 10^{11} to 6.5×10^{12} W cm^{-2}. By varying the intensity of the incident beam we can vary the shock pressure. It has been found [101] that the achievable laser-induced shock pressure obeys the following law:

$$P = 8.6\left(\frac{I_{\text{drive}}}{10^{14}}\right)^{2/3}\lambda_{\text{drive}}^{-2/3}\left(\frac{A}{2Z}\right)^{1/3} \quad , \tag{3.1}$$

where P is the ablation pressure in Mbar, I_{drive} is the intensity of the laser beam in W cm^{-2}, λ_{drive} is the light wavelength in µm and A and Z are the atomic and mass numbers of the target respectively. This power law of 2/3 between ablation pressure and laser intensity, despite a time dependence, approximately holds for a number of materials [102]. However, to evaluate the shock pressure in the driven material other diagnostics (described in the further parts of the thesis) were employed.

One key element of dynamic compression investigations is the planarity and uniformity of the produced shock. All the work presented in this thesis is based on

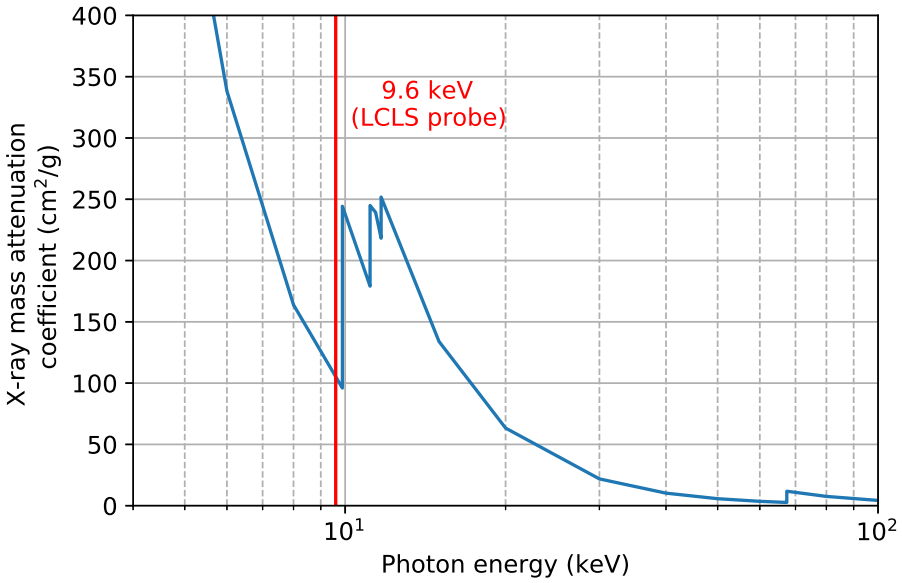


Figure 3.4: X-ray absorption coefficient of tantalum as a function of photon energy [103]. The red line (9.6 keV) appearing just below the absorption edge refers to the selected x-ray energy for the diffraction experiment.

the assumption that the nature of compression is one-dimensional. For an isotropic material, a laser irradiating a small surface will in general produce a spherical compression wave, as can be seen in the two-dimensional illustration in Figure 3.2. Therefore, in order to maintain the planar feature of the compression front, the thickness of the sample needs to be significantly smaller than the diameter of the driving laser spot. In this experiment this condition was achieved by using a set of Hybrid phase plates to modify the focal spot. These plates use surface features to shift the phase of the light, creating focal spots of 100 µm, 150 µm, and 250 µm diameter (depending on the required pressure) and at the same time smoothing out inhomogeneities in the 'top hat' intensity profile. We experimentally determined that the drive had remained planar over the region probed by the x-ray beam by observations of the VISAR patterns.

3.2.2 X-ray source

Monochromatic x-rays produced by the XFEL were 50-fs-long with a transverse dimension of about 20 µm positioned centrally at the location of the driving laser

spot as shown in Figure 3.10. In the most severe cases the beam pointing fluctuations with respect to the experimental setup reach 10-20% of the probe beam diameter. A significant difference in the spatial dimensions of the driving and probing laser pulses meant that only the central portion of the sample – which experienced uniaxial compression due to a flat shock wavefront – was investigated.

The size of the probe beam was larger than the grain size in the probed material where individual crystals had transverse dimension ∼0.1-0.5µm. This enabled the probing of a large number of grains in a single measurement.

In pump-probe experiments it is crucial to precisely setup spatial overlap between the two laser beams. The location of the X-ray beam was determined from the visible fluorescence produced by the X-rays interacting with the Ce:YAG scintillator. Visible and near-infrared wavelengths generate fluorescence in these materials, and the focal spot can be positioned in the same location as the X-ray spot. Therefore the overlap is achieved by steering the optical beam with a motorized focusing lens [104, 105].

Pump and probe lasers were synchronised, so that the x-ray beam was fired after a certain controllable delay with respect to the optical beam, in order to capture the moment when the shock wave penetrated a tantalum foil.

LCLS offers tunable hard x-rays in a range of up to ∼12 keV. The selection of an appropriate x-ray wavelength depends on two factors: the position of the detectors that capture diffracted light and the coefficient of x-ray absorption by the target. For the majority of materials, a simple model for x-ray interaction with the matter [106] states:

$$\mu(k) \propto \frac{1}{k^3} \quad , \tag{3.2}$$

where μ is x-ray absorption coefficient and k is the light's wavenumber. This relation works for a wide range of photon energies, but neglects the discrete nature of atomic energy levels. Taking into account the structure of the energy levels, we find the formation of well-known discrete absorption edges which are related to the excitation of core electrons to continuum by x-rays.

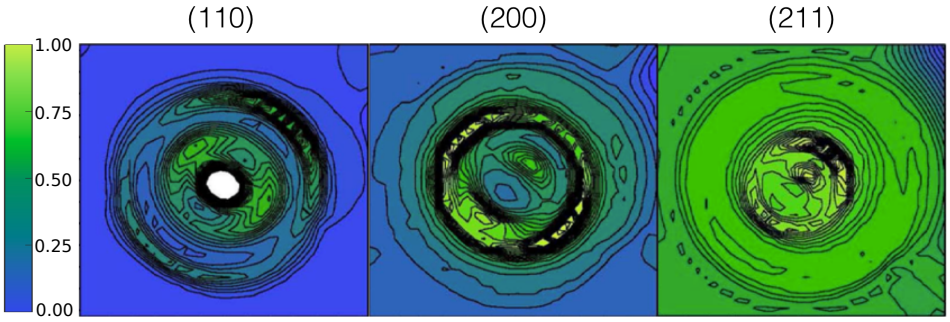


Figure 3.5: Pole plots (heatmap representing stereographic projection of crystal faces) of the fibre-textured tantalum foils for three sets of crystallographic planes: (110), (200), and (211). The white region in the central part of the (110) pole plot corresponds to the saturated signal which exceeds the provided scale.

Figure 3.4 shows the x-ray absorption coefficient of tantalum as a function of photon energy. As described above, the majority of the spectrum can be described by the k^{-3} trend, with the exception of a discontinuous feature at about 10 keV due to electron excitation between discrete energy levels. When selecting the energy of the x-ray source for the diffraction experiment, the primary goal is to avoid absorption edges. Improper source tuning may result in reduction in the x-ray absorption length, which leads to a reduction of the observed x-ray signal-to-noise ratio. Therefore in order to avoid this effect, the x-ray energy was tuned to a value of 9.6 keV – just below the absorption edge. The selection of the largest possible photon energy from the spectroscopic point of view is also beneficial in terms of the geometry of the experimental setup as, according to Bragg's law 2.51, larger x-ray energies create smaller Debye-Scherrer rings which generally translate to relatively larger k-space coverage by the detectors.

3.2.3 Targets

Each target consisted of a 50-µm-thick kapton ablator glued to a 6-µm-thick foil of tantalum. The thickness of the plastic was over 8 times larger than that of the sample and thus prevented reverberations from entering the tantalum before the initial shock had passed through the sample (Figure 3.6). The thickness of the ablator also helped to smooth out such spatial variations in the drive as were created by the speckle pattern of the laser spot [107, 108]. The tantalum foil was

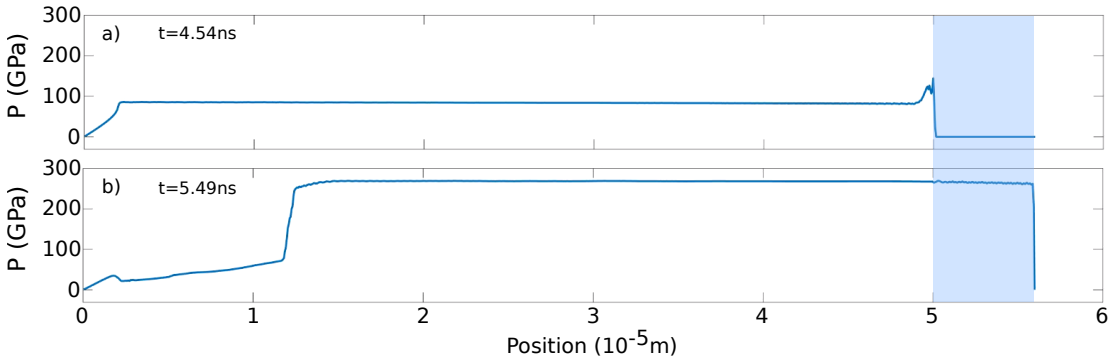


Figure 3.6: HYADES pressure profiles of the sample resembling the experimental sample at the moment of a) shock entering Ta layer (blue region) and b) shock reaching the free surface.

fabricated by vapour deposition onto an SiO_2 substrate at a temperature (about 450 °C) sufficient to create the bcc α-Ta phase and to delaminate the tantalum from the substrate upon cooling. Small amounts ($< 0.5\%$) of the β-Ta phase were also present in some of the samples. The deposition onto a substrate at a significant temperature allowed for the obtainment a tantalum foil with [110] fibre texture. An example of pole plots showing a symmetry about the direction of fibres is shown in Figure 3.5. The experiment used two batches of targets with different texture widths – the standard deviations in the distribution of grain orientations in the sample: r123 with a texture width of $\sim 2°$ and r127 with a texture width of $\sim 1°$. Such a small texture width resulted in a small azimuthal spread of the diffraction signal which, as will be shown, aids the analysis of the material's plastic response. The texture direction was parallel to the direction of the sample's normal. This means that the generated shock was traveling along the [110] direction in the polycrystalline material.

3.2.4 VISAR

A VISAR [27] diagnostic with a probe beam normal to the target was used to monitor the free-surface velocity U_{fs} of the tantalum during shock compression and release and to help set the diffraction timing, as shown in Figure 3.10. The schematic setup of the VISAR diagnostic is shown in Figure 3.7. It is based on the idea of the laser light interference after reflection from the moving surface of the target. The VISAR probe laser (Nd:YAG) sends a 523nm light beam towards

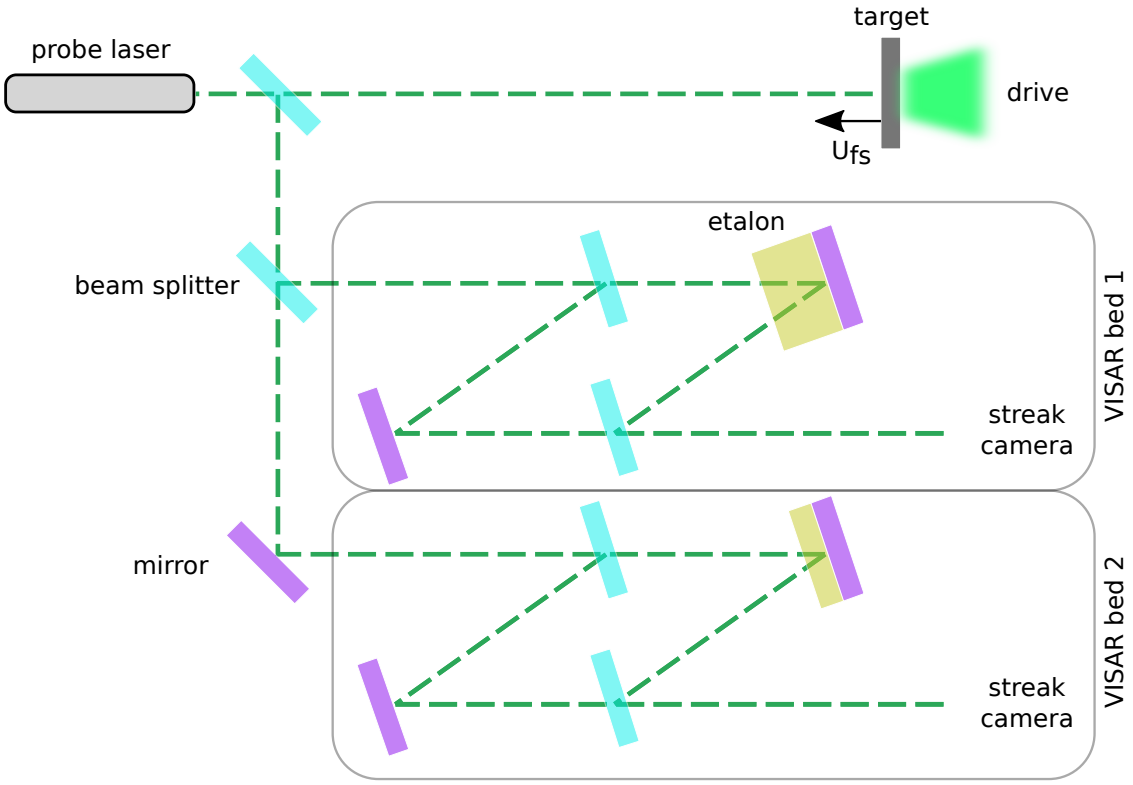


Figure 3.7: Simplified VISAR arrangement at MEC station.

the reflective rear surface of tantalum foil. The reflected signal is sent to Mach-Zehnder interferometer where it is split into two separate beams using a beam splitter. At this point both beams are sent along paths of different optical lengths before they are recombined and captured by the streak camera. The difference in optical paths introduces a relative delay between the beams which leads to phase difference between the two electromagnetic waves. In the case of perfect alignment of interferometer the streak camera captures a perfectly uniform intensity output due to the constant phase difference across the beam. However, by tilting one of the beam splitters of the interferometer, a linear path difference is introduced across the beam and the fringe light pattern emerges. The path difference between the two arms of the interferometer is created by introducing an etalon with high refractive index into one of the paths. The thickness of the etalon controls the amount of delay τ given by expression:

$$\tau = \frac{2h}{c}\left(1 - \frac{1}{n}\right) \tag{3.3}$$

where h is the thickness of the etalon, n is the refractive index of etalon, and c is the speed of light. The moving target results in a Doppler shift of the wavelength of the light:

$$\lambda(t) = \lambda_0\left(1 - \frac{2U_{fs}(t)}{c}\right) \tag{3.4}$$

where λ_0 is the original wavelength of the probe produced by the laser and U_{fs} is the velocity of the free surface of the target. Any change in the velocity of the reflective free surface of Ta foil causes observable an shift in the fringe pattern recorded by the streak camera.

In order to convert fringe pattern to the velocity profile, the Velocity Per Fringe (VPF) needs to be known. The order of interference is equal to the wavelength number difference between each of interferometer's paths:

$$N(t) = \frac{2h}{\lambda(t)}\left(n - \frac{1}{n}\right) \tag{3.5}$$

Therefore the fringe count F which is defined as the difference in the interference order with respect to the interference order prior to shock N_0 can be expressed as:

$$F(t) = N(t) - N_0 = 2h\left(n - \frac{1}{n}\right)\left(\frac{1}{\lambda(t)} - \frac{1}{\lambda_0}\right) \tag{3.6}$$

Combining above equation with Equation 3.4 we find:

$$F(t) = \frac{4hv(t)}{\lambda_0 c}\left(n - \frac{1}{n}\right) = \frac{2\tau v(t)}{\lambda_0} \tag{3.7}$$

where high order terms have been neglected.

Hence, VPF is:

$$VPF = \frac{v(t)}{F(t)} = \frac{\lambda_0}{2\tau} \tag{3.8}$$

In order to account for the change in the refractive index with the change in the wavelength additional correction δ is introduced:

$$VPF = \frac{\lambda_0}{2\tau(1+\delta)} \tag{3.9}$$

etalon (mm)	τ (ns)	VPF (km s^{-1})
20	0.108	2.393
50	0.260	0.993

Table 3.1: Summary of etalons used in the VISAR setup.

where for fused silica used in the experiment setup δ=0.0318 at λ=532nm [109].

MEC uses two interferometers within the VISAR setup with different thickness etalons. The summary of delays τ and VPFs associated with each of them is provided in table 3.1.

Examples of images captured by the streak camera are presented in Figure 3.8. The horizontal axes corresponds to time and the vertical axes correspond to distance along the free surface of the sample. The vertical discontinuity in the fringe pattern and the reduction in the intensity of the signal can be associated with the arrival of the shock wave. Streak images were processed by the VISAR analysis code developed by Andrew Comley. The code employs a Fourier Transformation method [110] to calculate fringe phase with respect to the reference streak image of the static material (prior shot) and produces velocity profile for known VPF (Figure 3.9). To ambiguity related to the number of integer fringe shifts added to the profile is solved by comparing profiles produced by the VISAR beds until both profiles overlap.

The optical streak camera system was used to confirm the planarity of the drive. The VISAR images show that the planar-driven region approximately corresponds to the size of the phase plates and is larger than the 20 µm x-ray beam.

After collection of the experimental data it became clear that the quality of the vast majority of VISAR images was poor. Moreover, on a number of occasions no VISAR signal was collected. Therefore, in Chapters 3 and 4, XRD images are utilized to extract information about the pressure in shocked material. Analysis of thermal effects on release (Chapter 5) identified potential problems related to using pressure information from XRD data for that particular work. Therefore VISAR shock profile analysis for several available shots was performed.

3.2.5 CSPADs and data collection

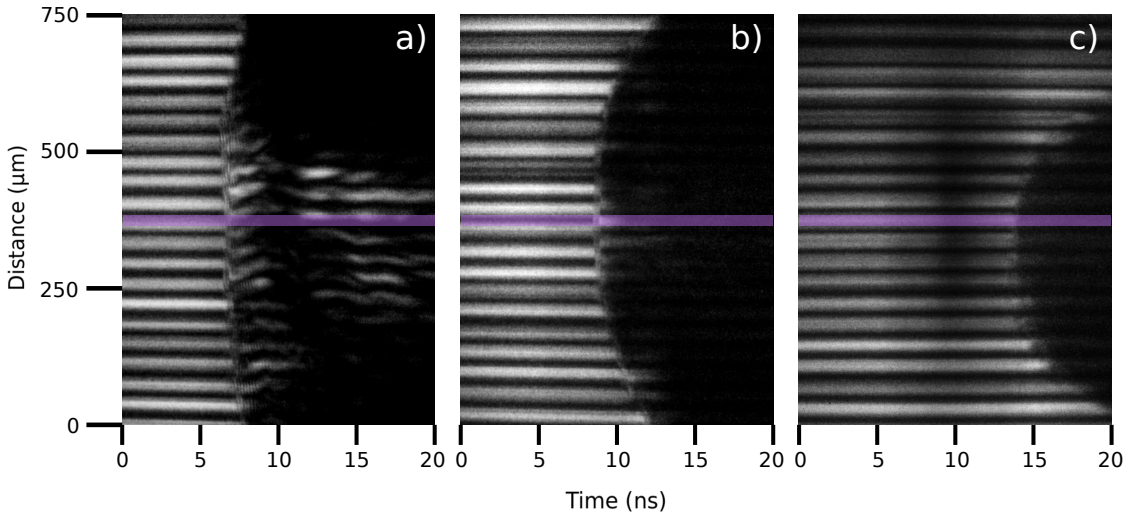


Figure 3.8: Example VISAR streak shock images using: a) 250, b) 150, and c) 100 μm phase plates. Bright parallel lines on the left-hand side of every image correspond to surface reflections prior to shock arrival. The planar region of the shock, which is roughly similar in dimensions to the phase plate, breaks out of the tantalum-free surface, causing a discontinuous shift in line location. The x-ray beam (marked with a purple region) probes a 20 μm region in the centre of the shock.

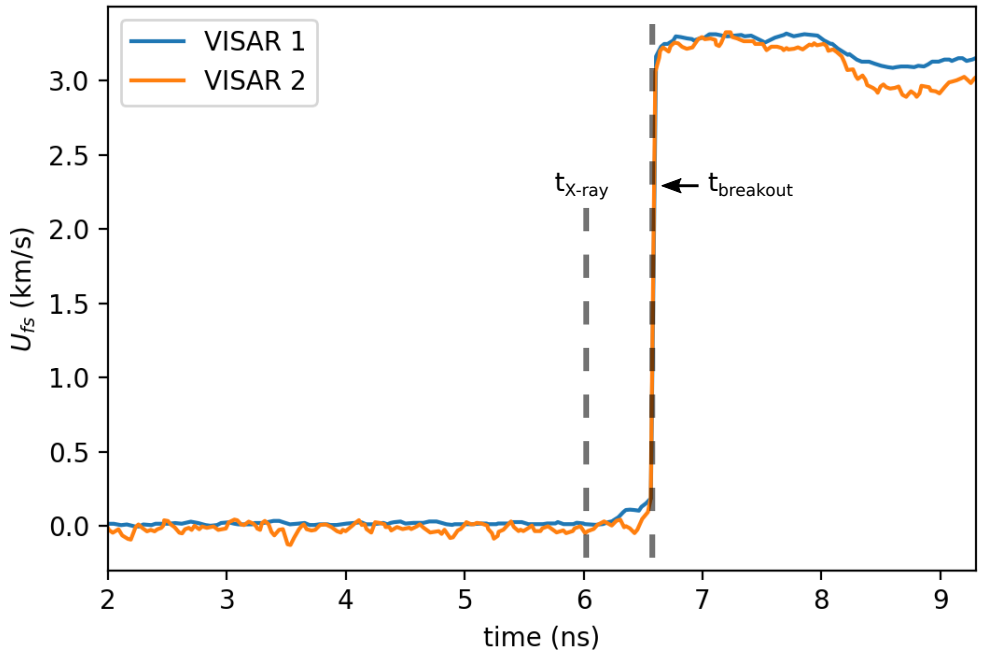


Figure 3.9: Velocity of the rear surface of the sample as a function of time. Two traces correspond to profiles extracted from the separate VISAR beds. The dashed lines indicate the timing of the x-ray probe with respect to the breakout time in order to study the shocked state of Ta ($t_{X\text{-ray}} < t_{breakout}$).

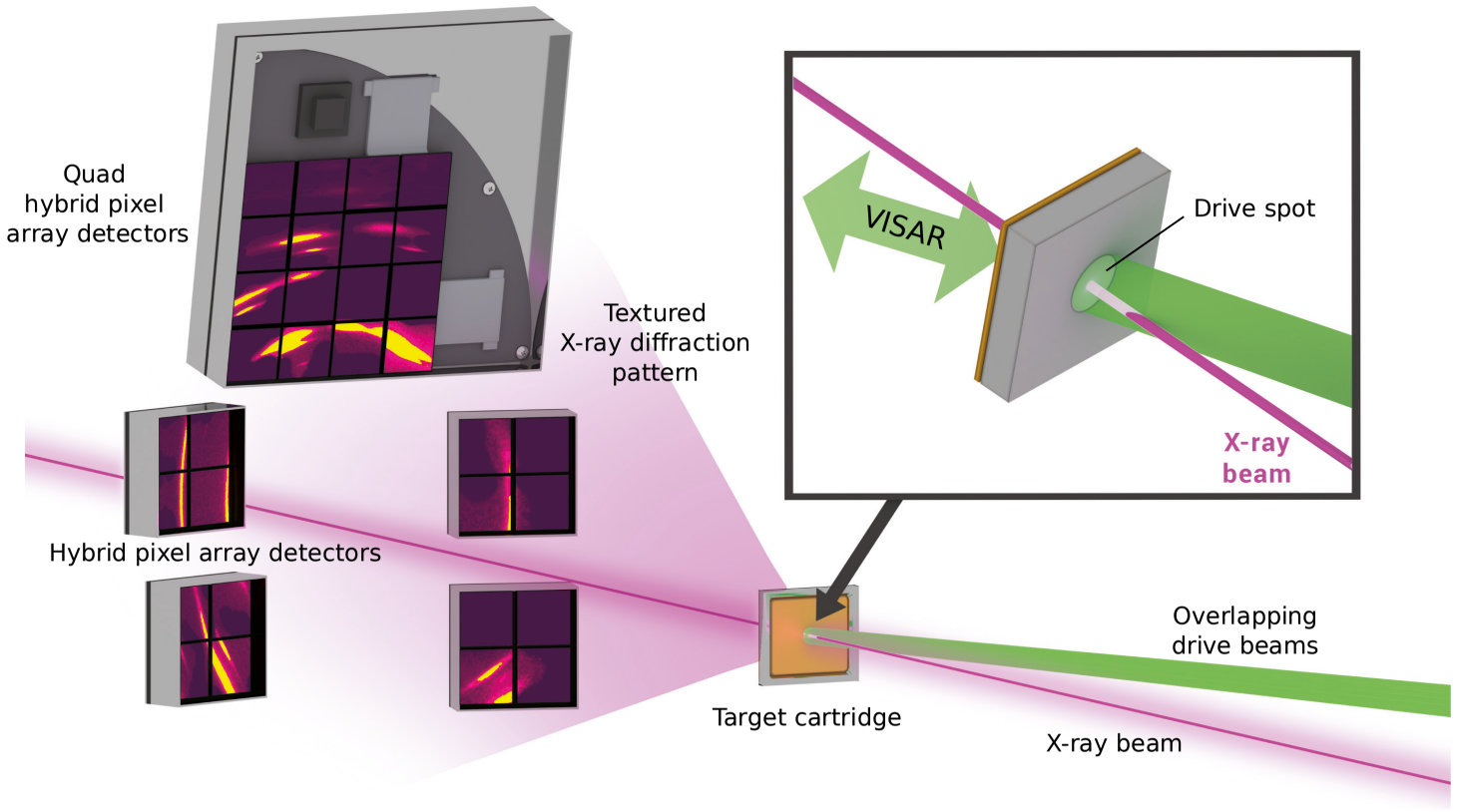


Figure 3.10: Experimental configuration for shock compression and *in situ* x-ray diffraction. A shock wave is driven by laser ablation (green beams) into the target cartridge, which consists of a plastic (50-µm-thick polyimide) ablator and 6-µm-thick tantalum foil with a (110) fibre texture. VISAR is used to monitor the free-surface velocity of the tantalum. The shock-compressed tantalum is probed by the x-ray beam (purple), and the resulting textured diffraction patterns are collected on an array of hybrid pixel array detectors.

The resulting diffraction patterns were captured on a number of Cornell-SLAC Pixel Array Detectors (CSPADs) [111] as shown in Figure 3.10. The position of the CSPADs and the diffraction angles were calibrated using a powder sample of LaB_6 and CeO_2 standards. The diffracted intensity was adjusted to account for the polarisation of the x-ray beam using the following factor:

$$f_{\text{polarization}} = [\cos^2(\phi)\cos(2\theta)]^2 + \sin^2(\phi) \quad , \tag{3.10}$$

where (2θ, ϕ) are the spherical coordinates of the diffracted signal, with 2θ being the polar angle and ϕ the azimuthal angle. This factor will be implicitly included in the methods outlined throughout the rest of this work. The majority of the quantitative analysis was performed in (2θ, ϕ)-space, i.e. collected images were warped such that the Debye-Scherrer rings from the unstrained calibrants formed a set of parallel lines.

The target was oriented such that the surface normal was aligned at an angle of 35° to the x-ray beam. Non-collinear probing geometry results in two features important for the execution of fundamental ideas of this experiment. Firstly, by bringing the x-ray beam at an angle to the compression axis, we were able to extract information about the deviatoric stress on compression, and as a result make an inference about tantalum's strength. This is possible since, as shown in previous works [66], symmetry breakage leads to deviations in the Debye-Scherrer circular pattern in the cases where there is a non-zero shear stress in the material. Secondly, in order to utilise textured diffraction technique, the x-ray beam and the direction of the fibres must be non-parallel with respect to each other. If this condition is satisfied, such a geometry does not produce full Debye-Scherrer rings, but rather distinct arcs on each ring, the azimuthal position of which provides direct information on the orientation of the planes with respect to the shock direction.

3.2.6 Ambient data

Prior to collecting a driven diffraction image, a set of 10 x-ray only images was recorded for every target. An example of raw ambient data projected onto a flat plane normal to the incoming x-ray direction is shown in Figure 3.11. In order to

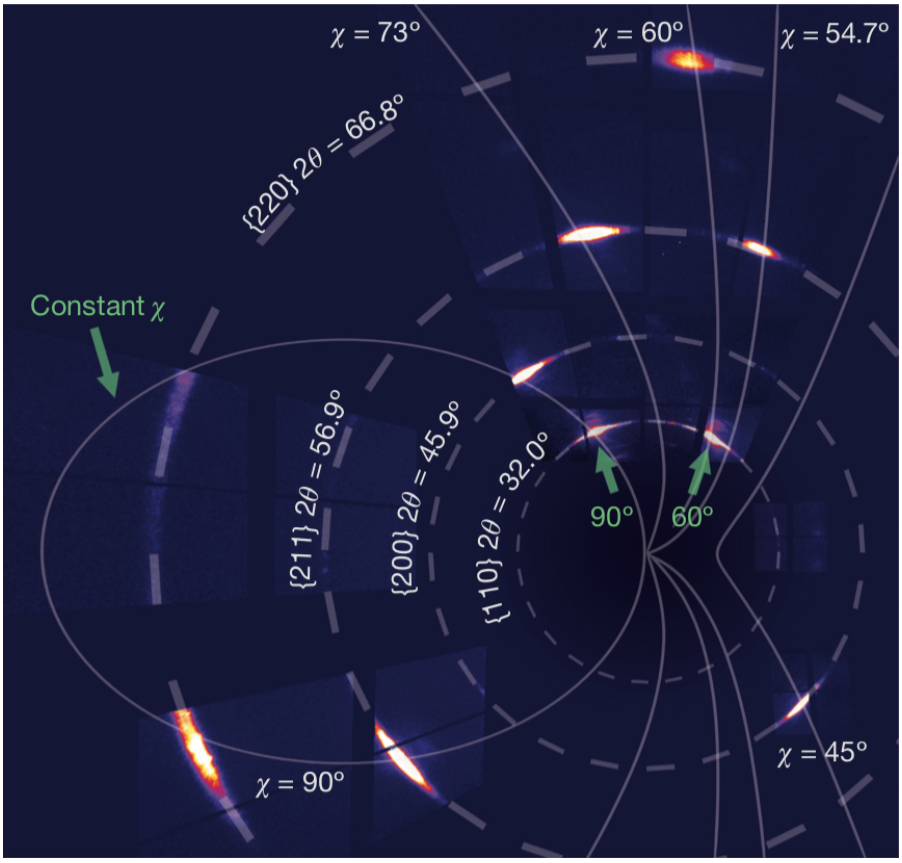


Figure 3.11: An example of an undriven XRD image. The diffraction data have corresponding {110} texture spots at certain χ angles, highlighted by green arrows. Solid curves indicate constant χ, corresponding to specific lattice planes: for {110}, $\chi = 60°$ and 90°; for {200}, $\chi = 90°$ and 45°; and for {211}, $\chi = 73°$ and 54.7°. The dashed curves indicate constant 2θ.

enhance the clarity of presentation of diffraction spots, their intensity has been presented on a logarithmic scale.

The azimuthal positions of the spots correspond to the angles of the respective diffraction planes. To understand the location of those spots, an angle χ is introduced; this is the angle the sample's normal forms with the diffracting plane, as illustrated in Figure 3.12a. Taking into consideration diffraction from the {110} family of planes, we notice that – due to the rotational symmetry of the fibre-textured material – it is possible to identify two families of distinct {110} planes with respect to the direction of the fibres. The two sketches of a tantalum unit cell (Figure 3.12b) demonstrate that the {110} planes have angles of 60° or 90° relative to the sample plane. As can be seen in the ambient diffraction image, two spots are visible

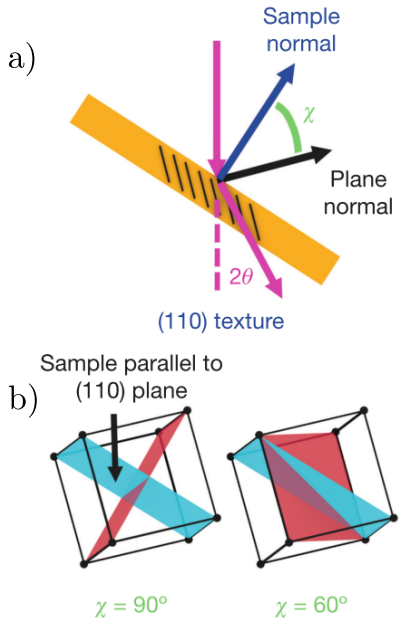


Figure 3.12: A sketch of the diffraction geometry describes the Bragg angle 2θ and the angle χ between the sample normal (blue arrow) and diffraction plane normal (black arrow). For a sample with (110) texture, in which the sample plane (blue) is parallel to the (110) plane, the remaining {110} planes (red) have either $\chi = 60°$ or $\chi = 90°$

hkl	χ (°)
{110}	60, 90
{200}	45, 90
{211}	54.7, 73, 90
{220}	60, 90

Table 3.2: List of the visible diffraction spots in the experimental geometry.

at the intersection of the {110} Debye-Scherrer ring (the constant Bragg angle of scattering 2θ is depicted with dashed lines) and constant χ curves which correspond to diffraction from $\chi = 60°$ and $\chi = 90°$ planes. Similar reasoning accounts for the azimuthal positions of texture spots for the other diffraction rings. A list of observed spots and their corresponding χ angles is given in Table 3.2. It is important to notice that every unique set of planes generates a signal at two different locations around one Debye-Scherrer ring. However, due to the experimental geometry, certain spots are not visible since they appear outside the detector coverage.

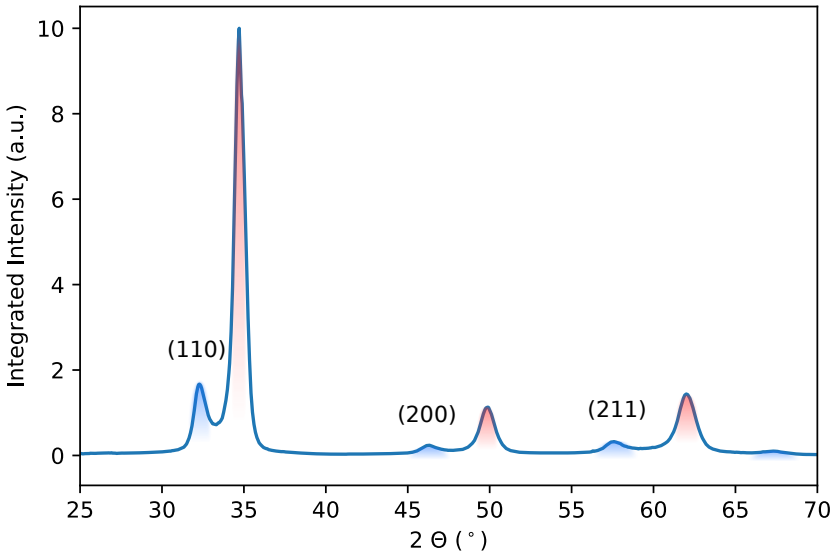


Figure 3.13: Diffraction angle (2θ) versus x-ray counts averaged over azimuthal coverage for a shock pressure of 73 GPa. The indices of the ambient pattern, which match the bcc phase with lattice parameter $d_0 = 3.308$Å, are marked in blue. The driven pattern (red peaks) matches the bcc phase with $d = 3.051$Å.

3.2.7 Driven data

The delay between the driving beam and x-rays was selected such that tantalum was probed during the initial transit of the shock through the metal. This means that the contributions to signal from both the undriven part of the sample in front of the shock and the driven part were captured in a single diffraction pattern.

An example of a driven signal warped into $(2\theta, \phi)$ space and integrated azimuthally is provided in Figure 3.13. Prior to transformation, the image has been preprocessed to remove the hot pixels appearing on the edges of the detectors. Additionally, averaging over the number of pixels in the azimuthal direction was performed in order to remove the cumulative contribution from a low signal background, which otherwise could have resulted in sharp discontinuities around the detector edges.

Compression of the material resulted in a decrease of the unit cell's size, which translated to an increase in the angle of the diffracted x-rays. Thus it was possible to observe two sets of Debye-Scherrer rings on the diffraction plane – the first one

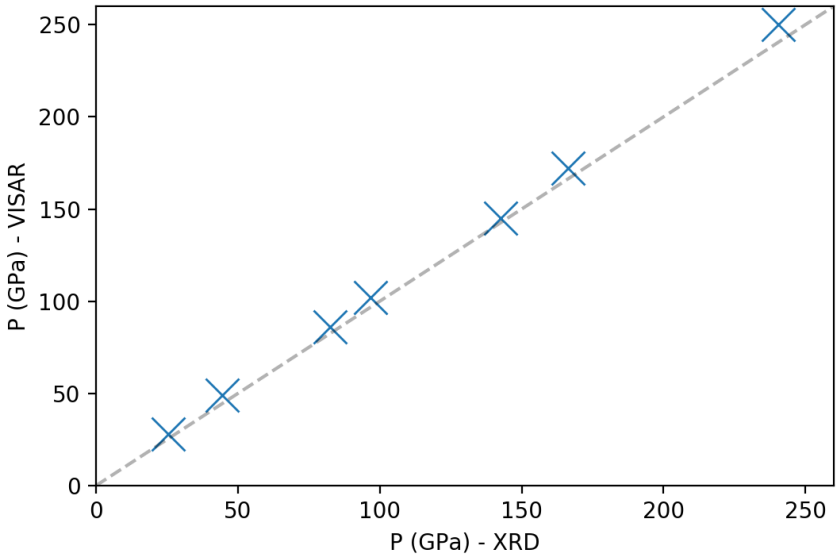


Figure 3.14: Comparison of the pressures in the shocked material evaluated using XRD and VISAR data. The dashed line provides a reference for a perfect agreement between the two methods.

referring to the structure of the undriven target and the second one (an expanded set of rings) coming from the shocked sample. This phenomenon is clearly displayed in the azimuthally-integrated lineout, where two sets of bcc peaks are highlighted in blue (ambient) and red (driven). The lattice constant can be estimated by performing a linear regression on the central position of the peaks using Bragg's law.

Pressures were determined by extracting the volumetric compression from diffraction by assuming a bcc structure and by using a known EOS data for Hugoniot. A line VISAR was used to measure rear surface velocities to provide an independent check of these values. Comparison of the pressures extracted from the XRD images and VISAR data during the initial passage of the shock wave through the sample is shown in Figure 3.19. Specifically, the modified expression for the shock pressure 2.84 was used:

$$P = \rho_0 C_0^2 \frac{1-(d/d_0)^3}{\left[1-S[1-(d/d_0)^3]\right]^2} \quad , \tag{3.11}$$

where d_0 and d are lattice parameters in the ambient and driven regions of the material, and ρ_0 is the initial specific density of tantalum. Over the years a few

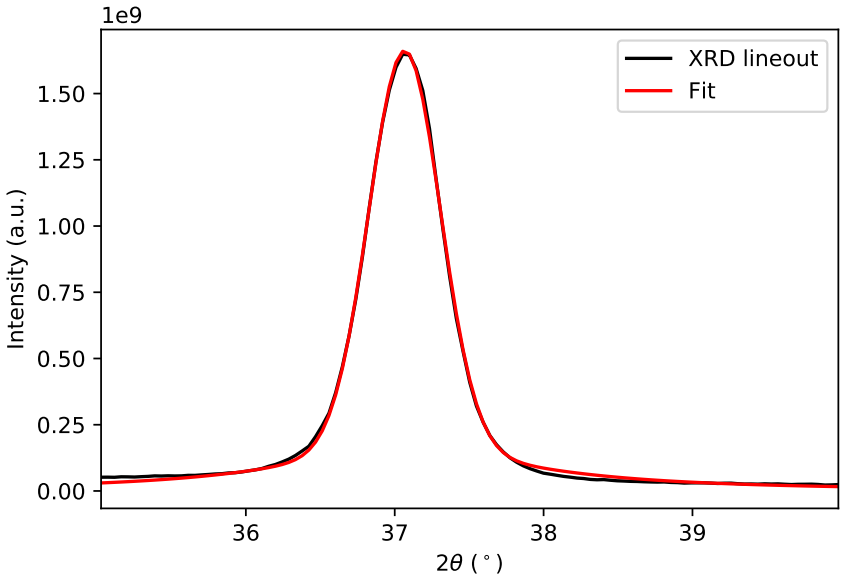


Figure 3.15: Integrated intensity lineout of the driven (110) peak (black line) and Pseudo-Voigt fit (red line).

experimental studies of tantalum's EOS on Hugoniot were performed [15, 100, 112–115]. However, experimental linear Hugoniot constants $C_0 = 3,293$ ms^{-1} and $S = 1.307$ determined by Mitchell and Nellis [100] were used, as it is a widely popular EOS in the shock physics community.

Errors in determined pressure arise directly from the extraction of peak positions. An example of an XRD signal and a fit is shown in Figure 3.15. The uncertainty associated with the central position of the fitted peak is of the order of $\sim 0.01°$ - a fraction of CSPAD's pixel. Central locations of multiple reflections are used where each of them provides a separate measurement of lattice spacing. The extracted lattice spacing d for a single shot is the weighted mean, and the error is the weighted standard deviation of the these measurements. The pressure uncertainty varies with the amount of volumetric compression due to the non-linear relationship between the pressure and the peak displacement in 2θ space. The errorbars on the estimated shock pressures (after conversion from lattice spacing) vary from about ± 2 GPa at low compression states ($\sim$30 GPa) to about ± 6 GPa at high compression states (>200 GPa). An additional source of pressure uncertainty may be the spatial and temporal non-uniformity in the drive. These non-uniformities would result in a

broadening of the diffraction peaks. This effect is not incorporated into the analysis since the VISAR records show that the drive is steady before the first reverberation.

3.3 Liquid diffraction

The strongest shocks were achieved using the smallest available phase plate size of 100 µm. Some of these high pressure driven diffraction patterns displayed a diffuse signal indicative of a liquid sample (Figure 3.16). Therefore the pressure could not be reliably measured either from the diffraction or from the VISAR. The pressure estimate from the laser ablation intensity was consistent with previous measurements of the shock melting pressure of about 300 GPa. An overview of the solid-liquid phase transition is displayed in the tantalum phase diagram (Figure 3.1) where the Hugoniot crosses the melt curve.

It is important to note that experimental work on liquid data at high pressure is challenging due to the nature of the liquid diffraction signal. Firstly, the reduction in atom ordering spreads out the x-ray signal over a wide surface, meaning that the intensity per unit solid angle goes down in comparison with solid diffraction. As a result, the characteristic features in diffraction images are less prominent and more sensitive to the influence of the background noise. Another important factor is the wide coverage of the Q range in the diffraction, which can be defined as:

$$Q = 4\pi \frac{\sin\theta}{\lambda} \quad . \tag{3.12}$$

Higher photon energies and an appropriate detector placement are required to observe multiple peaks in the data. It can be noticed through geometrical investigations that in 2θ-space the distances between consecutive liquid diffraction peaks are significantly larger than the distances between solid diffraction peaks.

The analysis of the liquid diffraction data followed a method developed by Eggert *et al.* [116] which leads to the extraction of the radial distribution $g(r)$ function and density of Ta based on Fourier Transformation of the structure factor $S(Q)$ defined as:

$$S(Q) = 1 + 4\pi\rho_0 \int_0^\infty r^2[g(r) - 1]\frac{\sin(Qr)}{Qr} \quad , \tag{3.13}$$

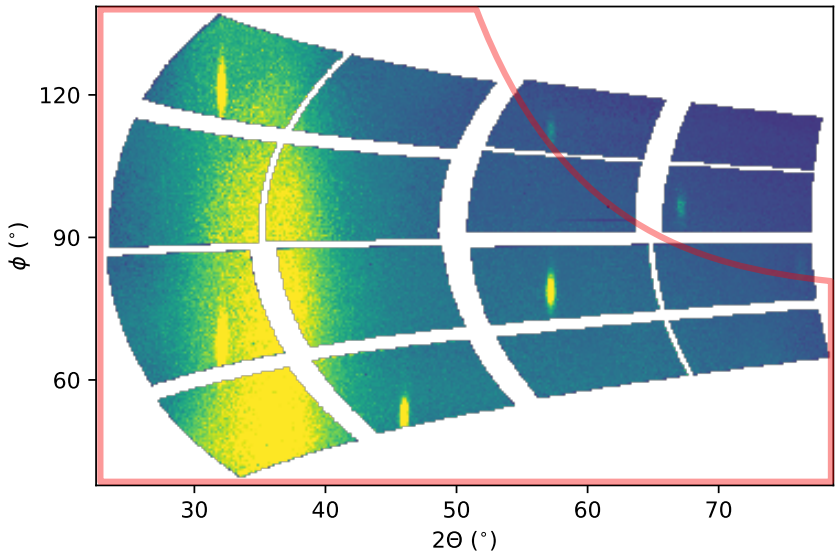


Figure 3.16: XRD image capturing compression of Ta to about 300 GPa. The broad textureless feature between $2\theta = 30°$ and $40°$ is a liquid peak indicating solid-liquid phase transition. The red contour indicates a region characterised by an attenuation factor larger than 0.2 that has been selected for the structure analysis.

where r is the distance between atoms.

Prior to an analysis of the data, images needed to be processed in order to remove any contributions to the signal other than diffraction from the melted part of the target. As can be noticed in Figure 3.16, the image is a superposition of the liquid and solid diffraction. They can be easily distinguished since solid-liquid phase transition introduces isotropicity in a material, which results in a loss of texture and the creation of Debye-Scherrer rings spanning the entire azimuthal space. The influence of the textured peaks was removed by applying an image mask at the location. The mask was generated based on a preshot signal which, upon exceeding a certain level, removed pixels from the grid (Figure 3.17). This mask was constructed separately for every image since the position of the peaks can vary slightly depending on the grain orientation in a specific target.

Before every driven shot 10 X-ray only shots were collected. The mean intensity image of these X-ray only shots was used to remove any background signal from CSPADs. An example of the liquid XRD integrated intensity lineout before and

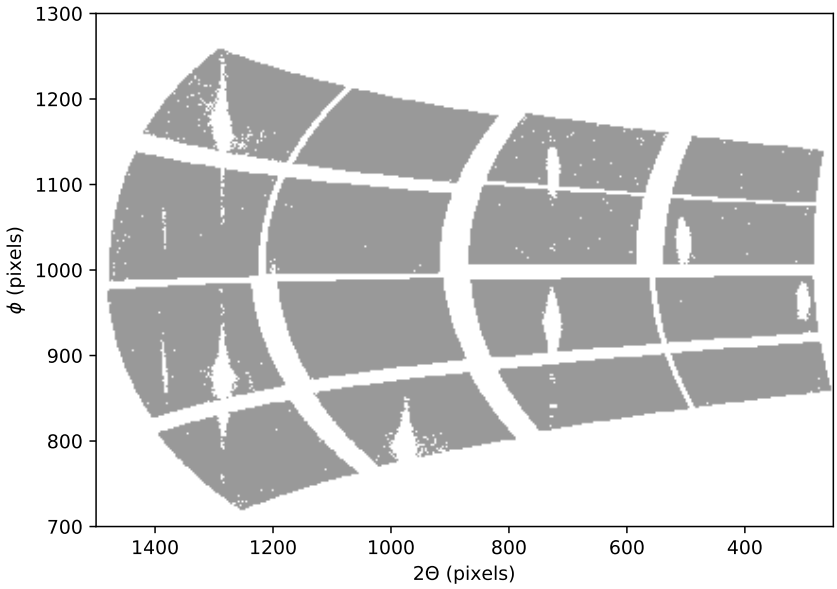


Figure 3.17: Sample mask applied to a driven diffraction image prior to analysis. The XRD signal appearing in the grey region remains unaffected while the signal within the white region is removed.

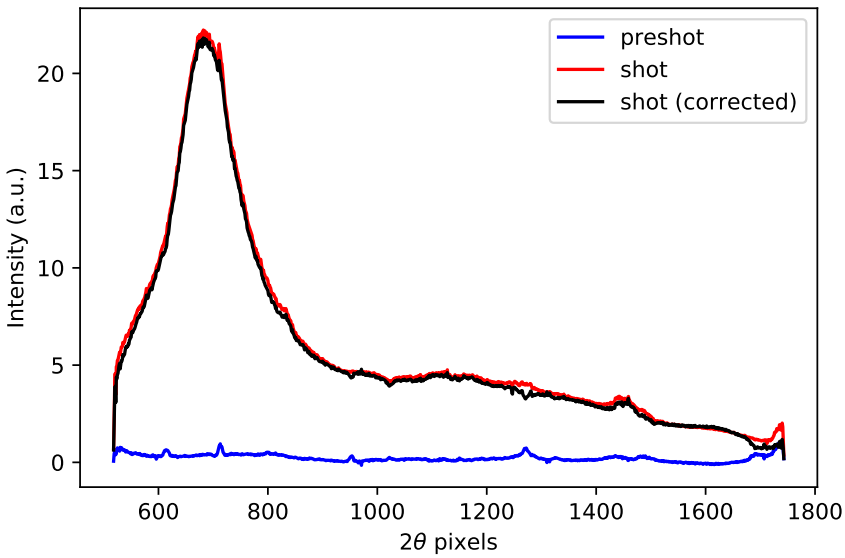


Figure 3.18: Integrated intensity of the liquid XRD image (red), the mean background signal (blue), and the driven intensity lineout after background noise removal (black).

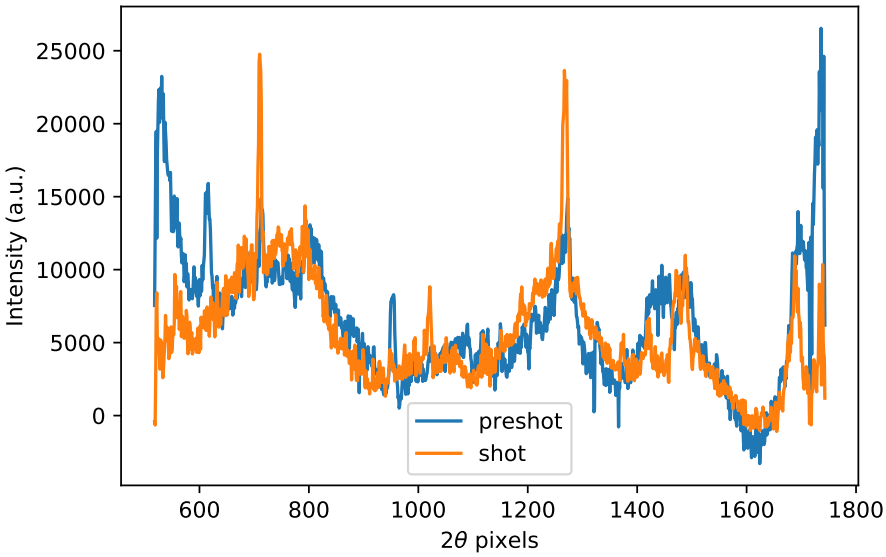


Figure 3.19: Comparison of the azimuthally-integrated averaged preshots and driven shot in the case when X-ray probing time was set to trigger before shock wave arrival in the target. The similar scale of fluctuations in both profiles indicates that the influence of the driving laser on the XRD signal is minimal.

after background noise removal is shown in Figure 3.18. Images with a probe fired before the shock wave reached the target were used to estimate the influence of the driving pulse on the pixel readout as well as the influence of the X-ray emission from the coronal plasma. Figure 3.19 compares integrated intensity lineouts from the averaged preshot signal and the driven diffraction shot with the x-ray probing time before the arrival of the shock wave in the target. The exposures generated by the 527 nm light turned out to be negligible.

A significant factor affecting the signal level is the self-attenuation of the x-rays traveling at various angles with respect to the sample's normal and therefore traveling through various amounts of tantalum layer. A clear display of this phenomenon is the gradual variation of signal level as in the azimuthal direction shown in Figure 3.16, where the diffraction towards higher ϕ angles is significantly reduced. Figure 3.20 can be used to analyse the amount x-ray self-attenuation as a function of a (2θ, ϕ) position on a detector. If ζ is the angle between sample's normal and wavevector

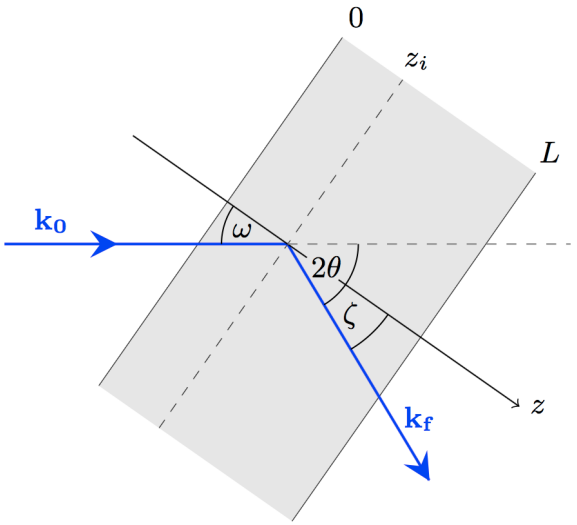


Figure 3.20: Diagram showing diffraction of an x-ray with the wavevector $\mathbf{k_0}$ at the distance z_i into the sample of total thickness L. In the 2D case shown above, diffracted light ($\mathbf{k_f}$) travels in the plane containing incident wavevector $\mathbf{k_0}$ and sample's normal $\hat{\mathbf{z}}$ (i.e. $\phi = 0$). Variation in the azimuthal position around the Debye-Scherrer ring results in the change of angle ζ, which in turn affects the length of material that the x-rays traverse after diffraction, and hence the overall attenuation.

of the scattered beam $\hat{\mathbf{k}}_\mathbf{f}$, then the following relation holds:

$$\cos\zeta = \hat{\mathbf{z}} \cdot \hat{\mathbf{k}}_\mathbf{f} = (\sin\omega,\, \cos\omega,\, 0) \cdot \begin{pmatrix} \cos\phi \sin 2\theta \\ \cos 2\theta \\ \sin\phi \sin 2\theta \end{pmatrix} \quad , \tag{3.14}$$

where ω is the angle between sample's normal ($\hat{\mathbf{z}}$ axis) and the wavevector of the incoming x-rays $\hat{\mathbf{k}}_\mathbf{i}$.

Consider a thin layer of tantalum of thickness dz parallel to the target's surface at a distance z from sample's front (the target's surface is illuminated by the probe beam). Simple geometric analysis gives the distance travelled by the x-rays which are diffracted by this lamina:

$$\text{photon travel distance} = \frac{z}{\cos\omega} + \frac{L - z}{\cos\zeta} \quad , \tag{3.15}$$

where L is the total thickness of the sample. Therefore the amount of the diffracted signal from the chosen lamina influenced by the x-ray attenuation can be expressed as:

$$dI \propto \exp\left(-\frac{L}{\lambda_{\text{att}} \cos\zeta} \right) \exp\left(z\left(\frac{1}{\lambda_{\text{att}} \cos\zeta} - \frac{1}{\lambda_{\text{att}} \cos\omega} \right) \right) dz \quad , \tag{3.16}$$

where λ_{att} is the characteristic length scale of x-ray self-attenuation in tantalum with a value of 5.97 µm for photons with energy of 9.6 keV [103].

Integrating equation 3.16 over all laminae within the shocked region between $z \in [0, z_0]$ where z_0 is the position of the shock wavefront, we find that the total amount of the signal diffracted at an angle $(2\theta, \phi)$ is self-attenuated by the following factor:

$$f_{\text{att}} = \frac{\exp\Big(-\frac{L}{\lambda_{\text{att}}\cos\zeta}\Big)}{\frac{1}{\lambda_{\text{att}}\cos\zeta} - \frac{1}{\lambda_{\text{att}}\cos\omega}}\Big[\exp\Big(z_0\Big(\frac{1}{\lambda_{\text{att}}\cos\zeta} - \frac{1}{\lambda_{\text{att}}\cos\omega}\Big)\Big) - 1\Big] \quad . \tag{3.17}$$

Figure 3.21a illustrates a heat map of the normalised values of this factor for the case of $z_0 = L$, i.e. at the moment when the wavefront reaches the free surface of the sample. It can be noticed that the variation in the attenuation factor between the azimuthal angles of 0° and 180° accounts for the gradual signal reduction in the collected data.

Another factor that needs to be considered in order to process the data is the atomic form factor (equation 2.65). Under the assumption that the electron density is spherically symmetrical so that its Fourier Transform only depends on the distance from the origin in the reciprocal space, we can express atomic form factor f_{aff} as a sum of Gaussian functions:

$$f_{\text{aff}} = \sum_i a_i \exp\Big(-b_i\Big(\frac{Q}{4\pi}\Big)^2\Big) + c \quad , \tag{3.18}$$

where for tantalum the coefficient a_i, b_i, and c are [117]:

$$a_1 = 29.2024, \quad a_2 = 15.2293, \quad a_3 = 14.5135, \quad a_4 = 4.76492,$$
$$b_1 = 1.77333, \quad b_2 = 9.37046, \quad b_3 = 0.295977, \quad b_4 = 63.3644,$$
$$c = 9.24354 \quad .$$

The atomic form factor for the Q-range of interest is shown in Figure 3.22. Combining the influence of x-ray attenuation and the atomic form factor, the total correction, shown in Figure 3.21b, is:

$$f_{\text{total}} = f_{\text{att}}|f_{\text{aff}}|^2 \quad . \tag{3.19}$$

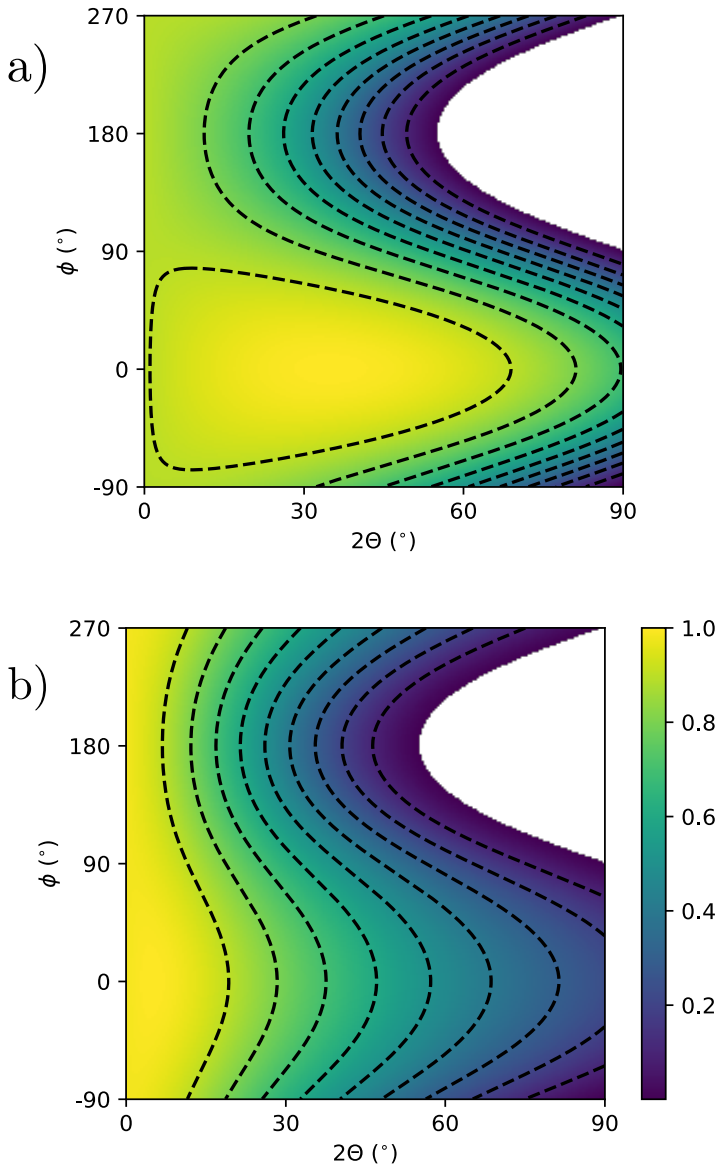


Figure 3.21: Heatmaps of the a) x-ray attenuation factor f_{att} and b) total x-ray intensity correction f_{total} as a function of angles 2θ and ϕ. Both maps are normalised such that the functions take values in range $[0, 1]$. Dashed lines represent contours of constant level, with neighbouring contours differing by a value of 0.1.

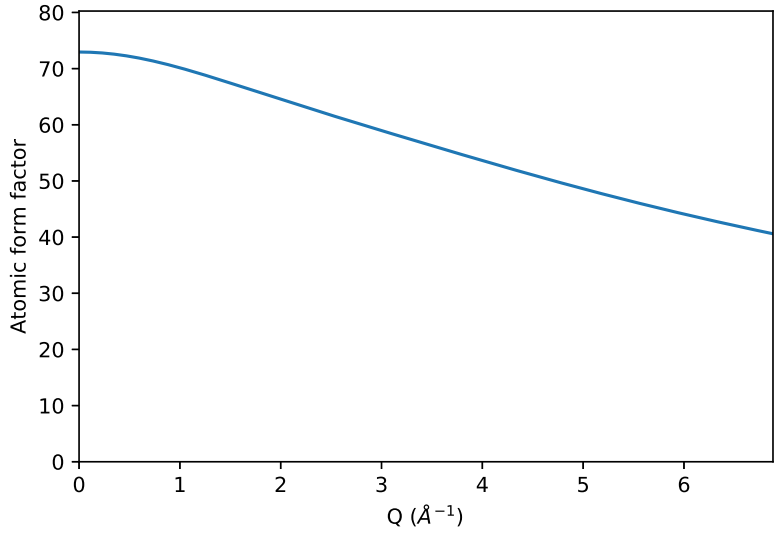


Figure 3.22: The atomic form factor of tantalum as a function of Q.

Dividing the intensity of the diffraction data by this factor should result in constant azimuthal profiles. The unknown position of the shock front z_0 acts as a free parameter which upon inspection can be chosen to generate such uniform profiles. For three available images $z_0 = 6\mu$m is selected. This selection can be independently checked against the X-ray probe time with respect to the shock breakout time as well as the shock traversal time extracted from the HYADES simulations. An example of analysis of shock traversal time in hydrodynamic simulation is shown in Figure 3.6 where a shock wave is launched into a target resembling the one in the experimental setup (50μm of CH and 6μm of Ta). The figure shows the output of the simulation modeling 265GPa shock (this is the highest pressure simulation performed). Pressure profiles at two time are shown - a) at 4.54ns after the launch of the driving laser beam, the shock wave enters the Ta layer (shaded blue region); b) at 5.49ns, the shock wave reaches the free surface of the target. Therefore it takes 0.95ns for the 265GPa shock wave to travel through Ta foil. VISAR data indicates that shock breakout happens 5.1ns after shock launch (this is consistent with HYADES as it is expected that a stronger shock of ∼300GPa travels faster). This breakout time and the X-ray laser delay indicate that XRD images were collected at: -0.1, 0.1, and 1.1ns with respect to the breakout time. The first two delays, which are

relatively small in comparison to expected 0.95ns traversal time, indicate that XRD was performed just before and after shock breakout, respectively. XRD 1.1ns after shock breakout suggests that the majority of the target is at ambient conditions (1.1 $>$ 0.95 ns). Therefore, the selection of $z_0 = 6\mu$m is consistent with the laser timings.

Processed diffraction images were averaged azimuthally to create a profile of intensity as a function of Q. Detector regions with values of f_{total} smaller than 0.2 were excluded from the analysis. Due to a low level of signal, those regions divided by f_{total} factor generated noisy data which affected the averaging routine in an uncontrollable way. The averaging was performed only in 2θ where the azimuthal coverage exceeded 100 pixels so that the influence of the insufficient number of pixels at the detector edges was minimised. The obtained lineouts were initially normalised so that the structure factor value at the maximal value of Q range was equal to 1. Additionally, the values below the minimal value of Q were linearly extrapolated down to a value of 0.

By adapting the Fourier analysis procedure [116], the precise value of the normalisation constant related to the mean density was found, as well as the pair distribution function $g(r)$, as seen in Figure 3.24.

Structure factors extracted from three diffraction images are shown in Figure 3.23. Two of them show profiles corresponding to a sample during compression while the third one represents a sample about 1 ns later, once it returned to ambient conditions. In the case of the released material, two liquid peaks can be clearly identified: the central locations of the first and second peak are marked as Q_1 and Q_2 respectively. The relative position of these peaks indicates the structural complexity of a fluid [92, 118].

In order to extract Q_1 and Q_2, Gaussian functions were fit to the appropriate parts of the XRD lineout as shown in Figure 3.25a). A major source of uncertainty related to the identification of the center of the peak is the selection of the part of the XRD lineout used during fitting. To incorporate the error associated with this selection a bootstrap method was used. For each liquid peak the Q range for fitting was selected by randomly sampling (uniform prior) the locations of its ends.

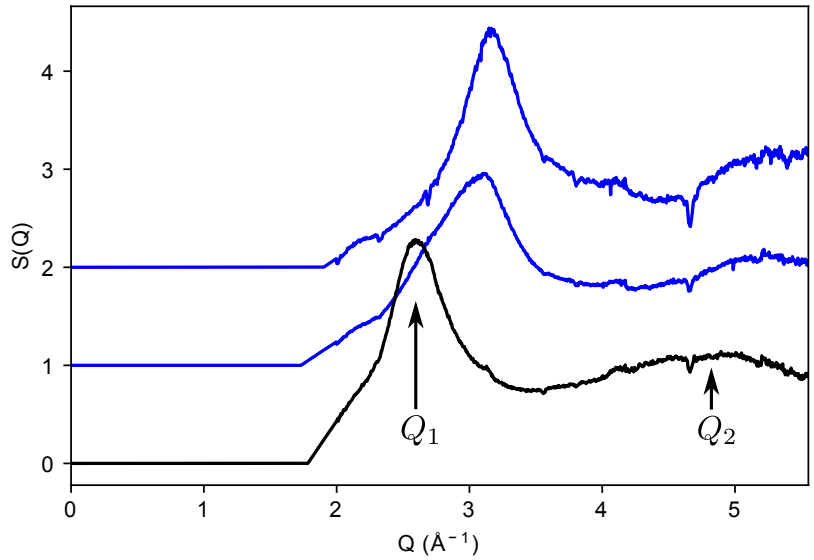


Figure 3.23: Structure factor of liquid tantalum at the elevated pressures of about 3 Mbar (blue) and after the return to ambient conditions (black). Blue profiles are displaced vertically for the clarity of the data visualisation. For the case of released material, locations of the first two liquid maxima are marked with arrows.

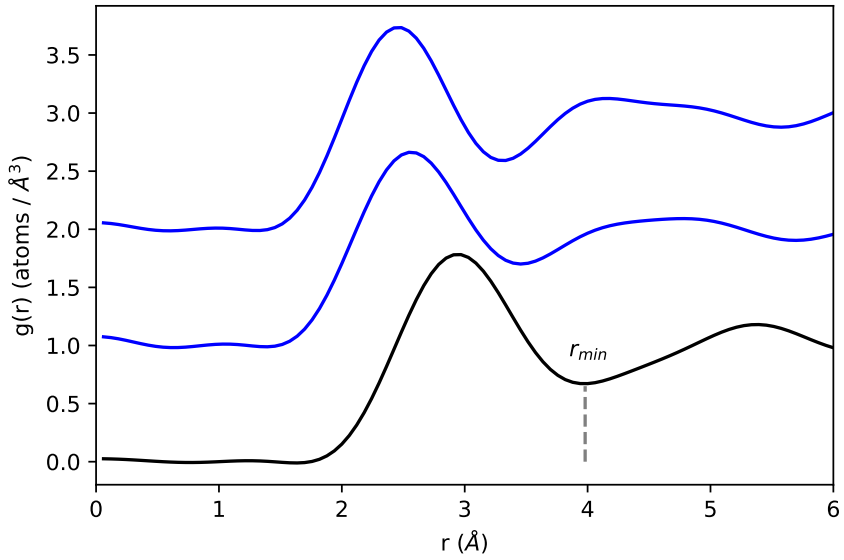


Figure 3.24: Atomic pair distribution as a function of the distance between atoms at elevated pressures (blue) and after release (black). The location of the first minimum at r_{min} is used as the upper limit for the first coordinate number analysis.

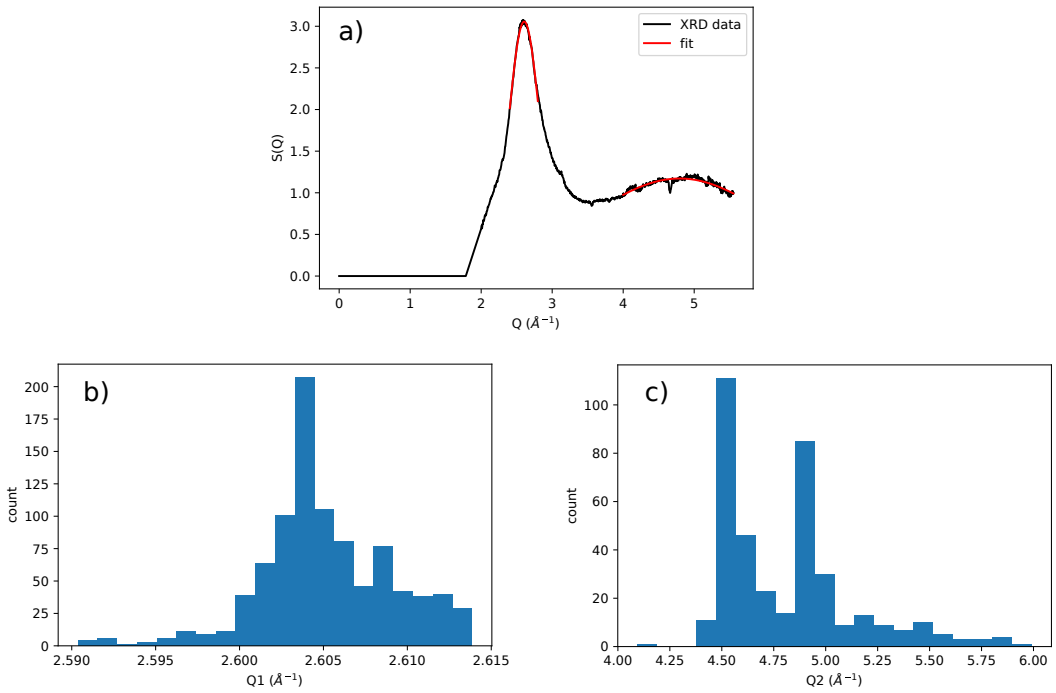


Figure 3.25: a) Structure factor corresponding to the liquid Ta at ambient conditions (black) and Gaussian fits to the central positions of the liquid peaks (red). b) and c) show distribution of the extracted first and second liquid peak positions following the error estimation based on the bootstrap method.

The range of the prior for every range end was manually selected. Figures 3.25 b) and c) show distributions of the extracted central peak locations for Q_1 and Q_2. The final estimation of liquid peak locations are means of these distributions and the uncertainties are their standard deviations.

The released liquid Q_1/Q_2 with a value of 1.84±0.12 corresponds in its range to a metallic simple liquid [119]. The pair distribution analysis suggests a density equal to 16.84±0.20 g/cm^3, a value marginally larger than the typical density of solid tantalum at 16.69 g/cm^3. This discrepancy can be explained by the large uncertainty associated with the convergence of the pair distribution extraction routine [116]. In order to estimate those errors, a large number of atomic pair distribution extractions have been performed with small amounts of artificial Gaussian noise applied to the data. By investigating the atomic density up to the location of the first minimum

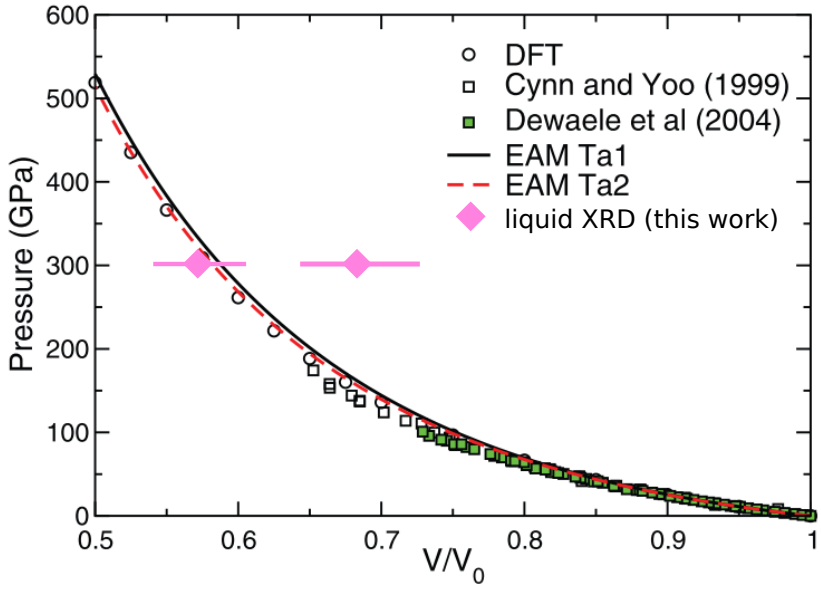


Figure 3.26: Pressure vs. volumetric compression in Ta from DFT [55] (white circles), DAC experimental data [120, 121] (white and green squares), MD [55] (black solid and red dashed lines), and this work (pink diamonds). Figure adapted from Ravelo et al. [55].

at $r_{\min}$, a coordination number can be estimated according to the following formula:

$$\mathrm{CN} = 4\pi\rho_0 \int_0^{r_{\min}} g(r)dr \quad . \tag{3.20}$$

The found value of 14.34±0.31 is consistent with the coordination value of 14 for the bcc material.

A similar type of analysis was performed for the data corresponding to compressed liquid. At high pressure both peaks shifted towards larger Q values, indicating smaller interatomic distances in a direct space. Unfortunately, due to the limited range of Q, the second liquid peak was only partially visible, which introduced large uncertainty to its position and which made the analysis of the liquid structure at the elevated pressure highly unreliable. The ratio Q_1/Q_2 for these high pressure states was reduced to 1.72±0.25 and 1.77±0.20. The obtained densities were 24.4±1.5 and 29.2±1.6 g/cm^3, with corresponding coordination numbers of 13.3±0.8 and 14.3±0.8. Figure 3.26 compares extracted densities of liquid tantalum with previous investigations. A large difference between the two measurements in this work could potentially be explained by the timing of the X-ray probes with respect to shock breakout. The lower density measurement ($V/V_0 = 0.644$)

corresponds to the image taken 0.1ns after shock breakout, which indicates that the release wave could reduce the high pressure state within a part of the target, thereby affecting the interpretation and analysis of the XRD results.

3.4 Data analysis

The analysis of the solid diffraction signal relied on the measurement of the positions (both radial and azimuthal) as well as the relative intensity of the peaks. The shape of diffraction peaks in the radial direction is commonly modelled using Voigt function [122], which is a convolution of Gaussian and Lorentzian functions. Using a combination of an ideal monochromatic source with a perfect crystal lattice, one would expect to observe diffraction peaks with a shape of infinitely narrow Kronecker delta functions. However, quasi-monochromatic LCLS x-rays with a finite bandwidth are a source of instrumental line broadening. Moreover, any form of lattice imperfection causes additional line broadening. For example, lattice defects and dislocations introduce localised strain variations normally distributed, while a single crystal broken into grains, twins or stacking faults is a source of Lorentzian broadening. For the purpose of data analysis, the simplified Pseudo-Voigt approximation has been employed [123]. The Pseudo-Voigt function $f(x)$ is a linear superposition of Gaussian $G(x)$ and Lorentzian $L(x)$ contributions which are weighted by free parameters w and $(w-1)$ taking the following form:

$$f(x) = G(x) \cdot w + L(x) \cdot (1 - w) \quad , \tag{3.21}$$

where $w \in [0, 1]$.

The peak broadening in the azimuthal direction is assumed to be mostly affected by the distribution of grain orientations about the texture direction. Therefore the peak fitting routine in the $(2\theta,\ \phi)$ image projection is based on fitting the following 2D function:

$$f(2\theta, \phi) = C_{\text{amp}} \cdot G_1(\phi)\Big(G_2(2\theta) \cdot w + L(2\theta) \cdot (1 - w)\Big) \quad , \tag{3.22}$$

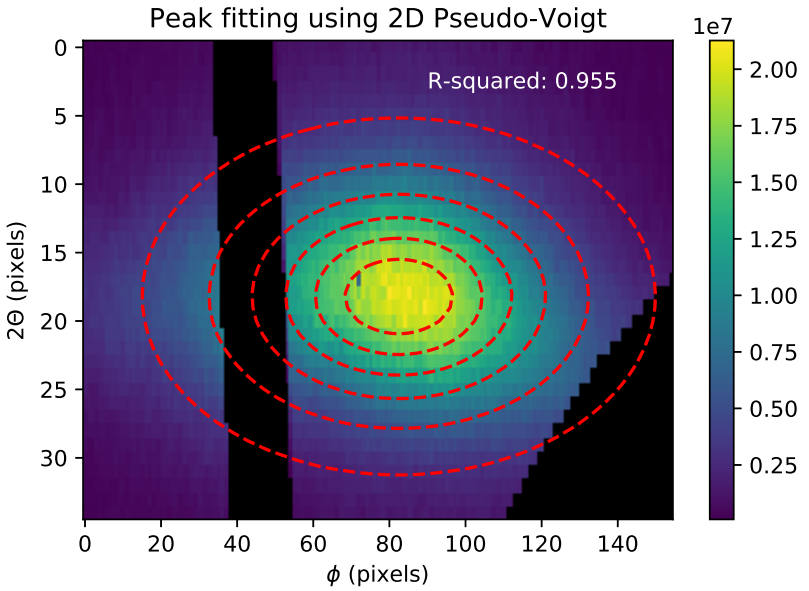


Figure 3.27: An example of 2D Pseudo-Voigt peak fitting. The contours of the fitted function are represented by the red dashed ovals. Black regions correspond to the positions of the gaps between the detectors not included in the analysis.

where subscripts 1 and 2 were used to distinguish Gaussian function acting in the azimuthal and radial directions. Each of the functions G_1, G_2, and L takes 2 free parameters: the central position of the function and the parameter controlling its width. The final parameter C_{amp} controls the total amplitude of the function.

The 2D shape given by formula 3.22 was fitted to a single peak in the diffraction data using the least squares method. The initial set of parameters used for regression was estimated using first (central location) and second (width) moments. The initial amplitude of the profile was evaluated by calculating the mean amplitude of the signal within the region around the central location bounded by the second moment.

The uncertainties of the locations of the peaks were estimated in two ways. Firstly, they were assessed via the uncertainty associated with the set of fitted parameters which, in case of peak location, was of the order of a few pixels for majority of the data. Certain peaks inconveniently appeared on the edges of the surface covered by the detectors. In several cases, a significant portion of the diffraction signal fell directly into a gap between the detectors, which limited the ability to extract information about the parameters of the shape of the peak. In

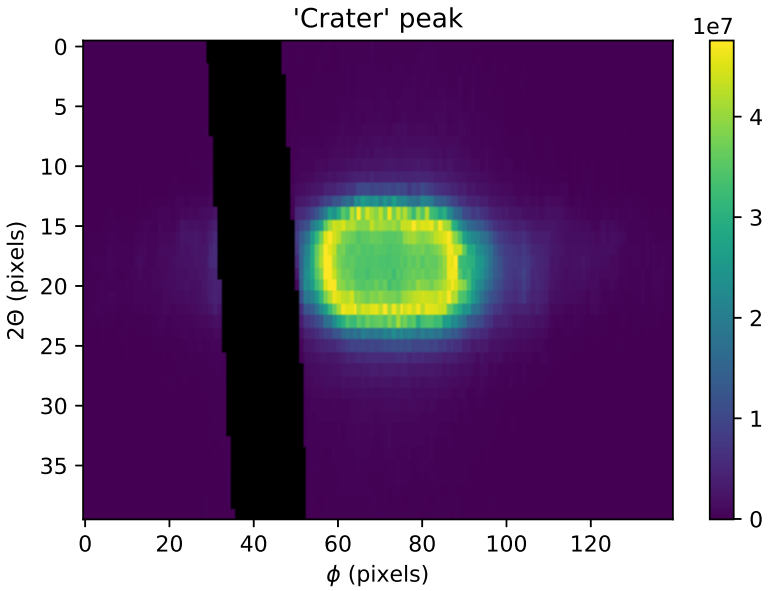


Figure 3.28: A diffraction peak with an altered 'crater' profile due to too high detector gain.

such cases, despite a relatively good fit to the profile given by the formula 3.22, and a relatively low parameter uncertainty, the fit was occasionally unreliable due to the lack of a significant amount of signal. This unreliability can be demonstrated by the high sensitivity of the parameters of the fit to their initial values fed into the least squares minimisation routine as well as any form of noise applied to the original data. The second method of estimating uncertainties relied on multiple fits in the Monte Carlo manner with randomly varying initial values of the profile's free parameters as well as with various applications of random noise to the data. Profile fits to the data well within the detector range consistently provided errors on the peak location of the order of a few pixels, while fits to the peaks partially beyond the edges suggested uncertainties orders of magnitude larger. The latter were eliminated from the quantitative analysis.

During the data analysis process, it was found that the sensitivity of the CSPADs had a limited working range. Beyond a certain signal threshold the detector readout was corrupted. This means that for undesirably high CSPADs' gain levels, diffraction spots tended to appear as craters, as shown in Figure 3.28. These spots were not used for the analysis involving the intensity of diffraction.

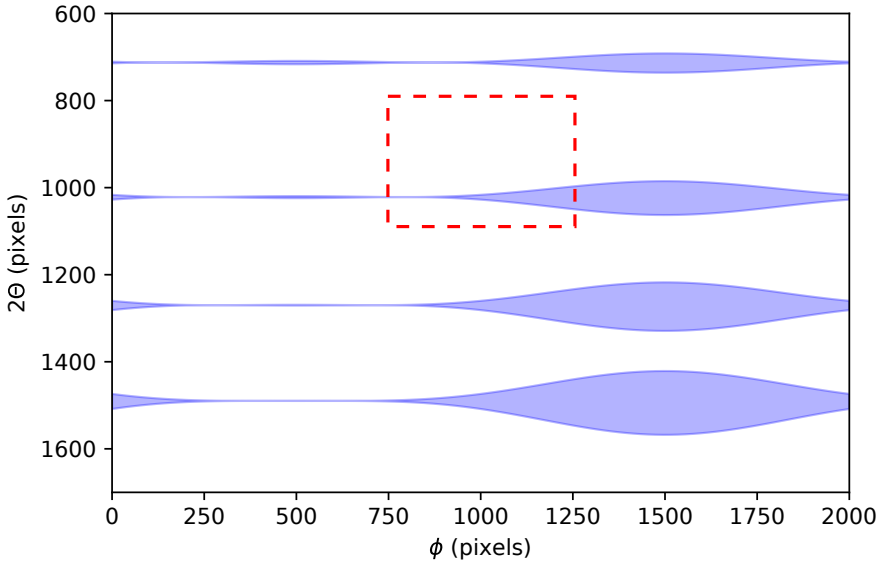


Figure 3.29: Theoretical predictions of the Debye-Scherrer patterns under the influence of constant transverse and longitudinal strains ranging from -5% to +5%. The wide purple areas denote regions with the greatest sensitivity to these kinds of variations in shear stress. The positions of the detectors are illustrated with grey regions. The red dashed line corresponds to the region shown in Figure 3.30.

3.5 Residual elastic shear stress

The Debye-Scherrer rings were analysed for deviations from circularity that would indicate shear stress in the shocked state. When using the Hugoniot jump conditions to calculate the pressure from the measured d-spacing, or when calculating the equivalent plastic strain (in the following part of this chapter), we assumed that the residual elastic shear stress was near zero. Residual elastic shear strain would inidicate that the strain is anisotropic, with higher elastic strain in the compression direction (shock-prorogation direction) and lower elastic strain in the transverse direction. This anisotropic elastic strain would manifest as a Debye ring distorted by varying d-spacing, making it appear elliptical [124].

In order to understand the distortion of the Debye-Scherrer ring, the orientation of the reciprocal lattice vectors was analysed. The reciprocal lattice vector is given by the difference of the incoming and scattered wavevectors. Aligning the coordinate

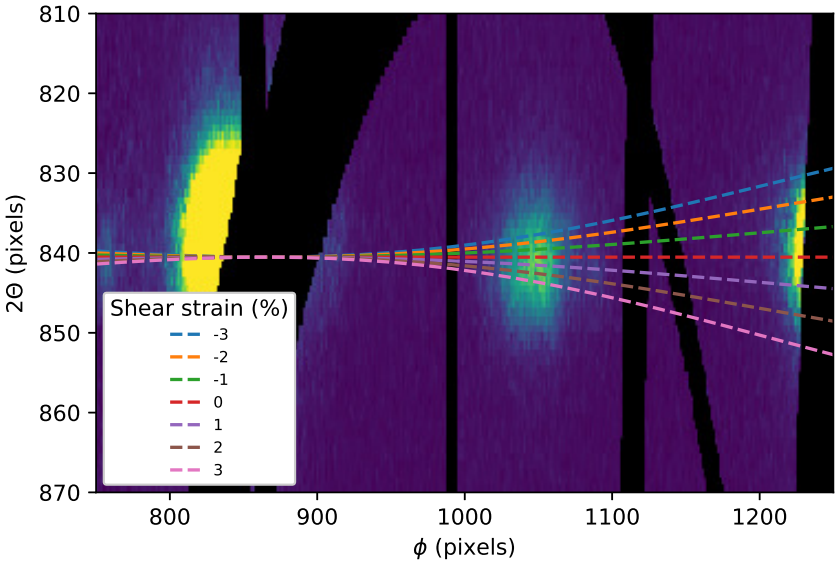


Figure 3.30: {110} driven diffraction signal within part of the detectors indicated in Figure 3.29 with a red dashed line. Dashed lines represent the theoretical positions of the diffraction pattern with various amounts of the residual shear strain.

system such that the initial wavevector is parallel to the z-axis we have:

$$\mathbf{G} = \mathbf{k_f} - \mathbf{k_i} = \frac{2\pi}{\lambda} \begin{pmatrix} \cos\phi \sin 2\theta \\ \sin\phi \sin 2\theta \\ \cos 2\theta - 1 \end{pmatrix} \quad . \tag{3.23}$$

The χ angle can be found by taking the dot product of the normalised reciprocal lattice vector $\hat{\mathbf{G}}$ and the shock direction $\hat{\mathbf{n}}$ (sample's normal):

$$\cos\chi = \hat{\mathbf{n}} \cdot \hat{\mathbf{G}} = \frac{1}{|\mathbf{G}|}(\sin\omega, 0, \cos\omega) \cdot \begin{pmatrix} \cos\phi \sin 2\theta \\ \sin\phi \sin 2\theta \\ \cos 2\theta - 1 \end{pmatrix} \quad . \tag{3.24}$$

Reciprocal lattice vectors can be decomposed into longitudinal and transverse components to the shock direction. For simplicity, only reciprocal lattice vectors in xz-plane are considered. The direction of $\mathbf{G}$ vector can be expressed in terms of χ angle in the following way:

$$\hat{\mathbf{G}} = \begin{pmatrix} \sin\chi \\ 0 \\ \cos\chi \end{pmatrix} \quad . \tag{3.25}$$

Once the deformation inducing longitudinal ϵ_L and transverse ϵ_T strains is applied, the reciprocal lattice vector rotates to a new position $\hat{\mathbf{G}}'$ forming an angle χ' with

the direction of shock propagation:

$$\hat{\mathbf{G}}' = \begin{pmatrix} \sin\chi' \\ 0 \\ \cos\chi' \end{pmatrix} = \frac{1}{1-\epsilon'} \begin{pmatrix} 1-\epsilon_T & 0 & 0 \\ 0 & 1-\epsilon_T & 0 \\ 0 & 0 & 1-\epsilon_L \end{pmatrix} \cdot \begin{pmatrix} \sin\chi \\ 0 \\ \cos\chi \end{pmatrix} \quad , \qquad (3.26)$$

where $(1-\epsilon')$ is the normalisation factor equal to the length of the deformed vector. This factor can be used to define the shape of the diffraction rings since it describes the deformation along the direction of the reciprocal lattice vector.

With no shear strain, the Debye-Scherrer ring has constant 2θ. As shear strain increases, the driven rings move to higher 2θ for low χ and to lower 2θ for high χ. An example demonstrating the distortion of the diffraction pattern in the experimental geometry is illustrated in Figure 3.29. Theoretical Debye-Scherrer rings, corresponding to a diffraction from a Ta sample with 0% longitudinal strain and exaggerated transverse strain ranging from -5% to +5%, are presented in the form of blue curves. It can be noticed that the most convenient way of demonstrating the existence of shear strain within a material is via wide azimuthal coverage. Even though the experimental geometry is lacking information from the ϕ=180° (1500 pixels) region (the location most sensitive to the longitudinal deformation of the unit cells), deviations within ϕ=45-135° (750-1250 pixels) provide a sufficient amount of data to estimate the residual elastic strain in a shocked sample. Figure 3.30 illustrates examples of the deviation in the circularity of the {110} driven line. Although 0% strain produces a good fit to the data, small shear strains may also match. We found that at 2-3% shear strain, the data no longer provided a good match. Therefore the assumption that the elastic shear strain is negligible is probably valid.

3.6 Driven textural changes

Solid diffraction data was collected for pressures from 15 GPa to 270 GPa. A lack of crystallographic phase transition at the elevated pressures indicated that the built-up shear stress needed to be resolved via another plastic deformation mechanism (i.e. slip or twinning).

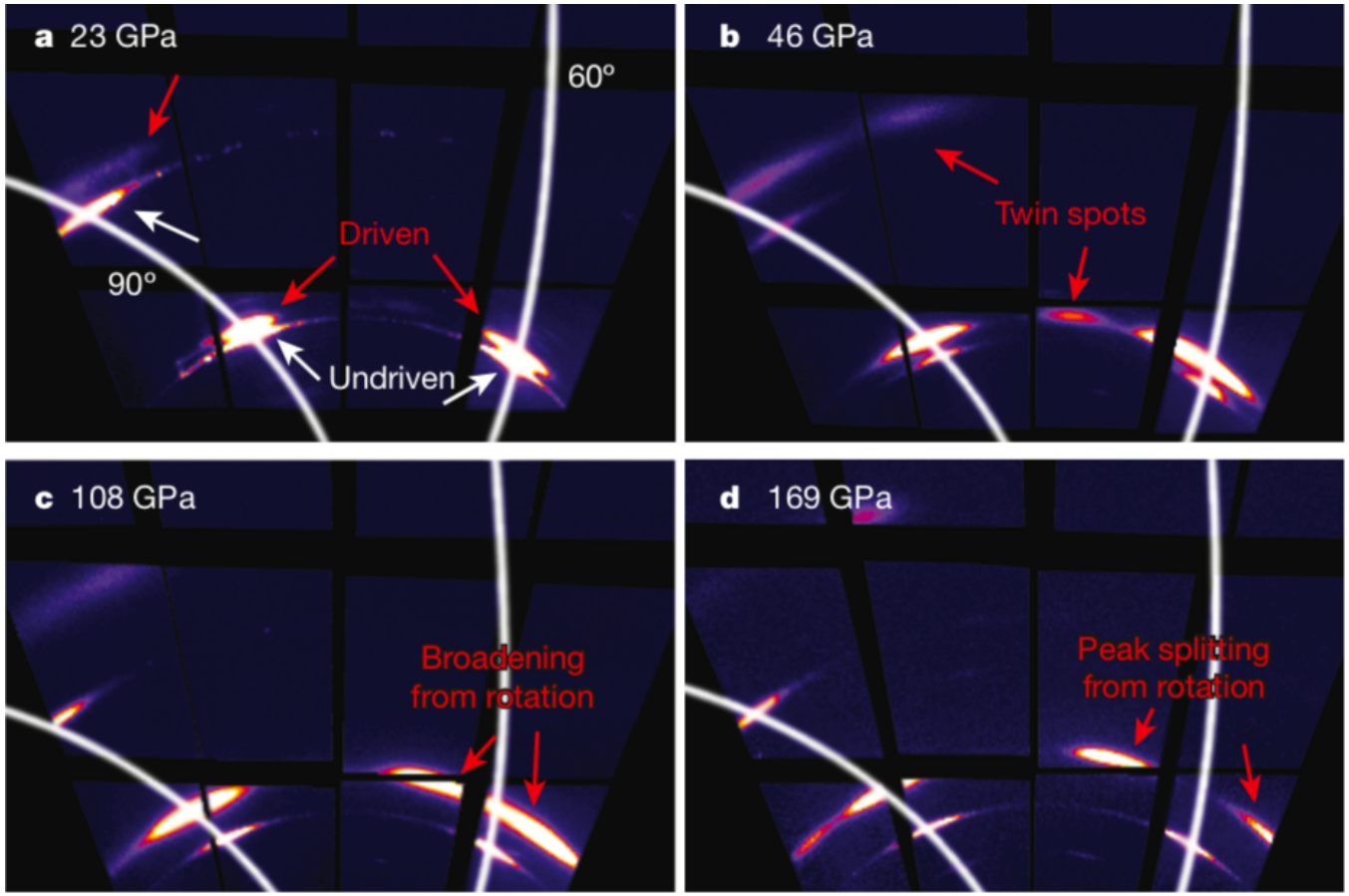


Figure 3.31: Diffraction patterns from tantalum from different shock – compression experiments. The spots corresponding to the driven portion of the sample (highlighted by red arrows) appear at higher diffraction angles than those corresponding to the undriven portion (highlighted by white arrows), appearing as a shift upwards in this view. Lines of constant χ are shown at 60° and 90° to illustrate the reorientation of the texture spots in driven tantalum. **a),** At 23 GPa, no reorientation is observed, because the diffraction spots for the driven and undriven sample have the same azimuthal location. **b),** At 46 GPa, new texture spots arise that correspond to twinning across a {112} mirror plane and an additional 2.5° rotation. **c), d),** At higher pressures (108 GPa, c; 169 GPa, d), large lattice rotations are observed, causing the $\chi = 60°$ (110) spot (highlighted by red arrows) to broaden and then split.

Texture changes were evident in the data for the driven material for a wide range of shock pressures, as shown in the example diffraction patterns in Figure 3.31. Comparing χ for the spots that correspond to the compressed and uncompressed material revealed the texture change during shock compression. As shown in Figure 3.31a (23 GPa), the distance between lattice planes decreased in the driven portion of the sample and the diffraction lines moved to higher 2θ angles, but no change in χ was observed. At 46 GPa (Figure 3.31b), new spots formed on the compressed Debye ring (marked with red arrows) that corresponded to the appearance of grains with new orientations within the driven part of the sample. Specifically a set of spots with $\chi = 70.5°$ for {110}, $\chi = 76.3°$ for {200}, and $\chi = 61.3°$ for {211} was observed. They corresponded to an orientation for twinning across a {112} mirror plane (the dominant twin plane in bcc tantalum). In the data for higher pressures (Figure 3.31c, d), the $\chi = 60°$ spot was elongated azimuthally; the texture spot spanned the detector gap (Figure 3.31c) and even split into two spots (Figure 3.31d). These changes in χ correspond to lattice rotation, whereby the rotation moves some planes to higher χ and other planes to lower χ. In contrast, no shift in χ was observed for the $\chi = 90°$ spot. This indicates that the lattice rotates about the $[1\bar{1}0]$, since reciprocal lattice vectors at $\chi = 90°$ remained parallel to the axis of rotation while the ones initially at $\chi = 60°$ moved towards larger or smaller χ values depending on the direction of rotation.

The induced twin fraction can be measured by comparing the ratios of the intensities of various peaks. In this experiment, the twin fraction was calculated by comparing the intensity of texture spots corresponding to the twin orientation with the intensity of other driven and undriven texture spots. In addition, the differing multiplicities of various planes associated with specific χ must be considered. For example, a unit cell in the twin orientation will have twice as many planes for $\chi = 90°$ than for $\chi = 70.5°$ (Figure 3.33), so the twin fraction is:

$$f_{\mathrm{tw}} = \frac{2I_{\mathrm{drvn}(110)\chi=70.5°}}{I_{\mathrm{drvn}(110)\chi=90°}} \quad , \tag{3.27}$$

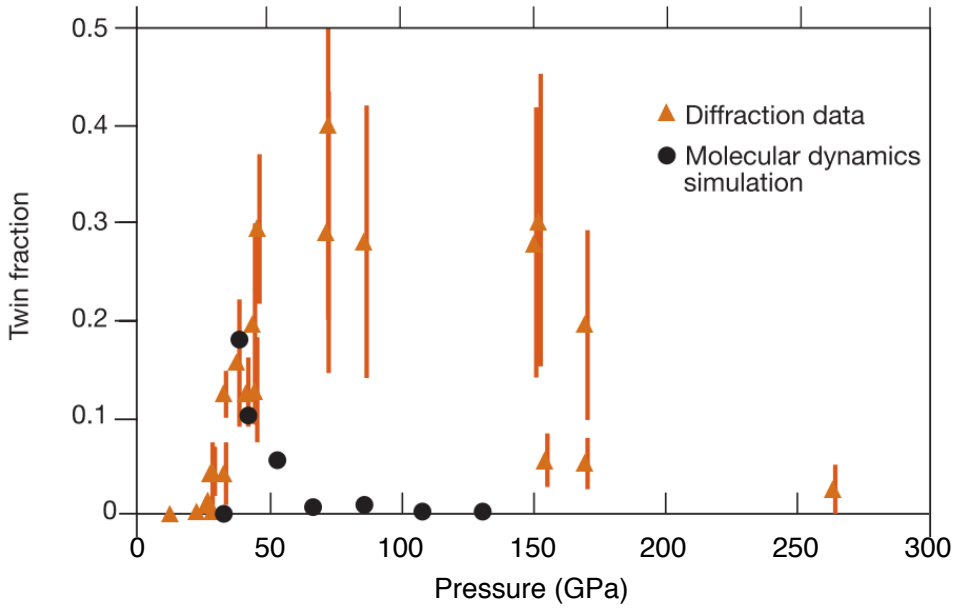


Figure 3.32: Twin fraction as a function of shock pressure, measured from diffraction data by the ratio of texture spots (orange triangles) and from molecular dynamics simulations (black circles).

where I_{drvn} refers to the integrated intensity of the specified diffraction spot. This equation assumes azimuthal symmetry, because the two spots being compared have different azimuthal positions. The azimuthal variation of the (110) fibre texture was not known before the experiments, so the variation was one of the sources of uncertainty in our measurements. Pole figure measurements were performed on the remaining samples. As can be seen in Figure 3.5, the pole plots are lacking perfect rotational symmetry. The analysis of the azimuthal lineouts indicated a variation in intensity of the order of ±30%.

For each image, similar twin fraction calculations were performed for the (200) χ = 76.3° and (211) χ = 61.3° twin spots, each of them given a separate twin fraction measurement:

$$f_{\mathrm{tw}} = \frac{I_{\mathrm{drvn}(200)\chi=76.3^\circ}}{I_{\mathrm{drvn}(200)\chi=90^\circ}} \quad , \tag{3.28}$$

$$f_{\mathrm{tw}} = \frac{I_{\mathrm{drvn}(211)\chi=61.3^\circ}}{I_{\mathrm{drvn}(211)\chi=54.7^\circ}} \quad . \tag{3.29}$$

The final twin fraction value is the mean of these measurements and the error bars were set to the standard deviation of the measurements. For shock pressures in

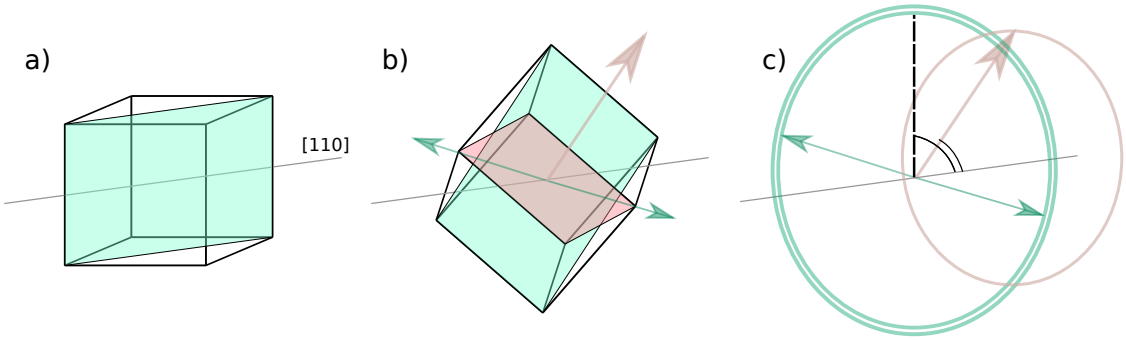


Figure 3.33: Explanation of the plane multiplicity for twin fraction calculation in equation 3.27. a) shows unit cell orientation with respect to the [110] compression axis in an non-deformed crystal. b) illustrates unit cell orientation in a twinned part of the crystal. In this case two (110) planes with normals non parallel to the compression axis can be distinguished (red and green planes). Due to the azimuthal symmetry of grain orientation in the fibre-textured material (110) plane orientation in a sample can be described by rings on a Polanyi sphere as shown in c). χ=90° (green plane) forms two rings while χ=70.5° (red plane) forms one ring.

the 50-150 GPa range, some of the driven twin spots fell into gaps between the detectors, limiting measurements in this pressure regime. The error was assumed to be 50% when twin spots were measured on only one diffraction line, reflecting the uncertainty in the azimuthal texture in both the twin spot and the reference spot.

The amount of change in texture due to twinning is plotted in Figure 3.32. The twin fraction is minimal (consistent with zero) below 25 GPa, and increases with shock pressure in the 25-75 GPa regime, reaching a twin fraction of about 30-40% at 75 GPa. Surprisingly, even though twinning is often associated with strongly driven metals, at higher shock pressures of more than 150-175 GPa the twin fraction falls to less than 10%.

Lattice rotations are directly related to both slip and twinning. The concept of lattice rotations induced by plastic deformation can be explained with the aid of the cartoon in Figure 3.34. A compressive stress σ acting on a material along the vertical axis results in a slip. Gliding planes produce an overall relative displacement of the two opposite ends of the crystal with respect to the compression axis. A simple geometrical argument suggests that plastically-deforming material needs to stay laterally confined. In the experimental setup presented in this work a small portion of the driven material was surrounded by the undriven block of tantalum.

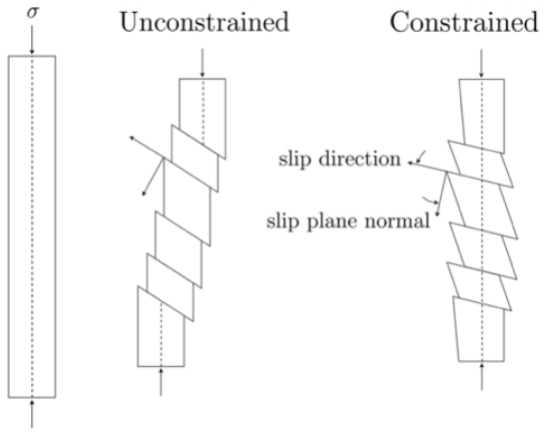


Figure 3.34: Illustration of lattice rotations induced by a vertical compressive stress σ. In the case of an 'unconstrained' deformation, slip results in a transverse displacement of the opposite ends of the material. Lateral confinement ('constrained' case) forces fragments of the crystal to rotate such that the angle between the compression axis and the slip plane normal is reduced.

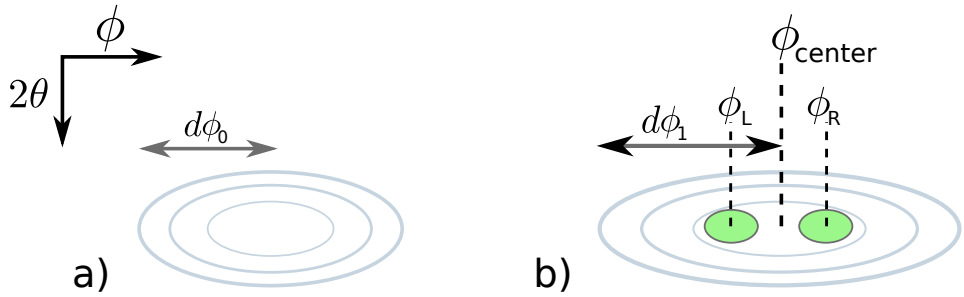


Figure 3.35: Illustration of the azimuthal peak broadening analysis. a) describes the shape of the undriven (110) $\chi = 60°$ peak, while b) describes the shape of the (110) $\chi = 60°$ driven peak, which is formed by two separate peaks.

This meant that there was no space for grains to perform motion transverse to the shock direction as neighbouring grains started pushing against one another. In order to keep this lateral confinement, plastically-deformed grains rotated as shown in Figure 3.34 ('Constrained' case). Experimental XRD images do not capture the evolution of the position of the rotated diffraction peaks which means that this deformation is taking place at timescales shorter than 100ps.

The lattice rotation can be analysed by fitting the azimuthal position of the peaks and finding the new orientation of the reciprocal lattice vectors using equation 3.23. After normalisation of the initial and compressed reciprocal lattice vectors corresponding to the same reflections, the relative orientation of those vectors

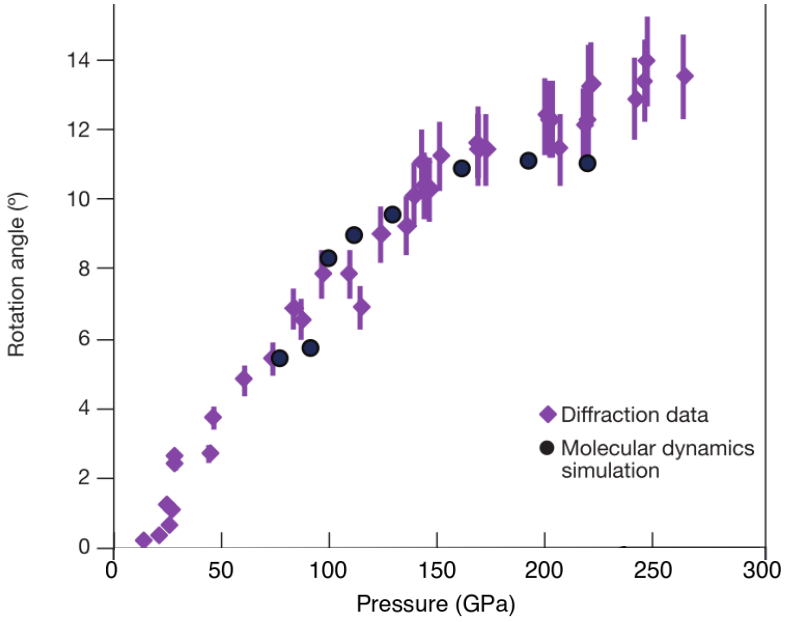


Figure 3.36: Lattice rotation angle as a function of shock pressure, measured from x-ray diffraction data (purple diamonds) and from molecular dynamics simulations (black circles).

was investigated. The lattice rotation was found by fitting the rotation matrix $\mathbf{R}_{\text{rot}}$ across multiple peaks:

$$\hat{\mathbf{G}}_{\text{undriven}} \cdot \mathbf{R}_{\text{rot}} = \hat{\mathbf{G}}_{\text{driven}} \quad , \tag{3.30}$$

where $\hat{\mathbf{G}}_{\text{undriven}}$ and $\hat{\mathbf{G}}_{\text{driven}}$ are the normalised reciprocal lattice vectors of the original (undriven) and rotated (driven) lattice.

For small rotations, as in the case of relatively low pressure states, there was a significant overlap between driven (110) $\chi = 60°$ peaks due to small grain rotations. A double Pseudo-Voigt fit was performed in those cases and the central locations of these peaks were subsequently used for reciprocal vector orientation calculation. In certain cases, driven $\chi = 60°$ peaks were indistinguishable leading to non-converging double Pseudo-Voigt fit. In those situations the broadening of the (110) $\chi = 60°$ peak was analysed. The central ϕ positions of both peaks were estimated to be at:

$$\phi_{L,R} = \phi_{center} \pm (d\phi_1 - d\phi_0), \tag{3.31}$$

where ϕ_{center} corresponds to the central location of the fitted peak, and $d\phi_0$ and

$d\phi_1$ correspond to the widths of the undriven and driven peaks, respectively, as shown in Figure 3.35.

The observed rotations were consistent with the crystal slipping on {112}<111> – the slip system with the largest Schmid factor for a bcc material. Figure 3.36 presents the extracted lattice rotations as a function of a shock's strength. Uncertainties are estimated by calculating the standard deviation of rotation angles extracted from multiple reflections. A clear, positively correlated, monotonic relationship between the induced rotations and the pressure was observed.

Lattice rotations are also induced by twinning which can be considered as a form of multiple slips between a number of consecutive planes. Figure 3.37 illustrates twin-induced lattice rotation in the case of twinning across {112} planes as observed in the experiment. By assigning the width of the grain to unity ($|AC| = 1$), we can conveniently express the twin fraction f_{tw} (the area of the shaded region) as the length of the segment $|BC|$. Following this logic we have:

$$|BC| = f_{\text{tw}}, \quad |AB| = 1 - f_{\text{tw}}, \quad |AD| = \sqrt{2}|AB| \quad . \tag{3.32}$$

By displacing the {112} planes, as described in the previous chapter, the twin is formed with $|JF| = \sqrt{2}|BC|$. Simple geometric analysis gives $\angle EJF$, i.e. the angle between [114] and [110], equal to 70.5°. Therefore:

$$|EJ| = \sqrt{2} f_{\text{tw}} \sin(70.5^\circ) \quad \text{and} \quad |EF| = \sqrt{2} f_{\text{tw}} \cos(70.5^\circ) \quad . \tag{3.33}$$

This leads to the formula for the angle of rotation of the lattice $\angle KLM$ as shown in Figure 3.37c:

$$\angle KLM = \tan^{-1}\left(\frac{|EJ|}{|AB| + |EF|}\right) = \tan^{-1}\left(\frac{\sqrt{2} f_{\text{tw}} \sin(70.5^\circ)}{1 - f_{\text{tw}} + \sqrt{2} f_{\text{tw}} \cos(70.5^\circ)}\right) \quad . \tag{3.34}$$

Since both slip and twinning cause lattice rotations, one might wonder if these rotations are correlated. That is to say, if the rotations were uncorrelated it would be possible to achieve rotational contributions in the same as well as the opposite direction. This kind of situation would lead to the appearance of a new diffraction signal across all Debye-Scherrer rings; however, this has not been observed. It is

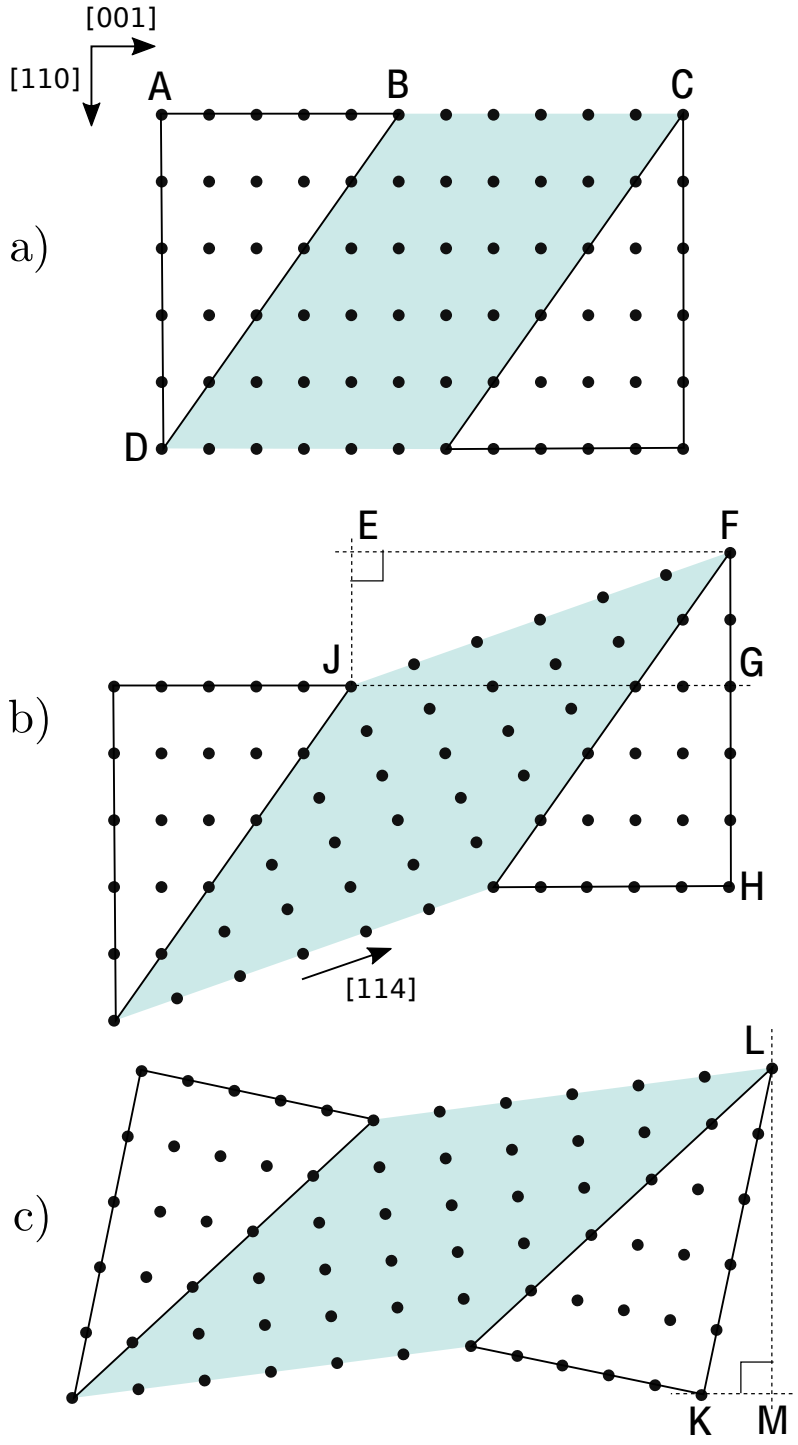


Figure 3.37: Illustration depicting the lattice rotations induced by twinning. In a), the blue region represents the part of the crystal that experiences twinning prior plastic deformation. b) and c) show twinning across {112} in unconstrained and constrained cases, respectively. In c) twinning leads to a rotation of the crystal lattice by angle $\angle KLM$.

also worth noticing that if both slip and twinning are present, they induce rotations in the same direction. If this statement was not true, it would not be possible to observe a smooth monotonic increase in the angle of measured rotation while the contribution of twinning to the overall deformation changes. This can be explained by the analysis of the Schmid factor for (112) type planes, which is the same for slip and twinning. As the angle of rotation increases, the Schmid factor favours a continuation of rotation in the same direction.

3.7 Equivalent plastic shear strain

The role of twinning and slip in the overall plastic response can be qualitatively determined by comparing the plastic strain from twinning with the total plastic strain imparted by the shock. Here I discuss the relationship between the plastic strain γ_p and the rotation that is measured. Throughout this analysis I assume that the residual shear stress in the shocked tantalum is zero or so small that it can be neglected. As shown in section 3.5, in the experimental setup the azimuthal coverage of the CSPADs restricted the analysis of the ring-distortion; however, it was still possible to estimate that the shear strain in the driven sample is minimal and does not exceed 1%. Therefore this justifies the assumption that the elastic strain in the shocked state is strictly hydrostatic, implying full plastic relaxation of the shear stress on the ultrashort timescale of the experiment [52]:

$$F_x^e F_y^e F_z^e = \frac{V}{V_0} \quad , \tag{3.35}$$

$$F_x^e = F_y^e = F_z^e = \left(\frac{V}{V_0}\right)^{\frac{1}{3}} \quad , \tag{3.36}$$

where F_z^e is the elastic deformation gradient along the shock direction, F_x^e and F_y^e are the transverse elastic deformation gradients, and V_0 and V are the volumes of a grain at ambient and high pressure conditions, respectively. Similarly, plastic strains are assumed not to change the volume:

$$F_x^p F_y^p F_z^p = 1 \quad , \tag{3.37}$$

where F_z^p is the plastic deformation gradient along the shock direction, and F_x^p and F_y^p are the transverse plastic deformation gradients. That uniaxial compression of crystals produces a rotation of the lattice is well known, and the rotation as a function of compression is [51]:

$$F_z^p = \frac{\cos\chi_0}{\cos\chi} \quad , \tag{3.38}$$

where χ_0 and χ give the initial and final angles between the slip-plane normal and the compression direction, respectively. Because the material is laterally constrained and compressed along the high-symmetry [110] direction, we assume that although individual grains may expand or contract in different transverse directions, the area of each grain transverse to the sample normal will remain the same:

$$F_x^e F_x^p F_y^e F_y^p = 1 \quad . \tag{3.39}$$

Combining equations 3.39 and 3.37 we find:

$$F_z^p = (F_x^e)^2 = \left(\frac{V}{V_0}\right)^{\frac{2}{3}} \quad . \tag{3.40}$$

Finally, by selecting an appropriate coordinate system, we can assume that $F_y^p = 1$. Then, from equation 3.37 we find:

$$F_x^p = (F_z^p)^{-1} \quad . \tag{3.41}$$

Plastic shear γ is defined as the difference between the longitudinal and transverse deformation gradients:

$$\gamma = \frac{1}{2}(F_x^p - F_z^p) = \frac{1}{2}\left[\left(\frac{V}{V_0}\right)^{\frac{2}{3}} - \left(\frac{V_0}{V}\right)^{\frac{2}{3}}\right] \quad . \tag{3.42}$$

Similarly, lattice rotations can be assigned to the equivalent plastic shear:

$$\gamma = \frac{1}{2}\left[\frac{\cos\chi_0}{\cos\chi} - \frac{\cos\chi}{\cos\chi_0}\right] \quad , \tag{3.43}$$

where for (211) slip plane $\chi_0 = 54.7°$.

In Figure 3.38, the equivalent plastic shear strain is plotted as a function of pressure. It can be noticed that by applying a shear strain definition relying on the true strain ($\gamma = \frac{1}{2}(\ln F_x^p - \ln F_z^p)$) simplified expressions can be found:

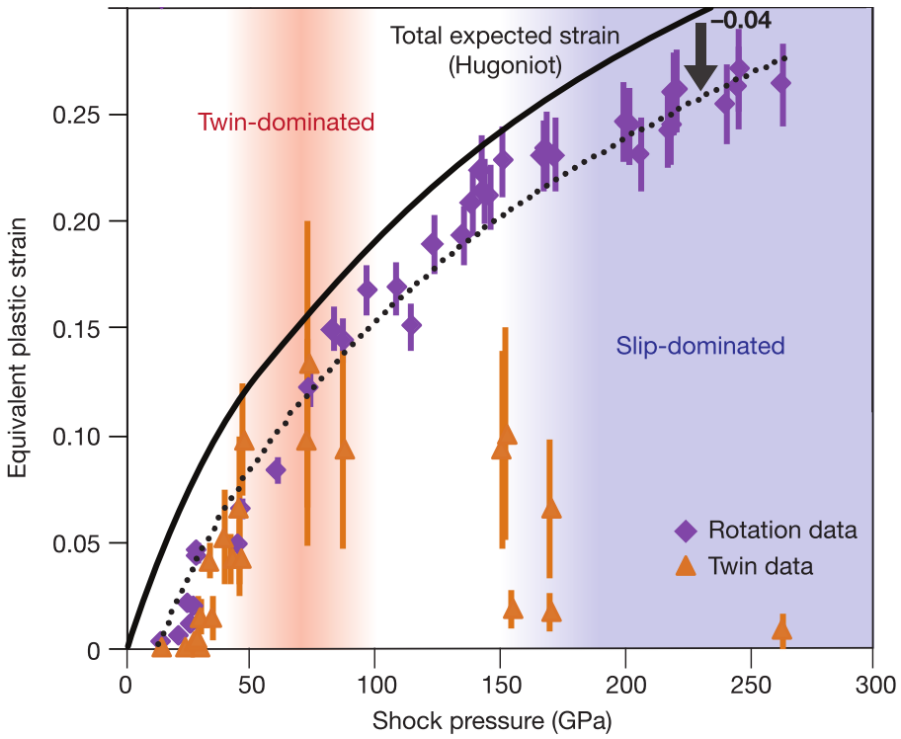


Figure 3.38: Equivalent plastic strain inferred from lattice rotation (purple diamonds) and twin fraction (orange triangles). The equivalent plastic strain for a material subject to hydrodynamic shock ('on the Hugoniot') is also plotted (black curve). The rotation data follow the Hugoniot line less 4% strain (dotted curve). Twinning accounts for the majority of the Hugoniot plastic strain in the 40-80 GPa range (pink shaded region); however, twinning-induced strain falls well below the total plastic strain above 150 GPa (blue shaded region), indicating that the response is slip-dominated. Error bars directly correspond to the uncertainties in the extracted lattice rotations and twin fractions transformed according to equations 3.45 and 3.46.

$$\gamma^p_{\mathrm{Hu}} = \frac{2}{3}\ln\left(\frac{V_0}{V}\right) \quad , \tag{3.44}$$

$$\gamma^p_{\mathrm{ro}} = \ln\left[\frac{\cos\chi}{\cos\chi_0}\right] \quad . \tag{3.45}$$

Subscripts are introduced in order to explicitly associate equivalent plastic shear strain with rotations (γ^p_{ro}; purple diamonds) and the total amount of deformation on the Hugoniot due to the hydrodynamic shock (γ^p_{Hu}; black line). Plastic shear strain due to twinning is estimated by evaluating γ associated with the rotations induced by twinning (Equation 3.34), which leads to the simplified expression for the conversion between twin fraction and the equivalent plastic shear strain (γ^p_{tw}; orange triangles):

$$\gamma^p_{\mathrm{tw}} = f_{\mathrm{tw}}\varepsilon_0 M \quad . \tag{3.46}$$

where ε_0 is the eigenstrain, and M is the Schmid factor (for [110] loading, $\varepsilon = 0.707$ and $M = 0.471$). The plastic strain from slip can be determined from the difference $\gamma^p_{\mathrm{ro}} - \gamma^p_{\mathrm{tw}}$. If either mechanism dominates the response, then the plastic strain from that mechanism will be a large fraction of γ^p_{Hu}. Whereas the onset of twinning occurs at 25 GPa, the plastic response is twin-dominated in the 40-80 GPa range. Above 150 GPa, the plastic strain from twinning falls well below the Hugoniot line, indicating that the plastic response becomes slip-dominated. Since the transition at ∼25 GPa is associated with the slip-twinning transition, we denote the second transition as the reverse twinning-slip transition. This result is unexpected as despite the common association between twinning and strong shocks, there is a transition from twinning to dislocation-slip-dominated plasticity at high pressure (more than 150 GPa). The common understanding of slip-twinning competition [95] indicates that above a certain pressure threshold, the stress required for twinning becomes less than the stress required for dislocation motion, which means that at high pressures twinning is the favoured plastic mechanism. The reversed twinning-slip transition above 150 GPa could indicate that the significant reduction in the timescale of the deformation results in the homogeneous nucleation of dislocations.

The trend for the lattice rotation follows the Hugoniot line with a small offset. There is a difference of 4% strain between the two curves $\gamma^p_{\mathrm{ro}} - \gamma^p_{\mathrm{tw}} \approx 0.04$, indicated by the dashed line in Figure 3.38. The lack of rotations below 15 GPa is not understood and remains a subject for future studies. One possible explanation of this observation could be related to a small amount of unaccounted-for slip along the slip plane. The presence of preexisting defects in the crystal could lead to a resolution of the shear stress along non-dominant slip systems. Such a deformation would potentially induce grain rotations not detectable in the experimental geometry.

An additional element, not considered in this study, is the temperature dependence of the twin formation. During shock compression the temperature increase is directly linked with the volume change along the Hugoniot, and is not treated as a separate variable. However, external heating sources need to be considered. Twinning is commonly associated with low temperature deformations, therefore the

presence of the additional source of heating could indicate that the observed twin fractions are lower than expected for shock compression of the material with the initial temperature of 300K. An example of such a source is x-ray radiation from the ablation plasma preheating the crystal. At the relatively low optical laser intensities used in the experiment (up to 10^{13}W cm^{-2}), it is expected that hard x-rays are not produced at the ablation surface. Furthermore, soft x-rays at the ablation surface are absorbed by the thick kapton ablator, and thus the underlying crystal is not heated by the ablation plasma. This is known experimentally because there is no thermal expansion shift in the x-ray diffraction patterns from the ambient part of a shocked crystal. We can compare the d spacing of a target that has been unshocked by the laser with the d spacing of the yet-to-be shocked material in the shocked case – the shocked case is not hotter; therefore, there is no preheat.

It is important to recall that any discussion on the plasticity mechanisms in shock-compressed tantalum is presented in the context of the specific original microstructure of the material. Fibre-textured tantalum was used in order to utilize unique capabilities of X-ray diffraction from highly-textured samples. The question for future studies is whether plastic mechanisms reported in this study are microstructure-specific. For example, it is believed that materials with columnar-structure-grains (similar in structure to the one used in this study) twin more easily [125]. Therefore, it would be interesting to further investigate plastic deformations in tantalum foils lacking such a microstructure.

3.8 Molecular dynamics simulations (shock)

In order to support experimental investigation, molecular dynamics simulations have been performed. The high strain present in shocked materials makes dynamic compression an ideal candidate for MD studies since it requires a smaller amount of simulated time and, by extension, a smaller number of timesteps. The simulations were carried out with LAMMPS code using EAM potentials developed by Ravelo *et. al.* [55]. Ravelo Ta1 and Ta2 were tailored to reproduce tantalum's behavior at pressures of the order of a megabar. These potentials were successful at predicting

the experimentally-determined pressure-volume curve at the ambient temperature [120, 121], the Hugoniot in the U_s-U_p plane [100], and the melt curve [126]. Both models provide predictions of plastic mechanisms reasonably representing the results of the recovery experiments [97]. They agree on the description of plasticity in Ta and screw dislocation core energies. The major differences between the two of them are the better reproduction of energetics of lattice defects by Ta1, and better estimation of thermal expansion and thermal pressure at high pressure by Ta2. Since the thermal properties of materials during this part of the project were not the main subject of investigation, plasticity modeling was performed using Ravelo Ta1.

The size of the simulation box is an important factor to consider prior to carrying out an investigation. Larger systems are able to capture phenomena in compressed systems better due to their more representative description of real material. The length of the simulation in the direction of shock propagation needs to be long enough in order to run it for a sufficient amount of time. This is associated with the timescale of plastic relaxation happening behind the shock front as well as with the ability to perform analysis on a statistically representative system, where various regions may display different behaviours. The transverse size of the box is also crucial, as lengths smaller than ∼50 atomic spacings may prevent certain plasticity mechanisms (e.g. defect nucleation). One factor which prevents the ability to simulate systems similar in size to real crystals is the computational cost. For the purpose of the analysis of shock-compression simulations, a box of atoms with size $100 \times 100 \times 800$ unit cells (330 Å× 330 Å× 2,644 Å, 16 million atoms) was used. The atoms were arranged such that the [110] axis was in the z-direction (the longest dimension of the box). [001] and $[1\bar{1}0]$ were aligned along x and y axes, respectively. Both transverse directions were periodic in order to mimic the behaviour of a large single crystal. The time increment between two consecutive steps of the simulation was 1 fs, and the initial temperature of tantalum was set to 300 K.

A portion of the end of the sample consisting of a few atomic planes was used as a piston generating a shock. That section was 'frozen' so that it would not respond to external forces. It was linearly ramped up to a set particle velocity

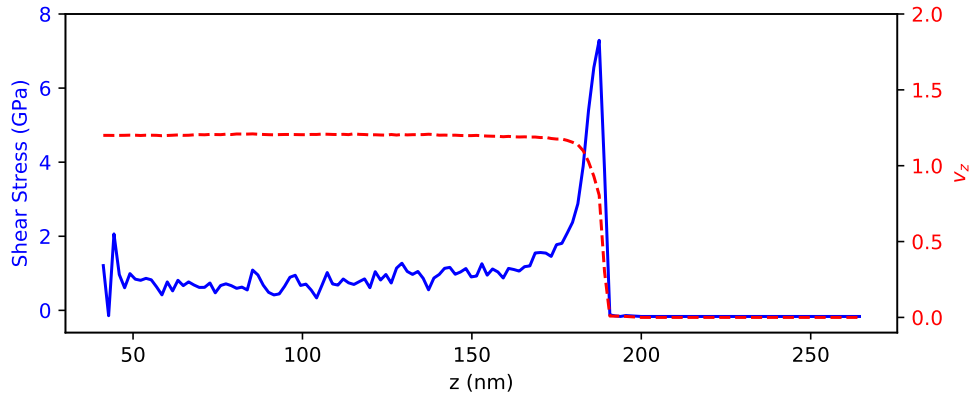


Figure 3.39: Shear stress (blue) and particle velocity along the compression direction (red) profiles after 40 ps from the launch of $\sim$ 100 GPa shock wave in MD.

U_p along the z-direction within the first 5 ps of the simulation in order to drive a compression wave. The purpose of using a gently-accelerating piston rather than an instantaneously-moving one is the issue of artificial heating associated with high-strain rate in the case of the latter. After about 20 ps beyond the initial ramp compression, the deformation steepened to form a shock wave. The simulation was run until the shock reached the free surface, and a release wave was lunched back into the bulk of the material. The analysis of the rarefaction waves in MD will be discussed in the following chapter of this thesis.

Multiple simulations were performed for various shock strengths ranging from $Up = 0.5$ km/s to > 2.0 km/s (from $\sim$ 30 to $\sim$ 200 GPa). The data files containing information about the atomic positions, velocities, stress components, etc. were dumped out every few picoseconds. Figure 3.39 shows the shear stress profile within a sample, along the direction of shock propagation after 40 ps from the launch of $\sim$ 100 GPa shock wave. It can be noticed that front of the wave is characterised by a sharp discontinuity in shear which gradually decreases with time. This effect is associated with a finite timescale of plastic relaxation happening behind the shock front. In order to focus the analysis on that section of the shocked sample which had enough time to resolve shear stress - a compressed part of the sample, far behind the shock front, was investigated.

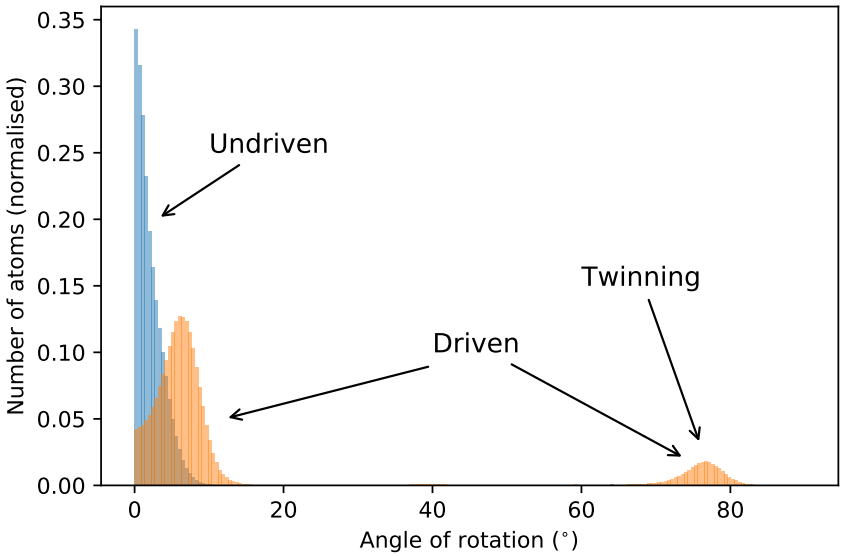


Figure 3.40: Histograms representing the rotations of the lattice about the $[1\bar{1}0]$ within a box of atoms in an MD simulation. The blue histogram refers to rotations prior to compression. These rotations can be described by a normal distribution with a mean at 0 (the plot represents the absolute angle of rotation). The orange histogram shows lattice rotations with a crystal driven along [110]. A shift towards small rotation angles is observed (<10°). A small peak, around $\sim 75°$, corresponding to twinned orientations is observed. Both histograms are normalised such that their total areas are the same.

The analysis of the grain orientation within the shocked part of the material was performed using a per-atom deformation gradient (PADG) code [94]. The fundamental functionality of PADG relies on the comparison of the crystal before and after deformation. At the beginning, for every atom in an undeformed state (simulation at the initial timestep) a list of indexes of all neighboring atoms within a certain cutoff radius is collected. Once the material is deformed, the relative location of atoms and their original neighbors is compared against their relative positions prior deformation. This way a deformation matrix associated with every atom in the simulation box is constructed. It can be deconvolved, via polar decomposition, into a pure lattice rotation and a pure deformation which strains the material. PADG was used to find rotation transformation of the simulated atoms with respect to their original orientations at the initial timestep of the simulation. Figure 3.43 illustrates a histogram of the absolute value of the rotational angles about the $[1\bar{1}0]$ axis before and after the compression. Prior to compression, lattice rotations are

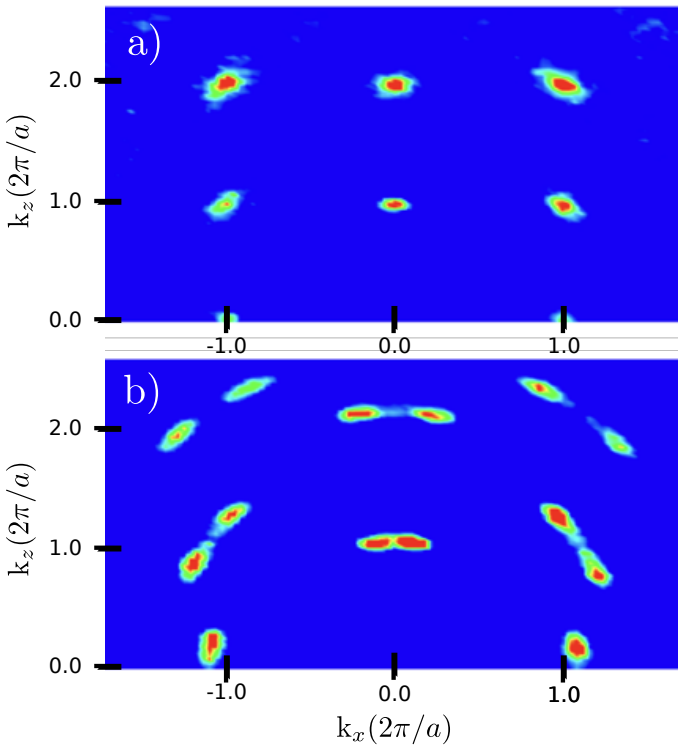


Figure 3.41: Heat maps of the 3D Fourier Transform from the atomic positions of the single crystal Ta before (a) and after (b) shock compression. Both figures represents $k_y = 0$ plane, which displays the lattice rotations about $[1\bar{1}0]$ in b).

normally distributed around 0°. In a driven material, two characteristic features can be observed. Firstly, the vast majority of distribution is shifted towards non-zero angles which can be associated with the kind of shock-induced lattice rotations observed in the experimental data. Secondly, a small peak around the $\sim$ 75° angle suggests an appearance of a new lattice orientation which is consistent with twinning. By measuring the portion of atoms contributing to the appearance of this large reorientation peak, twin fraction can be extracted. Figure 3.32 shows the simulated twin fraction as a function of pressure (black circles). The molecular dynamics simulations show the onset of twinning occurring at similar pressures as indicated by the data, although the decrease in twin fraction occurs at a much lower pressure in the simulations.

The output of the molecular dynamics simulations has been analysed in the reciprocal space as well. A set of atomic positions (x, y, z) before and after compression has been 3D Fourier Transformed into (k_x, k_y, k_z). The results of

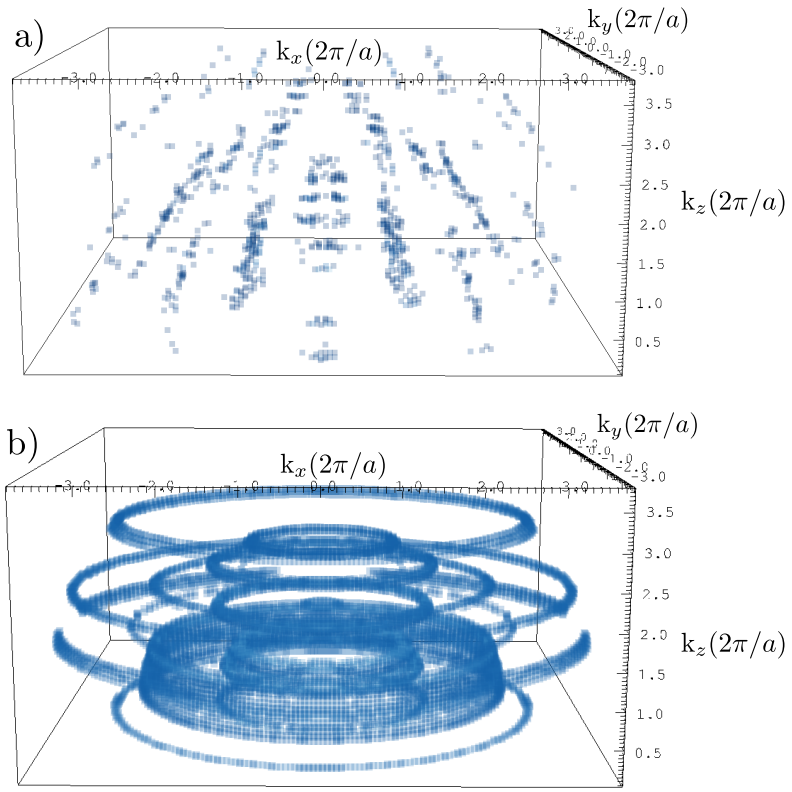


Figure 3.42: a) three-dimensional representation of the Fourier Transform of the atomic positions in MD. For clarity, only points above a certain amplitude threshold are displayed. b) shows the result of the summation of the data in a) rotated about k_z axis, which simulates the effect of fibre-texture in the reciprocal space.

this transformation are shown in Figure 3.41a and b where both images display FT representation within $k_y = 0$. It can be noticed that, due to smaller lattice spacing, peaks in an FT from a driven material are shifted towards higher |k| values. However, the most interesting observation is the splitting of the peaks caused by two opposite directions of rotation about k_y axis.

Finally, the results of the MD simulations are used to generate diffraction patterns in the experimental geometry which can give a direct confirmation of the x-ray data interpretation. The 3D FT of the textured material was simulated via summation of multiple 3D FTs from a single crystal rotated about the k_z axis. This process in illustrated in Figure 3.42. The result of this transformation was the conversion of the singular spots into a set of rings in a reciprocal space. By using DIFFRACT, an x-ray diffraction analysis software developed by A. Higginbotham, fibre-textured 3D FT was raytraced onto a flat diffraction plane reassembling the

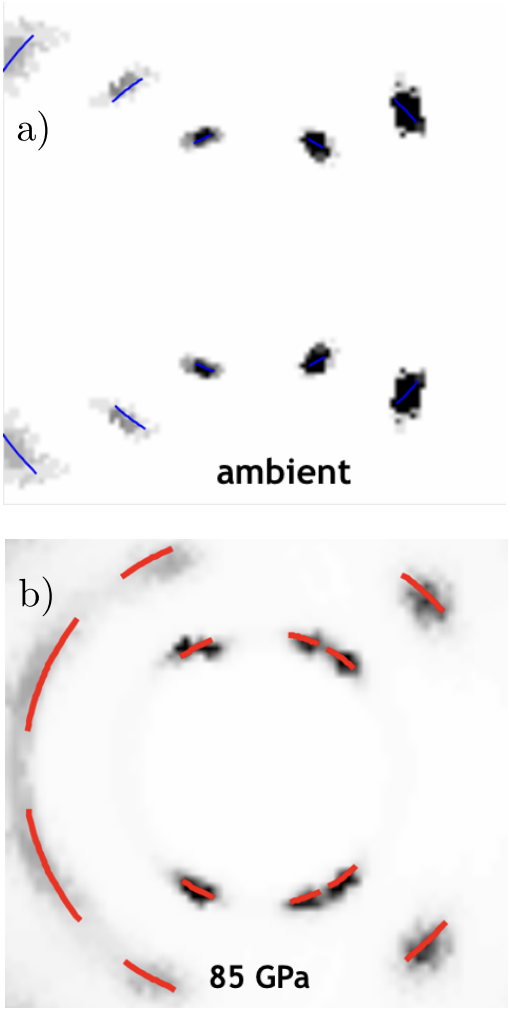


Figure 3.43: Simulated diffraction patterns from the MD simulations referring to the undriven (a), and driven (b) material. The images have been presented on a logarithmic scale for clarity. Solid arcs represent the theoretical location of the diffraction peaks from a fibre-textured material with no rotations (blue) and with rotations about the $[1\bar{1}0]$ axis (red).

one used in the experiment. The simulated diffraction patterns for tantalum at ambient conditions and driven by 85 GPa shock are shown in Figure 3.43. The solid lines provide theoretical predictions of the location of diffraction spots with [110] fibre-texture along the z-direction (blue lines in Figure 3.43a) and with the direction of fibres rotated about $[1\bar{1}0]$ (red lines in Figure 3.43b). By setting the texture width to a sufficiently low number, a good agreement between the simulated and the theoretical diffraction patterns was obtained. As in the case of the experimental data, the $\chi = 60°$ (110) diffraction spot split due to shock-induced lattice rotations

while $\chi = 90°$ remained in the same location. The lattice rotations in MD were extracted from both the population of rotation angles extracted via PADG code as well as peak locations in the reciprocal space. Both methods provided consistent results. Figure 3.36 shows the simulated lattice rotation as a function of pressure (black circles). The simulated lattice rotation was in good agreement with the data in the 75-200 GPa pressure range. A feature of the high pressure simulations (shocks above ∼200 GPa) worth mentioning is the formation of a partially premelted region right behind the shock front. This phenomenon was previously documented by Ravelo et al. [55]), as well as other authors [127–130]. It has been identified that the formation of the premelt is associated with high strain rates that strong shocks produce. This premelting occures at temperatures much below the equilibrium melt temperature. Driven material recrystallizes shortly behind the shock front. For shock stronger than 220GPa the entire sample experiences a full premelt and recrystalization leading to the formation of nanograins with a completely isotropic orientation. The liquid-solid transition could potentially explain the discrepancy between lattice rotations observed in the XRD experiment and MD simulations. As can be seen in Figure 3.36, experimentally-observed lattice rotations increase beyond 200GPa to about 12-13°, while lattice rotations in MD tend to remain at a similar level of 11°. For example, at 220GPa the experimental lattice rotation measurements indicate 12.6±0.7° of rotation (number estimated using the three datapoints in that region) while the MD output indicates 11.0°. The appearance of premelted regions could potentially suppress the shear stress built-up or even completely resolve it, resulting in a reduced amount of grain rotation. It does not directly affect the analysis of twinning since the transition to a slip-dominated region appears at pressures much lower than pressures associated with premelting. The full understanding of this mechanism will remain a subject for future studies.

3.9 Summary

The pump-probe experiment with the use of the LCLS x-ray beam was performed in order to investigate plasticity mechanisms in dynamically-compressed tantalum.

The unique fibre-texture geometry allowed for the observation of an azimuthal redistribution of the diffraction signal within the Debye-Scherrer rings. Specifically, the analysis of the diffraction pattern allowed for the first *in-situ* observation of shock-induced twinning and measurement of the twin fraction. Additionally, lattice rotations associated with twinning and slip across {112} were observed. The experimental data indicates that below ∼80 GPa the dominant plastic mechanism is twinning, whilst at higher pressures (>150 GPa) the dominant plastic mechanism is slip. The molecular dynamics simulations of a shock-compressed single crystal Ta confirm our experimental findings.

4

Shock release of tantalum

Contents

4.1 Introduction 116
4.2 Diffraction pattern interpretation 118
4.2.1 Inverted lattice rotations 119
4.2.2 Detwinning 120
4.3 Molecular dynamics simulations (release) 123
4.4 Strain profile evolution 125
4.4.1 X-ray halo 126
4.4.2 Algorithm 127
4.4.3 Release modelling 132
4.4.4 Strain profile in simulations (MD) 137
4.4.5 Strain profile in simulations (HYADES) 138
4.4.6 Results 140
4.5 Summary 142

This chapter continues the description of the experimental work performed at SLAC to study plasticity in tantalum. This part of the thesis focuses on the subset of the x-ray diffraction data capturing material releasing after shock breakout. It will start with a description of the scientific motivations and literature overview, and will continue with an analysis of the lattice rotations and twinning on release, a study of the MD and hydrodynamic simulations investigating rarefaction waves, and a description of the strain profile extraction code from XRD data. The majority of the work presented in this chapter forms the core of the publication M. Sliwa

et al. Phys. Rev. Lett. **120**, 265502 (2018).

4.1 Introduction

An understanding of the rapid deformation mechanisms occurring during the shock process at the lattice level, such as the generation and motion of defects, or deformation twinning, has long been sought [131–133]. Of particular interest is the observation that in many cases the high rates of plastic strain observed at the shock front not only cannot be mediated by pre-existing dislocations, but are also inconsistent with the defect densities found via *post facto* analysis [96]. That is to say a direct application of Orowan's equation 2.50 [59] implies (under the assumption of sub-sonic dislocations) dislocation densities behind the shock front that can be several orders of magnitude greater than both those initially present, and those found in recovered samples.

Whilst defect densities consistent with observed plastic strain rates are not found in recovered samples [98, 134], such high densities are observed in many MD simulations [54, 93], and long prior to those simulations the generation of high densities of homogeneously nucleated dislocations at the shock front had been proposed [132]. A resolution to this discrepancy is suggested by further MD simulations that show that upon the shock unloading at a free surface, and subsequent rarefaction, most of dislocations annihilate [135], implying that *post facto* analysis of recovered samples may at best not provide a full picture of the conditions present during the passage of the shock itself. The large defect densities thought to be present under shock compression may also be pertinent to apparent contradictions in measured melting temperatures at high pressure [136–138]. Common methods of interrogating sample response, such as velocimetry techniques using VISAR [28], rely on measurements of the velocity of the free surface in order to deduce the sample's response [73]. However, this kind of method provides a limited amount of information since it does not probe either the plastic behaviour at the lattice level or the state of the entirety of the material at one particular moment. It thus cannot

be used to address the above hypothesis that microstructural plastic deformation during the shock can be, at least to some extent, eliminated upon release.

It is within the context outlined above that this chapter presents the results of experiments where, via femtosecond XRD, the microstructural effects of shock-induced plasticity were directly observed being reversed in polycrystalline tantalum during shock breakout as the rarefaction wave traveled back into the sample (although overall entropy increase, evinced by shock heating, would still be irreversible). In particular, it was possible to directly observe the reduction of shock-induced twins as well as a significant reversal in the lattice rotation imparted during the shock-compression process. These results, which are in good agreement with MD simulations, provide conclusive evidence that the release of stress after shock events, and the associated subsequent rarefactions and reverberations, can significantly alter the microstructure of the sample from that extant during the shock itself, highlighting the importance of *in situ* measurements.

This chapter is a direct extension of the previous part dedicated to LCLS experiment to study plasticity in tantalum. Experimental data presented in this chapter were collected during the same campaign as the images capturing fibre-textured tantalum during shock compression along [110] direction. Thus this discussion will omit a description of the experimental setup, as the details have been provided in the preceding chapter. The only major difference between the methods used to study shock-compression and release is the timing of the probe with respect to the timing of the driving beam. With the aid of the VISAR and preceding XRD images, the delay time of the x-ray probe was appropriately increased to allow the shock wave to reach the free surface and the material to start unloading. This task, to a certain degree, relied on a trial and error method and required multiple shot repetitions to achieve the desired measurements. The main reason for this approach was a fluctuation in the power output of the driving laser. This meant that two consecutive shots with the same setup parameters could have different power outputs resulting in different shock strengths, causing shocks to arrive at two different locations within the sample during the X-ray probe time. The process was

monitored by analysing VISAR images in real time. Decisions on whether the X-ray probe time should be increased or decreased (typically by ±0.1-0.5ns) were based on the extracted shock breakout information. Qualitative real time X-ray image analysis provided an independent check on the probe timing with respect to the breakout time through identification of the XRD features characteristic for release.

4.2 Diffraction pattern interpretation

The shock wave is characterised by a high-strain-rate resulting in a sharp discontinuity in the strain at the shock front. Therefore, during the passage of the shock before it reaches the rear free surface, diffraction from both compressed and ambient material is observed, resulting in arcs lying on two distinct, well-defined Debye-Scherrer rings, with negligible diffraction signal between them, as shown in Figure 4.1a. When the shock encounters the free surface, the normal component of the stress at that surface must remain zero, so a rarefaction wave is launched back into the sample, allowing material to expand quasi-isentropically [52]. In contrast to the extremely rapid change of strain at the shock front, a rarefaction fan ensues, owing to the reduction in the local speed of sound as the pressure drops, leading to a release of strain at a decreasing rate as the rarefaction proceeds. This much lower strain gradient exhibits itself as a clear diffraction signal over the whole range of Bragg angles between those Debye-Scherrer rings that correspond to fully-compressed and fully-released material, as shown in Figure 4.1b. As will be shown below, the distribution of diffracted intensity in this region allows for the extraction of the instantaneous strain-depth profiles in the rarefaction fan.

Several important observations can be made immediately from the data. As demonstrated in the previous chapter, by analysing the azimuthal positions of the diffraction peaks, plastic response induced by the shock can be inferred. A similar approach is used in the analysis of the diffraction signal from the released material with particular attention to XRD pattern modifications due to lattice rotations and twins.

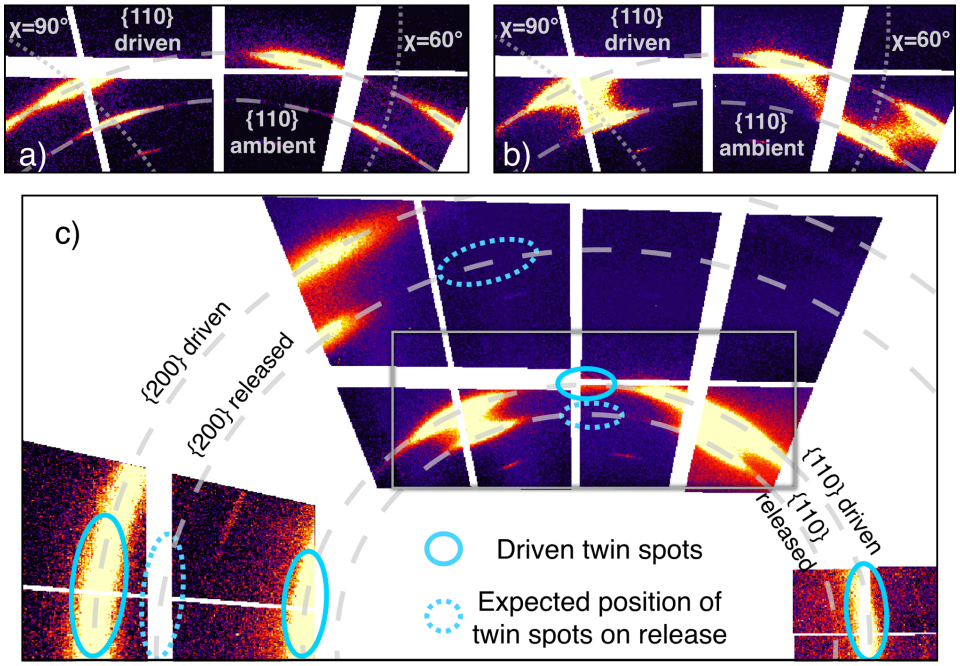


Figure 4.1: XRD images of Ta during a) the initial shock passage at 167 GPa and b) release following 150 GPa and c) 75 GPa shocks. In c), diffraction due to twins is marked with full circles, and the positions of the expected locations of twin spots on release are marked with dashed circles. Images a) and b) correspond to the CSPADs' coverage marked with the rectangle encompassing c).

4.2.1 Inverted lattice rotations

Figure 4.1a shows an example of lattice rotations inferred from the (110) Bragg reflections for a shock pressure of 150 GPa, where the diffraction signal on the left follows the $\chi_0 = 90°$ path while the $\chi_0 = 60°$ diffraction signal splits on compression into $\chi > 60°$ and $\chi < 60°$, and the magnitude of the splitting implies a lattice rotation of just over 10° in the shocked state.

On release we observed diffraction along paths connecting the diffraction signal from the fully-compressed and fully-released material at the rear surface, which provides an explicit *in situ* history of lattice rotations during rarefaction. As shown in Figure 4.1b, the diffraction signal traces out a path along the $\chi = 90°$ line, while the $\chi = 60°$ signal, split during compression, traces paths back close to its initial position. This is indicative of reversed lattice rotations on release about $[1\bar{1}0]$. Reversed lattice rotations, even though not explicitly confirming dislocation annihilation, suggest inverted dislocation motion. It should be noted that a small

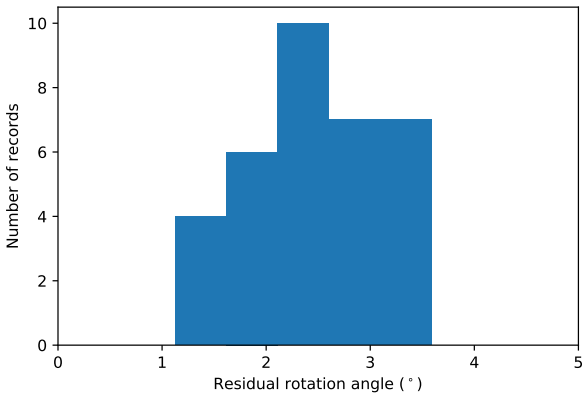


Figure 4.2: The distribution of the extracted residual lattice rotations on release.

residual azimuthal split between peaks which were originally at $\chi_0 = 60°$ in the ambient sample is observed. The precise location of each of these peaks is extracted by modelling their shape with partially overlapping double Gaussians. According to equation 3.30, by converting these positions into normalised orientations of the reciprocal lattice vectors, the rotation angles were found. For each pair of $\chi_0 = 60°$ peaks the extracted residual rotations were consistent. Figure 4.2 presents the distribution of the extracted residual lattice rotations from shock in the investigated pressure range. No pressure dependence on the magnitude of residual lattice rotation was observed, with the majority of rotation in ∼2-3° range.

4.2.2 Detwinning

Another piece of analysis considers shock-induced twinning. By comparing the new set of diffraction spots on compression with the diffraction signal on release, the evolution of the shock-induced twinning can be inferred. Figure 4.1c shows a diffraction pattern during release, 0.3 ns after breakout of a 75 GPa shock wave, which on compression generates large amounts of twinning, with the diffraction associated with the twins marked both under compression, and where they would be expected to appear under release. The calculation of the location of twin spots in a released part of material corresponds to {112} twinning in a crystal with [110] axis along the shock direction at ambient conditions. It is based on the observation that the location of the XRD release signal closely matches the location of the



Figure 4.3: A SEM micrograph of the Ta sample shows the columnar microstructure that gives rise to the fibre texture.

XRD signal before the compression. It can be seen that no signal corresponding to twins is observed in the released state, indicating disappearance upon rarefaction (to a fraction below 1%, a figure determined by the noise background). The same observation was reported for XRD images capturing Ta deformation at various times after the shock breakout. None of the XRD images taken from just after the breakout up to 10ns after the breakout displayed any sign of twinning signal on release, indicating no detwinning time dependence. The lack of twins at early stages of release (where the strain rates within the sample are high) suggests that this deformation takes place at timescales shorter than 100ps.

This experimental observation of detwinning, supported by MD simulations is interesting in the context of previous *post facto* studies. In contrast to monocrystalline [89, 96, 97] and polycrystalline [95] samples which show significant amounts of twinning remaining after the shock, nanocrystalline materials [98] have not shown traces of twins. This phenomenon has been considered in terms of the Hall-Petch effect which suggests that large grains twin more easily. However, the evidence of detwinning in the high-strain-rate experiment brings a new perspective on those studies. Furthermore, twinning-detwinning deformation in grains with transverse dimensions of the order of 100 nm (see micrograph in Figure 4.3) may be analogous to the cyclic loading-unloading experiments performed on nanopillars [125], suggesting pseudoelastic properties of the nanoscale materials not only on the static, but also on the dynamic timescales.

Figure 4.4: Average rotation angle about $[1\bar{1}0]$ direction (a) and shear stress defined as $(\sigma_{zz} - \sigma_{zz})/2$ (b) along the Lagrangian position in a single crystal Ta as a function of time in the MD simulation, with 100 GPa shock moving to the right and the rarefaction wave propagating to the left (after 70 ps).

a)

b)

Figure 4.5: a) and b) show the visualisations in Eulerian coordinates of the regions rotated by more than 20° at the timesteps 80 ps and 100 ps for the case of 50 GPa shock. This method allows for an easy observation of the twinned parts (thick, well-defined red lines). Blue and purple regions correspond to the non-twinned shocked and released parts of the sample respectively.

4.3 Molecular dynamics simulations (release)

In order to complement these observations of the partial reversal of lattice rotation and detwinning upon release MD simulations were performed. Using the Ravelo EAM Ta1 potential [55], we simulated the response of a 100×100×950 cells (33×33×314 nm) Ta single crystal at 300 K to a moving piston along the [110] direction, with periodic boundaries in transverse direction. Piston velocities in the range 0.7-1.2 km s^{-1} were applied, which drove shocks of strengths between 50-100 GPa. The simulation time was sufficiently long enough that we could observe both shock propagation and subsequent rarefaction from the rear surface. Upon release (which occurs just before 70 ps in the simulations), the shear stress changed its sign with respect to the one observed during initial shock passage, as shown in Figure 4.4a for a shock of 100 GPa. Using the nearest neighbour analysis, we identified variations in lattice orientation across the sample. Figure 4.4b presents the average lattice rotations about the $[1\bar{1}0]$ direction as a function of the longitudinal position within the sample at different times. In agreement with the experiment, it can be observed that the simulated sample experiences reversed lattice rotations as a result of rarefaction. The quantitative rotations are in excellent agreement with the experiment, where we also observed a rotation of the lattice of order 8° at 100 GPa. Furthermore, the simulations indicate that upon rarefaction not all of the rotation is reversed, with a residual rotation of approximately 3° persisting in the simulation.

It is worth pointing out that a significant dip in the extracted rotational angles was observed within the first 100nm of the simulation box in Figure 4.4b). This could be explained by the evolving shock conditions within that part of the sample. The initial shock modeling via frozen piston method suffers artificial features if the speed of the piston is changed in an instantaneous way, i.e. from 0 to U_p within 1 timestep. Such a change corresponds to inappropriately large strain rates for shocks modeled in this work, which results in the artificial heating of the sample. This problem was resolved by increasing the velocity of the piston to its target velocity over a short period of time (5ps). However, this means that strong

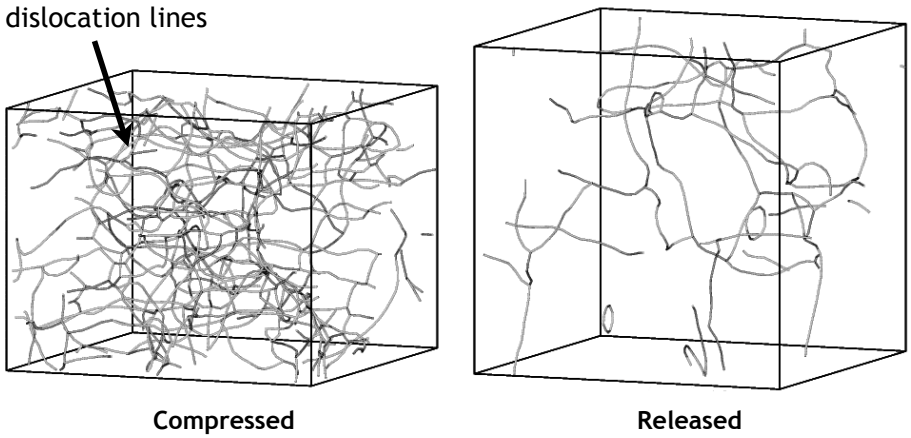


Figure 4.6: Visualisation of the dislocation network from a block of atoms in MD. The box on the left corresponds to a 100 GPa state, while the box on the right represents subsequent release to ambient conditions.

shock conditions are developed a certain distance behind the front surface once the acoustic wave steepens up. This distance corresponds to the first ∼100nm where a noticeable dip in the extracted rotational angles is observed. In order to minimize the influence of the non stable shock effects the analysis was focused on the region behind the initial 100nm of the sample.

Using dislocation extraction analysis (DXA) [139, 140] in OVITO (software for molecular dynamics simulation analysis), a list of dislocations present in a simulation box was obtained. Dislocation densities from the material behind the shock front as well as from a released material were estimated according to the following formula:

$$\rho_d = \frac{\sum_i^N l_i}{V} \quad , \tag{4.1}$$

where summation is performed over N dislocation lines of length l_i within volume V. We find a reduction of a factor of 2.5 of the dislocation upon rarefaction from a peak value of $5 \times 10^{13}\text{cm}^{-2}$ behind the shock. Figure 4.6 presents the visual representation of the dislocation network from an event imitating a shock-release scenario. A box of atoms was uniformly compressed along [110] by remapping the location of atoms every timestep at a strain rate $1.5 \times 10^{10}\text{s}^{-1}$ – a number that corresponds to a 100 GPa shock according to Swegle-Grady relation 2.86.

After 100 ps of equilibration in a fully-compressed state at $V/V_0 = 0.75$, material was unloaded at a strain rate 10^8 s^{-1}. A clear reduction in dislocation density by a factor of 4 upon release was observed.

In addition, as can be seen Figure 4.5a, the MD simulations with 50 GPa shock predict significant twinning (a twin fraction of 6%) upon compression, but (in agreement with the experiment) the twins disappear upon release, as can be seen in Figure 4.5b. It has to be pointed out that a region with a large twin fraction is formed immediately behind the shock front. These twins, as previously observed by Ravelo [55], continuously anneal out, which leads to a reduction in twin density relative to the distance from the shock front. This phenomenon mostly affects thin, 2-atomic-layer thick, twins. Thicker twins are more stable than thin twin embryos. However, even twins as thick as 20-25nm may experience slow annealing behind the shock front once the shear stress drops below 1.0-1.5 GPa [55]. A display of this effect can be observed in Figure 4.5a and b around the position 140nm where a twin experiences a reduction in size between snapshots at 80ps and 100ps before the arrival of the release wave. This indicates that at longer timescales detwinning due to release (shear stress reversal) can be partially enhanced by detwinning due to annealing effects.

4.4 Strain profile evolution

The experimental data allowed us to extract the rotation angle and strain transverse to shock propagation direction as a function of depth. The strength of the diffraction signal at a particular angle between that corresponding to the totally released material, and that still under peak compression, is a measure of the amount of material at a given strain. As shown in the following sections, this allowed us to iteratively construct a transverse $[1\bar{1}0]$ strain profile (for this direction the elastic component of the strain, to which diffraction is sensitive, is equal and opposite to the plastic strain) that is consistent with the diffraction image, under the assumption that the strain within the sample varies monotonically. Such algorithms have been used previously to deduce strain profiles from diffraction profiles [141, 142].

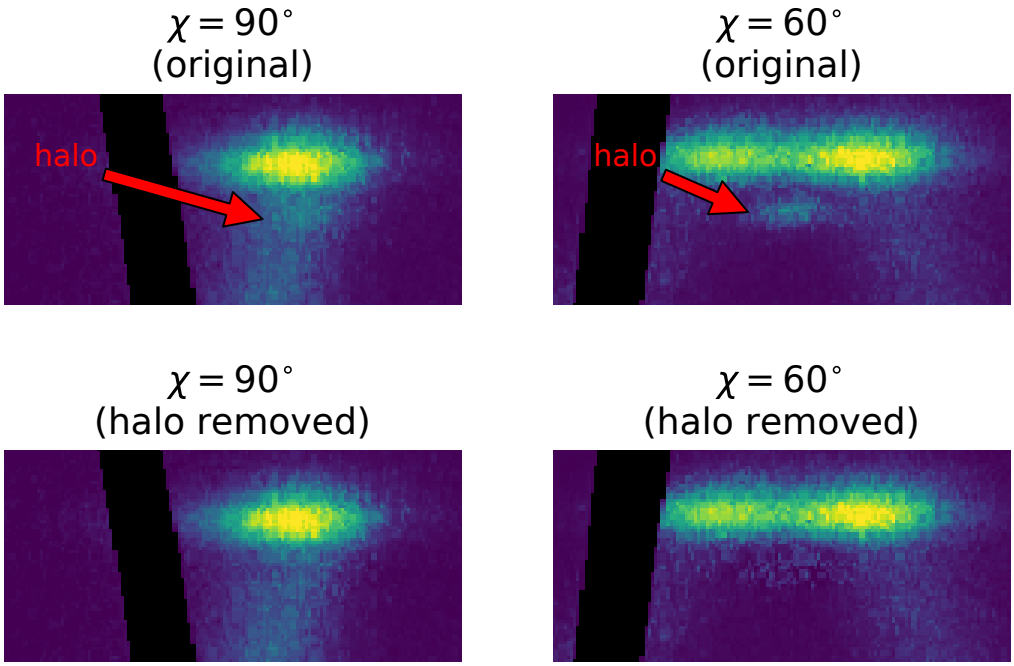


Figure 4.7: Images of the $\chi = 90°$ and $\chi = 60°$ before (top row) and after (bottom row) halo signal removal for the driven shot capturing release.

4.4.1 X-ray halo

The size of x-ray spot probing the material was much smaller than the size of the optical laser spot, resulting in the majority of the x-rays diffracting from a driven spot. However, due to the scattering in the Be lenses that focused the x-rays, a wide x-ray halo which probed the undriven part of the material was formed. This resulted in the appearance of weak undriven diffraction spots, shown in Figure 4.7. The 'halo' signal partially overlapped with the diffraction from the driven material, interfering with strain profile analysis. The following procedure was used for the identification of the halo signal and for its removal before the application of the strain profile algorithm (Figure 4.7):

1. Both the halo signal in the driven image and XRD signal in preshots are the effect of probing undeformed tantalum in the same sample. Therefore, certain properties of the halo signal observed in the driven image can be inferred from the undriven signal observed in the corresponding preshot images. The

shapes (widths of the Pseudo-Voigt profile), locations, and amplitude ratios of the $\chi = 90°$ and $\chi = 60°$ are expected to be the same for the halo signal and preshot XRD, and can be measured using the preshot XRD.

2. Due to residual rotations on release, the $\chi = 60°$ halo signal can be distinguished from the signal between the release paths as shown in Figure 4.7b. Amplitude of this signal is measured.

3. Knowing the absolute amplitude of the $\chi = 60°$ halo signal as well as the ratio of intensities of the $\chi = 60°$ and $\chi = 90°$, and the shape of $\chi = 90°$ signal, the amplitude of the $\chi = 90°$ can be calculated:

$$\frac{(\chi = 90° \text{ preshot signal})}{(\chi = 60° \text{ preshot signal})} \cdot (\chi = 60° \text{ halo signal}) = (\chi = 90° \text{ halo signal}) \quad . \tag{4.2}$$

4. Finally, a Pseudo-Voigt signal with the shape parameters and location based on the $\chi = 90°$ preshot and the amplitude inferred from Equation 4.2 is subtracted from the driven image. A similar approach is applied to the $\chi = 60°$ halo removal without the need for ratio calculation presented in step 3.

Since the true amount of halo signal within the $\chi = 90°$ signal is not known, a numeric performance metric for halo removal methodology is not available. The performance of this process was evaluated by visual inspection of the processed lineouts. Application of the halo removal process resulted in the disappearance of the additional peak in the lineout (Figure 4.8), which suggests that the contribution of the halo signal was removed reasonably.

4.4.2 Algorithm

An algorithm based on an iterative procedure was developed to extract the strain profile from the angular dependence of the diffraction signal. A crucial element of the algorithm is the fact that it is based on the relative intensities of the signal, which means that it is not sensitive to shot-to-shot X-ray probe beam intensity

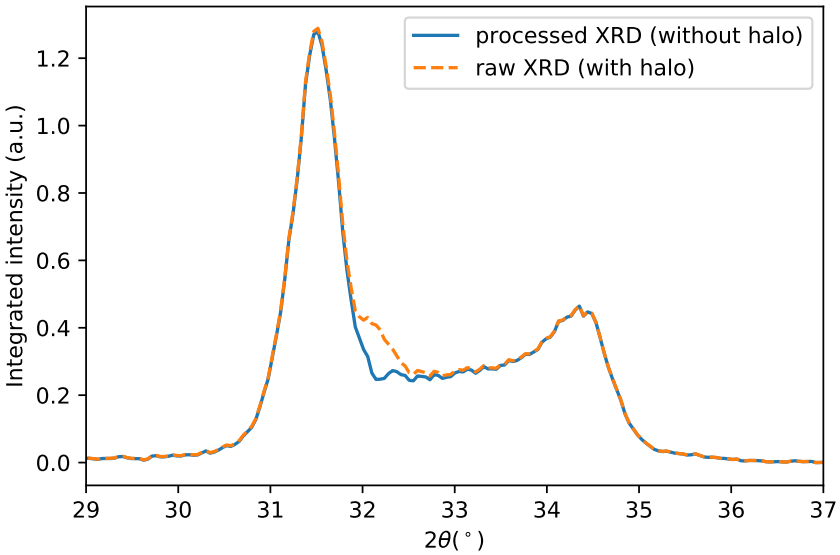


Figure 4.8: Driven XRD signal of the (110) $\chi = 90°$ peak during release before and after halo removal.

variations. The angular-dependent diffraction is calculated based on an assumed strain profile, and then adjusted (based on the difference between computed and experimental diffraction) to iterate towards a best fit to the strain profile within the sample, under the assumption that the strain profile is monotonic. The dominant features of strain profiles extracted from MD and HYADES simulations support this assumption (Figure 4.16). However, it is worth mentioning that a small amount of pressure reduction in a shocked state can be caused by release from the front. This release is the result of the expansion of the plasma's critical surface at the front of the ablator, which causes a reduction in the shock's strength generation. Such a release could cause a slight non-monotonic modification to the strain profile during rear surface release. This can be observed in a small tilt in the horizontal part of the strain profile extracted from the HYADES simulation (Figure 4.16b).

The sample was divided into equally-sized laminae along the z-axis, each of which was assigned a strain with an initial linear variation along the sample. The simulated, azimuthally integrated, diffraction profile was calculated by summing the contributions to the diffraction signal from each of the laminae. The XRD signal

from each lamina was modelled as a Pseudo-Voigt in a form of equation 3.21:

$$f_{PV} = w \underbrace{\frac{1}{1+\left(\frac{2\theta_0-2\theta}{\delta\theta}\right)^2}}_{\text{Lorentzian}} + (1-w) \underbrace{\exp\left[-\log 2\left(\frac{2\theta_0-2\theta}{\delta\theta}\right)^2\right]}_{\text{Gaussian}} \quad , \tag{4.3}$$

where $2\theta_0$ is the centre of the Bragg peak. For simplicity, in order to reduce the number of free parameters, the linewidths of the Gaussian and Lorentzian contribution were set to equal value $\delta\theta$.

As previously shown in Figure 3.20, the amplitude of the XRD from a lamina depends on the following factors: the width of the lamina, the length of the x-ray attenuation within the sample both before and after the lamina (which depends on the incident and scattering angles), the angular spread of the signal, and the atomic form factor. An additional factor of $\delta\theta^{-1}$ is included to account for the signal reduction due to angular spread of signal from a singular lamina. This factor is required in a case when local diffraction maxima are formed due to large parts of the sample being strained by a constant amount. This leads to the amplitude of the Pseudo-Voigt from the i-th lamina:

$$dI_i = I_0 \exp\left(-\frac{z_i}{\lambda\cos\omega}\right)\exp\left(-\frac{L-z_i}{\lambda\cos\zeta_i}\right)|f_{\text{aff}}|_i^2 \frac{1}{\delta\theta_i} dz_i \quad , \tag{4.4}$$

where I_0 is the incident intensity (which can vary on a shot-to-shot basis), dz is the size of the lamina, and z is the depth into the sample taken at a midpoint of the lamina.

The extraction of the transverse $[1\bar{1}0]$ strain profile was obtained by comparing the experimental azimuthally-integrated diffraction signal for the $\chi = 90^\circ$ (110) release line as a function of 2θ with the simulated diffraction. Assuming a fully hydrostatic response by use of Bragg's law, we can relate the diffraction angle to an associated amount of elastic strain. Note that in the direction transverse to shock propagation direction the elastic strain should be equal and opposite to the plastic strain, and the $[1\bar{1}0]$ diffraction signal is not sensitive to pure elastic strain along the shock direction. Equation 4.4, through ζ_i, depends implicitly on the azimuthal position of the diffracted signal. The location of the release

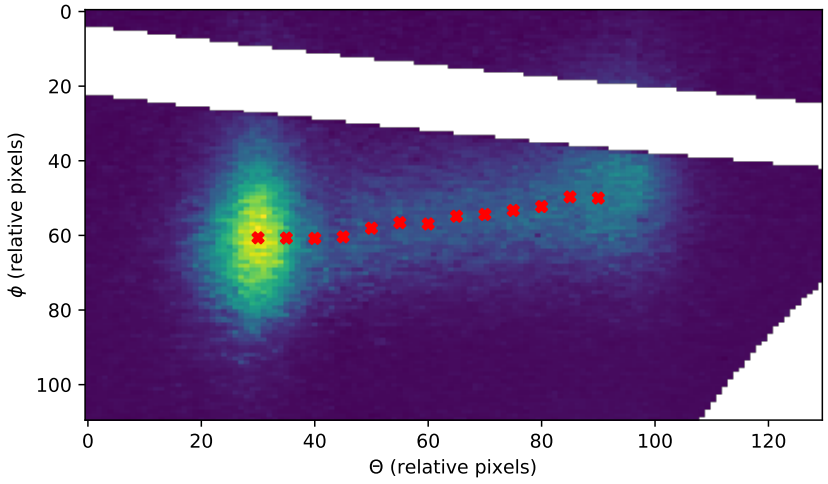


Figure 4.9: Location of the release path signal (red crosses) extracted via analysis of the azimuthal XRD profiles.

path was obtained by fitting a Gaussian profile to cross-sectional lineouts in the azimuthal space. An example of extracted $(2\theta, \phi)$ relationship, fed into the strain extraction algorithm, is shown in Figure 4.9.

For each iteration, the algorithm decreased the thickness of laminae that corresponded to areas where the generated lineout showed a higher intensity than the data. The modified size of the bin δz_i after the j-th iteration of the code is given by:

$$\delta z_i[j+1] = \delta z_i[j](1 + \Delta\text{Signal}[j]_i \cdot \frac{\beta}{\delta z_i[j]}) \quad , \tag{4.5}$$

where β is a hyperparameter describing the magnitude of the modification and $\Delta\text{Signal}[j]_i$ is the difference the between the experimental XRD signal and the signal generated in the j-th step of the algorithm at a Bragg angle that corresponds to the strain in the i-th lamina. An additional condition preventing the sizes of the laminae from taking negative values was introduced. This procedure was done in such a way that ensured that the sum of the thicknesses of all laminae remained a constant. Since the number of x-rays in the LCLS beam can vary from shot to shot, the algorithm scaled its output to match the integrated area under the signal for each shot.

Two strategies regarding modification of the laminae were examined. In the first one, in each iteration only the lamina with the largest $\Delta\text{Signal}[j]$ was modified.

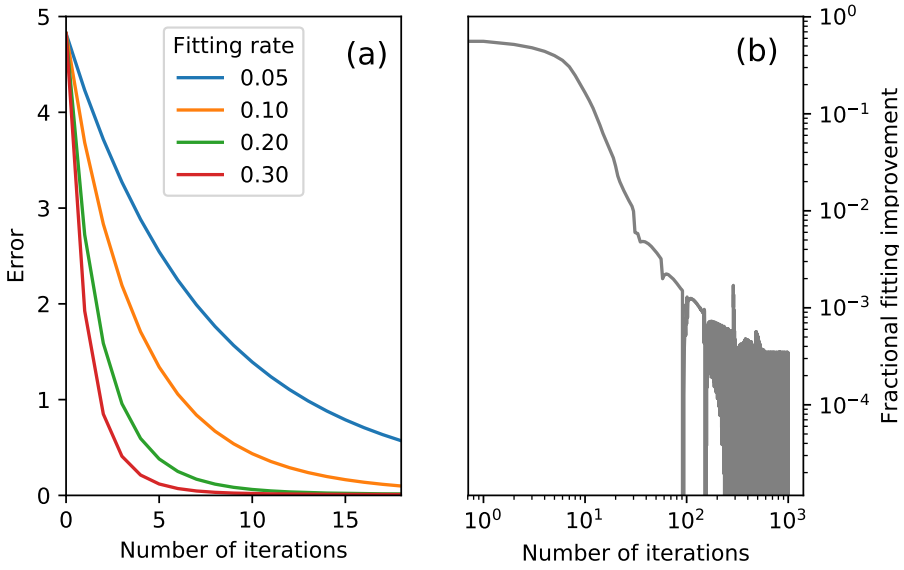


Figure 4.10: a) Loss function dependence on the number of iterations for various selections of the fitting rate β. b) Fractional fitting improvement as a function of number of iterations for the case of β=0.3.

It turned out that this method generated low-quality fits to the experimental XRD lineouts. When profile modifications, during two consecutive iterations, had counteractive effects, the improvement of the fit was stopped. In order to increase the robustness of the routine to the local optimisation minima, in each iteration the size of all laminae was updated according to equation 4.5. Apart from better fits to the experimental XRD profiles, this method offered significantly increased computational performance of the algorithm.

The selection of the parameter controlling the fitting rate β was performed by monitoring the loss function defined as the sum of squares of a difference between the experimental and fitted XRD lineouts. Figure 4.10a presents the loss function's dependence on the number of iterations for various fitting rates. It was found that for $\beta > 0.6$ poor convergence was obtained. The value of β=0.3 was selected as it provided good convergence and computational performance. Figure 4.10b shows the fractional fitting improvement between consecutive iterations of the algorithm for the case of β=0.3. Three distinct regimes can be distinguished. During the first 10 iterations, the algorithm performs the fitting of the major features in the XRD

lineouts. During the next ∼100 iterations fitting of the fine features is performed. Finally, in the last stage, fitting exceeding the abilities of the routine leads to noisy performance feedback. A value below 0.005% in the fractional fitting improvement was selected as the convergence condition.

Another test evaluating the performance of the algorithm was based on the extraction of the known strain profile from the analytically-generated XRD lineout. A strain profile resembling a rarefaction wave propagating through the material was created by introducing two large plateaus connected by a region where strain varied linearly as a function of depth, as shown in Figure 4.11. After 188 iterations the routine converged, providing a good fit to the XRD lineout and the target strain profile.

By use of this method a simulated diffraction signal was found that matched that of the experimental data, an example of which is shown in Figure 4.12.

A source of uncertainty in the strain profiles was caused by the intrinsic width (in 2θ) of the diffraction profiles. The linewidths fed into the algorithm were estimated based on the fit of singular Pseudo-Voigts to peaks corresponding to fully-compressed and fully-released material. It was found that the linewidth of the diffraction from unshocked material was slightly less than that from the fully-shocked sample. In order to take this into account in the algorithm, it was assumed that the linewidths for the intermediate strain states vary linearly with strain between these two values. Analysis of the algorithm's output shows that the details of the linewidth do not affect the computed location of the rarefaction wave or its steepness significantly, as shown in Figure 4.13. The parts of the strain profile most affected by the size of $\delta\theta$ are regions of constant strain, which became shallower for larger linewidths.

4.4.3 Release modelling

In a Lagrangian frame of reference, under the assumption of purely plastic response of Ta on release, the leading edge of the rarefaction front travels at the bulk sound speed of the Hugoniot state C_{BL}, while the tail travels at the ambient bulk sound speed C_0 [52, 143]. Therefore, the width of the rarefaction front increases linearly with time as $\Delta z = (C_{BL} - C_0)t$, where time can be expressed in terms of the position

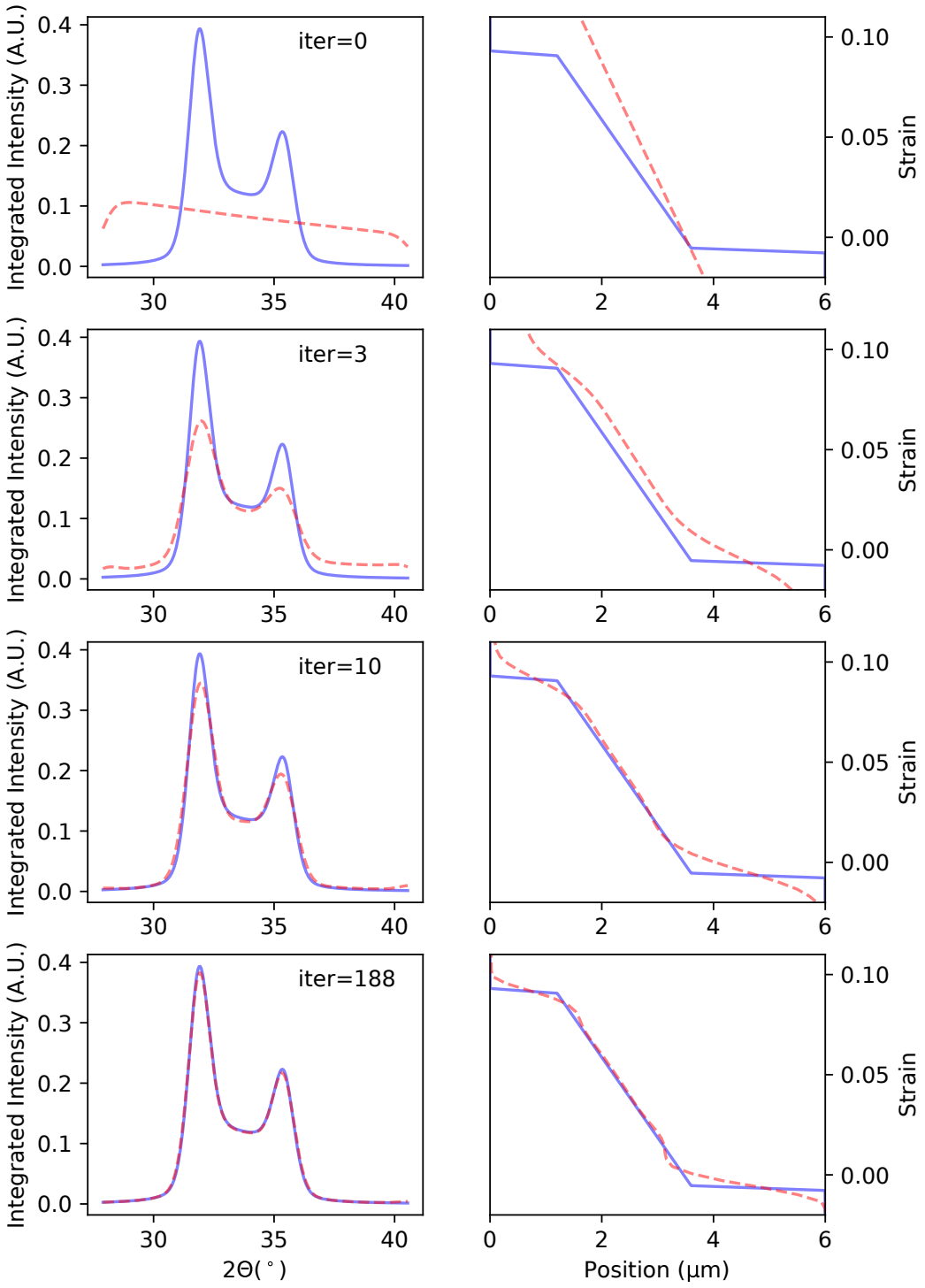


Figure 4.11: Output of the strain extraction algorithm before the first iteration, and after 3, 10, and 188 iterations. Blue curves on the left correspond to an analytically-generated lineout from a predesigned strain profile (blue curves on the right). Red dashed lines on the left are the fitted XRD lineouts constructed from the modified strain profiles (red dashed curves on the right). It can be noticed that the algorithm fits both the release wave position as well as the slope of its fan correctly.

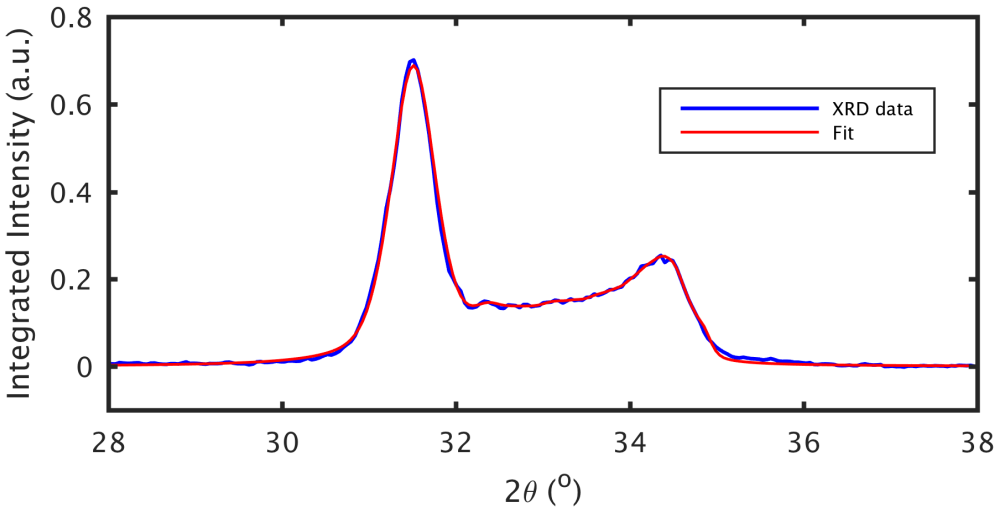


Figure 4.12: Lineout of the azimuthally-integrated $\chi_0 = 90$ signal (blue), and generated fit (red).

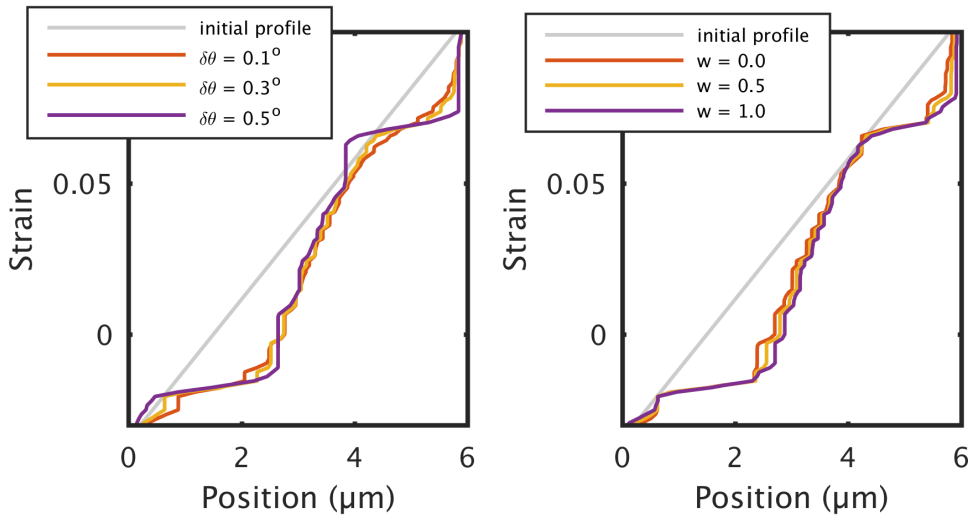


Figure 4.13: The computed strain profiles for various values of assumed intrinsic linewidth. The grey lines correspond to the initially assumed linear strain profiles. Solutions are shown for the linewidths corresponding to that of the peak from fully-compressed material, and as a function w parameter when the fitted values ($\delta\theta = 0.3°$ and $w = 0.3$) are varied.

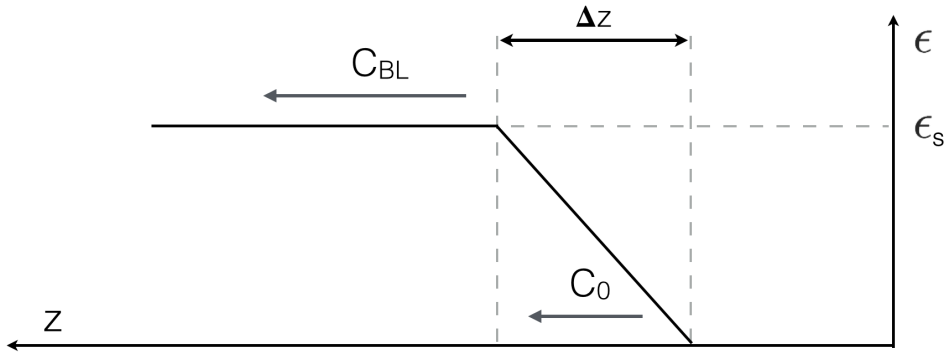


Figure 4.14: Schematic description of wavespeeds in a rarefaction fan traveling from right to left.

of the tail of the release wavefront: $t = z/C_0$. The assumption of purely plastic response is an approximation for the purpose of simplified release fan analysis. The leading edge of release wavefront is believed to contain an elastic precursor travelling at the elastic sound speed as shown in Figure 2.25. Previous works on the rear surface of tantalum indicate that elastic release affects a relatively small portion of the release fan [144, 145]. Additionally, in order to study bulk sound speeds at high pressures, researchers [72, 144] proposed a method where the strain within the plastic portion of the fan is linearly extrapolated to Hugoniot state, which is equivalent to neglecting the influence of the elastic precursor.

Using the cartoon shown in Figure 4.14, we define the strain gradient α within the rarefaction fan as function of the position of the release tail:

$$\alpha = \frac{\epsilon_s}{\Delta z} = \frac{\epsilon_s C_0}{(C_{BL} - C_0)z} \quad , \tag{4.6}$$

where ϵ_s is the strain in the shock state. C_{BL} can be related to the Eulerian bulk sound speed C_{BE} by $C_{BL} = C_{BE}(\rho/\rho_0)$, where ρ_0 and ρ are the material's density at ambient and shock conditions respectively.

Assuming a perfectly hydrostatic response of the lattice, the strain gradient within the rarefaction fan α is inversely proportional to the position of the release tail z:

$$\alpha = \frac{\epsilon_s C_0}{(C_{BE}(1-\epsilon_s)^{-3} - C_0)z} \quad . \tag{4.7}$$

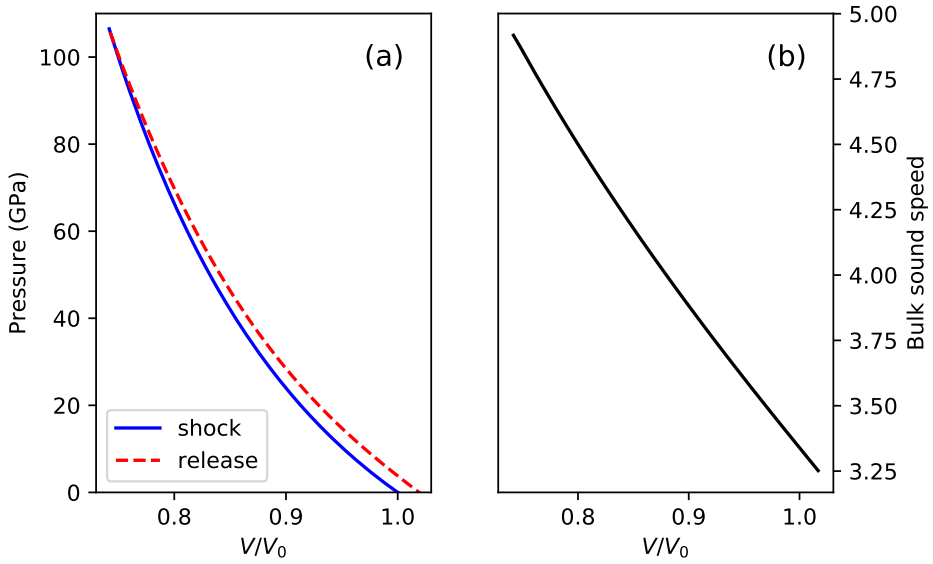


Figure 4.15: a) Hugoniot and release isentrope for shock compression to $V/V_0 = 0.74$ state. Eulerian bulk sound speed estimated from the release isentrope in a) using equation 4.11.

Therefore α strongly depends on the position of the rarefaction wave and weakly on the deformations ϵ_s caused by shocks in the investigated range (up to ~150 GPa).

The assumption of the perfectly hydrostatic response is expected to be a simplification of the complex nature of release dynamics. The non-negligible strength of tantalum would suggest that a certain amount of non-relieved shear stress can be supported. This means that strain profiles along the three principal crystallographic directions may not be identical, which indicates that the release wave model presented in this work describes only an approximate behavior of the bulk of material.

In order to find the bulk sound speed in the shocked material, the Mie-Grüneisen model was assumed. Walsh *et al.* [15] explain that states on Hugoniot and the release isentrope are related in the form of the following differential equation:

$$\frac{dE_H}{dV} = \frac{d}{dV}(\frac{V}{\gamma})(P_H - P_R) + \frac{V}{\gamma}(\frac{dP_H}{dV} - \frac{dP_R}{dV}) \quad , \tag{4.8}$$

where E is internal energy, γ is the Grüneisen parameter, subscript H refers to states on Hugoniot, and subscript R refers to states on release isentrope.

The following relationship holds for two states on Hugoniot:

$$E_H - E_{H0} = \frac{1}{2}(P_H + P_{H0})(V_{H0} - V) \quad , \tag{4.9}$$

where for convenience one of the states is the foot of the Hugoniot - subscript 0.

Combining equations 4.8 and 4.9 we obtain a first order differential equation:

$$\frac{dP_R}{dV}\frac{V}{\gamma} + P_R\frac{d}{dV}\left(\frac{V}{\gamma}\right) - \frac{d}{dV}\left(\frac{V}{\gamma}\right)P_H - \frac{V}{\gamma}\frac{dP_H}{dV} - \frac{1}{2}\left(\frac{dP_H}{dV}(V_{H0}-V) - P_H\right) = 0 \tag{4.10}$$

that can be solved for $P_R(V)$ using basic $\gamma = \gamma_0 V/V_0$ relation for Grüneisen parameter's dependence on the specific volume, where $\gamma_0 = 1.7$ [15]. The analytically-calculated Hugoniot curve and release isentrope are shown in Figure 4.15a.

Finally, the Eulerian bulk sound speed is found (Figure 4.15b):

$$C_{BE} = \sqrt{(\partial P/\partial \rho)_S} \quad . \tag{4.11}$$

where subscript S indicates differentiation at constant entropy.

4.4.4 Strain profile in simulations (MD)

Evolution of the strain profile within the rarefaction wave in molecular dynamics simulations was investigated. Since strain rates within release fan depend on the position of release wave, simulating a material large in size along the shock propagation direction is beneficial. Spatially long simulations enable the study of a wide range of strain rates, which is especially crucial in the context of the comparison of simulations against those experimental findings which involve release waves in micron-scale material. Therefore a long (over a micron-long) simulation of 100 GPa shock and subsequent release was performed. The setup of the simulation was similar to the setup of the previous simulations where the only difference was the increased size of the longitudinal dimension of the simulated box of atoms. The output of the simulation was processed with PADG code which provided strain profiles along x, y, and z directions. Profiles along [100] and $[1\bar{1}0]$ were combined to form the mean transverse strain profile as shown in Figure 4.16a. The strain rate within the rarefaction fan was measured by calculating the derivative of the

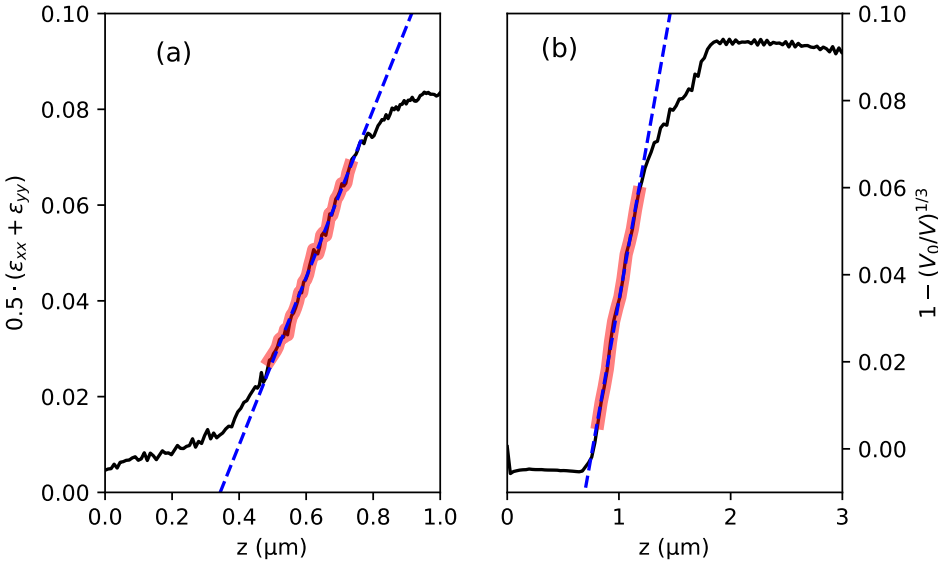


Figure 4.16: a) transverse strain in MD and b) mean strain profiles in HYADES simulations. Red regions refer to the central parts of the rarefaction fan where strain rate analysis was performed. Blue dashed lines represent lines used for tracking the foot of the release wave.

strain with respect the Lagrangian position z between two cutoff values of strain. This method ensured that the measurement was performed over the central part of the release fan where strain profile was linear. The position of the foot of the fan was selected to be the position of the cross-section of the 0 strain axis and a line fitted to central part of the release wave profile.

4.4.5 Strain profile in simulations (HYADES)

Similar investigations of the release profile were performed from the 1D hydrodynamic simulations perspective. One of the main advantages of such simulations over MD is their computational cost, as their purpose is to represent the behaviour of the bulk of the material, and not individual atoms. Therefore hydrodynamic simulations allow us to model the evolution of the target-source (of energy) interaction from the moment when the optical laser is switched on to the moment when the target returns to ambient conditions. In this work 1D hydrodynamic HYADES code [146] was used to simulate a ∼100 GPa shock wave launched into 50 µm of CH and 6

µm of Ta – a simulation reassembling the experimental scenario. HYADES was selected as it offers an easy-to-use interface build with the purpose of experimental design which makes it a popular tool in the shock-compression community. Its primary goal is to capture simple laser-matter interactions without the need of a researcher's full-time commitment to achieve meaningful results, in contrast to other hydrodynamic computational frameworks.

Tantalum as well as CH were modeled using HYADES built-in libraries derived from realistic models, such as LANL SESAME library (the details of the simulation input script can be found in Appendix A). Materials were made of 1-dimensional mesh where calculations were performed on every mesh point to approximate the behaviour of the bulk. In order to accurately simulate the complex nature of the laser-matter interaction at the surface of CH layer, feathering was employed. This technique relies on using fine mesh to simulate material in direct contact with the laser and on the gradual increase in mesh size with the distance from that surface to reduce computational cost of the simulation. The shock strength was controlled by changing the intensity of the light source. To generate $\sim$ 100 GPa shock, an intensity of the order of $\sim$ 1 TW/cm^2 was used. The top-hat shape of the optical laser pulse was simulated by:

- rapidly increasing the intensity of the 527 nm light source within 0.05 ns to the peak intensity;
- keeping the intensity at a constant elevated value for 5ns;
- rapidly reducing the intensity to 0 within 0.05 ns.

In the case of the hydrodynamic simulations, instead of a direct analysis of strain profiles, the density profiles were extracted and converted to the mean strain, as shown in Figure 4.16b. HYADES offers modeling materials without consideration of their strength as well as modeling materials using built-in Steinberg strength model [147]. We found that by introducing a strength model into a simulation, an elastic precursor was observed on release. This is in agreement with the theory

of release waves outlined in Chapter 2. In a similar fashion to the analysis of the strain rate in MD simulations, the gradient of the central part of the release fan that corresponds to the plastic response of material was measured.

4.4.6 Results

The deduced strain profiles as a function of depth and time are shown in Figure 4.17a. Given that the elastic strain that we measure is that transverse to the shock direction, and thus insensitive to any purely elastic longitudinal release, we approximate the strain gradient within the rarefaction fan as a function of the position of the release tail (equation 4.7). As expected, the strain gradient becomes shallower as the rarefaction proceeds. Indeed, our simple model of the propagation of the release wave shows that the rate of reduction of the strain gradient is consistent with the theoretical prediction.

Figure 4.17b shows the evolution of the strain gradient extracted from the data as a function of time, as well as analytic values from equation 4.6 and the prediction of the 1D hydrodynamic and the MD simulations. The four datapoints from MD correspond to release profiles 50, 100, 150, and 200 ps after 100 Gpa shock breakout. Strain profiles from MD simulation were converted to the Lagrangian reference frame by evaluating densities of thin laminae and appropriately scaling the position of the extracted Eulerian strain profiles by a factor ρ/ρ_0. Strain gradient errorbars were estimated using the uncertainty of the calculated derivative of the strain profile within the central part of the rarefaction fan. Release wave position errorbars were calculated using the intersection between the fitted line to the central part of rarefaction fan and $\epsilon = 0$. The gradient of the fitted line was varied according to the variations of the slope derivative which introduced the uncertainty in the position of the wavefront's foot estimation. Good agreement has been found between the experimental data, analytic calculations, and HYADES results. The slightly lower than predicted experimental inverse strain gradient at 3.7 µm is due to the onset of release on the front (driven) side of the Ta foil. By rearranging equation 4.6, for

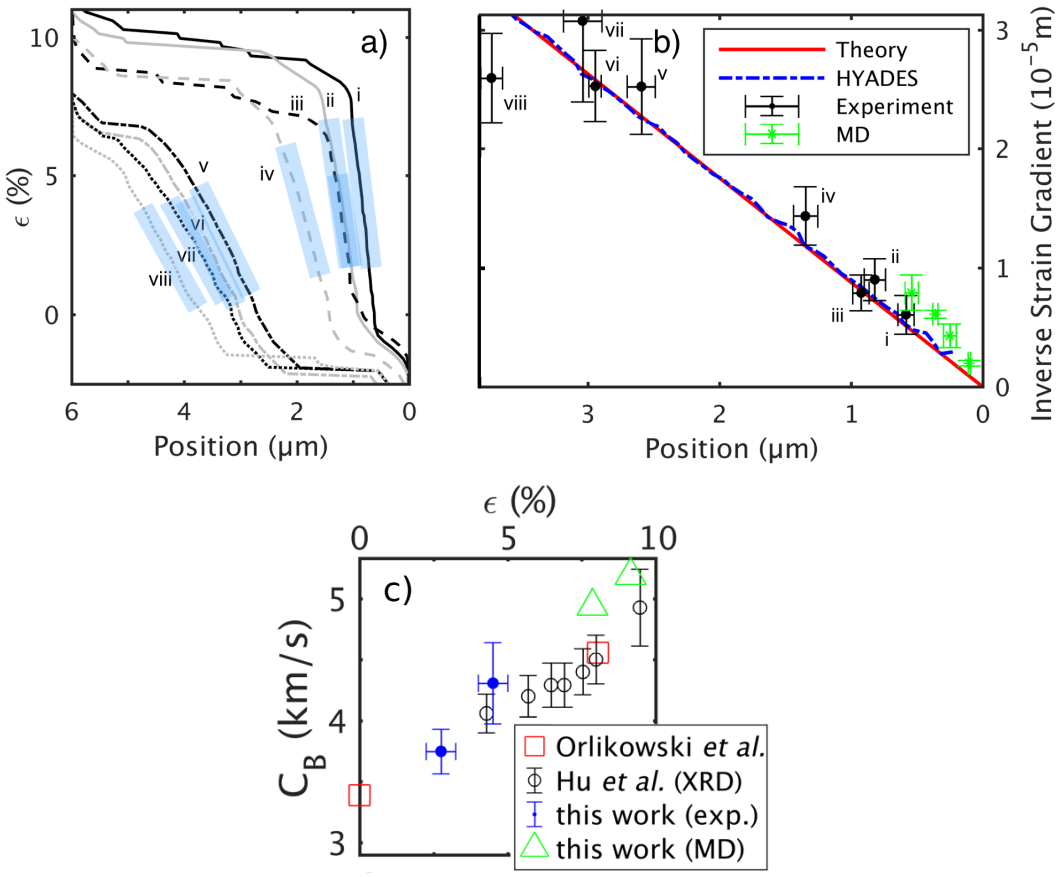


Figure 4.17: a) Extracted transverse strain profiles from the XRD images as a function of the Lagrangian position (default frame of reference of the algorithm's processes) of the sample along the shocked direction with 0 µm and 6 µm referring to the back surface and the polyimide/Ta interface respectively. Selected profiles correspond to samples driven by shocks of 50-100 GPa. b) Inverse strain gradient (from the shaded regions in (a)) as a function of the position of the tail of release wavefront (taken at $\epsilon = 0$). A theoretical prediction (red line), HYADES (blue dashed line) and MD (green asterisks), obtained for the case of 100 GPa shock, are also shown. c) shows inferred bulk sound speed as a function of transverse elastic strain, and compares this with previous data assuming hydrostatic response.

$C_0 = 3293$ m/s [100], bulk sound speed in the shocked state can be estimated:

$$C_{BE} = (\frac{\epsilon_s C_0}{\alpha z} + C_0)\frac{\rho_0}{\rho} = (\frac{\epsilon_s C_0}{\alpha z} + C_0)(1 - \epsilon_s)^3 \tag{4.12}$$

Strain gradient α is evaluated by calculating the mean derivative of the extracted strain profile over the central part of the rarefaction fan as shown in Figure 4.17a) where shaded blue regions correspond to the central 40% of the fan. The location of the wavefront z is evaluated at the intersection of the line fitted to the aforementioned central part of the fan and the line ϵ=0. ϵ_s is selected as the halfway point between ϵ=0 and the top plateau of the profile.

While the MD simulations predict slightly lower strain gradients than those seen experimentally, the finite size of the simulations means that significant elastic-plastic kinetics may still be occurring during the simulation time, and consequently the MD implies slightly larger sound speeds than suggested by the XRD measurement and previous studies [144, 148]. Due to computational limitations shock only within relatively thin layers of Ta can be simulated. Strain rates present within the first few tenths of the material's surface experience higher strain rates than the rest of the sample, which means that the elastic-plastic behaviour of the material near the rear surface may differ from the behaviour of the deeper layers of the crystal during release. The effects of finite shear strain within the rarefaction fan are not taken into account when calculating sound speeds. Therefore, at such short length scales the influence of the non-hydrostatic release effects may be non-negligible. What is clear, however, is that the rate of the reduction of the strain gradient deduced from the diffraction signal is consistent with what was expected.

4.5 Summary

In conclusion, we have performed *in situ* femtosecond XRD studies of the release of shocked fibre-textured polycrystalline tantalum. We observe that the significant lattice rotations imparted by the shock are largely reversed upon shock breakout as the rarefaction wave travels back into the sample. We also observe a complete reversal of the shock-induced twinning. The experimental data are in good agreement

with MD simulations, and this direct observation of the reversal of microstructural changes upon release emphasises the important contribution that such *in situ* studies can make to our understanding of the physics of shock deformation at the lattice level. Additionally, an algorithm which extracts strain profiles from the XRD signal was developed. The results of its output are consistent with both the theory and simulations of release waves.

5

Thermal effects upon shock breakout

Contents

5.1 Introduction 145
5.2 Grüneisen parameter in MD 146
5.3 Elastic release 151
5.4 Heating upon shock breakout (MD) 158
5.5 Heating upon shock breakout (experiment) 163
5.6 Summary 171

This chapter describes a molecular dynamics study of thermal effects during shock release of tantalum. These computational investigations are supported by experimental evidence from the XRD experiment presented in the previous chapters. The standard model of isentropic release is challenged via energy budget, highlighting the importance of plastic heating. Additionally, this chapter contains information about the study of the Grüneisen parameter for various MD potentials, an analysis of thermal effects in purely elastic release, and a description of a method to extract release temperatures from XRD based on the thermal expansion of the metal. It has to be emphasised that significant contributions to the work presented in this chapter were made by P. G. Heighway, who performed the energy budget outlined in section 5.4 and R. E. Rudd, who performed large scale MD simulations. The

majority of the work presented in this chapter forms the core of the publication P. G. Heighway, M. Sliwa *et al.* (forthcoming).

5.1 Introduction

Thermal effects associated with dynamically-compressed materials are a subject of active research. In addition to many theoretical investigations, studies have recently begun to focus on the development of techniques to address the lack of available experimental data. The reason for the insufficient amount of experimental insight is related to the challenges associated with temperature measurements at the short timescale of shock events. Such temperature measurement methods of dynamically-compressed materials as are currently available have various limitations resulting in questionable performance. For example, streaked optical pyrometry (SOP), a method using spectrometer and streak camera to measure the time-dependent black-body radiation from the back of the target to determine temperature, does not provide information about the temperature of the bulk of the material and therefore may not describe a full picture of a material's thermal history. This method is also affected by a limited knowledge of the emissivities of materials. Moreover, SOP primarily works at temperatures of a few eV and above since below that threshold there are not enough photons.

From a theoretical point of view, the standard picture of shock compression describes the discontinuous jump to the Hugoniot state as a highly non-isentropic process significantly increasing a material's temperature. On the other hand, the subsequent release is considered a relatively slow isentropic process. It is believed that during this isentropic expansion, the temperature of the material decreases monotonically with volume due to the thermoelastic effect [149] at a rate governed by γ, the Grüneisen parameter [150]. According to this description, a sample shock-compressed to a pressure of the order of few megabar is expected to cool by several hundred degrees as it returns to ambient conditions during unloading.

Strain rates present within the rarefaction fan are indeed considerably lower than those experienced by the material at the shock front, and continue to reduce

as the release wave travels back into the bulk of the solid. However, the above picture of isentropic expansion does not take into account the amplitude of strain rates during strong shock unloading, which can exceed 10^9 s^{-1} within the first few microns of deformation, as shown in the previous chapter. Molecular dynamics [54, 151, 152] and laser-compression [35, 153, 154] studies have shown that during high strain rate plastic deformation ($\dot{\epsilon}$>10^7 s^{-1}), materials exhibit strength of the order of a few gigapascals. Therefore, because of its significant strength, a solid will not only experience heating due to plastic deformation during the initial compression, but also during release. Plastic-work heating has been previously shown by Swift *et. al.* [155] to have a considerable influence on a material's temperature by opposing the isentropic cooling due to volumetric expansion and considerably modifying a material's thermal history.

Additionally, the standard picture of isentropic expansion ignores the process of converting work into energy that is stored in defect-mediating plastic flow during shock compression. It is believed that in order to accommodate extreme plastic strain rates, shocks generate large amounts of dislocation. As shown in the previous chapter, these large defect densities can be partially annihilated upon release. It is estimated that the energy stored in the defect network constitutes 5-15% of the total plastic work performed on compression [60, 156–159]; therefore the process of recovering this energy needs to be considered. That is to say the dislocation annihilation process upon release may also contribute to the heating of the solid, further deviating the release path from the isentrope.

5.2 Grüneisen parameter in MD

The key to understanding thermal effects in solids is the Grüneisen parameter γ. It describes the change in the vibrational properties of a crystal as a result of variations in the volume of the lattice. The Grüneisen parameter is defined as:

$$\gamma = V\left(\frac{\partial P}{\partial E}\right)_V \quad , \tag{5.1}$$

where E is the internal energy of the crystal.

Walsh *et al.* [15] provide the experimentally-measured γ in Ta as a function of volumetric compression determined by using velocimetric techniques on explosively-driven samples. In order to select a potential for our molecular dynamics simulations, the performance of a few of them was tested in terms of Grüneisen parameter estimation. Investigated potentials were designed with various purposes and some of them were not designed with the purpose of high pressure research at 1 Mbar. Therefore the aim of the following study is not to understand the physics of simulated environments of the individual potentials, but to quickly identify candidates for further study. The experimental results published by Walsh *et al.* were used as benchmark for this selection process. It is known that the two EAM potentials developed by Ravelo [55] (Ta1 and Ta2) fail to capture the thermal properties of tantalum at ambient conditions by underestimating the Grüneisen parameter by 61% (Ta1) and 37% (Ta2). This discrepancy could mean that, at first glance, both potentials underestimate the amount of cooling during shock release, artificially increasing the temperature of the released material and negatively affecting the potential's performance with respect to the experimental data. However in order to fully evaluate the accuracy of the cooling rate given by the potentials, it is necessary to estimate the Grüneisen parameter in a compressed material.

Six potentials were examined: Zhou [161], Pun [162], Gao [163], Li [164], Ravelo Ta1 and Ta2 [55]. A number of small (20×20×20 atomic spacings) single-crystal simulations with periodic boundary conditions in x, y, and z directions were performed. Various amounts of hydrostatic compression were applied to the simulation boxes ranging from V/V_0=1 to 0.8. Upon initialization of the simulation box, the energy of the system is not partitioned between potential and kinetic energies, and all the energy is stored in form of kinetic energy. Therefore, each simulation box was equilibrated for 5 ps in order to allow the system to reach a stable state at a target temperature equal to half the initialization temperature with precision up to 1%. After that time, the average pressure and internal energy were estimated based on the 5 ps window. Two simulations of crystals at the same amount of volumetric compression, performed at temperatures different

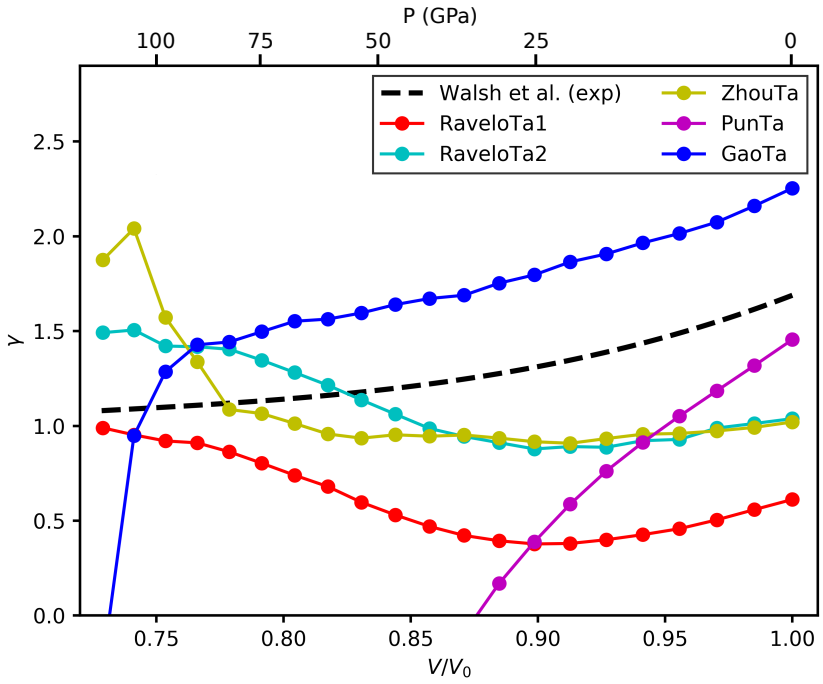


Figure 5.1: Comparison of the Grüneisen parameter dependence on the amount of hydrostatic compression for various MD potentials. All measurements were performed for the theoretical temperatures at the corresponding volumetric compressions on Hugoniot. This means that for a set volumetric compression, the temperature of the material was adjusted appropriately to simulate a state on the Hugoniot curve. This was done using SESAME EOS 3520 [160] (blue curve in Figure 5.17). The black dashed curve refers to the experimental result [15].

by 50 K, were compared. The Grüneisen parameter was estimated from the differences in the obtained pressures and internal energies between these simulations. Figure 5.1 shows a comparison between the Grüneisen parameter as a function of volumetric compressions for the investigated potentials and the experimental benchmark (experimental data [15] used for evaluating the simulations). The simulations represented the Grüneisen parameter estimation on the Hugoniot, which means that they were performed at theoretically-predicted temperatures in a shocked state for corresponding amounts of volumetric compression.

The obtained results are subject to a few caveats. Firstly, the fit to the experimental data was constructed by using shock data reaching only $V/V_0 = 0.82$. Therefore, the part of the curve plotted at higher pressures ($V/V_0 < 0.82$) was a low-order polynomial extrapolation. Secondly, the $\gamma(V/V_0)$ curve based

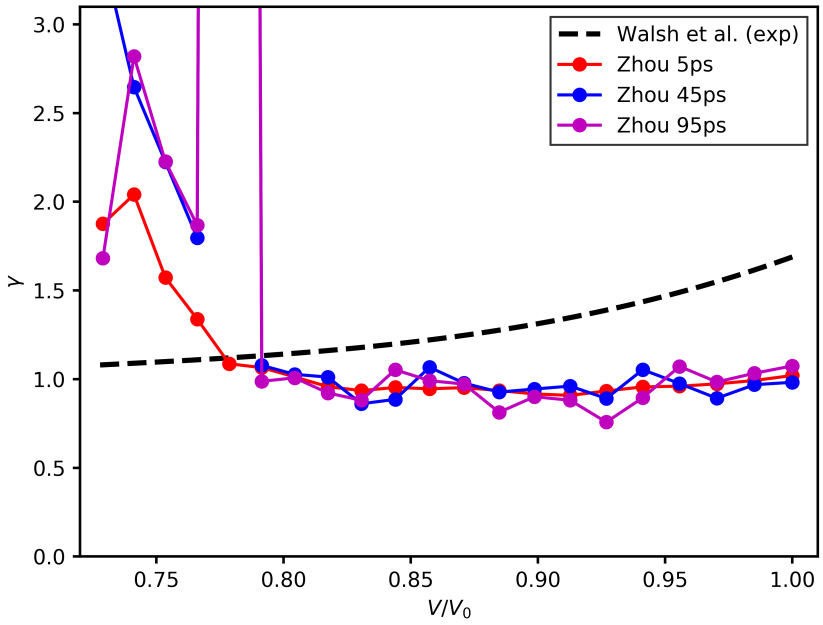


Figure 5.2: Comparison of the Grüneisen parameter, extracted from MD simulations based on the Zhou potential, estimated after various periods of equilibration.

on the potential provided by Li *et al.* was excluded from Figure 5.1 for clarity, given the large variations in its profile. Finally, it was found that the potential by Zhou *et al.* displayed large variations in the $\gamma(V/V_0)$ profile below V/V_0=0.8 that were time-dependent as shown in Figure 5.2. This may indicate the appearance of the unstable crystal in non-equilibrium state simulated by the potential at those high-pressure conditions.

Basic models of γ predict its monotonic dependence on V/V_0, where the Grüneisen parameter decreases with the amount of compression. This effect can be observed in the experimental curve provided by Walsh in Figure 5.1. Despite an initial reduction in magnitude at low compressions, the γ parameter, given by Ravelo Ta2, increases for states towards 100 GPa (V/V_0=0.75). It can be noticed that while the Grüneisen parameter provided by Ravelo Ta2 is underestimated at ambient conditions, it is overestimated at high pressure states. The overall thermoelastic cooling effect for release from 100 GPa shocked state can be calculated according to the following expression:

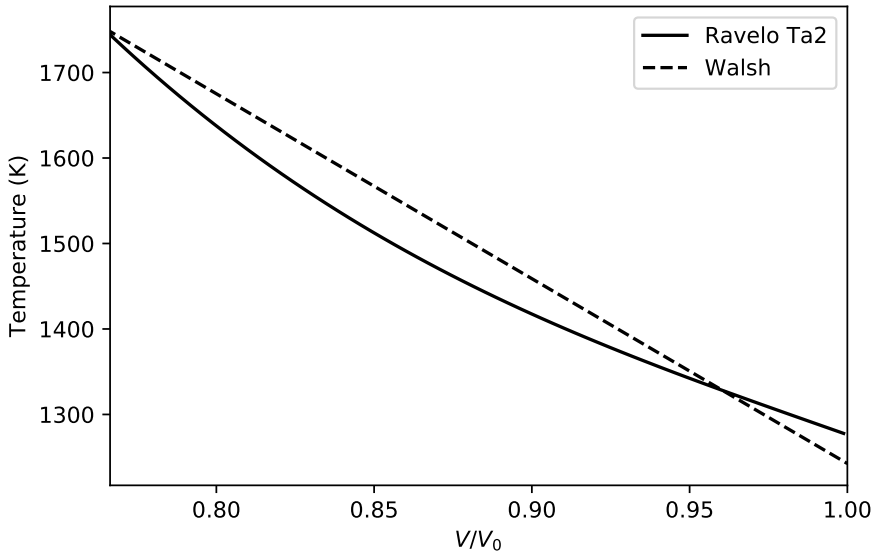


Figure 5.3: Release paths from the 100 GPa shock state to ambient volume V_0 according to the integration of the cooling rate given by formula 5.2.

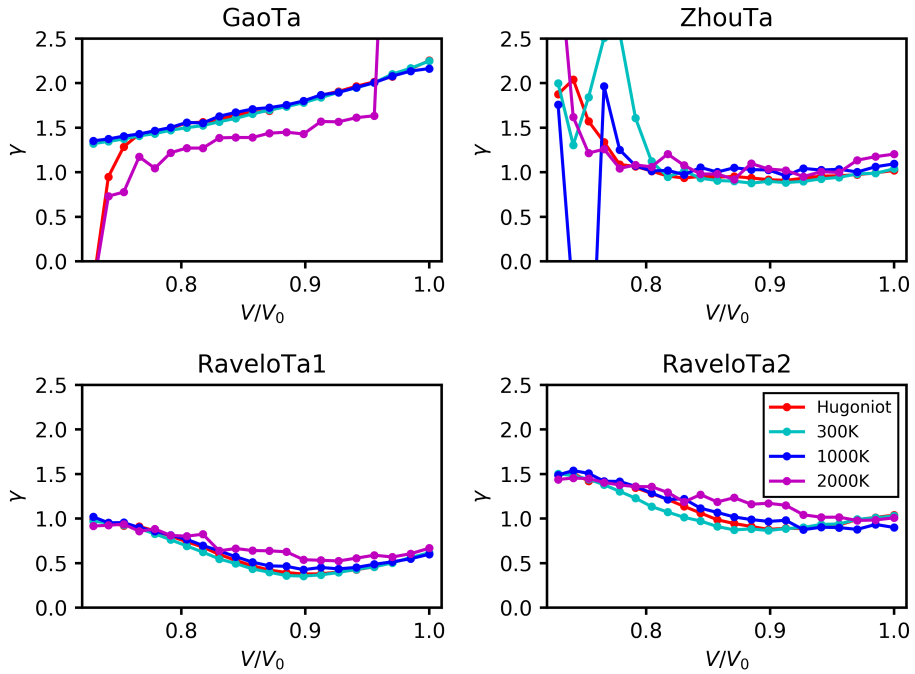


Figure 5.4: Grüneisen parameter dependence on volumetric compression for constant temperatures: 300K, 1000K, and 2000K; as well as temperatures along the Hugoniot. Large instabilities in ZhouTa potential at high pressure can be associated with the time-dependence of the measurement, potentially suggesting non-equilibrium state at the investigated conditions.

$$\frac{dT}{T} = -\gamma(V,T)\frac{dV}{V} \quad , \tag{5.2}$$

where T is the temperature of the of the material. It turns out that the pressure dependence of γ for Ravelo Ta2 is such that the total amount of cooling it predicts for a release from around a megabar differs only by a small margin (about 40 K) with respect to release temperature calculations based on the experimentally-measured γ (Figure 5.3). The reason for this is the balancing effect between the mismatched Grüneisen parameter at low and high compression states, which produces similar cooling rates for both curves. It is important to point out the Grüneisen parameter dependence on the amount of volumetric compression is evaluated on Hugoniot states, while the cooling factor analysis is performed on a release isentrope. Therefore, the temperature influence on γ needs to be considered. It has been shown that this relation is much weaker than the volume dependence [165, 166]. Tests on a few examined potentials were performed in order to establish the effect of various temperatures on the γ parameter estimation. The results, shown in Figure 5.4, indeed indicate a weak temperature dependence on the value of γ for Ravelo Ta2. Therefore, we can conclude that the amount of thermoelastic cooling predicted by the molecular dynamics simulations at megabar pressure provides a reasonable description of this effect.

5.3 Elastic release

Release from a shocked state is a combination of the initial uniaxial elastic release followed by elasto-plastic deformation. Good understanding of the thermal effects due to purely elastic compression is required before proceeding to analyse the influence of plasticity on the material's temperature. An example of free elastic deformation is considered in the context of the theory of isentropic expansion given by 5.2.

A block of single crystal tantalum (50×50 atomic lattice spacings cross section) was compressed uniaxially along [110] direction by 10%. The amount of compression, which did not exceed this number, ensured that the crystal remained in a defect-free form by not allowing it to flow plastically. After 4 ps of equilibration in a

compressed state, the periodic boundary conditions preventing the material from releasing along the compression direction were changed to non-periodic conditions. One of the sides of the crystal was turned into a 'frozen' piston. This meant that only one rarefaction wave penetrated the material, which prevented information duplication and allowed for the analysis of larger timescales limited by the amount of releasable material. The simulation box contained a few thin sheets of atoms providing information about their properties every 0.1 ps. These atomic slices were selected at various distances from the releasing free surface, which allowed for the analysis of unloading at various strain rates.

Since the block of atoms experienced a collective motion along the z-direction (direction of release), the temperature of the material was estimated using two transverse components of the particle's velocity (v_x, v_y):

$$T = \frac{m}{2k_B}(v_x^2 + v_y^2) \quad , \tag{5.3}$$

where k_B is the Boltzmann constant, m is the mass of the tantalum atom and a factor of 3/2 normalises the temperature measurement over three degrees of freedom.

Figure 5.5 depicts a thermal history of two atomic slices, 55 nm and 440 nm from the releasing end of the crystal. The first one unloaded within just 3 ps (due to its close proximity to the free surface and therefore high strain rate), while the second one released over the course of 20 ps. Both parts, with the same initial temperature of 321 K, did not experience any plastic flow and their final hydrostatic states have the same lattice spacing.

Since thermo-elastic cooling was the only factor affecting the temperature of the atomic layers, according to equation 5.2, their temperature drops might have been expected to be identical. However, this was not the case. Slower release resulted in a temperature reduction larger than 2 K in comparison to the release near the free surface. Therefore, it is important to understand whether these temperature profiles follow the theory of isentropic expansion given by formula 5.2.

In the above scenario of uniaxial elastic release, material expands non-isotropically. This means that the extracted Grüneisen parameter as a function of volumetric

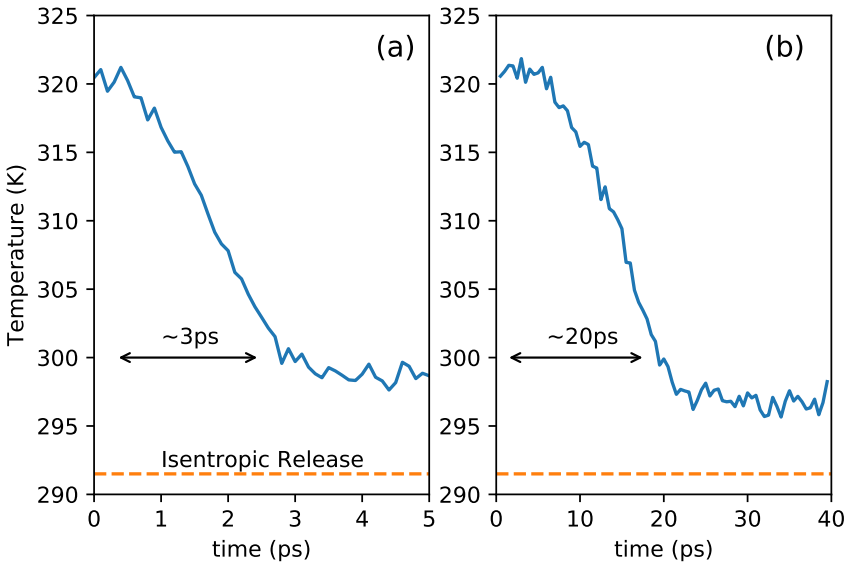


Figure 5.5: Temperature histories of the elements located 55 nm (a) and 440 nm (b) from the free surface during purely elastic release. Temperature of 292 K (orange dashed line) represents the analytically-estimated release temperature from the given initial condition under the assumption of isentropic expansion.

compression is not a relevant quantity to consider since it is estimated under the assumption that the deformation is hydrostatic. The direction-specific version of equation 5.2 reads:

$$\frac{dT}{T} = -\gamma_{ii}(V,T)\frac{dV}{V} \quad , \tag{5.4}$$

where γ_{ii} is the component of the Grüneisen parameter tensor describing the thermoelastic properties due to uniaxial deformation along the i direction.

Specific components of Grüneisen parameter tensor (γ_{xx}, γ_{yy}, and γ_{zz}) are estimated in a fashion similar to previous hydrostatic Grüneisen parameter studies in MD. The main modification is the consideration of specific components of the stress tensor σ_{ii} rather than the hydrostatic pressure:

$$\gamma_{ii} = V\left(\frac{\partial \sigma_{ii}}{\partial E}\right)_V \quad . \tag{5.5}$$

Two kinds of compression were investigated: hydrostatic deformation and uniaxial deformation along [110] (z-direction). The results of this analysis are shown in Figure 5.6. It can be noticed that during hydrostatic compression all Grüneisen

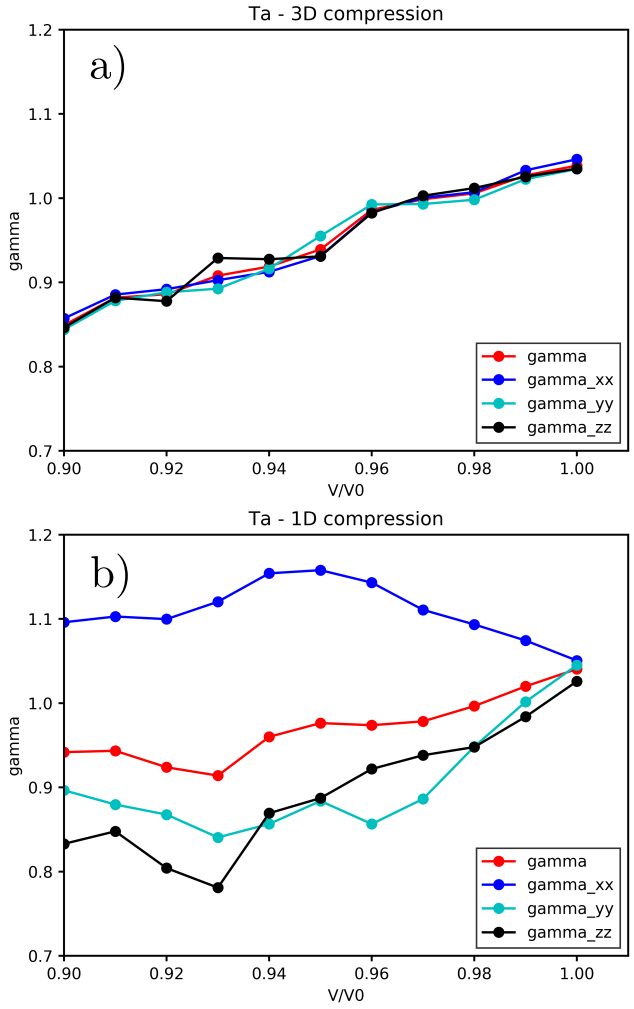


Figure 5.6: γ_{xx}, γ_{yy}, γ_{zz}, and γ as a function of volumetric compression in the case of: a) isotropic compression, and b) uniaxial compression along [110] direction. x, y, and z refer to directions [001], [1$\bar{1}$0], and [110], respectively.

parameter components varied in a similar way as a function of the amount of volumetric compression, while clear deviations from a uniform trend were present during uniaxial compression. Significantly different behaviour of γ_{xx} curve could be explained by the difference in the properties of the material along directions with different atomic spacing during uniaxial compression (atomic spacing along [001] is smaller than the spacing along the other two principal directions).

PADG analysis provided the history of the longitudinal strain in lamine experiencing free expansion, and confirmed the lack of residual transverse elastic strains in a fully-released state. Using equation 5.4, direction-specific Grüneisen

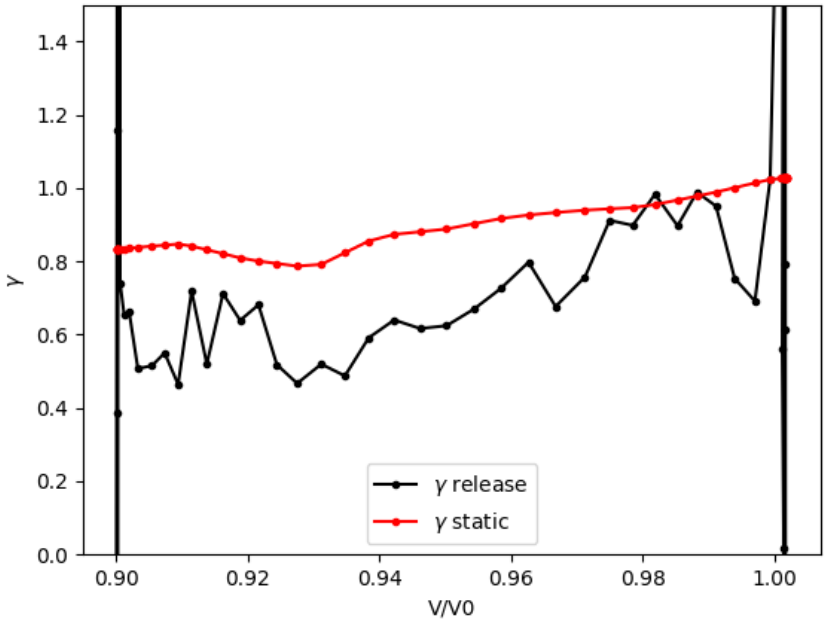


Figure 5.7: A component of the Grüneisen parameter along the z-direction as a function of volumetric uniaxial compression along [110] at ∼300 K. The red curve corresponds to the γ_{zz} extracted from static simulations, while the black curve corresponds to the γ_{zz} extracted from dynamic simulations.

parameter components, and the strain history of tantalum during elastic expansion, the theoretical value of the final temperature in the fully-released sample was estimated via integration of equation 5.4 along the release wavefront. It was found that the material releasing from 10% uniaxial compression state at 321 K should reach a final temperature of 292 K. This meant that the temperature drop in different parts of the crystal during unloading at two different strain rates was significantly smaller than the temperature change estimated using the extracted Grüneisen parameter and formula 5.4. The simulations were designed in such a way that the potential energy of the elastically-compressed lattice was converted into the kinetic energy of the atoms with no external sources of energy. Therefore, the origin of this discrepancy was not identified and remains a subject for further studies.

The Grüneisen parameter extracted via comparison of statically-held boxes of atoms at different temperatures was compared against the Grüneisen parameter extracted directly from dynamic simulations. The latter was evaluated using

equation 5.4 in the following form:

$$\gamma_{zz}(\frac{V[i+1]+V[i]}{2}) = -\frac{V[i+1]+V[i]}{T[i+1]+T[i]} \cdot \frac{T[i+1]-T[i]}{V[i+1]-V[i]} \quad , \tag{5.6}$$

where $V[i]$ is the volume and $T[i]$ is the temperature of the sample at timestep i.

One problem associated with the above approach is a relatively large amount of step-to-step random noise in the temperature profile which conversely introduces large variations in the estimated Grüneisen parameter. This noise is related to the finite number of atoms used for the calculation of the average temperature within a thin slab of atoms around a certain longitudinal position. Firstly, even in the equilibrium state, neighbouring atoms interact with each other exchanging energy which leads to small temperature fluctuations across the sample. Secondly, temperature calculation relies only on velocities along transverse directions; therefore, inferred temperature per atom is not exact. This noise can be reduced by increasing the transverse size of the simulation box, which increases the computational cost. Another method that minimises this effect is the application of a low-pass filter which effectively smooths out the investigated time series. A Savitzky-Golay [167] filtering approach was employed in order to remove 'noisy' features from temperature profiles. The method relies on fitting a low-order polynomial to a time series within a window around an evaluated datapoint. Applying a moving window approach created a new, smooth profile based on the outcome of multiple fits. This profile was then used as an input for a Grüneisen parameter estimation according to equation 5.6. Results of this analysis performed on the lamina 440 nm behind the free surface are shown in Figure 5.7. Large variations at the edges of the analysed spectrum ($\frac{V}{V_0}$= 0.9 and 1.0) were observed. These are an artificial effect arising due to the method of Grüneisen parameter calculation. Any small variations in temperature or strain in a fully-compressed or fully-released material result in large variations in the estimate of γ_{zz}. It can be noticed that for a majority of the investigated volumetric range, the Grüneisen parameter extracted from dynamic simulations was significantly underestimated with respect to the static simulations.

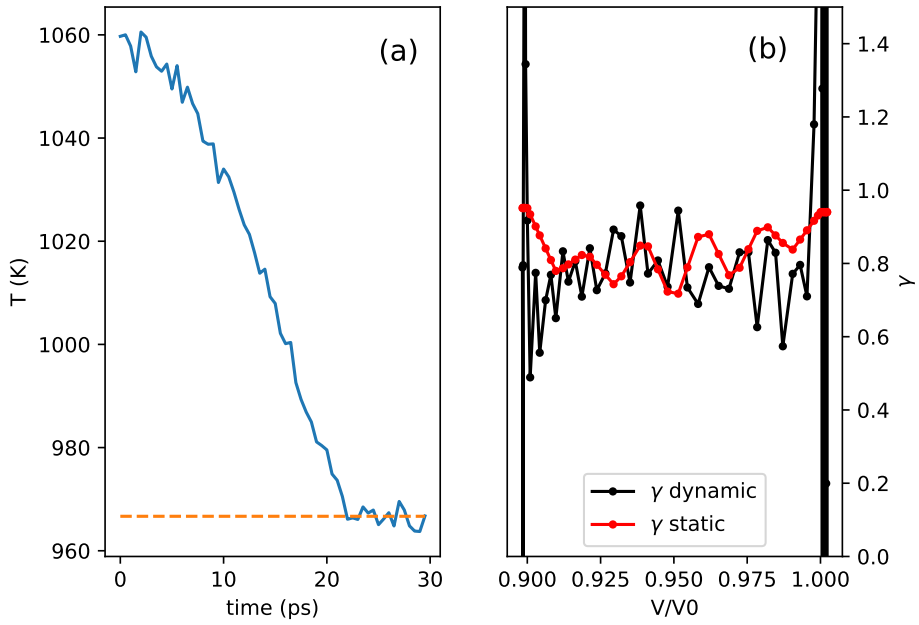


Figure 5.8: (a) The temperature history of the element located 440 nm from the free surface during purely elastic release. The temperature of 967 K (orange dashed line) represents the analytically-estimated release temperature from the given initial conditions under the assumption of isentropic expansion. (b) A component of the Grüneisen parameter along z-direction as a function of volumetric uniaxial compression along [110] at ∼1000 K. The red curve corresponds to the γ_{zz} extracted from static simulations, while black curve corresponds to the γ_{zz} extracted from dynamic simulations.

The final test associated with the analysis of the elastic release focused on the influence of the initial temperature on the thermal release path. An 'elastic release' simulation at the elevated temperature of 1060 K was investigated. Figure 5.8a presents the temperature evolution of the element 440 nm behind the free surface. In this case, the final temperature matched the expected analytical calculation (marked with a dashed orange line). Figure 5.8b reveals a close match between the Grüneisen parameter extracted from static and dynamic simulations, in contrast to simulations at 300 K.

To sum up the findings of the above analysis of the 'free elastic release' MD simulations, we notice that the timescale of the deformation as well as the initial temperature of the material affect the final temperature deviation from the analytical calculations based on an isentropic expansion model and Grüneisen parameter

extracted from static simulations. Larger release timescales as well as higher temperatures lead to a better match between the results of the simulations and theoretical calculations. After unloading, lasting only a few ps, material remains at the elevated temperature in comparison to the temperature calculated using the isentropic expansion model. This indicates that once the material unloads it reaches equilibrium state, and the temperature discrepancy can be associated with the deformation itself. This observation suggests that perhaps purely elastic release may not be classified, under certain conditions, as an isentropic expansion. It may be that in the case of a real material this phenomenon could be explained by comparing the short timescale of the deformation ($\dot{\epsilon} > 10^{11}\mathrm{s}^{-1}$) with the timescale of the fastest phonons in the sample. However, molecular dynamics simulations are governed by the laws of classical mechanics, which means that such reasoning is inapplicable, leaving this puzzling phenomenon a subject for future work.

5.4 Heating upon shock breakout (MD)

In order to investigate thermal effects during release following a shock, large-scale MD simulations were performed. The analysed setup corresponded to the one described in Chapter 4, where a moving piston drove a 100 GPa shock wave, which upon the breakout from the free surface was followed by a rarefaction wave. Atomic behaviour was modelled using the Ravelo EAM Ta2 potential, due to its representative description of the thermoelastic cooling, as discussed in the proceeding sections. This study concentrated on the analysis of a thin (10 nm thick) Lagrangian element at the distance of 0.2 µm from the free surface.

The atomic positions within this element were processed with PADG code to obtain a deformation tensor describing the lattice. By performing this analysis on the dump files generated every 0.5 ps, a history of the elastic strains along three main axis (ϵ^e_{xx}, ϵ^e_{yy}, and ϵ^e_{zz}) was created, as shown in Figure 5.9. We distinguished four distinct regions marked with letters A, S, E, and P. Initially, the element remained at ambient conditions (A), which corresponded to a lack of elastic deformation. Then, at about 185 ps, shock (S) reached the element – this stage was characterised

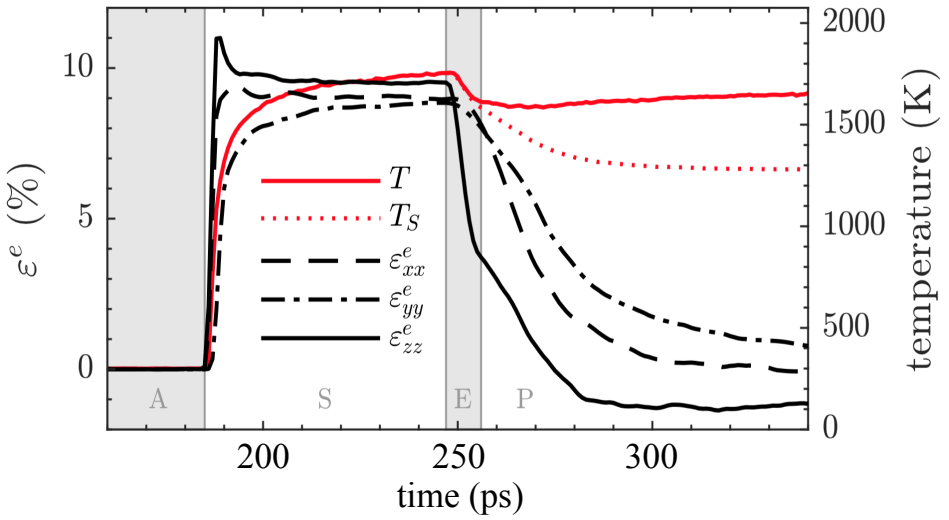


Figure 5.9: Time-evolution of the strain ϵ^e and temperature T characterising a Lagrangian element situated 0.2 μm behind the surface in a piston-driven simulation. T_S refers to the modelled temperature along the isentropic release path from the shocked state.

by a sharp discontinuity in the longitudinal strain. The element remained under compression for 62 ps. During this time the material relaxed to an almost a hydrostatic state: the shear stress was reduced to a value of 0.9 GPa, and the shear strain to a value of 0.3%. At 247 ps the unloading due to elastic precursor (E) at the front of the release wave began. Both transverse strains ϵ^e_{xx} and ϵ^e_{yy} remained mostly unchanged while the longitudinal strain ϵ^e_{zz} displayed a reduction in magnitude from 9.5% to 4.4%. Once the shear strain during the elastic portion of release reached 2.1%, material started deforming plastically (P). This plastic response continued until the material reached ambient conditions.

Apart from elastic strain, Figure 5.9 shows the evolution of the temperature throughout the entire event (red curve). The initial temperature of 300 K refers to the temperature at ambient conditions. The arrival of the shock wave rapidly heated up the sample, which reached 1750 K in a fully-relaxed shocked state. This is consistent with the idea of a large thermal jump onto a state on a Hugoniot curve. Once the elastic portion of the release wave approached the element, the temperature of the material started decreasing. Since plastic relaxation during this state was minimal, the temperature drop can be purely associated with thermoelastic cooling.

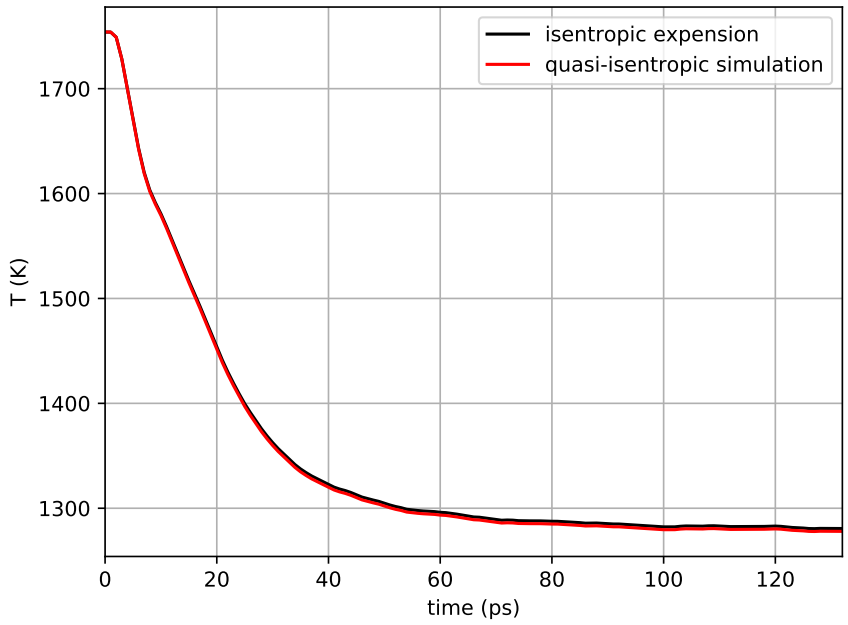


Figure 5.10: Temperature of a defect-free crystal experiencing manually-varied elastic deformation corresponding to release from 100 GPa shock (red) and temperature theoretically calculated according to heat equation 5.7 (black).

Thermal behaviour is compared against the theoretical reduction in temperature due to the elastic expansion of the unit cell [168]:

$$\frac{dT_{\text{elastic}}}{dt} = T\gamma : \frac{d\epsilon^e}{dt} \quad . \tag{5.7}$$

With $\gamma \approx 1.5$ at 100 GPa, according to equation 5.7, the integration of the temperature decrease suggests a temperature drop of 130 K within the elastic portion of the rarefaction fan. This number matches the temperature output of the simulations, indicating cooling due to isentropic expansion. Inspecting the history of the temperature (T) and the history of the temperature under the assumption of isentropic cooling from a shocked state (T_S), a clear observation regarding their agreement can be made. As soon as the material started flowing plastically on release, T and T_S diverged, with the sample reaching a temperature over 300 K larger than the expected output in the case of purely isentropic deformation. It is clear that additional heating effects associated with plasticity on release took place.

In the preceding sections, the effects of elastic uniaxial release in Ta were discussed. The initial unloading in a shock-release scenario happens uniaxially, which can be directly associated with the study of uniaxial elastic release. However, the elastic deformation of the unit cell during plastic release cannot be treated as a one-dimensional expansion. To confirm that the T_s of a sample experiencing the elastic strain history described by the ϵ^e_{xx}, ϵ^e_{yy}, and ϵ^e_{zz} curves on release in Figure 5.9 indeed matches the results of the purely elastic MD simulation, the approach proposed by Ravelo *et al.* [169] was used. A small block of undefective atoms at 1750 K with fully-periodic boundary conditions was simulated subject to manual deformations corresponding to elastic deformations from a 100 GPa shocked state (as described above) to ambient conditions. The size of the simulation box was varied according to pre-designed strain profiles, where the positions of the atoms were remapped via an affine transformation. To prevent the artificial heating associated with external forces controlling the deformation of the material, the equations of motion of every atom were modified in the following way:

$$\dot{r}_{ii} = \frac{p_{ii}}{m} + \dot{\epsilon}_{ii} r_{ii} \quad , \tag{5.8}$$

$$\dot{p}_{ii} = F_{ii} - \dot{\epsilon}_{ii} \quad , \tag{5.9}$$

where subscripts ii refer to direction along the principal axis ($ii = xx$, yy, and zz), r is the position, p is the momentum, F is the overall force acting on the atom, and $\dot{\epsilon}$ is the strain rate varied according to the provided strain profiles. The temperature evolution extracted from the quasi-isentropic simulation was compared against the theoretically-calculated temperature, which obeys the heat equation 5.7. The Grüneisen parameter at various intermediate temperatures was selected by linear interpolation of hydrostatic γ parameters measured at 1000 K and 2000 K. The results of this analysis are shown in Figure 5.10. It was noticed that the temperature in a quasi-isentropic release simulation closely followed the theoretically-predicted thermal evolution of the material.

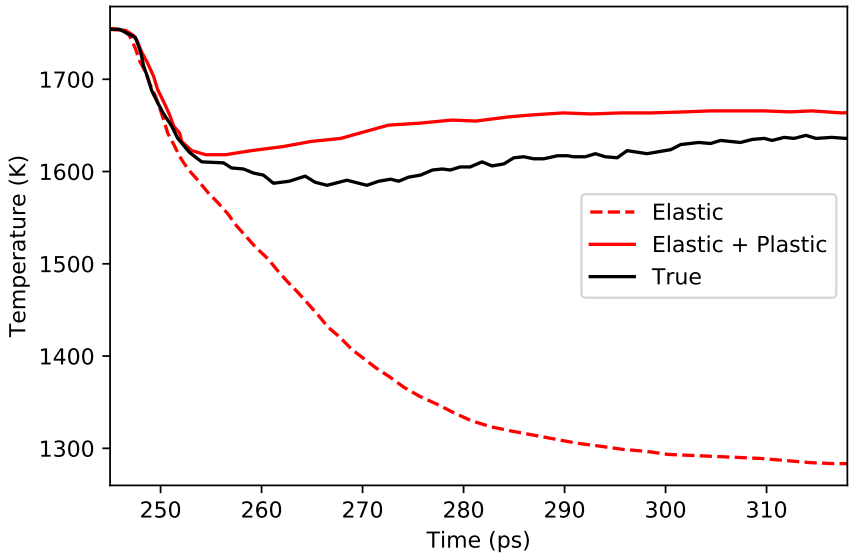


Figure 5.11: Evolution of the temperature in a material during release from a 100 GPa shock in MD simulation (black). Solid and dashed red curves correspond to a theoretical response using elastic and elasto-plastic models, respectively.

Having a good understanding of the thermal effects associated with elastic release, additional sources of heating during the plastic response within the rarefaction fan were examined. The heating rate due to plastic deformation is expressed as:

$$\frac{dT_{\text{plastic}}}{dt} = \frac{1}{c_V}\sigma : \frac{d\epsilon^p}{dt} \tag{5.10}$$

where c_V is the volumetric heat capacity, σ is the Cauchy stress tensor, and ϵ^p is the plastic strain. As shown in Figure 5.11, a temperature model incorporating thermoelastic cooling and heating due to plastic work provides a reasonable agreement with the true temperature curve. This indicates that the vast majority of energy counteracting thermoelastic cooling is a result of high shear stress present in a material during unloading. A discrepancy between profiles can be associated with secondary effects, e.g. microstructure evolution and energy recovery from dislocation annihilation.

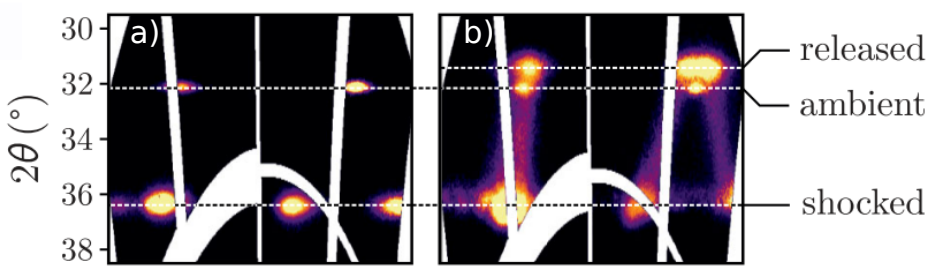


Figure 5.12: {011} diffraction peaks from Ta sample loaded to 130 GPa before (a) and after breakout (b).

5.5 Heating upon shock breakout (experiment)

The analysis of the location of the x-ray diffraction signal corresponding to the material in a fully-released state was performed. It was found that the positions of that signal were shifted towards lower 2θ angles with respect to the position of the x-ray halo spots (Figure 5.12). This observation indicates that the fully-released material is in an underdensed state compared to the material prior to compression. It is known that once the release waves from the rear surface and front surface (the release wave launched at the moment of driving pulse termination) meet within a sample, a tensile wave is formed leading to a spall formation. As it has been previously shown [170], void nucleation is a process producing a large amount of heat and therefore leading to a significant increase in a material's temperature. The time Δt at which the x-rays scatter from the target relative to the breakout time was monitored using a streak camera recording the VISAR signal. This was possible since the x-ray probe timing was synchronized with the VISAR system, which meant that $t_{X\text{-}ray}$ shown in Figure 3.9 was controllable and the VISAR streak image was used to evaluate the position of $t_{breakout}$ (to study shock release $t_{X\text{-}ray} > t_{breakout}$). The uncertainty of the breakout timing measurement (and therefore Δt) was 0.2ns - the number associated with the uncertainty of the shock front location extracted from the VISAR signal. To exclude effects associated with the arrival of the release wave from the front surface and to exclude the effect of thermal diffusion with a timescale larger than 10 ns, only 'early' release data, where $\Delta t < 1$ ns, were considered. Figure 5.13 shows three stages of pressure profile evolution during

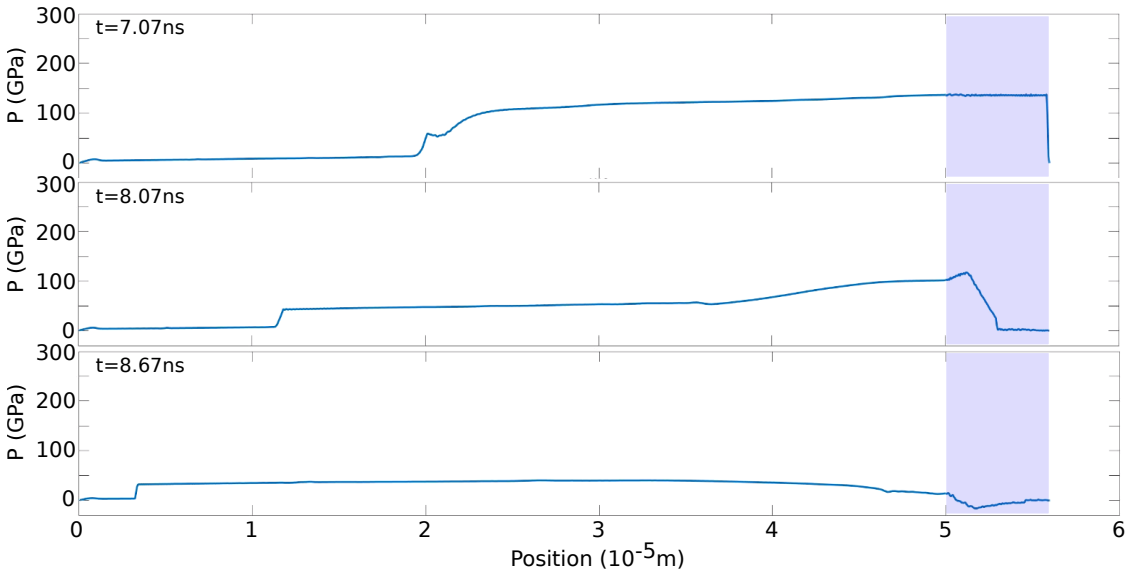


Figure 5.13: Three stages of pressure profile evolution during release from 140 GPa state in HYADES: at the shock breakout, 1ns after the breakout, and 1.6ns after the breakout. The shaded region corresponds to the Ta layer.

release from 140 GPa state in HYADES. It can be noticed that 1ns after shock breakout, the front release wave (propagating through the ablator) is about to reach the Ta layer and 1.6ns after shock breakout, the Ta is put into tension. Therefore, the volumetric expansion observed relative to the ambient state can be interpreted as a pure thermal expansion due to the shock and elasto-plastic effects from the first release wave. This meant it was possible to infer the temperature of the Ta sample as a function of tensile strain, given the knowledge of the thermal expansion coefficient of tantalum. The rest of this chapter details this procedure.

It was identified that some shots suffered a pressure reduction (up to ∼15 GPa) in the shocked part of the sample on release in comparison to the shocked part of the sample during the initial passage of the shock wave. This was due to the expansion of the plasma's critical surface at the front of the ablator, which decreased the amount of energy transfer into the acoustic wave in the target over time. An example of a VISAR trace from such a shot is shown in Figure 5.14. Available VISAR streak images were used to evaluate the shock's strength instead of the crystal's volumetric changes observed in XRD images. For each VISAR fringe image, three pressure measurements were made using velocity profiles constructed with

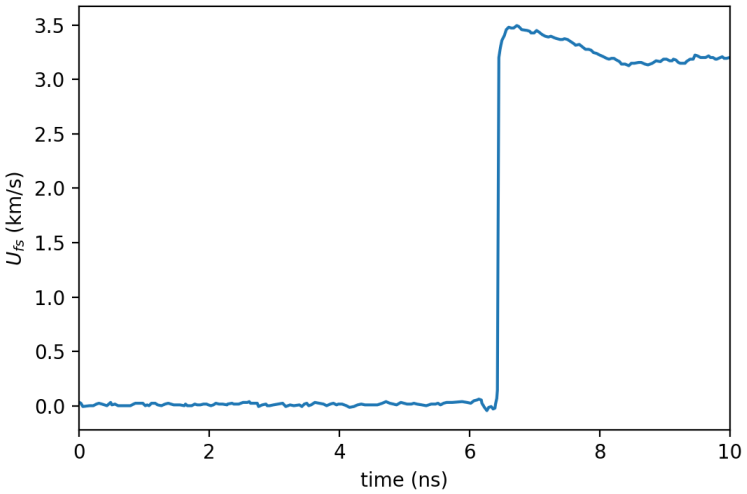


Figure 5.14: VISAR trace of the rear surface velocity profile displaying a slow reduction in pressure right after reaching peak ∼150GPa state.

three different regions across the shock wavefront (six measurements per shot were made since two VISAR beds were used). The VISAR laser was used to probe the surface of the Ta foil directly (no window). It was approximated that the release adiabat is similar to Hugoniot in the particle velocity-pressure space, which meant that $2U_p \approx U_{fs}$ [171]. The extracted particle velocity was converted to pressure using known EOS [100]. The error in the extracted mean pressure was evaluated using standard deviation of six measurements made for every shot.

It was noticed that even at relatively long timescales of hundreds of picoseconds, a small amount of shear strain (∼0.5%) was present in the released material in MD. This means that the effect of non-isotropic expansion needs to be considered while extracting the temperature from the volumetric expansion of the material, leading to the idea of 'free' strain – a combination of elastic coefficients and longitudinal and transverse strains. In the case of isotropic expansion, the following relation holds:

$$\begin{pmatrix} \sigma_0 \\ \sigma_0 \\ \sigma_0 \end{pmatrix} = \begin{pmatrix} C_{11} & C_{12} & C_{12} \\ C_{12} & C_{11} & C_{12} \\ C_{12} & C_{12} & C_{11} \end{pmatrix} \cdot \begin{pmatrix} \epsilon_0 \\ \epsilon_0 \\ \epsilon_0 \end{pmatrix} \quad , \tag{5.11}$$

where σ_0 is the tensile stress acting along every axis and ϵ_0 is the free linear strain. As shown by Fukuhara and Takano [172], for the basic case of uniaxial expansion

along [001] a similar equation reads:

$$\begin{pmatrix} \sigma_T \\ \sigma_T \\ \sigma_L \end{pmatrix} = \begin{pmatrix} C_{11} & C_{12} & C_{12} \\ C_{12} & C_{11} & C_{12} \\ C_{12} & C_{12} & C_{11} \end{pmatrix} \cdot \begin{pmatrix} \epsilon_T \\ \epsilon_T \\ \epsilon_L \end{pmatrix} \quad , \tag{5.12}$$

where subscripts T and L refer to transverse and longitudinal strains and stresses. Comparing the longitudinal stresses in the isotropic and non-isotropic cases ($\sigma_0 = \sigma_L$), a formula for free strain expressed in terms of longitudinal and transverse strains is derived:

$$\epsilon_0 = \frac{2C_{12}\epsilon_T + C_{11}\epsilon_L}{2C_{12} + C_{11}} \quad . \tag{5.13}$$

Similar reasoning can be applied to the derivation of free strain in the case of tensile strain along [011] direction. However, this time the full stiffness tensor needs to be considered:

$$\begin{pmatrix} \sigma_{T_1} \\ \sigma_{T_2} \\ \sigma_L \\ 0 \\ 0 \\ 0 \end{pmatrix} = \mathbf{C}' \cdot \begin{pmatrix} \epsilon_{T_1} \\ \epsilon_{T_2} \\ \sigma_L \\ 0 \\ 0 \\ 0 \end{pmatrix} \quad , \tag{5.14}$$

where T_1 and T_2 subscripts refer to [100] and [0$\bar{1}$1] directions respectively. Due to the choice of coordinate system, the [011] direction is aligned along the $\hat{\mathbf{z}}$-axis. Therefore $\mathbf{C}'$ is a stiffness tensor given by 2.44 appropriately rotated. The above investigation leads to the final expression for free strain:

$$\epsilon_0 = \frac{C_{12}}{C_{11} + 2C_{12}}\epsilon_{T_1} + \frac{C_{11} + C_{12} - 2C_{44}}{2(C_{11} + 2C_{12})}\epsilon_{T_2} + \frac{C_{11} + C_{12} + 2C_{44}}{2(C_{11} + 2C_{12})}\epsilon_L \quad . \tag{5.15}$$

Tantalum's elastic coefficients at ambient conditions are [173]:

$$C_{11} = 261\,\text{GPa}, \quad C_{12} = 157\,\text{GPa}, \quad C_{44} = 82\,\text{GPa} \quad .$$

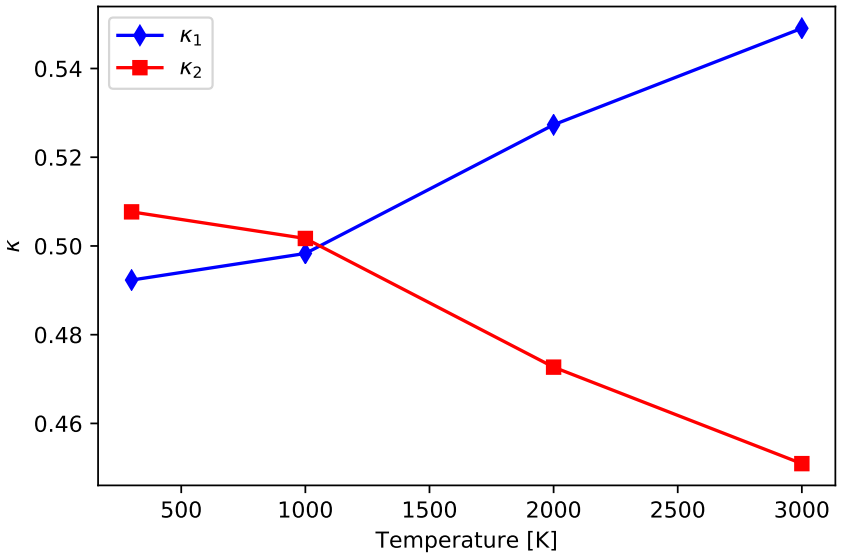


Figure 5.15: Coefficients κ_1 and κ_2 at ambient pressure as a function of temperature in MD according to Ravelo Ta2 potential.

Throughout the analysis it was assumed that the two transverse strains are equivalent $(\epsilon_{T_1}{=}\epsilon_{T_2}{=}\epsilon_T)$, which means that:

$$\epsilon_0 = \kappa_1\epsilon_T + \kappa_2\epsilon_L = 0.4939\epsilon_T + 0.5061\epsilon_L \quad . \tag{5.16}$$

It has to be pointed out that the values of the elastic coefficients correspond to measurements taken at 300K, which means that they may differ from the values of the elastic coefficients at elevated temperatures. Figure 5.15 illustrates variations of the coefficients κ_1 and κ_2 as a function of temperature in MD.

It was recognised that some of the images capturing driven diffraction may suffer from a slow reduction in the pressure of the shocked state at long time scales. Therefore the pressure was deducted from the measurement of the velocity of the rear surface of the foils by the use of a VISAR. The locations of diffraction peaks corresponding to the fully-released material were examined in order to determine longitudinal and transverse strains present in the sample. In order to account for the effects associated with the x-ray energy jitter during XRD image processing, the x-ray halo was used as a reference for energy tuning. 2θ positions of multiple halo spots were extracted for every driven XRD image and the weighted mean value of

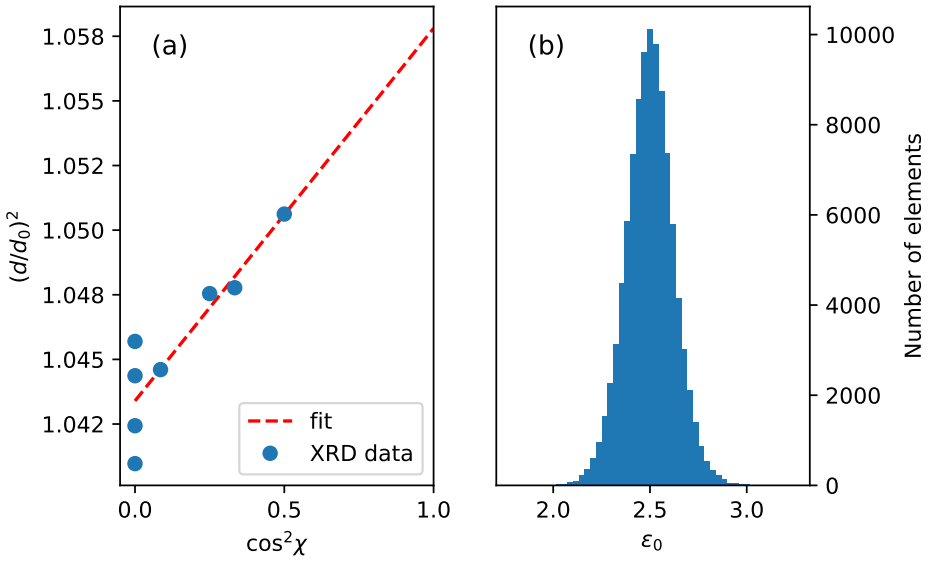


Figure 5.16: a) An example of elastic deformation of the lattice along directions at various χ angles extracted from the location of the signal from released material. The red dashed line represents the best fit to the XRD data. b) The distribution of the free strain obtained by bootstrap method performed on the data shown in a).

the X-ray energies extracted from these locations was used to calculate (via Bragg's law) the corresponding energy of the X-ray beam for every shot.

Theoretical strength investigations [66] indicate a linear relation between the $\cos^2\chi$ and $(d/d_0)^2$. Therefore, the analysis of multiple reflections covering a range of χ space can provide information about the non-isotropic strain state of the material. An example of this analysis is shown in Figure 5.16a. By performing a linear regression, a fit (red dashed line) was obtained. Fitted values of $(d/d_0)^2$ at $\cos^2\chi$=0 and 1 provided information about lattice deformation along the directions perpendicular and longitudinal to direction of shock propagation, respectively. Two sources of errors were considered: the uncertainty associated with the extraction of the central position of the peak (∼1 pixel) and the uncertainty related to evaluation of the longitudinal and transverse strains based on the strength analysis of the material. In order to estimate the uncertainty in the equivalent strain, the uncertainty in the $(d/d_0)^2$ vs $\cos^2\chi$ fit was incorporated by using a bootstrap method. This method relied on resampling data points from normal distribution

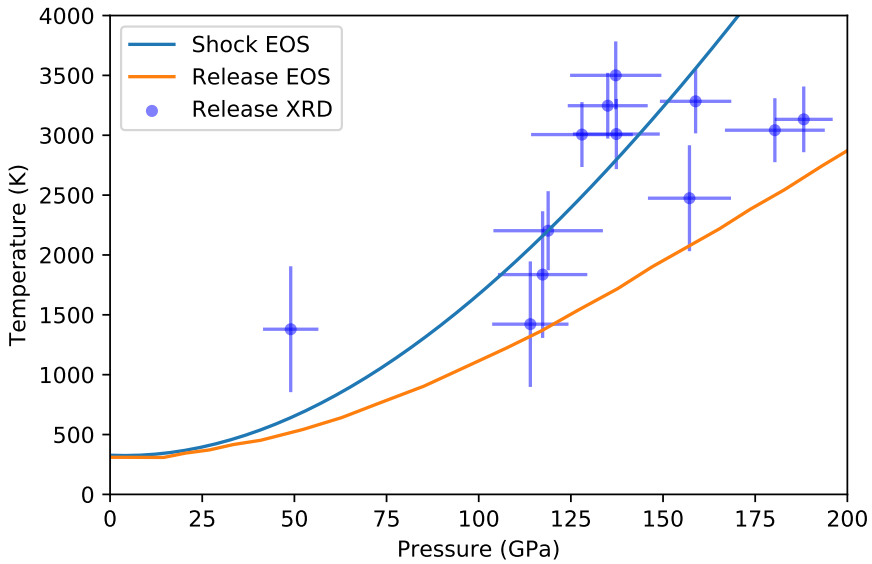


Figure 5.17: Temperature of the released material inferred from the XRD images as a function of the strength of the shock (blue circles). Blue and orange curves correspond to the theoretically-calculated temperatures on shock and release, respectively, from SESAME EOS 3520 [160].

centred around the values of the original data points with standard deviation:

$$\sigma_{\text{sample}} = \sqrt{\frac{1}{n-2}\sum_{i=1}^{n}(y_i - \hat{y}_i)^2} \quad , \tag{5.17}$$

where n is the number of data points, and y_i and $\hat{y}_i$ are true and fitted $(d/d_0)^2$ values, respectively. This routine was repeated multiple times and, for newly resampled datasets, linear fits were performed giving estimations of a free strain. A histogram of collected free strains from a single XRD image is shown in Figure 5.16b. The standard deviation of this distribution provided an uncertainty in the free strain estimation.

Extracted free strains are directly correlated with the temperature of a material via thermal expansion coefficient. Thermal expansion of materials ΔL approximately varies with temperature ΔT in a linear fashion: $\Delta L \propto \Delta T$. However, to include a non-linear relation between temperature and strain at high temperature, the experimentally-measured relationship between interatomic spacing and temperature for tantalum [174] was used. Additionally, MD simulations suggest that due to

variations in the strain rate on release, the amount of heating on release may vary; the temperature of the front surface of the sample can differ from the temperature of the back surface of the sample by about 200 K. This number was incorporated in the extracted temperature uncertainty.

Figure 5.17 presents the extracted temperatures of the fully-released material as a function of the strength of the shock. It was found that for about 100 GPa shock, the temperature of the release material was indeed larger than the temperature on the theoretical release isentrope (orange curve). In some cases, the amount of plastic heating overcame the thermoelastic cooling, resulting in temperatures above Hugoniot temperatures (blue curve). This is consistent with the findings of MD simulations and with the idea of non-isentropic release from a shocked state.

The method of temperature extraction presented in this work relies on multiple assumptions described through the thesis. First of all, it is assumed that the change in the lattice spacing is directly linked to the thermal expansion of the material. Since the free-boundary condition at the rear surface of the material requires the normal stress $\sigma_{zz}$to be equal to zero, the change in the lattice spacing can be associated with the thermal effects. For deeper layers of the sample this link may not be that simple, since release from the front surface will eventually put the sample in tension, leading to the increased interatomic spacing. Experimental data presented in Figure 5.17 refers to the measurement under 1ns after shock breakout. This threshold, identified through HYADES simulations, does not allow the release wave from the front to reach the Ta foil for the majority of the investigated shocks. However, for relatively low shock pressures (i.e. below 50 GPa), it was found that the sample may be affected by the release wave from the front, which could explain the unexpectedly large release temperature after the passage of the 50 GPa shock.

Another element suggesting that the lattice expansion is directly linked to thermal effects is related to tantalum's melting point at ambient conditions. It can be noticed that the experimental data more closely follows the Hugoniot up to around 150 GPa. Above that pressure, the release temperature saturates around

the melt temperature of 3270 K. This saturation point can be associated with the finite enthalpy of melting, preventing the release path from crossing the melt curve.

External sources of heating the sample also need to be considered, as their influence may inflate the amount of heating associated with plastic deformations. X-rays produced by the ablation plasma may be absorbed by the Ta foil leading to its preheating. As described in section 3.7 this is not the case. At relatively low optical laser intensities, hard X-rays are not produced, while soft X-rays are absorbed by the thick kapton ablator. This can be confirmed experimentally, by monitoring the thermal expansion of the part of the sample surrounding the shocked spot via the change of the location of the halo spots. No change of the halo spot location between driven and undriven images is observed; therefore the effect of preheating of the sample is negligible.

The major drawback of the presented temperature measurement method is the large size of uncertainties. There are a number of factors that need to be taken into account for the errorbar estimation. Experimental data is used to evaluate the uncertainties such as error in the peak location extraction from pseudo-Voigt fitting, errors in the longitudinal and transverse elastic strains extracted via strength analysis, and errors in X-ray energy jitter. However, the experimental geometry presented in this work is not sensitive to the precise estimations of the temperature gradient within the sample. Therefore, the estimation of the error due to the temperature gradient is based on the MD simulations. Similarly, the error due to the elastic constants' dependence on the temperature is based on MD results since such experimental data is not available. The combination of all these uncertainties leads to temperature measurements with relatively large errorbars as shown in Figure 5.17.

5.6 Summary

In conclusion, this study investigated thermal effects upon shock breakout from the free surface in tantalum. By performing a number of molecular dynamics simulations, thermoelastic properties of the material were identified. It was observed that due

to the material's strength, large shear stresses within the rarefaction fan result in heating via plastic flow, significantly altering the thermal history of the material with respect to the theoretical isentropic expansion. *In situ* femtosecond XRD data provided information about the state of tensile strain present in the released material, which allowed for the deduction of the temperature of the sample upon its return to ambient conditions. Experimental data agree with the results of MD simulations, suggesting temperatures significantly larger than temperatures on the release isentrope. This is consistent with the picture of a highly non-isentropic return to ambient conditions from a shocked state.

6
Summary and future work

Contents

6.1 Summary **173**
6.2 Future work **175**

6.1 Summary

In Chapter 3, a shock-compression experiment on tantalum, which is the main subject of this thesis, was introduced. Its primary purpose was the investigation of plasticity mechanisms in dynamically-compressed material. The unique feature of the experimental setup was the usage of fibre-texture geometry, which resulted in the appearance of incomplete Debye-Scherrer rings. This allowed for the observation of the azimuthal redistribution of the diffraction signal upon microstructural evolution due to plastic flow. The high quality of the diffraction signal produced by the LCLS beam led to the first *in situ* observation of shock-induced twinning, including the first instance of twin fraction measurement. Moreover, two distinct pressure regimes displaying two different plastic responses were identified. Specifically, it was observed that for shocks below 100 GPa the dominant plastic mechanism is twinning, while above 150 GPa the dominant plastic mechanism is slip.

Following the analysis of deformations during shock, the release portion of the dynamic compression event was investigated. A continuation of the study of the signal within diffraction rings revealed that the majority of microstructural changes induced by shock-compression are reversed upon release. Detwinning and reversed lattice rotations have significant implications in the context of comparisons between this study and *post facto* recovery experiments, highlighting the importance *in situ* investigations. The results of the experimental work are supported by the large scale molecular dynamics simulations, suggesting good agreement with the XRD data of Ta on both shock and release. A large portion of Chapter 4 was dedicated towards an analysis of the intensity of the signal from the release diffraction paths. An algorithm based on the iterative procedure and able to extract strain profiles from the diffraction images was developed, providing results consistent with the theory of rarefaction fan evolution.

Finally, a description of the study analysing thermal effects after shock breakout from the free surface was provided. The textbook picture of a rarefaction wave treats it as an isentropic deformation, meaning that the material experiences a temperature drop due to the thermoelastic cooling associated with the volumetric expansion of the unit cell during unloading. Performed molecular dynamics simulations indicate that this description is incomplete, as the plastic heating associated with the relaxation of large shear stresses present in the rarefaction fan needs to be included in the temperature evolution model. MD simulations suggests that temperature correction due to plastic heating can be as large as a few hundred Kelvin. This idea of non-isentropic release was experimentally examined by measuring the thermal expansion of the fully-released material from XRD. The inferred temperatures of Ta indicate that, after return to ambient conditions, the sample is significantly hotter than the model of isentropic expansion predicts, which is in agreement with the molecular dynamics study.

6.2 Future work

This work on plastic deformations in tantalum is the first approach of using x-ray diffraction geometry utilizing highly-textured materials. The method has proven to provide insights into the microstructural state of bcc metal during shock compression. An obvious area of further enquiry would be materials with different crystallographic structures. For example, work by Suggit *et al.* [34] has already demonstrated shock-induced lattice rotations in single-crystal copper; the technique outlined in this thesis could be used to extend that study to polycrystalline Cu samples.

Another potentially fruitful subject of investigation could be the influence of the original microstructure of the sample on the character of plastic flow. Grain boundary effects bring another dimension into the study of plasticity. Further investigations on targets with various grain sizes and textures would make it possible to examine whether the deformation mechanisms reported by this study are microstructure-specific. For example, in the discussion regarding detwinning it was remarked that *ex situ* studies on the recovered sample with large grain sizes report non-negligible amounts of the twinning. This suggests that polycrystalline materials with a small cross-sectional area of grains may be more sensitive to the disappearance of shock-induced twins during release.

Finally, the molecular dynamics study of thermoelastic effects in releasing tantalum revealed a noticeable temperature-sensitive discrepancy between true and theoretical temperature evolution. An explanation of this phenomenon in MD simulations would require further investigation. In order to understand this effect, it may be worth studying a longer range of initial temperatures as well as various potentials in the context of purely elastic release; however, at present this phenomenon remains a mystery.

Appendices

A
HYADES

An example of the HYADES input script. The purpose of the simulation is to represent the application of a 5ns long top-hat laser pulse onto a CH/Ta target which launches a shock wave into the target. Lines starting with the letter 'c' are ignored by the code interpreter and provide comments on the script structure.

```
140GPa shock - MEC_Ta
c
c 50.0 um CH layer
c
mesh 1 1000 0. 0.002 1.0073
mesh 1000 1208 0.002 0.005
region 1 1207 1 1.044
material 1 6. 12. 0.5
material 1 1. 1. 0.5
eos 32 1
c
c 6.0 um Tantalum layer
c
mesh 1208 1871 0.005 0.0056
```

```
region 1208 1870 2 16.65
material 2 73. 180.95 1.
eos 271 2
c define the strength model
c region number, shear modulus, strength model
strength 2 2 3 1 $Steinberg model, and maximum principal stress model
c Ta shear, yield & melt values from Steinberg's blue book.
data shear 2 6.9e+11 1.45e-12 1.3e+3
data yield 2 2.7e+10 22 0 0.283 0.7e+11
data tmelt 2 3.74e-4 1.3 1.67
c specify laser, wavelength, direction of propagation
source laser .527 1
c this is a multiplier for your laser power
sourcem 0.5
c specify pulse shape
c this produces about 140 GPa shock
tv 0. 0.
tv 0.05e-9 4e19
tv 5.05e-9 4e19
tv 5.10e-9 0.
c
c these commands help when using hyades to study solid materials
parm temin 2.5689E-05
parm timin 2.5689E-05
parm trmin 2.5689E-05
parm flxlem .05 $ almost always use for laser driven materials
c
c setup us post processing
pparray r rcm rho pres te u
c
```

```
c how often to write to your post processing file
parm postdt 0.3e-10
c
parm editdt 1.e-10
parm nstop 9999999
parm tstop 30.0e-9
parm itmcyc 10
```

References

[1] W J Macquorn Rankine. *On the Thermodynamic Theory of Waves of Finite Longitudinal Disturbance*. Tech. rep. 1870, pp. 277–288.

[2] Peter O. K. Krehl. *History of Shock Waves, Explosions and Impact*. Springer-Verlag Berlin Heidelberg, 2009.

[3] J. N. Johnson and R. Cheret. "Shock waves in solids: an evolutionary perspective". *Shock Waves* 9 (1999), pp. 193–200.

[4] J. R. Ashworth and H. Schneider. "Deformation and transformation in experimentally shock-loaded quartz". *Physics and Chemistry of Minerals* 11 (1985), pp. 241–249.

[5] Dennison Bancroft, Eric L. Peterson, and Stanley Minshall. "Polymorphism of Iron at High Pressure". *Journal of Applied Physics* 27 (1956), p. 291.

[6] John M. Walsh and Russell H. Christian. "Equation of State of Metals from Shock Wave Measurements". *Physical Review* 97 (1955), pp. 1544–1556.

[7] D Keefe. "Inertial Confinement Fusion". *Annual Review of Nuclear and Particle Science* 32 (1982), pp. 391–441.

[8] W. H. Gust and E. B. Royce. "Axial Yield Strengths and Two Successive Phase Transition Stresses for Crystalline Silicon". *Journal of Applied Physics* 42 (1971), pp. 1897–1905.

[9] R. F. Smith et al. "Orientation and rate dependence in high strain-rate compression of single-crystal silicon". *Physical Review B* 86 (2012), p. 245204.

[10] S. Pappu et al. "Microstructure analysis and comparison of tungsten alloy rod and [001] oriented columnar-grained tungsten rod ballistic penetrators". *Materials Science and Engineering: A* 262 (1999), pp. 115–128.

[11] M. W. Chen et al. "Dynamic plasticity and failure of high-purity alumina under shock loading". *Nature Materials* 5 (2006), pp. 614–618.

[12] K Thoma et al. "An approach to achieve progress in spacecraft shielding". *Advances in Space Research* 34 (2004), pp. 1063–1075.

[13] Neil K. Bourne. "Materials science: Atomistic views of deformation". *Nature* 550 (2017), pp. 461–463.

[14] Bevan M French and Christian Koeberl. "The convincing identification of terrestrial meteorite impact structures: What works, what doesn't, and why". *Earth-Science Reviews* 98 (2010), pp. 123–170.

[15] John M. Walsh et al. "Shock-Wave Compressions of Twenty-Seven Metals. Equations of State of Metals". *Physical Review* 108 (1957), pp. 196–216.

[16] R. G. McQueen and S. P. Marsh. "Equation of State for Nineteen Metallic Elements from Shock-Wave Measurements to Two Megabars". *Journal of Applied Physics* 31 (1960), p. 1253.

[17] R. G. Shreffler and W. E. Deal. "Free Surface Properties of Explosive-Driven Metal Plates". *Journal of Applied Physics* 24 (1953), pp. 44–48.

[18] A.C. Charters. "Development of the high-velocity gas-dynamics gun". *International Journal of Impact Engineering* 5 (1987), pp. 181–203.

[19] A. V. Pavlenko et al. "A one-stage light-gas gun for studying dynamic properties of structural materials in a range up to 40 GPa". *Instruments and Experimental Techniques* 56 (2013), pp. 482–484.

[20] J. Michael Brown and Robert G. McQueen. "Phase transitions, Grüneisen parameter, and elasticity for shocked iron between 77 GPa and 400 GPa". *Journal of Geophysical Research: Solid Earth* 91 (1986), pp. 7485–7494.

[21] N. C. Holmes et al. "The equation of state of platinum to 660 GPa (6.6 Mbar)". *Journal of Applied Physics* 66 (1989), pp. 2962–2967.

[22] R. G. Meyerand and A. F. Haught. "Gas breakdown at optical frequencies". *Proc. of 6th Intern. Conf. on Ionization Phemomena in Gases*. Paris, 1963, p. 479.

[23] C. E. Bell and J. A. Landt. "Laser-induced high-pressure shock waves in water". *Applied Physics Letters* 10 (1967), pp. 46–48.

[24] N. C. Anderholm. "Laser-generated stress waves". *Applied Physics Letters* 16 (1970), pp. 113–115.

[25] R F Smith et al. "Ramp compression of diamond to five terapascals". *Nature* 511 (2014).

[26] J.H. Eggert et al. "Ramp compression of tantalum to 330 GPa". en. *High Pressure Research* 35 (2015), pp. 339–354.

[27] L. M. Barker and R. E. Hollenbach. "Laser interferometer for measuring high velocities of any reflecting surface". *Journal of Applied Physics* 43 (1972), pp. 4669–4675.

[28] P M Celliers et al. "Line-imaging velocimeter for shock diagnostics at the OMEGA laser facility". *Review of Scientific Instruments* 75 (2004), pp. 4916–4929.

[29] Quintin Johnson et al. "X-ray diffraction during shock-wave compression". *Physical Review Letters* 25 (1970), pp. 1099–1101.

[30] Quintin Johnson, Arthur Mitchell, and L. Evans. "X-ray Diffraction Evidence for Crystalline Order and Isotropic Compression during the Shock-wave Process". *Nature* 231 (1971), pp. 310–311.

[31] Quintin Johnson and A C. Mitchell. "First X-Ray Diffraction Evidence for a Phase Transition during Shock-Wave Compression". *Physical Review Letters* 29 (1972), pp. 1369–1371.

[32] Quintin Johnson, Arthur C. Mitchell, and L. Evans. "X-ray diffraction study of single crystals undergoing shock-wave compression". *Applied Physics Letters* 21 (1972), pp. 29–30.

[33] A Loveridge-Smith et al. "Anomalous Elastic Response of Silicon to Uniaxial Shock Compression on Nanosecond Time Scales". *Physical Review Letters* 86 (2001), pp. 2349–2352.

[34] M J Suggit et al. "Nanosecond white-light Laue diffraction measurements of dislocation microstructure in shock-compressed single-crystal copper." *Nature communications* 3 (2012), p. 1224.

[35] A J Comley et al. "Strength of Shock-Loaded Single-Crystal Tantalum [100] Determined using In Situ Broadband X-Ray Laue Diffraction". *Physical Review Letters* 110 (2013), p. 115501.

[36] C E Wehrenberg et al. "Lattice-level observation of the elastic-to-plastic relaxation process with subnanosecond resolution in shock-compressed Ta using time-resolved in situ Laue diffraction". *Physical Review B* 92 (2015), p. 104305.

[37] J. S. Wark et al. "Shock launching in silicon studied with use of pulsed x-ray diffraction". *Physical Review B* 35 (1987), pp. 9391–9394.

[38] Justin S. Wark et al. "Subnanosecond X-ray diffraction from laser-shocked crystals". *Physical Review B* 40 (1989), pp. 5705–5714.

[39] D. H. Kalantar et al. "Direct Observation of the alpha - epsilon Transition in Shock-Compressed Iron via Nanosecond X-Ray Diffraction". *Physical Review Letters* 95 (2005), p. 075502.

[40] D.H. Kalantar et al. "In situ diffraction measurements of lattice response due to shock loading, including direct observation of the alpha-epsilon phase transition in iron". *International Journal of Impact Engineering* 33 (2006), pp. 343–352.

[41] Stefan J. Turneaure et al. "Real-time microstructure of shocked LiF crystals: Use of synchrotron x-rays". *Journal of Applied Physics* 105 (2009), p. 053520.

[42] Stefan J. Turneaure and Y. M. Gupta. "Real time synchrotron x-ray diffraction measurements to determine material strength of shocked single crystals following compression and release". *Journal of Applied Physics* 106 (2009), p. 033513.

[43] Y. M. Gupta et al. "Real-time, high-resolution x-ray diffraction measurements on shocked crystals at a synchrotron facility". *Review of Scientific Instruments* 83 (2012), p. 123905.

[44] Stefan J. Turneaure, N. Sinclair, and Y. M. Gupta. "Real-Time Examination of Atomistic Mechanisms during Shock-Induced Structural Transformation in Silicon". *Physical Review Letters* 117 (2016), p. 045502.

[45] Stefan J. Turneaure et al. "Twinning and Dislocation Evolution during Shock Compression and Release of Single Crystals: Real-Time X-Ray Diffraction". *Physical Review Letters* 120 (2018), p. 265503.

[46] D Milathianaki et al. "Femtosecond visualization of lattice dynamics in shock-compressed matter." *Science (New York, N.Y.)* 342 (2013), pp. 220–3.

[47] M. G. Gorman et al. "Direct Observation of Melting in Shock-Compressed Bismuth With Femtosecond X-ray Diffraction". *Physical Review Letters* 115 (2015), p. 095701.

[48] A. E. Gleason et al. "Ultrafast visualization of crystallization and grain growth in shock-compressed SiO2". *Nature Communications* 6 (2015), p. 8191.

[49] R. Briggs et al. "Ultrafast X-Ray Diffraction Studies of the Phase Transitions and Equation of State of Scandium Shock Compressed to 82 GPa". *Physical Review Letters* 118 (2017), p. 025501.

[50] A. E. Gleason et al. "Compression Freezing Kinetics of Water to Ice VII". *Physical Review Letters* 119 (2017), p. 025701.

[51] Anthony Kelly and Kevin M Knowles. *Crystallography and Crystal Defects*. John Wiley & Sons, 2012.

[52] M A Meyers. *Dynamic Behaviour of Materials*. New York: John Wiley and Sons, Inc., 1994.

[53] B. E. Warren. *X-ray diffraction*. Dover Publications, 1990.

[54] E. M. Bringa et al. "Shock deformation of face-centred-cubic metals on subnanosecond timescales". *Nature Materials* 5 (2006), pp. 805–809.

[55] R Ravelo et al. "Shock-induced plasticity in tantalum single crystals: Interatomic potentials and large-scale molecular-dynamics simulations". *Physical Review B* 88 (2013), p. 134101.

[56] R E Rudd et al. "Theory and simulation of 1D to 3D plastic relaxation in tantalum". *AIP Conference Proceedings*. Vol. 1426. 2012, pp. 1379–1382.

[57] J .F. Nye. *Physical Properties of Crystals*. Oxford University Press, 1985.

[58] Steven H. Simon. *The Oxford Solid State Basics*. Oxford University Press, 2013.

[59] E. Orowan. "Problems of plastic gliding". *Proceedings of the Physical Society* 52 (1940), pp. 8–22.

[60] G. I. Taylor. "The Mechanism of Plastic Deformation of Crystals. Part I. Theoretical". *Proceedings of the Royal Society A* 145 (1934), pp. 362–387.

[61] W. T. Read. *Dislocations in Crystals*. McGraw-Hill, 1954.

[62] P. Hirsch et al. "50 Years of TEM of dislocations: Past, present and future". *Philosophical Magazine* 86 (2006), pp. 4519–4528.

[63] M. Polanyi. "Das Rontgen-Faserdiagramm (Erste Mitteliung)". *Zeitschrift fur Phys.* 7 (1921), pp. 149–180.

[64] M. Polanyi. "Das Rontgen-Faserdiagramm (Zweite Mitteilung)". *Zeitschrift fur Phys.* 9 (1922), pp. 123–130.

[65] Norbert Stribeck. "On the determination of fiber tilt angles in fiber diffraction". *Acta Crystallographica A* 65 (2009), pp. 46–47.

[66] David McGonegle et al. "Simulations of x-ray diffraction from uniaxially-compressed highly-textured polycrystalline targets". *Journal of Applied Physics* 118 (2015), p. 065902.

[67] Lynn M. Barker. "The development of the VISAR, and its use in shock compression science". AIP Publishing, 2003, pp. 11–18.

[68] D. R. Bland. "On Shock Structure in a Solid". *IMA Journal of Applied Mathematics* 1 (1965), pp. 56–75.

[69] Gregory H Miller, Edward M Stolper, and Thomas J Ahrens. *The Equation of State of a Molten Komatiite 1. Shock Wave Compression to 36 GPa*. Tech. rep. 1991, pp. 831–842.

[70] D. E. Grady. *Physics of Shock and Impact*. IOP Publishing, 2017.

[71] J. W. Swegle and D. E. Grady. "Shock viscosity and the prediction of shock wave rise times". *Journal of Applied Physics* 58 (1985), pp. 692–701.

[72] J. R. Asay and L. C. Chhabildas. "Determination of the Shear Strength of Shock Compressed 6061-T6 Aluminum". *Shock Waves and High-Strain-Rate Phenomena in Metals*. Boston, MA: Springer US, 1981, pp. 417–431.

[73] P A Rigg, R J Scharff, and R S Hixson. "Sound speed measurements in tantalum using the front surface impact technique". *Journal of Physics: Conference Series* 500 (2014), p. 032018.

[74] Steve Plimpton. "Fast Parallel Algorithms for Short-Range Molecular Dynamics". *Journal of Computational Physics* 117 (1995), pp. 1–19.

[75] Benjamin FrantzDale, Steven J. Plimpton, and Mark S. Shephard. "Software components for parallel multiscale simulation: an example with LAMMPS". *Engineering with Computers* 26 (2010), pp. 205–211.

[76] Loup Verlet. "Computer "Experiments" on Classical Fluids. I. Thermodynamical Properties of Lennard-Jones Molecules". *Physical Review* 159 (1967), pp. 98–103.

[77] Murray S. Daw and M. I. Baskes. "Semiempirical, Quantum Mechanical Calculation of Hydrogen Embrittlement in Metals". *Physical Review Letters* 50 (1983), pp. 1285–1288.

[78] Giles Kimminau et al. "Simulating picosecond x-ray diffraction from shocked crystals using post-processing molecular dynamics calculations". *Journal of Physics: Condensed Matter* 20 (2008), p. 505203.

[79] David J. Benson and David J. "Computational methods in Lagrangian and Eulerian hydrocodes". *Computer Methods in Applied Mechanics and Engineering* 99 (1992), pp. 235–394.

[80] G. R. Johnson and W. H. Cook. "A constitutive model and data for metals subjected to large strains, high strain rates and high temperatures." *Proceedings of the 7th International Symposium on Ballistics* 21 (1983), pp. 541–547.

[81] D. J. Steinberg, S. G. Cochran, and M. W. Guinan. "A constitutive model for metals applicable at high-strain rate". *Journal of Applied Physics* 51 (1980), pp. 1498–1504.

[82] Frank J. Zerilli and Ronald W. Armstrong. "Dislocation-mechanics-based constitutive relations for material dynamics calculations". *Journal of Applied Physics* 61 (1987), pp. 1816–1825.

[83] C. Pellegrini. "The history of X-ray free-electron lasers". *The European Physical Journal H* 37 (2012), pp. 659–708.

[84] G Margaritondo and Primoz Rebernik Ribic. "A simplified description of X-ray free-electron lasers." *Journal of synchrotron radiation* 18 (2011), pp. 101–8.

[85] R. W. Buckman. "New applications for tantalum and tantalum alloys". *JOM* 52 (2000), pp. 40–41.

[86] S. Taioli et al. "Melting curve of tantalum from first principles". *Physical Review B - Condensed Matter and Materials Physics* 75 (2007), p. 214103.

[87] Moriarty et al. "Quantum-based atomistic simulation of materials properties in transition metals". *Journal of Physics: Condensed Matter* 14 (2002).

[88] Martin Magnuson et al. "Electronic structure of β-Ta films from X-ray photoelectron spectroscopy and first-principles calculations". *Applied Surface Science* 470 (2019), pp. 607–612.

[89] L M Hsiung and D H Lassila. "Shock-induced deformation twinning and omega transformation in tantalum and tantalum–tungsten alloys". *Acta Materialia* 48 (2000), pp. 4851–4865.

[90] C.-H. Lu et al. "Phase Transformation in Tantalum under Extreme Laser Deformation". *Scientific Reports* 5 (2015), p. 15064.

[91] Chengda Dai, Jianbo Hu, and Hua Tan. "Hugoniot temperatures and melting of tantalum under shock compression determined by optical pyrometry". *Journal of Applied Physics* 106 (2009), p. 043519.

[92] M. G. Gorman et al. "Femtosecond diffraction studies of solid and liquid phase changes in shock-compressed bismuth". *Scientific Reports* 8 (2018), p. 16927.

[93] D Tramontina et al. "Molecular dynamics simulations of shock-induced plasticity in tantalum". *High Energy Density Physics* 10 (2014), pp. 9–15.

[94] A Higginbotham et al. "Molecular dynamics simulations of shock-induced deformation twinning of a body-centered-cubic metal". *Physical Review B* 88 (2013), p. 104105.

[95] L E Murr et al. "Shock-induced deformation twinning in tantalum". *Acta Materialia* 45 (1996), pp. 157–175.

[96] C H Lu et al. "Laser compression of monocrystalline tantalum". *Acta Materialia* 60 (2012), pp. 6601–6620.

[97] J N Florando et al. "Analysis of deformation twinning in tantalum single crystals under shock loading conditions". *Journal of Applied Physics* 113 (2013), p. 083522.

[98] C H Lu et al. "Laser compression of nanocrystalline tantalum". *Acta Materialia* 61 (2013), pp. 7767–7780.

[99] Jyoti Prakash, L P Pathak, and M P Hemkar. "Phonon Dispersion Relations for Chromium and Tantalum". *Aust. J. Phys.* 28 (1975), pp. 57–61.

[100] A. C. Mitchell and W. J. Nellis. "Shock compression of aluminum, copper, and tantalum". *Journal of Applied Physics* 52 (1981), pp. 3363–3374.

[101] D. Batani et al. "Ablation pressure scaling at short laser wavelength". *Physical Review E* 68 (2003), p. 067403.

[102] Damian C. Swift et al. "Shock pressures induced in condensed matter by laser ablation". *Physical Review E* 69 (2004), p. 036406.

[103] J H Hubbell and S M Seltzer. "X-Ray Mass Attenuation Coefficients". *NIST Standard Reference Database 126* (2004).

[104] Bob Nagler et al. "The Matter in Extreme Conditions instrument at the Linac Coherent Light Source". *Journal of Synchrotron Radiation* 22 (2015), pp. 520–525.

[105] Michael P. Minitti et al. "Optical laser systems at the Linac Coherent Light Source". *Journal of Synchrotron Radiation* 22 (2015), pp. 526–531.

[106] J. Als-Nielsen and D. McMorrow. *Elements of modern X-ray Physics*. Wiley, 2000.

[107] James Dunn et al. "1 – 10 Mbar Laser-Driven Shocks Using the Janus Laser Facility". *AIP Conference Proceedings* 620 (2002), p. 1371.

[108] Shalom Eliezer and Kunioki Mima. *Applications of Laser-Plasma Interactions*. CRC Press, 2009.

[109] I. H. Malitson. "Interspecimen Comparison of the Refractive Index of Fused Silica". *JOSA* 55 (1965), pp. 1205–1208.

[110] Claude Roddier and François Roddier. "Interferogram analysis using Fourier transform techniques". *Applied Optics* 26 (1987), p. 1668.

[111] Hugh T Philipp et al. "Pixel array detector for X-ray free electron laser experiments". *Nuclear Instruments and Methods in Physics Research Section A* 649 (2011), pp. 67–69.

[112] R. G. McQueen and S. P. Marsh. *Report No. GMX-6-566*. Tech. rep. Los Alamos Sci. Lab, 1964, pp. 51–62.

[113] R. G. McQueen et al. *The equation of state of solids from shock wave studies*. New-York: Academic Press, 1970, pp. 293–417.

[114] S. P. Marsh. *LASL Shock Hugoniot Data*. Tech. rep. Berkeley: Univ. California Press, 1980.

[115] Trunin et al. "Compression of porous metals in shock waves". *Zh. Eksp. Teor. Fiz.* 96 (1989), pp. 1024–1038.

[116] Jon H. Eggert et al. "Quantitative structure factor and density measurements of high-pressure fluids in diamond anvil cells by x-ray diffraction: Argon and water". *Physical Review B* 65 (2002), p. 174105.

[117] P J Brown et al. "Chapter 6.1 Intensity of diffracted intensities". *International Tables for Crystallography. Vol. C*. 2006, pp. 554–595.

[118] S V Raju et al. "High pressure and temperature structure of liquid and solid Cd: implications for the melting curve of Cd". *Materials Research Express* 1 (2014), p. 046502.

[119] L Calderin, L E Gonzalez, and D J Gonzalez. "An ab initio study of the structure and dynamics of bulk liquid Cd and its liquid–vapor interface". *Journal of Physics: Condensed Matter* 25 (2013), p. 065102.

[120] Agnès Dewaele, Paul Loubeyre, and Mohamed Mezouar. "Equations of state of six metals above 94 GPa". *Physical Review B* 70 (2004), p. 094112.

[121] Hyunchae Cynn and Choong-Shik Yoo. "Equation of state of tantalum to 174 GPa". *Physical Review B* 59 (1999), pp. 8526–8529.

[122] Th. H. de Keijser et al. "Use of the Voigt function in a single-line method for the analysis of X-ray diffraction line broadening". *Journal of Applied Crystallography* 15 (1982), pp. 308–314.

[123] F Sanchez-Bajo and F L Cumbrera. *The Use of the Pseudo-Voigt Function in the Variance Method of X-ray Line-Broadening Analysis*. Tech. rep. 1997, pp. 427–430.

[124] Andrew Higginbotham and David McGonegle. "Prediction of Debye-Scherrer diffraction patterns in arbitrarily strained samples". *Journal of Applied Physics* 115 (2014), p. 174906.

[125] Jiangwei Wang et al. "In situ atomic-scale observation of twinning dominated deformation in nanoscale body-centred cubic tungsten". *Nature Materials* 14 (2015), pp. 594–600.

[126] Agnès Dewaele et al. "High Melting Points of Tantalum in a Laser-Heated Diamond Anvil Cell". *Physical Review Letters* 104 (2010), p. 255701.

[127] Ramon Ravelo et al. "Directional-dependence in shock-induced melting of FCC metals". *AIP Conference Proceedings*. Vol. 845 I. 2006, pp. 270–273.

[128] Qi An et al. "Melting of Cu under hydrostatic and shock wave loading to high pressures". *Journal of Physics Condensed Matter* 20 (2008).

[129] Valery I. Levitas and Ramon Ravelo. "Virtual melting as a new mechanism of stress relaxation under high strain rate loading". *Proceedings of the National Academy of Sciences of the United States of America* 109 (2012), pp. 13204–13207.

[130] Mikalai M. Budzevich et al. "Evolution of shock-induced orientation-dependent metastable states in crystalline aluminum". *Physical Review Letters* 109 (2012).

[131] C. S. Smith. "Metaliographic Studies of Metals after Explosive Shock". *TMS-AIME* 212 (1958), p. 574.

[132] Marc A. Meyers. "A mechanism for dislocation generation in shock-wave deformation". *Scripta Metallurgica* 12 (1978), pp. 21–26.

[133] F. A. Bandak, R. W. Armstrong, and A. S. Douglas. "Dislocation structure for one-dimensional strain in a shocked crystal". *Physical Review B* 46 (1992), pp. 3228–3235.

[134] L L Hsiung. "Shock-induced phase transformation in tantalum". *Journal of Physics: Condensed Matter* 22 (2010), p. 385702.

[135] H N Jarmakani et al. "Molecular dynamics simulations of shock compression of nickel: From monocrystals to nanocrystals". *Acta Materialia* 56 (2008), pp. 5584–5602.

[136] D Errandonea et al. "Melting of tantalum at high pressure determined by angle dispersive x-ray diffraction in a double-sided laser-heated diamond-anvil cell". *Journal of Physics: Condensed Matter* 15 (2003), pp. 7635–7649.

[137] Christine J. Wu et al. "Shear-induced anisotropic plastic flow from body-centred-cubic tantalum before melting". *Nature Materials* 8 (2009), pp. 223–228.

[138] Javier Ruiz-Fuertes et al. "Microscopic evidence of a flat melting curve of tantalum". *Physics of the Earth and Planetary Interiors* 181 (2010), pp. 69–72.

[139] A. Stukowski. "Visualization and analysis of atomistic simulation data with OVITO–the Open Visualization Tool". *Model. Simul. Mater. Sci. Eng.* 18 (2010).

[140] A. Stukowski and K. Albe. "Extracting dislocations and non-dislocation crystal defects from atomistic simulation data". *Model. Simul. Mater. Sci. Eng.* 18 (2010).

[141] B. C. Larson et al. "Time-resolved x-ray diffraction measurement of the temperature and temperature gradients in silicon during pulsed laser annealing". *Applied Physics Letters* 42 (1983), pp. 282–284.

[142] Christoph Rose-Petruck et al. "Picosecond–milliångström lattice dynamics measured by ultrafast X-ray diffraction". *Nature* 398 (1999), pp. 310–312.

[143] R. G. McQueen, J. W. Hopson, and J. N. Fritz. "Optical technique for determining rarefaction wave velocities at very high pressures". *Review of Scientific Instruments* 53 (1982), pp. 245–250.

[144] Jianbo Hu et al. "Sound velocity measurements of tantalum under shock compression in the 10-110 GPa range". *Journal of Applied Physics* 111 (2012), p. 033511.

[145] Feng Xi et al. "Sound velocity of tantalum under shock compression in the 18–142 GPa range". *Journal of Applied Physics* 117 (2015), p. 185901.

[146] Jon T. Larsen and Stephen M. Lane. "HYADES—A plasma hydrodynamics code for dense plasma studies". *Journal of Quantitative Spectroscopy and Radiative Transfer* 51 (1994), pp. 179–186.

[147] Daniel J Steinberg. *Equation of State and Strength Properties of Selected Materials*. Tech. rep. Livermore: Lawrence Livermore National Laboratory, 1996.

[148] Daniel Orlikowski, Per Söderlind, and John A. Moriarty. "First-principles thermoelasticity of transition metals at high pressure: Tantalum prototype in the quasiharmonic limit". *Physical Review B* 74 (2006), p. 054109.

[149] W Thomson. "On the Dynamical Theory of Heat". *Transactions of the Royal Society of Edinburgh* 20 (1853), pp. 261–288.

[150] A. M. Molodets. "Use of the Gruneisen Coefficient in Calculations of Temperature along the Isentrope of Elementary Substances". *Combustion, Explosion, and Shock Waves* 37 (2001), pp. 455–460.

[151] E. M. Bringa et al. "Ultrahigh Strength in Nanocrystalline Materials Under Shock Loading". *Science* 309 (2005), pp. 1838–1841.

[152] Robert E. Rudd. "High-Rate Plastic Deformation of Nanocrystalline Tantalum to Large Strains: Molecular Dynamics Simulation". *Materials Science Forum* 633-634 (2009), pp. 3–19.

[153] M.A. Meyers et al. "Laser-induced shock compression of monocrystalline copper: characterization and analysis". *Acta Materialia* 51 (2003), pp. 1211–1228.

[154] W J Murphy et al. "The strength of single crystal copper under uniaxial shock compression at 100 GPa". *Journal of Physics: Condensed Matter* 22 (2010), p. 065404.

[155] Damian C. Swift et al. "Shock and release temperatures in molybdenum: Experiment and theory". *Physical Review B* 76 (2007), p. 054122.

[156] W. S. Farren and G. I. Taylor. "The Heat Developed during Plastic Extension of Metals". *Proceedings of the Royal Society A* 107 (1925), pp. 422–451.

[157] P. Rosakis et al. "A thermodynamic internal variable model for the partition of plastic work into heat and stored energy in metals". *Journal of the Mechanics and Physics of Solids* 48 (2000), pp. 581–607.

[158] J.J. Mason, A.J. Rosakis, and G. Ravichandran. "On the strain and strain rate dependence of the fraction of plastic work converted to heat: an experimental study using high speed infrared detectors and the Kolsky bar". *Mechanics of Materials* 17 (1994), pp. 135–145.

[159] M.B Bever and L.B Ticknor. "The energy stored during the cold working of a gold-silver alloy". *Acta Metallurgica* 1 (1953), pp. 116–122.

[160] B. Bennett. *Sandia National Laboratories Report No. SCRR-70-28*. Tech. rep. 1983.

[161] X. W. Zhou, R. A. Johnson, and H. N. G. Wadley. "Misfit-energy-increasing dislocations in vapor-deposited CoFe/NiFe multilayers". *Physical Review B* 69 (2004), p. 144113.

[162] G.P. Purja Pun et al. "Angular-dependent interatomic potential for the Cu–Ta system and its application to structural stability of nano-crystalline alloys". *Acta Materialia* 100 (2015), pp. 377–391.

[163] H Gao et al. "An empirical model for silver tantalate". *Modelling and Simulation in Materials Science and Engineering* 21 (2013), p. 055002.

[164] Youhong Li et al. "Embedded-atom-method tantalum potential developed by the force-matching method". *Physical Review B* 67 (2003), p. 125101.

[165] Ronald E. Cohen and O. Gulseren. "Thermal equation of state of tantalum". *Physical Review B* 63 (2001), p. 224101.

[166] Zhong-Li Liu et al. "Ab initio refinement of the thermal equation of state for bcc tantalum: the effect of bonding on anharmonicity". *Journal of Physics: Condensed Matter* 21 (2009), p. 095408.

[167] A Savitzky and M J E Golay. "Smoothing and Differentiation of Data by Simplified Least Squares Procedures". *Analytical Chemistry* 36 (1964), pp. 1627–1639.

[168] J.D. Clayton. "Dynamic plasticity and fracture in high density polycrystals: constitutive modeling and numerical simulation". *Journal of the Mechanics and Physics of Solids* 53 (2005), pp. 261–301.

[169] Ramon Ravelo et al. "High Strain Rates Effects in Quasi-Isentropic Compression of Solids". *AIP Conference Proceedings*. Vol. 1195. American Institute of Physics, 2009, pp. 825–828.

[170] Eric N Hahn et al. "On the ultimate tensile strength of tantalum". *Acta Materialia* 126 (2017), pp. 313–328.

[171] Gerald I Kerley. *Calculation of Release Adiabats and Shock Impedance Matching*. Tech. rep. 2008.

[172] A. Fukuhara and Y. Takano. "Determination of strain distributions from X-ray Bragg reflexion by silicon single crystals". *Acta Crystallographica Section A* 33 (1977), pp. 137–142.

[173] F. H. Featherston and J. R. Neighbours. "Elastic Constants of Tantalum, Tungsten, and Molybdenum". *Physical Review* 130 (1963), pp. 1324–1333.

[174] Kai Wang and Robert R. Reeber. "The role of defects on thermophysical properties: Thermal expansion of V, Nb, Ta, Mo and W". *Materials Science and Engineering: R: Reports* 23 (1998), pp. 101–137.